

An investigation into the complementary capabilities of X-ray computed tomography and hyperspectral imaging of drill core in geometallurgy



Dineo Mashaba

A thesis submitted to the University of Cape Town in fulfilment of the
degree of

Master of Science

Department of Chemical Engineering

University of Cape Town

2022

The copyright of this thesis vests in the author. No quotation from it or information derived from it is to be published without full acknowledgement of the source. The thesis is to be used for private study or non-commercial research purposes only.

Published by the University of Cape Town (UCT) in terms of the non-exclusive license granted to UCT by the author.

Declaration

I declare that this thesis is my work. It is being submitted for the Master of Science (MSc) degree at the University of Cape Town. This thesis has not been submitted before any degree or examination in any other university.

Dineo Mashaba

Signed by candidate

Abstract

The mining industry is faced with the challenge of mining and processing low grade, heterogeneous, and complex ores, a phenomenon known as ore variability. These ores need to be managed at an early operational stage, ideally during drill core exploration, to avoid risks during the project phase (such as project delays and failure) and operational phases (such as plant instabilities), ultimately affecting the cash flow. The discipline of geometallurgy has arisen to manage the risks associated with ore variability by acquiring upfront knowledge of the mineral assemblage and texture before mining and processing. As we head towards the fourth industrial revolution (4IR), machine learning, intensive and automated data derived from drill cores are becoming more common. In this case, using non-destructive, rapid, and inexpensive automated scanning techniques such as 2D hyperspectral imaging (HSI) and 3D X-ray computed tomography (XCT) have the potential to be incorporated into the machine learning dataset.

Hyperspectral imaging is a critical component of continuous drill core scanning in geometallurgy for identifying problematic minerals in downstream mineral processing, such as the phyllosilicates (e.g., kaolinite, serpentine and talc). However, it only provides 2D imaging of the core, and its mineral identification is limited to minerals that show a definitive spectral response. On the other hand, XCT provides 3D imaging of drill cores, but is more routinely used in research applications and does not independently give the mineral assemblage. Mineral identification and discrimination for XCT is limited and requires prior mineralogical knowledge and sufficient mineral density and attenuation coefficient variation greater than 6%.

No systematic study to date appears to have explored how the results from these two techniques can be integrated using a local South African magmatic nickel-copper-platinum group element (Ni-Cu-PGE) ore case study. This opened an opportunity to couple the two techniques to address and emphasize the image scanning techniques for drill core in geometallurgy and to provide further knowledge on the practicality of the HSI and XCT in drill core from image acquisition to processing. Ultimately, the aim is to investigate how well the techniques complement each other for mineral and texture identifications and, if combined, will produce additional mineralogical and textural information. The objective of this study was achieved by moving HSI cores to smaller samples than standard practice to produce 25 mm diameter mini cores instead of standard cores (e.g., 50 mm in diameter). For accurate mineral assemblage and textural characterisation of the drill cores, manual core logging, quantitative evaluation of minerals by scanning electron microscopy (QEMSCAN) and quantitative X-ray diffraction (QXRD) were used as supporting techniques.

The results showed HSI scanning on the magmatic Ni-Cu-PGE drill core to be challenging because of pervasive mineral alteration and the nature of the rock types (mafic and ultra-mafic rocks) - providing limited information on the mineral assemblage and texture due to low scanning resolution and pervasive alteration (serpentinisation and chloritization) in the rocks. The limited mineral identification includes mixed-phases (such as serpentine-olivine in visible-shortwave infrared and plagioclase-chlorite in the

longwave infrared) and unclassified minerals in the core. The resultant mineral assemblage was comparable to QEMSCAN and QXRD in terms of minerals present with generally similar abundances. However, useful information on the alteration mineralogy can still be extracted, such as the presence of serpentine, chlorite and talc and their association with other silicate minerals. Other parameters such as mineral grades and grain sizes were quantified on MATLAB using specially developed scripts. The interconnected grains could not be separated due to invisible boundaries on the HSI maps. Therefore, only a small number of grains were generated with larger grain size values, likely underestimating the real grain numbers.

XCT provided information on valuable high-density minerals (including possible platinum-group minerals (PGMs)) and mineral texture in the cores. Due to extensive alteration in the rocks, discrimination between grey values was, however, challenging. Grey level segmentation into the different mineral groups was also noted to be dependent on the rock type. For example, plagioclase and orthopyroxene were more easily discriminated in the less altered rocks (feldspathic pyroxenite and anorthosite) than the more altered rocks (altered harzburgite and pegmatoidal pyroxenite). The high scanning resolution allowed for the extraction of mineral texture, such as mineral association and grain size distribution (GSD). The 3D XCT derived GSD was slightly coarser than the 2D QEMSCAN derived GSD. The differences in GSD are attributed to a combination of both stereological and sampling effects. However, sufficient information on ore variability can be obtained when using the pertinent scanning parameters and careful segmentation processes.

These two techniques provide variable information on the mineral assemblage and texture, such as the identification of silicate minerals (particularly alteration minerals) in HSI and high-density minerals in XCT and good textural information on XCT than HSI. With the information provided, possible image overlapping scenarios of the two techniques were identified: (1) using XCT for high-density minerals, and HSI for silicate identification, (2) using XCT data with good mineral and texture discrimination (silicate associated with sulphides) to map unclassified areas in HSI, (3) is the opposite of the second scenario. Ultimately, the two scanning techniques will likely offer complementary information, although the application of this combined technique for routine work will be limited in practicality. Additionally, more work needs to be carried out with revised scanning and processing to improve the sustainability of the techniques in geometallurgy.

Acknowledgements

Glory to the almighty!

- SUPERVISORS

First, I would like to thank my supervisors A/Prof Megan Becker and A/Prof Jodie Miller. Thank you for your support, guidance, insight, knowledge, and constructive feedback throughout this project. To Megan, thank you for supporting me through the hard times, encouraging me to do better, and pushing me to the limits that made me realise my potential. I will forever be grateful for your contribution to research and life in general. Thank you for your understanding and patience; thank you for uplifting my confidence and helping me see things from a different perspective.

I would also like to thank Adj/Prof Glen Nwaila, my honours former supervisor. Thank you for seeing in me that nobody could see (even myself); thank you for trusting with this opportunity and believing in me. I would not be writing this if it was not for you; I will forever be grateful. I pray that all-mighty grant you more success and life, give you the strength and heart to continue giving back. I would like to thank you for coming on board in the later months of this project as a project advisor. Your time and effort are appreciated.

- DATA COLLECTION AND PROCESSING

Thank you to the Sedibelo Platinum mine team, Mpho Ramonotsi and Jan van der Merwe, for providing drill core samples used in this project.

I would also like to thank Terracore and X-sight X-ray services for using their system to collect data for this project. To the Terracore team, especially Mike Donze and Clement Ndou, thank you for being patient with me. Thank you to Clement and the team for helping to acquire my data, lifting those heavy core trays, always checking up on me if I am progressing with data processing, and providing tools and documents to assist me. To Mike, thank you for helping me with data processing and constantly liaising with my queries and questions. Your teachings did not go in vain.

To the X-sight X-ray services team, Paul and Colm Keanly, thank you for assisting me in acquiring my XCT data. Thank you, Paul, for the insight Knowledge on the XCT system and processing.

To Lunga Bam, thank you for your teaching on XCT (acquisition and processing); mostly, I am genuinely grateful for assisting me with XCT data processing and making me all those coffees that put me awake until the end of the day. Thank you for all the motivational talks.

Marcelene Voigt, thank you for your support and encouragement. Thank you for sharing with me your knowledge in XCT. I am fortunate that I had someone like you at the beginning of my thesis to guide me and guide me.

To Keshree Pillay and Lorraine Nkemba, thank you for preparing and running my QEMSCAN samples. Lorraine, thank you for your welcome to your lab and for preparing my ore blocks when I was away.

Keshree, thank you for running the QEMSCAN block and sending my samples for QXRD analysis. I am also thankful for teaching me how to process my data. Your work and efforts were not in vain. To Sabine, thank you for running XRD for my samples.

To Maximillian Richter, thank you for assisting me with MATLAB. The HSI grain size analyses were made possible because of your knowledge.

Megan, thank you again for insisting that I process my data.

- FRIENDS AND FAMILY

To my family, Thembi, Emily, Tumi and Lesego Mashaba, Princess and Alfred Mkhombo, thank you for the support, encouragement and motivation. Thank you for being my strength and believing in me when I thought of giving up. To my late dad, Mr Joel Mooketsi, thank you for your guidance.

To my best friends, Semola Rabede and Pretty Sithole, thank you for all the distressing moments and motivation.

To my sisters in the thesis, Sage Govender, Ayanda Sibiyi and Andrea Molifie, thank you for your motivations and input. I genuinely appreciate your support. To Sage and Ayanda, thank you for accommodating me in my last year; you are indeed God sent.

To Ms Charmaine, thank you for accommodating me for the first few months in Cape Town, for your warm welcome and for taking me to the beach for the very first time; and for allowing me to be your first passenger in your new car, and introducing me to your lovely family.

To Katlego Mokone, thank you for being my strength, for your support, stressless moments and for forgetting to push my thesis. To Clive Gwala, thank you for being a supportive friend and being there for the emotional support.

To the CMR family, thank you for welcoming me and for your support throughout this journey. To Monde Bikaphi and Kenneth, thank you for welcoming me to your lab, and arranging a working space. I thank you for helping me lift all those heavy cores, unpacking and packing them. To Shireen, thank you for your assistance throughout my lab work, and for arranging courier service to and from the University of Cape Town. To Andrea Molifie, Conchita Kamanzi and Resoketswe Manenzhe, thank you for being my motivation. I appreciate the part you've played throughout. To Andrea, I thank you for the insight, input and knowledge.

Apollonia Charamba, Nolihle Ndamase, Tanaka and Mathew Dzingai, thank you for being friends I needed from first-year throughout. To Noli and Tanaka Tafirenyika, it was such a pleasure to share the postgraduate representative position with you. Not forgetting Resoketswe, thank you again for the wonderful and stressless moments you shared with me.

- SPONSORS

This project was funded by the National Research Foundation (NRF) of South Africa (Grand Numbers: 123380 and 131464), South African Minerals to Metals Research Institute (SAMMRI) and the

Department of Science and Innovation (DSI) which I am grateful for. I am genuinely thankful for the extended funding post-Covid outbreak.

Table of Contents

Declaration	i
Abstract	ii
Acknowledgements	iv
Table of Contents	vii
List of Figures	xi
List of Tables	xviii
Acronyms and abbreviations	xx
Glossary	xxi
Chapter 1: Introduction	1
1.1 Introduction	1
1.2 Problem statement	7
1.3 Objective and key questions	7
1.4 Project scope	8
1.5 Chapter descriptions	9
Chapter 2: Literature review	10
2.1 Case study: South African Magmatic-Ni-Cu-PGE sulphide ore	10
2.1.1 Hydrothermal alteration and weathering reactions of rock-forming minerals common in magmatic Ni-Cu-PGE ores.....	12
2.2 Techniques for mineral and texture characterization	14
2.3 Visual logging	15
2.4 Automated Scanning electron microscopy with energy dispersive X-ray spectrometry (Auto-SEM-EDS)	16
2.4.1 Principles of auto-SEM-EDS	16
2.4.2 Mineral identification	17
2.4.3 Scanning and data acquisition	17
2.4.4 Data processing and reporting.....	18
2.4.5 Challenges and limitations	19
2.4.6 Applications in geometallurgy and the characterisation of magmatic Ni-Cu-PGE ores.....	19
2.5 Hyperspectral imaging	19
2.5.1 Principles of hyperspectral imaging	20

2.5.2 Mineral Identification	21
2.5.3 Scanning and data acquisition	24
2.5.4 Data processing and analysis	25
2.5.5 Challenges and limitations	27
2.5.6 Applications in geometallurgy and the characterisation of magmatic Ni-Cu-PGE ores.....	27
2.6 X-ray computed tomography	28
2.6.1 Principles of X-ray computed tomography	29
2.6.2 Mineral identification	29
2.6.3 Scanning parameters and data acquisition.....	30
2.6.4 Data Processing	31
2.6.5 Challenges and limitations	32
2.6.6 Applications in geometallurgy and the characterisation of magmatic Ni-Cu-PGE ores.....	33
2.7 Supporting techniques	35
2.8 The knowledge of contribution and research gap.....	36
Chapter 3: Materials and methods	38
3.1 Case study	39
3.1.1 Core/sample collection.....	39
3.1.2 Manual core logging and petrography	39
3.2 Sample preparation.....	39
3.3 Hyperspectral imaging	40
3.3.1 Data acquisition.....	40
3.3.2 Data processing and analyses	44
3.4 X-ray computed tomography	45
3.4.1 X-ray computed tomography data acquisition.....	45
3.4.2 Data processing and analyses	45
3.5 Supporting techniques	46
3.5.1 Quantitative Evaluation of Minerals by Scanning Electron Microscope.....	46
3.5.2 Quantitative X-ray diffraction (QXRD).....	47
3.6 Image overlapping	47
Chapter 4: Sample characterization	48
4.1 Drill core TU277	49

4.1.1 Mineral assemblage and texture of drill core TU277	50
4.2 Drill core RD015	56
4.2.1 Mineral assemblage and texture of drill core RD015.....	58
4.3 Department of base metal sulphide minerals	63
Chapter 5: Scanning technologies	65
5.1 Hyperspectral imaging	65
5.1.1 Standard core scanning	65
5.1.2 Mini core scanning	71
5.1.3 Spectral and mineral reclassification	74
5.1.4 Mineral texture	86
5.2 X-ray computed tomography	90
5.2.1 Phase segmentation	91
5.2.2 Mineral Identification	94
5.2.3 Mineral grades and texture	101
5.2.4 3D Volume visualization.....	107
5.3 Image overlapping	109
Chapter 6: Discussion	111
6.1 A systematic workflow for extraction of mineralogical and textural characteristics in drill cores.....	111
6.2 Benefits and limitations for mineralogical and textural characterisation (from acquisition to processing)	114
6.3 Extent of data automation	117
6.4 Comparisons in characterisation of the mineral assemblage and texture from HSI and XCT	117
6.4.1 Quantitative mineralogical characterisation	119
6.4.2 Mineral texture characterisation.....	120
6.4.3 Quantitative textural characterisation.....	120
6.5 Effects of rock types and hydrothermal alteration on HSI and XCT.....	121
6.6 Image overlapping	124
6.6.1 Challenges associated with data processing and analysis from overlapping technique ...	126
Chapter 7: Conclusion and recommendations	128
7.1 Conclusion.....	128

7.2 Recommendations	131
References	132
Appendix	146
Appendix A: Scanning parameters	146
Appendix B: Core logging	147
Appendix C: Bulk mineral grades.	154
Appendix D: Hyperspectral imaging	159
Appendix E: X-ray computed tomography	175
Appendix F: Online files	180

List of Figures

Figure 1.1: 3D geometallurgical block model for bond work index (BWi) parameter (After King and MacDonald, 2016).....	2
Figure 1.2: Schematic diagram illustrating the hierarchy of the different data types used within a geometallurgical program (Adapted from Cloete & Slabbert, 2018 and references therein; Lechuti-Tlhalerwa & Gilika, 2018).....	3
Figure 1.3: Illustration of the study's scope within the broader disciplines of economic geology, process mineralogy and geometallurgy. This study focuses on the parameters in bold.....	8
Figure 1.4: Schematic diagram of the thesis layout.....	9
Figure 2.1: Geological location of the Bushveld Igneous Complex and Sedibelo Platinum Mine located on the Western Limb of the Bushveld Complex (Modified from Sehoole, 2019). 10	10
Figure 2.2: A general stratigraphic section of the Bushveld Complex illustrating the Upper Critical Zone Reefs (UG2, Pseudo and Merensky Reef), taken from (Becker et al., 2012, adapted from Crossling and Mupakati).....	11
Figure 2.3: Various techniques to characterize mineralogy and texture on drill core at different scales (Adapted from Butcher, 2020).....	15
Figure 2.4: QEMSCAN false colour particle images in the -75 +38 mm fraction recovered in batch floatation tests of the Great Dyke magmatic Ni-Cu-PGE sulphide ore, Zimbabwe. Orthopyroxene and talc composites represent naturally floatable gangue in these ore types. Talc rims orthopyroxene in ore 1; orthopyroxene in ore 1 and 2 are pervasively altered talc, leaving relics of orthopyroxene (Dzingai et al., 2021).	18
Figure 2.5: Schematic representation of the HSI acquisition (Adapted from Lorenz et al., 2019).....	25
Figure 2.6: Output results of the processing stages of hyperspectral imaging. (a) Mineral map of drill core; (b) Spectral signature of the mineral map (From ALS and Terracore international).	26
Figure 2.7: Linear attenuation coefficient of various minerals as a function of X-ray energy (Kyle, 2015).	30
Figure 2.8: Schematic diagram of the XCT cone-beam configuration.....	31
Figure 2.9: Schematic diagram for a generic XCT data processing (Adapted from Godel, 2018).	31

Figure 3.1: Schematic flow diagram summarizing the methodology of the project. Yellow indicates the major scanning techniques; pink – the supporting techniques; blue - 2D images; grey - processing systems and software; green - outputs from each technique. 38

Figure 3.2: Selected areas for mini core extraction (circles), XQRD samples (blue rectangles), and rescanned HSI core (marked with X). 40

Figure 3.3: Calibration board for the HSI system calibration. The calibration board is placed under the system cameras, moving in the conveyor belt. A: anodized aluminium squares are used to ensure image completeness and correct aspect ratio. B: examples of standard materials used to ensure spectral calibration, the centre object being a slab of styrofoam. C: reference glass and plastic are used to ensure camera calibration. D: Kodak colour and focus sheets to ensure correct colour balance, focus, and aspect ratio (Photo courtesy of Terracore). 41

Figure 3.4: Interior of the SisuRock Gen2 Hyper-logger system showing the camera setup. A- RGB camera, B- FENIX (co-registered VNIR and SWIR), and C- OWL camera (LWIR). (Photo courtesy of Terracore)..... 42

Figure 3.5: Illustration of the HSI scanning a tray of drill core moving in a conveyor belt under the system cameras (FENIX, OWL and RGB). 43

Figure 4.1: Photographs of TU277 and RD015 drill cores investigated with the selected marked areas for QEMSCAN (circles) and QXRD (rectangle) analyses sampled on the drill cores. Core depths are indicated with green lines marking the change in lithologies with associated changes in mineral assemblage and texture. TU277 core depths are labelled from 82 m to 86 m and RD015 from 25 m to 29 m. 48

Figure 4.2: Stratigraphic column for drill core TU277 from the UG2 Hanging wall to the Merensky Reef Footwall. The column shows the major minerals in the rock types under each stratigraphy. 50

Figure 4.3: QEMSCAN field images for TU277, stratigraphically from (a) Gabbronorite, (b) Altered harzburgite, (c) Pegmatoidal-olivine pyroxenite, (d) Pegmatoidal pyroxenite and (e) Pyroxenite. 52

Figure 4.4: Bulk mineral grades obtained from (QEMSCAN analyses for the different lithologies for drill core TU277. Differences in mineral grades between QEMSCAN and QXRD analyses (Table 4.1) are considered to be due to sampling effects. 54

Figure 4.5: QEMSCAN determined grain size distribution for selected minerals in drill core TU277: serpentine (Srp), orthopyroxene (OPX) and plagioclase (Pl) in the (a) anorthosite, (b) pegmatoidal olivine-pyroxenite, (c) altered harzburgite and (d) feldspathic pyroxenite. The pegmatoidal pyroxenite

and pegmatoidal-olivine pyroxenite constitute similar minerals, and only one was chosen for GSD analysis. The d50 in microns is also given..... 55

Figure 4.6: Stratigraphic column for Drill core RD015 from the UG2 hanging wall (bottom) to the Merensky Reef Footwall (top) with minerals identified in each rock type during manual core logging. 57

Figure 4.7: QEMSCAN field images for TU277, stratigraphically from (a) Anorthosite, (b) Altered harzburgite, (c) Pegmatoidal-olivine pyroxenite, (d) Pegmatoidal pyroxenite and (e) Pyroxenite. 60

Figure 4.8: Bulk mineral grades obtained from QEMSCAN analyses for different lithologies in drill core RD015. Differences in mineral grades between QEMSCAN and QXRD analyses (Table 4.2) are considered to be due to sampling effects. 62

Figure 4.9: Grain size distribution for selected minerals in drill core RD015: serpentine (Srp), orthopyroxene (orthopyroxene (OPX)) and plagioclase (Pl) in (a) anorthosite, (b) pegmatoidal pyroxenite, (c) altered harzburgite and (d) feldspathic pyroxenite. The pegmatoidal pyroxenite GSD was excluded due to intensive interconnected grains that could not be separated. The number of grains is given in Appendix C (Table C3). 63

Figure 4.10: Base Metal sulphides quantified from QEMSCAN field images for different rock types in (A) drill core TU277 and (B) drill core RD015. Other represent sulphide minerals not mentioned above. 64

Figure 4.11: Selected area from the olivine pegmatoidal pyroxenite of the drill core TU277 showing the textural association of the base metal sulphide. 64

Figure 5.1: Drill core TU277-Mineral maps for the readily identified mineral assemblage (before data validation and interpretation) detected with the VNIR-SWIR and LWIR sensors scanned at 1.64 mm pixels; and RGB images at 0.16 mm pixel. 50 mm core diameter..... 67

Figure 5.2: Drill core RD015-Mineral maps for the readily identified mineral assemblage (prior to data validation and interpretation) detected with the VNIR-SWIR and LWIR sensors scanned at 1.64 mm pixels; and RGB images at 0.16 mm pixel. 50 mm core diameter..... 69

Figure 5.3: Comparisons between mineral maps of the standard scanning (a and b) with selected rescanned cores (*a and *b). The selected cores are illustrated with white boxes sampled from standard drill cores. VN-SWIR mineral maps for (drill core RD015) standard cores (a) with selected rescanned cores (*a), and LWIR mineral maps (for drill core TU277) standard cores (b) with selected rescanned cores (*b). 50 mm core diameter. 70

Figure 5.4: Drill core TU277 (mini cores)-Mineral maps for the readily identified mineral assemblage (prior to data validation and interpretation) detected with the VNIR-SWIR and LWIR sensors scanned at 0.4 mm pixels. Sample 1 to 2 represents the anorthosite, sample 3 is upper pegmatoidal pyroxenite, sample 6 to 7-represents altered harzburgite, samples 8 to 10 represents pegmatoidal pyroxenite, and sample 11 and 12 represents feldspathic pyroxenite. Mini cores are 25 mm in diameter. 72

Figure 5.5: Drill core RD015 (mini cores)-Mineral maps for the readily identified mineral assemblage (prior to data validation and interpretation) detected with the VNIR-SWIR and LWIR sensors scanned at 0.4 mm pixels. Sample 1 represents the anorthosite, samples 2 to 7 represent altered harzburgite, samples 8 to 10 represent pegmatoidal pyroxenite, and sample 11 represents feldspathic pyroxenite. Mini cores are 25 mm in diameter. 73

Figure 5.6: Reclassified mineral maps for drill core TU277 scanned at high resolution. Sample 1 to 2 represents the anorthosite, sample 3 is upper pegmatoidal pyroxenite, sample 6 to 7-represents altered harzburgite, samples 8 to 10 represent pegmatoidal pyroxenite, and sample 11 represents feldspathic pyroxenite. The mineral false colours were changed from those initially represented in Figure 5.4 and 5.5 to match with the QEMSCAN field images data in Figure 4.3. Mini cores are 25 mm in diameter. 78

Figure 5.7: Spectral absorption features for illite, prehnite and muscovite. 79

Figure 5.8: Reclassified mineral maps for drill core RD015 scanned at high resolution. Sample 1 represents the anorthosite, samples 2 to 7 represent altered harzburgite, samples 8 to 10 represent pegmatoidal pyroxenite, and sample 11 represents feldspathic pyroxenite. The mineral false colours were changed from those initially represented in Figure 5.4 and 5.5 to match with the QEMSCAN field images data in Figure 4.3. Mini cores are 25 mm in diameter. 81

Figure 5.9: Mineral grades for the selected RD015 mini cores scanned with QEMSCAN and HSI after the spectral reclassification. QEMSCAN mineral grades for those minerals with no spectral response (base metal sulphides, magnetite and chromite) are shown as 'other/unclassified'. The errors bars represent the relative error at 2σ standard deviation. 82

Figure 5.10: Mineral grades for the selected TU277 mini cores scanned with QEMSCAN and HSI after the spectral reclassification. QEMSCAN mineral grades for those minerals with no spectral response (base metal sulphides, magnetite and chromite) are shown as 'other/unclassified'. The errors bars represent the relative error at 2σ standard deviation. 83

Figure 5.11: Drill core TU277- Reclassified hyperspectral mineral maps for VN-SWIR and LWIR spectral sensors scanned at 1.64 mm pixels. There is a lot of spectral mixing in LWIR. The mineral false colours were changed from those initially represented in Figure 5.1 and 5.2 to match with the QEMSCAN field images data in Figure 4.3. 50 mm core diameter. 84

Figure 5.12: Drill core RD015- Reclassified hyperspectral mineral maps for VN-SWIR and LWIR spectral sensors scanned at 1.64 mm pixels. There are a lot of mixed phases in LWIR, e.g., chlorite-biotite. The false mineral colours have been changed from those initially represented in Figure 5.1 and 5.2 to match the QEMSCAN data. 50 mm core diameter. 85

Figure 5.13: Grain size distribution for predominant minerals identified by HSI in drill core TU277. Selected minerals are presented: (a) Anorthosite, (b) Altered harzburgite, (c) Pegmatoidal olivine-pyroxenite and (d) Pyroxenite. 87

Figure 5.14: Grain size distribution for major minerals detected by HSI across various lithologies for drill core RD015. Selected minerals (or mixed mineral phases) are presented for the (a) Anorthosite, (b) Altered harzburgite, (c) Pegmatoidal olivine-pyroxenite and (d) Pyroxenite. The number of grains (N) analysed is also given. 88

Figure 5.15: Different views of the core in VG studio, showing the uppermost slices exposed to air and touched by styrofoam in the 3D volume scanned with XCT. Stippled lines indicated the section that was exposed to air. The mini core is 25 mm in diameter. 92

Figure 5.16: An illustration of phase-to-phase segmentation in the core with different regions colour coded for easier discrimination (pegmatoidal olivine-pyroxenite-TU277). The images illustrate the segmentation from one grey value range (top left) to the next until all phases (bottom right) in the cores are segmented. The mini core is 25 mm in diameter. 93

Figure 5.17: The illustration of XCT image slices with corresponding grey value range histogram for selected rock types: (a) Pegmatoidal pyroxenite and (b) pegmatoidal olivine-pyroxenite, from drill core TU277. QEMSCAN false colour compositional field images for similar slices are used for direct mineral identification in each slice. 1-QEMSCAN legend and 2- XCT grouping. Mineral abbreviations from Whitney and Evans, (2010). 96

Figure 5.18: The illustration of XCT image slices with corresponding grey value range histogram for selected rock types in drill core RD 015: (a) Anorthosite, (b) Pyroxenite, and (c) Altered harzburgite. QEMSCAN false colour compositional field images for similar slices are used for direct mineral

identification in each XCT slice. The y-axis is plotted with actual numbers (black) and a log scale (grey).

1-QEMSCAN legend and 2- XCT grouping. Mineral abbreviations from Whitney and Evans, (2010) .99

Figure 5.19: Drill core TU277-The comparison between the false-colour XCT image slices (e-h) after mineral segmentation with QEMSCAN false colour field images (a-d). NB. Mineral colours in XCT are not constant..... 100

Figure 5.20: Drill core RD015-The comparison between the false-colour XCT image slices (e-h) after mineral segmentation and identification with QEMSCAN false colour field images (a-d). NB. Mineral colours in XCT are not constant..... 101

Figure 5. 21: Drill core TU277-QEMSCAN mineral grades grouped according to the XCT mineral grouping obtained by mineral segmentation. QEMSCAN data reported is area percent and XCT in volume percent. All rock types are presented: (a) anorthosite, (b) altered harzburgite, (c) pegmatoidal pyroxenite and (d) feldspathic pyroxenite. The graphs are plotted with relative error at a 95% confidence interval..... 102

Figure 5.22: Drill core RD015-QEMSCAN mineral grades grouped according to the XCT mineral grouping obtained by mineral segmentation. QEMSCAN data reported is area percent and XCT in volume percent. All rock types are presented: (a) anorthosite, (b) altered harzburgite, (c) pegmatoidal pyroxenite and (d) feldspathic pyroxenite. The graphs are plotted with relative error at a 95% confidence interval..... 103

Figure 5. 23: The serpentine grain sizes in pegmatoidal olivine pyroxenite grouped according to a volume colour scale, demonstrated in 3 sections and volume. The volume is calculated in mm³. 104

Figure 5.24: Grain size distribution of 3D XCT ESD (left) and 2D QEMSCAN ESD (right) for rocks types in drill core TU277: (a) Pegmatoidal pyroxenite and (b) Feldspathic pyroxenite grain distribution. ESD-Equivalent spherical diameter. The XCT is plotted with (circular-shaped) and without (diamond-shaped) the maximum grains..... 105

Figure 5.25: 3D XCT and 2D QEMSCAN minerals grain size distribution for rocks types in drill core RD015. (a) altered harzburgite, the erode-dilate function was applied to serpentine-olivine grains. (b) Pegmatoidal pyroxenite. ESD-Equivalent spherical diameter. The XCT is plotted with (circular-shaped) and without (diamond-shaped) the maximum grains..... 106

Figure 5.26: 3D view of the LPR pegmatoidal pyroxenite of (Drill core TU277) with segmented BMS (yellow) and possible PGM (red)..... 108

Figure 5.27: Manual image overlapping for HSI mineral maps on XCT greyscale slices. All the unclassified areas represent scenario one (well demonstrated in A). B and C illustrate scenario two (high attenuation minerals in XCT and grey value overlap due to partial volume effect). D and E demonstrate scenario 3 (where minerals can be discriminated both in HSI and XCT). Mini cores are 25 mm in diameter. 110

Figure 6.1: Flow chart for acquiring mineralogical and textural information from the two scanning techniques (HSI and XCT).....112

Figure 6. 2: Segments of rock types from the drill cores illustrating lighter and darker rocks. A and B are anorthosites from drill core RD015 and TU277, respectively. C and D are the altered harzburgite from RD015 and TU277, respectively. 123

Figure 6.3: A conceptual diagram illustrating the possible overlapping scenarios. The scenarios are illustrated with the data obtained from HSI and XCT for this study. *Numbers are grey values.....126

List of Tables

Table 1.1: Different scanning techniques for mineral assemblage and elements and their requirements for drill core scanning.	5
Table 2.1: Bulk mineral assemblage of the Silicate Reef. The green highlighted sections are the alteration minerals formed due to oxidation and weathering reactions (From Becker et al., 2014)....	12
Table 2.2: Summary of the typical hydrothermal alteration reactions common in the rock-forming minerals of rocks similar to the Silicate Reef.	13
Table 2.3: Wavelength ranges of the infrared regions' divisions with the spectral ranges commonly used for mineral identification. Table adapted from (Linton et al., 2018; Sriram et al., 2016).	21
Table 2.4: Summary of hyperspectral imaging sensors and their abilities for mineral identification. Green-Good; Orange-Moderate; Red-Bad and White-Uncertain. Adapted from (Linton et al., 2018) 2018.). The yellow rectangle shows the assistance of HSI of problematic minerals in geometallurgy.	22
Table 2.5: A summary of factors influencing spectral variation for mineral identification.	23
Table 2.6: Summary of XCT and Hyperspectral imaging technologies from the literature.	37
Table 3.1: Mini core sampling and labelling from each borehole.	39
Table 3.2: Camera specifications of the SisuRock Gen2 core scanning system used for standard drill core scanning.	43
Table 3.3: Camera specifications of the SisuRock Gen2 Hyper logger system used for mini cores core scanning.	44
Table 3.4: XCT scanning parameters.	45
Table 3.5: Summary table for rock types sampled from drill core (RD015 and TU277) for QXRD and QEMSCAN analyses.	46
Table 4.1: QXRD bulk mineral assemblage for different rock types sampled in drill core TU277 (in wt. %). Minerals indicated with a hyphen were not detected in the selected sample. *Spinel covers chromite and Fe-oxides. Base metal sulphides were below the detection limit.	51
Table 4.2: QXRD bulk mineral assemblage for different rock types sampled in drill core RD015 (in wt. %). Minerals indicated with a hyphen were not detected in the selected sample. *Spinel covers chromite and Fe-oxides. Base metal sulphides were below the detection limit.	58

Table 5.1: Readily identified mineral assemblage detected under VNIR-SWIR and LWIR sensors before data validation and interpretation. The green-highlighted minerals annotated are the predominant minerals detected by each spectral sensor.....	65
Table 5.2: Readily identified HSI mineral assemblage (prior to data validation and interpretation) of the mini cores scanned at high resolution (0.15 mm pixel size). Minerals in green are the predominant minerals under each spectral sensor.	71
Table 5. 3: Detected mineral assemblage in QEMSCAN, QXRD and HSI mini cores (before the spectral reclassification).	75
Table 5.4: Summary table for HSI mineral reclassification from readily identified (before) to reclassified (after). Minerals in green are the predominant minerals under each spectral sensor.	76
Table 5. 5: Summary table of the mineral median grain size (d50, μm) determined using both SWIR and LWIR data from HSI compared with QEMSCAN for drill core TU277. The selected minerals are the common (predominant) minerals identified by both techniques. Minerals that do not respond under the specific sensor or interconnect minerals that gave only one value are annotated with a hyphen (-). ..	87
Table 5.6: Summary table of the mineral median grain size (d50, μm) determined using SWIR and LWIR data from HSI compared with QEMSCAN for drill core RD015. The selected minerals are the common (predominant) minerals identified by both techniques. Minerals that do not respond under the specific sensor or interconnected grains that gave only one value are annotated with a hyphen (-).	89
Table 5.7: Summary of major minerals detected by QEMSCAN for each lithology in the drill cores. ...	90
Table 5.8: The simplified QEMSCAN bulk mineral assemblage is grouped based on the relative mineral densities to calculate the attenuation coefficient using Bam et al., 2020. Density information was obtained from various (Bam et al. 2020; http://www.webmineral.com/ ; Bartheemy, 2019; Molifie, 2021).	91
Table 6.1: Summary table of the benefits and limitations for HSI and XCT for mineralogical and textural information as relevant to the measurements in this study.....	116
Table 6.3: A summary of the minerals/mineral groups identified in HSI (SWIR and LWIR) and XCT in this study. Minerals highlighted in green are phyllosilicates.	118
Table 6.4: Relative error at the 95% confidence interval for mineral grades (of drill core RD015) obtained in QEMSCAN, HSI and XCT, reported by area % (QEMSCAN and HSI) and volume % (XCT).....	120

Acronyms and abbreviations

2D	Two-dimensional
3D	Three-dimensional
BIC	Bushveld Igneous Complex
BMS	Base metal sulphides
CPX	Clinopyroxene
D50	Cumulative 50% point of diameter
ESD	Equivalent spherical diameter
GSD	Grain size distribution
HSI	Hyperspectral imaging
Lld	Lower limits of detection
LWIR	Longwave infrared
OPX	Orthopyroxene
PGE	Platinum-group element
PGM	Platinum group minerals
QEMSCAN	Quantitative Evaluation of Minerals by Scanning Electron Microscope
QXRD	Quantitative X-ray diffraction
RLS	Rustenburg layered suite
ROI	Region of interest
SWIR	Shortwave infrared
UG2	Upper Group Two Chromitite
VNIR	Visible-near infrared
Vol. %	Volume percent
Wt.%	Weight percent
XCT	X-ray computed tomography

Glossary

Rock names

Anorthosite	a coarse-grained igneous rock consisting of more than 90% plagioclase and 10% of darker minerals (pyroxenes and olivine).
Feldspathic	contains a significant amount of feldspar
Gabbro	is an ultramafic rock that is composed of 50% clinopyroxene and 50% plagioclase.
Gabbronorite	when more than 5% of clinopyroxene in the gabbro is replaced by orthopyroxene.
Harzburgite	composed of orthopyroxene (80-90%) and olivine (10-20).
Leuco	Prefix applied to a rock name to denote a lower proportion of olivine and pyroxenes than what the original rock normally contains.
Norite	composed of 50% plagioclase and 50% orthopyroxene.
Pegmatite	an exceptionally coarse-grained plutonic rock. Mostly have granitic composition. The simple pegmatite contains minerals such as plagioclase, mica and quartz.
Peridotites	group of ultramafic rocks containing more than 40% olivine with orthopyroxene and clinopyroxene.
Poikilitic	larger grains enclosed in a smaller randomly oriented crystal.
Pyroxenite	is a plutonic rock that is composed of more than 90% of pyroxenes minerals and is classified as olivine-pyroxenite if it contains more than 10% of olivine.
Serpentinite	is a metamorphosed ultramafic rock, composed of more than 50% serpentine minerals forming from altering olivine and orthopyroxene-bearing rocks.

Textures

Adcumulate	cumulus crystals continuing to grow to display intercumulus liquid.
Alteration	changes in minerals' chemical composition and crystallography are induced by chemical or physical processes.
Anhedral	irregular grain shape.
Cumulate	accumulation of crystals formed during crystal-melt fractionation.
Euhedral	well-formed crystal with defined faces.
Intercumulus	minerals filling the spaces between cumulate grains.

Pegmatoidal has exceptionally coarse grains.

Vein and veinlet a fissure filled by different mineral assemblage to the surrounding rock's mineral assemblage. Veinlet is used to denote smaller veins.

Chapter 1: Introduction

This chapter provides the background, problem statement, objectives, key questions, project scope and layout of the thesis.

1.1 Introduction

The characteristics of ores vary from one location to another at a micro-, meso- and macro-scale- a phenomenon generally known as ore variability. Ore variability can arise from different geological processes, for example, the alteration in mineral assemblage and texture of ores caused by the interaction with hydrothermal fluids. In the early years of mining, ores with considerable variability were generally low grade and this, combined with the resultant mineralogical and textural complexities, made them uneconomical to process (Baum, 2014; Lund et al., 2015). However, due to the depletion of high-grade ores, i.e., ores with lower degrees of ore variability, the current global demand for raw materials has driven the need to mine and process mineralogically and texturally more complex ores. This requirement is one of the significant techno-economic challenges currently facing the modern mining and processing industries. Mismanagement of these heterogeneous ores may result in project delays or project failures and inconsistency of the plant feed (Lamberg, 2011; Lund et al., 2015). These types of problems ultimately affect the cash flow and viability of the mining operation. To mitigate the risks associated with ore variability, an advanced approach to managing these risks is needed throughout the mining value chain, that is, the mine design, operation, and closure stages (Baumgartner et al., 2011; Mwangi et al., 2015).

As a discipline, geometallurgy has been developed to minimize risks resulting from ore variability and maximise the value of the ore body (Lamberg 2011; Nguyen, 2013; Yildirim et al., 2014). Geometallurgy is the practical amalgamation of ore geology, mining, mineral processing and finance representing a multidisciplinary approach that combines geology and the ore's metallurgical response within a spatially constrained 3-dimensional (3D) block model (Williams, 2012; Hunt et al., 2019). Geometallurgy requires an in-depth knowledge of the primary ore variables (mineral grades/chemistry, mineral assemblage, mineral texture and alteration) and the response variables (e.g., grinding, recovery, grade distribution, particle density) to understand the ore variability. These variables are used to create a 3D geometallurgical model for the mining operation, such as the variation of bond work index a measure of the ore's resistance to crushing and grinding in comminution) through the ore body (Figure 1.1). The process of designing, maintaining and applying geometallurgical models is referred to as a geometallurgical program. In practical terms, a geometallurgical program is a structured approach to creating useful and practical models' that are representative of the ore body, and which can be implemented on the mining and processing sites (Lamberg, 2011; Lishchuk et al., 2015).

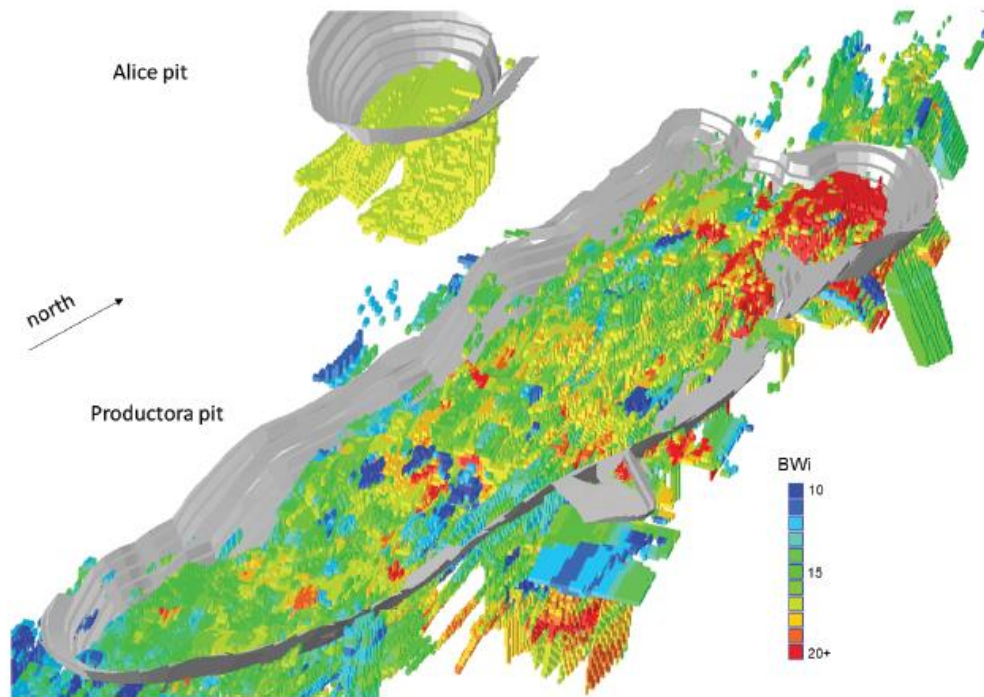


Figure 1.1: 3D geometallurgical block model for bond work index (BWi) parameter (After King and MacDonald, 2016).

When running a geometallurgical program, several hierarchical data types are considered to describe the ore variability spanning from simple (Level 1) to complex measurements (Level 4), as illustrated in Figure 1.2. Level 1 and 2 data types are associated with extensive small-scale sampling accompanied by rapid, inexpensive measurements. Level 3 and 4 data types are related to significantly larger scale/bulk sampling and more time-consuming and costly measures. The data types also vary according to their correlation to plant performance, with some measurements acting as simple proxies (level 2, 3) rather than providing direct measurements (Level 4) (Cloete and Slabbert, 2018; Keeney and Walters, 2008; Lechuti-Tlhalerwa and Gilika, 2018). As a result, appropriate sampling is crucial to obtaining relevant data on all levels throughout the mining life.

Given the need for the extensive small-scale sampling of the ore variability at levels 1 and 2, these data types are derived from geological drill core, or on reverse circulation drilling and blast holes, depending on the operation. Drill cores are ideal samples for use in geometallurgy because they are routinely acquired and logged ahead of mining (Becker et al., 2016; Koch et al., 2019). Critical attributes measured from drill cores include primary variables such as rock type /lithologies, rock fabric, mineral grades, mineral texture, degree of the alteration, and various geotechnical parameters used in building block models (Coward et al., 2009). 'Primary' variables are additive and therefore more easily embedded into the 3D block model (Lotter et al., 2017), compared to 'response variables' such as grinding efficiency, liberation, recovery, grade distributions, rheology, where the combination of properties is non-linear (Coward et al., 2009). Rock types and mineralogical data are one of the most

crucial primary variable inputs for block models as most ores are strongly linked to their host rocks which ultimately influences the type of mineralisation and mineralogical composition.

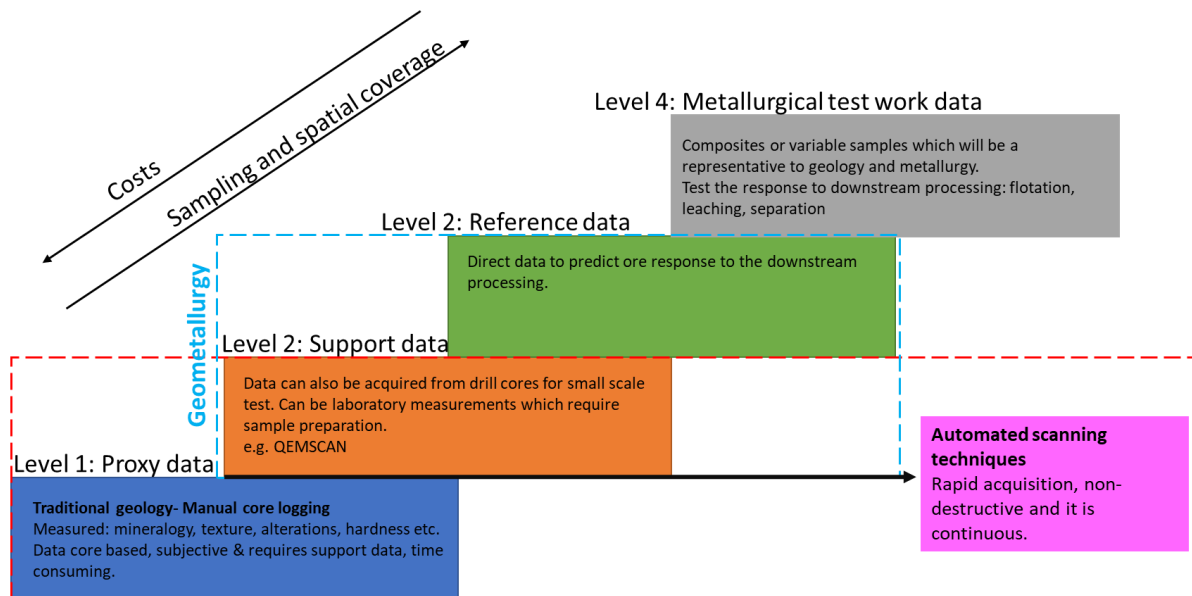


Figure 1.2: Schematic diagram illustrating the hierarchy of the different data types used within a geometallurgical program (Adapted from Cloete & Slabbert, 2018 and references therein; Lechuti-Tlhalerwa & Gilika, 2018).

The acquisition of mineralogical data at all levels is central to developing geometallurgical models (Lamberg et al., 2013). The mineral assemblage characterizes the mineral properties and chemical composition, including their formation conditions (Level 1). The mineral texture is also one of the significant factors of the mineral assemblage contributing to ore variability. 'Mineral texture' is defined as a "holistic term which includes grain size, grain shape, spatial distribution, and interrelationships on a mineral-by-mineral grain basis" (Voigt et al., 2020). Some parameters can be less complicated to acquire (e.g., grain sizes or grain size distribution). In contrast, other parameters can be more complicated to characterize and might require expertise (such as the mineral association and their spatial distribution). In exploration, the mineral texture is essential to understanding the ore-forming processes which are crucial to tracking the ore concentration and grades. In mineral processing and metallurgy, the measurement and quantification of mineral texture are crucial to defining the grindability of ore, degree of liberation (Lotter, 2011; Nwaila 2011), mineral dissolution/concentration (e.g., leaching risks) and post-mining/processing effects (e.g., acid rock drainage) (Ghorbani et al., 2011; Parbhaker-Fox et al., 2013; Cracknell et al., 2018). In-depth knowledge of both the ore mineral assemblage and mineral texture is key to understanding ore complexities.

Although these parameters can be obtained via manual core logging and other time-consuming techniques, automated measurements are preferred to avoid human bias. Ideally, these automated techniques should provide continuous, rapid, inexpensive, and most importantly, quantitative analyses of the ore – mineralogical and textural properties. The need to acquire rapid mineralogical and textural

information, especially in drill core, is in high demand for managing the effects of ore variability (Duée et al., 2019). In addition, big data analytics in conjunction with machine learning and data mining will emerge even more frequently in this era of the fourth industrial revolution (4IR) for automated mineralogical measurements (Chauhan et al., 2016; Koch et al., 2019; McCoy & Auret, 2019; Signoroni et al., 2019; Koch & Rosenkranz, 2020).

Various scanning technologies have been developed in recent years, capable of providing rapid mineralogical data on drill cores. The most popular methods are scanning technologies providing either continuous or non-continuous data. Modern scanning techniques provide data acquisition that is faster than methods that require extensive sample preparation. The current scanning technologies available include (a) Automated RGB (Red Green Blue) imaging-scanning system, (b) measurement while drilling data (MWD), (c) Raman spectroscopy, (d) Laser-induced breakdown spectroscopy (LIBS), (e) continuous full automated online X-ray fluorescence (XRF), (f) multi-sensor system core logger (MSCL), (g) hyperspectral imaging (HSI), and X-ray computed tomography (XCT); see Table 1.1 for more details. Some of these techniques provide real-time data, whereas others may require lengthy post-analysis data processing. A necessary aspect that needs to be considered when gathering data is selecting the appropriate approach to handle the large amounts of sample data, cost-effectively and rapidly.

Introduction

Table 1.1: Different scanning techniques for mineral assemblage and elements and their requirements for drill core scanning.

	Mineralogical scanning techniques	Acquisition speed	Sampling	Information	Drawbacks	Reference
				Accuracy and relevance to geomaterials		
2D	Hyperspectral imaging (HSI)	25 mm/s	From mm to the whole tray of drill core	Maximum geological information that can be used for mining operations and design. Provide quantitative consistency distribution data of alteration minerals. Data provides alteration minerals for downstream processing	Sulphide identification and mapping are challenging.	(Duée et al., 2019)
	Infrared thermography	mm/s	Drill core size needs to be reduced to fit the field of view for the thermal cameras.	Can detect almost all the minerals Allows for sulphide detection with microwave heating	It can be passive if the object is at high temperature than the surrounding areas.	(Armengol, 2015)
	Measurement while drilling/Logging while drilling (MWD)	m/min	2 cm while drilling	Provides geotechnical and geological data, such as density and porosity.	Data variety is influenced by drilling speed	(Vezhapparambu et al., 2018)
	Multi-sensor system core logger (MSCL)	0.002 m/s	20-30 cm	Acquire more than one parameter, i.e., mineral assemblage and geochemical.	More than one acquisition due to different sample requirements for each technique.	(Ross et al., 2013)
	Laser-induced breakdown spectroscopy (LIBS)	1mm res. 3cm/min	Single spot	Elemental measurements. Future potential for mineral identification and grain size quantification.	Time-consuming in larger drill core volumes—due to a small spot size measurement.	(Haavisto et al., 2013; McMillan et al., 2007; Sharma et al., 2007)
	Portable XRF (PXRF)	mm/s- cm/min	Selected single area- mm - cm	Geochemical composition, identify lithology, alteration. Immediately available to the operator, minimizing turnaround time	Measurements are prone to attenuation of low-energy fluorescence X-rays, limiting the elemental detection (elements lighter than Na)	(Alexandre, 2018; Duée et al., 2019)
	Raman spectroscopy	60-100 s	Spot measurement 2-5 μm^2 at 3 mm interval	Provides mineralogical information.	Fluorescence signature in minerals can mask the Raman signature. Mineral discrimination is limited.	(Sharma et al., 2007; Agangi et al., 2015; Duée et al., 2019; Gasser et al., 2019; Ramanaidou, et al., 2015; Wells, 2015)
3D	X-ray computed tomography (XCT)	~0.2 mm/min to 0.5 mm/min	Small- samples must fit on the rotating stage and be within the field of view- mm	High-resolution data- 3D volumes in greyscale for mineral ID. Good qualitative texture. Coupled with GLCM can give quantitative texture Provides high-resolution data with internal structures	Routinely applied in research	(Guntoro et al., 2019; Voigt et al., 2020)

The HSI technique uses a range of spectral bands to determine mineral types using multiple infrared and visible sensors to detect reflectance properties. HSI is a non-destructive scanning technique that allows the whole drill core's mineral assemblage and mineral texture information to be captured continuously and rapidly. Depending on the system used, the acquisition speed is approximately 25 mm/s (Tusa et al., 2019). The HSI technique fits between level 1 and 2 geometallurgy data types (Figure 1.2). Moreover, it is one of the routinely used techniques for mineral identification (especially alteration minerals) in geosciences and geometallurgy (Bioucas-Dias et al., 2013). The technique is well known for its strength in identifying hydrous phyllosilicate minerals such as talc, serpentine, montmorillonite, illite and kaolinite, which are problematic to downstream processing (Mauger et al., 2007; Kruse et al., 2012; Ndlovu et al., 2014; Mathieu et al., 2017; Tusa et al., 2019; Lishchuk & Pettersson, 2020). Most of the HSI work appears to have been conducted on mineral deposits containing rocks with abundant 'light coloured' minerals (such as quartz and feldspars) in sedimentary deposits (Johnson et al., 2019; Mohamed, 2018; Wells, 2013) or hydrothermal deposits (Mauger et al., 2007; Mathieu et al., 2017; Sture et al., 2019; Thiele et al., 2021) where HSI performs well in identification of minerals. Few remote sensing studies have been done on deposits dominated by mafic minerals or ultramafic minerals containing dark-coloured minerals, for example, the South African magmatic Ni-Cu-PGE deposits from the Bushveld Igneous Complex. However, since HSI is only a surface scanning technique that provides 2-Dimensional (2D) information on the sample properties, it inherently does not characterize the entire drill core volume compared to a 3D (3-dimensional) scanning technique such as X-ray computed tomography (XCT).

XCT is another popular and well established, non-destructive scanning technique, although it has mostly been applied in the research environment to date. XCT gained traction in geoscience in the early 2000s for the characterisation of ore deposits (Kyle et al., 2008; Howard et al., 2011; Kyle & Ketcham, 2015; Becker et al., 2016), including the platinum mineral group (PGM) ores (Ballhaus and Sylvester, 2000; McCall, 2016; Miller, 2014). XCT is a unique scanning technology that can penetrate and capture the material's internal structure, producing 3D volumes, and eliminating stereological errors associated with 2D images. Materials are characterized and phases identified based on their linear attenuation coefficients - a function of mineral density, chemical composition and atomic number equivalent to greyscale values. The output comprises the greyscale image stacks reconstructed to 3D volumes. Minerals with differences in attenuation coefficient less than 6% are difficult to discriminate (Bam et al., 2020). The quantitative analysis of the mineral assemblage and simple textural attributes is relatively straightforward (e.g., grain size distribution), but complex quantitative textural characterization remains an area of research interest. There has been recent interest in furthering the use of XCT data using quantitative complex textural parameters such as grey level co-occurrence matrices, local binary pattern and covariance and variograms (Jardine et al., 2018; Guntoro et al., 2019).

It appears that one of the approaches to overcoming the lack of positive mineral identification within any form of analysis is by combining the technique with other complementary mineralogical methods. Since each technique may be measuring different parameters, e.g., elemental composition or crystallography (Table 1.1). This is common when analysing a new deposit or a case study where the

mineral assemblage is unknown—supporting techniques such as the automated scanning electron microscopy with energy dispersive spectrometry (auto-SEM-EDS) platforms like Quantitative Evaluation of Minerals by Scanning Electron Microscope (QEMSCAN), MLA (Mineral Liberation Analyzer), TESCAN Integrated Mineral Analyzer (TIMA) or Mineralogic as well as Quantitative X-ray diffraction (QXRD) have been used extensively for this (Armengol, 2015; Koerting et al., 2015; Tusa et al., 2019; Voigt et al., 2020). Therefore, this study aims to use both the XCT and HSI in the same case study as complementary techniques for characterising a magmatic Nickel-Copper-Platinum element (Ni-Cu-PGE) ore from the Bushveld Igneous Complex, South Africa.

1.2 Problem statement

Hyperspectral imaging is a critical component of continuous drill core scanning in geometallurgy. However, it only provides 2D imaging of the drill core, and its mineral identification is limited to minerals that show a definitive spectral response. On the other hand, XCT provides 3D imaging of drill core but is more routinely used in research applications and does not independently give the mineralogical composition. Therefore, combining the two techniques should provide more information than one technique individually. This hypothesis is tested on magmatic Ni-Cu-PGE ores. To date, no systematic study has explored how the results from these two techniques can be integrated, especially using the magmatic Ni-Cu-PGE ore from the Bushveld Igneous Complex, South Africa as the case study.

1.3 Objective and key questions

The overarching aim of this study is to investigate how XCT scanning technology complements the more routinely practised hyperspectral scanning technology of drill cores using a case study approach. To achieve this aim, the following objectives have been identified:

- i. To investigate the practical parameters influencing the extraction of mineralogical and textural information on each technique.
- ii. To compare and contrast the mineral assemblage and textural information provided by each technique on PGM ores.
- iii. To investigate the potential of obtaining more detailed mineralogical information from the combined output images of the two techniques.

The following key questions were proposed to address the objectives of the project:

- i. What are the benefits and limitations of each technique for accurate mineralogical and textural characterization?
- ii. What steps are needed to extract quantitative information from each technique?
- iii. Can we combine the two datasets to provide practical mineralogical and textural information?

1.4 Project scope

The study is centred within the cross-cutting disciplines of economic geology, process mineralogy and geometallurgy. Moreover, it focuses on analysing the magmatic Ni-Cu-PGE drill cores used as a case study. Hyperspectral imaging and X-ray computed tomography are the only two drill core scanning techniques investigated. However, analyses from auto-SEM-EDS and QXRD will also be incorporated as complementary and supporting techniques enabling positive mineralogical identification. The focus and limitations of this study are illustrated in Figure 1.3. The study will focus on the abilities of the scanning techniques for characterization of the mineral assemblage and I textural with further image analysis as needed to combine the output images (after processing) to investigate the potential to extract more information than from each technique alone.

The underlying scope from geology to geometallurgy is broad, with countless fields, including the aspects and parameters making up the fields. Only specific parameters are covered relative to the area of focus to provide valuable information and broaden the knowledge for that area, also keeping in mind other respective fields linked to the area of focus. This study focussed on the initial stages of drill core analyses (written in bold) under each field specified (e.g., economic geology and process mineralogy) in Figure 1.3. Other parameters, such as ore-forming processes, flotation, and block modelling, are beyond this project's scope.

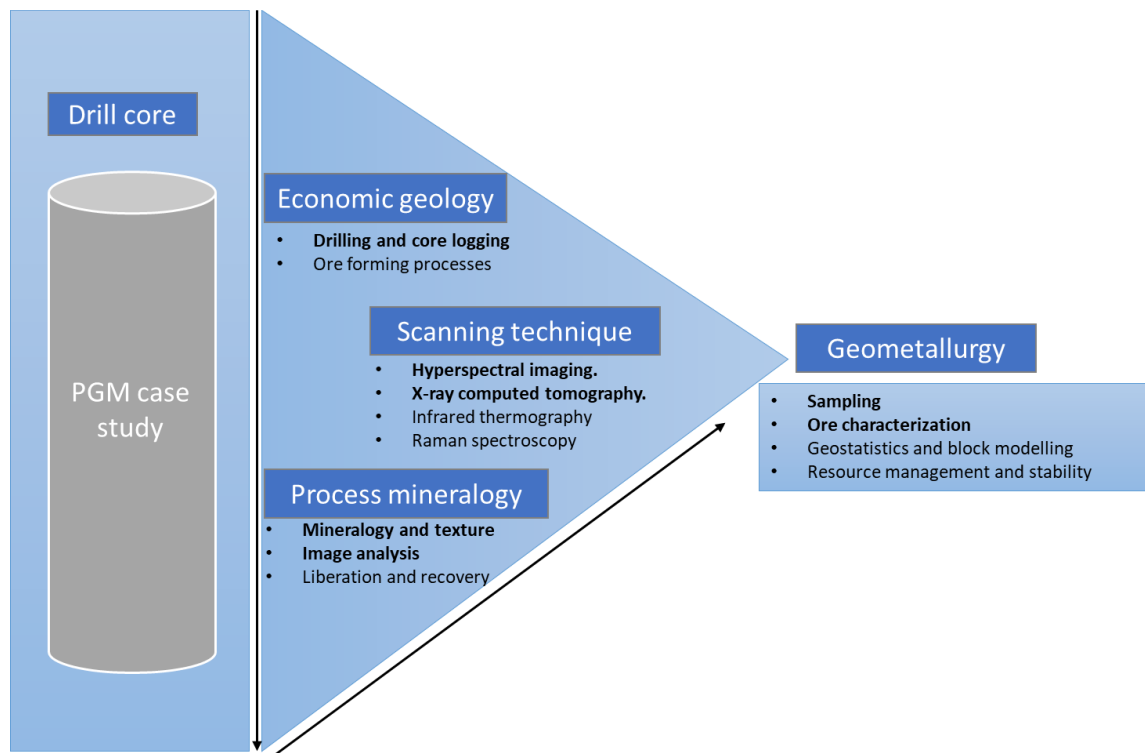


Figure 1.3: Illustration of the study's scope within the broader disciplines of economic geology, process mineralogy and geometallurgy. This study focuses on the parameters in bold.

1.5 Chapter descriptions

The thesis presents seven chapters (Figure 1.4): The introduction presented in Chapter 1 gives the background of the study, scope, the problem statement, aims and objective and key questions formulated to address the goals, and a summary of the thesis structure. Chapter 2 reviews the related literature to this research, synthesizing the findings and highlighting the literature gaps. Chapter 3 provides a detailed and systematic description of the materials, methods and equipment used in the project. The magmatic Ni-Cu-PGE drill core case study is presented in Chapter 4, describing the manual core logging and mineralogical characterization using QXRD and QEMSCAN. Results from HSI and XCT drill core scanning are presented in Chapter 5, alongside an investigation into combining output images of HSI and XCT. This is followed by Chapter 6, with a discussion on XCT and HSI's complementary capabilities, evaluating whether the objectives of this study were achieved (including their scanning practicalities and output information) and the ability for image co-registration. The conclusion in Chapter 7 will be drawn based on the findings and discussion, followed by recommendations for further investigation.

CHAPTER 1: INTRODUCTION	This chapter presents the background study of the project, outlining the scope of the project and the driving force to commencing the study.
CHAPTER 2: LITERATURE REVIEW	This chapter reviews the related work of the project to address the gap.
CHAPTER 3: MATERIALS AND METHODS	This chapter will be giving a detailed methodology carried to outline the scope of the project and addressing the research objective.
CHAPTER 4 : CORE CASE STUDY	Chapter 4 presents results (mineral assemblage and textural characterization) of the manual core logging, QXRD and QEMSCAN
CHAPTER 5: SCANNING TECHNIQUES	Chapter 5 presents the results of the scanning techniques: HSI and XCT together with overlapping outputs. The overlapping results are also covered in this chapter
CHAPTER 6: DISCUSSION	This chapter all the relevant discussions following the given results.
CHAPTER 7: CONCLUSION	Conclusion based on the results given and following the discussion. Recommendations for future studies are also given

Figure 1.4: Schematic diagram of the thesis layout

Chapter 2: Literature review

This chapter reviews the related literature for this project. This review starts with the geological setting of the case study followed by details of typical alteration reactions in magmatic Ni-Cu-PGE sulphide ores. It then covers the commonly used technologies for mineral and textural characterization focusing on specific measurement techniques relevant to the project (HSI and XCT). The review is concluded with a summary of the knowledge contribution of the reviewed literature highlighting the research gap.

2.1 Case study: South African Magmatic-Ni-Cu-PGE sulphide ore

The Bushveld Igneous Complex (BIC), South Africa, contains ~80% of the world's PGE resources. It is one of the world's extensive layered intrusions covering 65 000 km² and extending 450 km from west to east and 350 km from north to south (Naldrett et al., 2008), covering parts of Limpopo, Mpumalanga, Gauteng and the North-West Provinces (Figure 2.1). The complex consists of five limbs: the Eastern, Western, Northern, and Southern Limb and an unexposed South-eastern Limb covered by younger sediments (Cawthorn and Webb, 2001). The Rustenburg Layered Suite is prominent as the largest, oldest and most economic layered mafic intrusion that is part of the broader BIC.

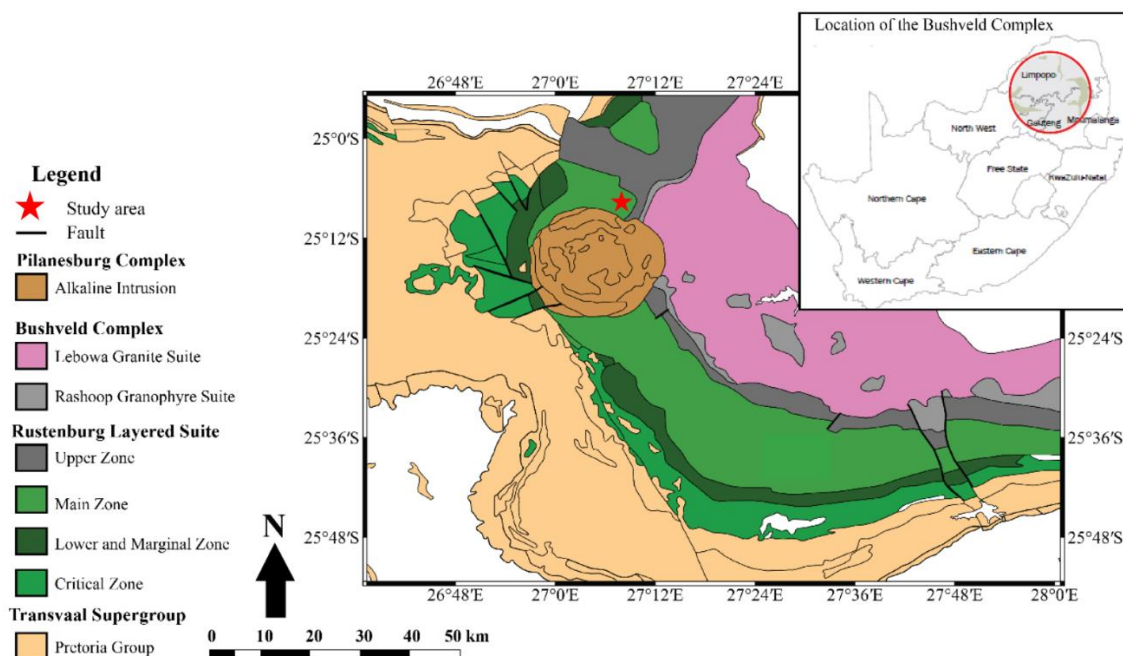


Figure 2.1: Geological location of the Bushveld Igneous Complex and Sedibelo Platinum Mine located on the Western Limb of the Bushveld Complex (Modified from Sehoole, 2019).

The Rustenburg layered suite consists of mafic-ultramafic rocks hosting Ni-Cu-PGE, Cr and V mineralization. The suite is further divided into five zones: (1) Marginal Zone, (2) Lower Zone, (3) Critical Zone, (4) Main Zone and (5) Upper Zone. The Critical Zone is approximately 1500 m thick and is characterized by cyclic economic packages that contain multiple chromitite stringers. The Critical Zone is subdivided into the Lower sub-zone and Upper sub-zone. The Upper Critical Zone's economic chromitite layers include the Upper Group Chromitite (UG2), stratigraphically overlain by 'Pseudo Reef' and Merensky Reef (Figure 2.2).

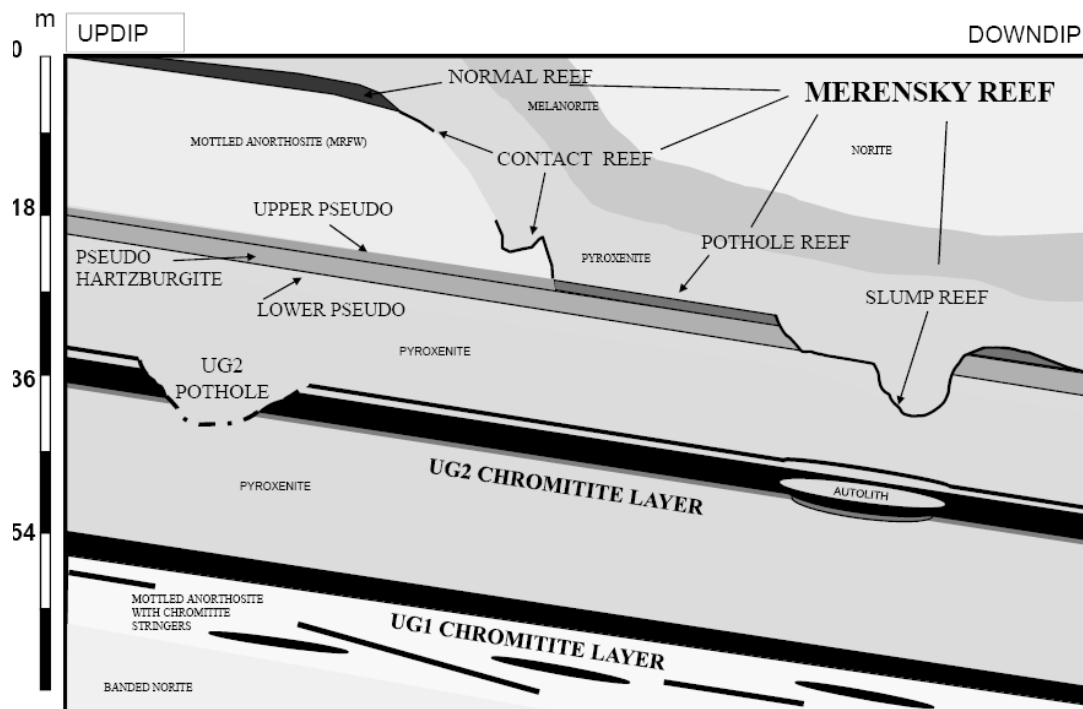


Figure 2.2: A general stratigraphic section of the Bushveld Complex illustrating the Upper Critical Zone Reefs (UG2, Pseudo and Merensky Reef), taken from (Becker et al., 2012, adapted from Crossling and Mupakati).

The ore of interest in this study is from the Sedibelo Platinum Mine (SPM), located on the Western Limb of the Bushveld Complex (Figure 2.1). The exploited reefs at SPM are the UG2 chromitite and the 'Silicate Reef'; mined PGEs in these Reefs are in the denomination of 3PGE (Pt, Pd, Rh + Au) at 1 to 3 g/t (Viring and Cowell, 1999). The 'Silicate Reef' represents in-house terminology at Sedibelo to describe the mining cut traversing the Footwall of the well-known Merensky Reef and the Pseudo Reef (Becker et al., 2012).

Pseudo Reef is a feldspathic harzburgite dominated Reef resembling the Merensky Reef (Mitchell et al., 2019). The Reef is dominated by silicate minerals (~80 wt.%) that have experienced extensive hydrothermal alteration, as observed by the relative abundance of alteration minerals such as serpentine, talc, chlorite and epidote (Becker et al., 2012; Molifie, 2021) (Table 2.1.). The Pseudo Reef

is divided into the lower and upper units (Figure 2.2.) (Scoon, 1987; Viring and Cowell, 1999). The lower Pseudo Reef is characterized by a pegmatoidal pyroxenite and pegmatoidal feldspathic pyroxenite. The lower and the upper Pseudo Reef is separated by a thin chromitite stringer known as the P1 marker (Viring and Cowell, 1999). Overlaying the P1 marker is the upper Pseudo Reef comprising a feldspathic harzburgite, locally known as 'tarentaal' (c.f. guinea fowl due to its spotted texture) with a 1 cm chromitite stringer (Viljoen, 1999). The upper Pseudo Reef is terminated by the 1-2 cm basal Merensky chromitite. Minerals in the Silicate Reef are characterised by a high abundance of alteration minerals such as serpentine, talc and chlorite formed from hydrothermal alteration and weathering reactions (Table 2.1). Numerous processing challenges arising from hydrothermal alteration and weathering reactions have been recognised in this ore, such as affecting the recoveries of PGMs (Becker et al., 2014).

Table 2.1: Bulk mineral assemblage of the Silicate Reef. The green highlighted sections are the alteration minerals formed due to oxidation and weathering reactions (From Becker et al., 2014).

Minerals	Wt.%
Base metal sulphides	0.2
Olivine	3.8
Orthopyroxene	24.6
Clinopyroxene	10.3
Serpentine	10.6
Talc	18.0
Chlorite	5.1
Plagioclase	6.8
Epidote	4.4
K-feldspar	1.2
Mica	0.1
Calcite	0.9
Quartz	1.0
Chromite	0.3
Fe-Oxides	11.0
Other	0.9

2.1.1 Hydrothermal alteration and weathering reactions of rock-forming minerals common in magmatic Ni-Cu-PGE ores

Peridotites, such as harzburgite and pyroxenite, are ultramafic rocks that are stable at high temperatures and pressure. Under different conditions, such as low temperature and pressure at shallow crustal levels, these rocks can become unstable and fragile, making them susceptible to post-emplacement secondary alteration (Schwarzenbach et al., 2014). Surface weathering and interaction with hydrothermal fluids may result in the modification of rock-forming minerals such as olivine and orthopyroxene to secondary alteration minerals. The degree of alteration can vary from incipient

alteration where the relict minerals and textures are still preserved to pervasive alteration when the original minerals and textures may be destroyed. The development of veins is regarded as direct evidence of the flow of hydrothermal fluids because changes in the mineral assemblage and mineral composition can only occur in the presence of a considerable influx of hydrothermal fluids.

Talc, serpentine and chlorite are the major phyllosilicate alteration minerals in the Silicate Reef (Table 2.1) which are formed from the hydrothermal alteration and weathering of the primary minerals in the various host lithologies comprising the Silicate Reef. A summary of some of the key alteration reactions typical of these ores is given in Table 2.2. This includes the formation of other non-phyllosilicate alteration minerals.

Table 2.2: Summary of the typical hydrothermal alteration reactions common in the rock-forming minerals of rocks similar to the Silicate Reef.

Rock-forming minerals	Alteration minerals	Type of alteration	Reference
Olivine	Serpentine +brucite + magnetite	Serpentinization	(McCollom and Bach, 2009; Schwarzenbach et al., 2014)
Olivine	Serpentine	Serpentinization	(Shervais et al., 2005; Tzamos et al., 2020)
Orthopyroxene	Serpentine-aqueous silica	Serpentinization	(Shervais et al., 2005)
Orthopyroxene	Serpentine + talc	Serpentinization	(Molifie, 2021; Shervais et al., 2005; Tzamos et al., 2020)
Orthopyroxene	Talc +olivine	Orthopyroxene-talc alteration	(Iyer et al., 2008; Schwarzenbach et al., 2014)
Biotite	Chlorite + k-feldspar	chloritization	(Chayes, 1955)
Plagioclase	Epidote	Epidotization	(Li et al., 2004; Pacey et al., 2020)
Epidote	Chlorite	Chloritization	(Brammall, 1936; Byrne et al., 2020)
Plagioclase	Chlorite	Chloritization	(Wu et al., 2019)

Serpentine can form from olivine and orthopyroxene under different conditions, generating different by-products. Olivine is more prone to serpentinisation and the first to be altered if it occurs with orthopyroxene (like in the harzburgites) (Schwarzenbach et al., 2014; Shervais et al., 2005). The degree of alteration may vary from one stage to the next. In the early alteration, relicts of olivine and orthopyroxene may be present. In the later stage, these minerals may be fully replaced by serpentine forming serpentinite rocks (when serpentine is more abundant). Talc and magnetite may form as the by-products of serpentinization (Table 2.2). Iron and magnesium from olivine may be released during

the reaction to form magnetite veins (McCollom and Bach, 2009; Shervais et al., 2005). Talc can form as a by-product of the orthopyroxene-serpentine reaction. Orthopyroxene hydrothermal reaction is most likely to form talc minerals; either as a by-product from serpentinisation or directly from orthopyroxene-talc reaction (Table 2.2).

Another dominant alteration mineral is chlorite. Chlorite is an alteration mineral forming from different primary minerals such as biotite, plagioclase and epidote under different conditions (Table 2.2). According to Wu et al., (2019) Type I chlorite is formed from biotite and may retain biotite Pseudomorphism if partially altered; chlorite formed from feldspar as irregular distributed grains is Type II and the one occurring as veins are Type III. Plagioclase and chlorite are likely to be associated with epidote (Li et al., 2004; Smith et al., 2013). Epidote is an alteration mineral that can form from plagioclase during hydration reactions known as epidotisation; and may itself be altered by chlorite forming a plagioclase-epidote-chlorite assemblage.

2.2 Techniques for mineral and texture characterization

Various methods can be used to characterise the mineral assemblage and classify texture in drill cores from the established time-consuming manual to the more rapid, automatic approaches. The techniques are generally chosen based on their applicability for mineral identification of the sample concerned, speed, cost and practicality. Some of the techniques provide statistical data and some produce images that can be analysed at a later stage. Imaging techniques have advanced as analytical measurements capable of providing mineral characterization have been developed. Nevertheless, not all techniques can produce high-quality images. The various imaging techniques used commonly include visible light (such as optical microscopy and visual logging), electron beam (e.g., scanning electron microscopy with energy dispersive X-ray spectrometry), infrared (e.g., hyperspectral imaging) and X-ray technologies (e.g., X-ray diffraction, X-ray fluorescence and X-ray computed tomography) - all of which make use of the electromagnetic spectrum in some manner. Most of these techniques are 2D and a few are 3D illustrated in the diagram by Butcher (2020) (Figure 2.3). They can be performed at different scales to provide increased resolution of the dataset. The routine application of these techniques assists in providing positive data in predictive geometallurgy (van den Boogaart and Tolosana-Delgado, 2018). Only techniques used in this thesis are reviewed extensively.

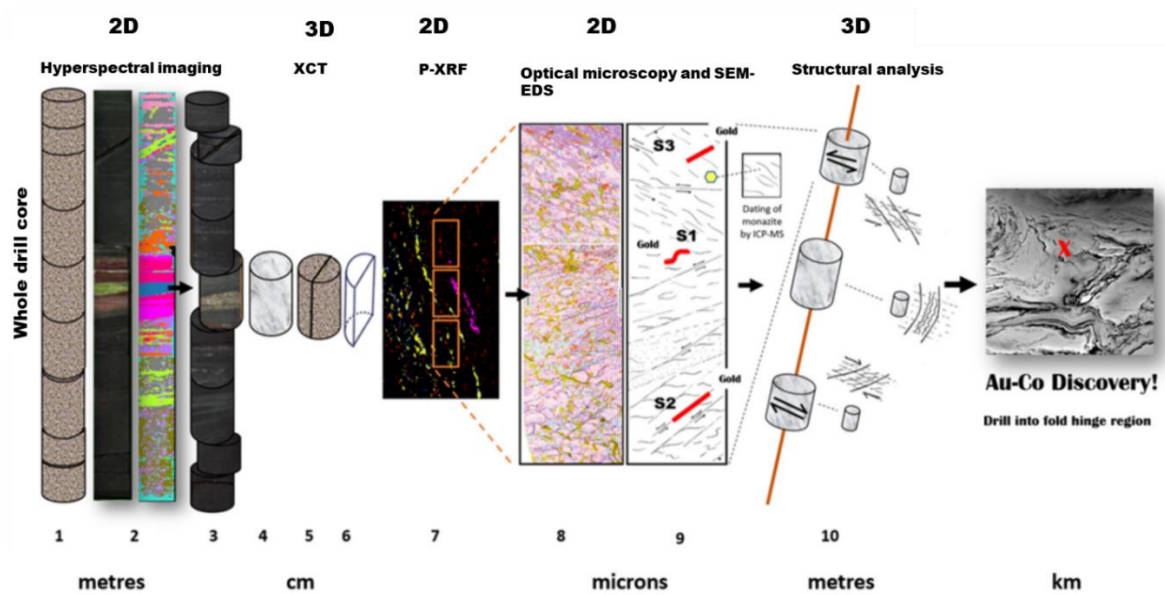


Figure 2.3: Various techniques to characterize mineralogy and texture on drill core at different scales (Adapted from Butcher, 2020).

2.3 Visual logging

Visual logging is the traditional method that has been used for decades by geologists to identify lithologies, texture and mineral assemblage on the drill cores acquired during exploration. This method is usually considered first for rock characterization before any other techniques can be applied. Several logging techniques, tools (e.g., hand-lens, magnet, acid, clinometer, measuring tape or ruler, pencil and a notebook) and procedures can be used (Hartman and Mutmanský 2002; Murphy and Campbell 2007). Ultimately, the logging should provide information such as the borehole localities, drilling orientations, drilling methods and coordinates as well as rock descriptions.

The different approaches to logging as described by Marjoribanks, (2010) are as follows:

- (i) **Prose logging** is a descriptive method conducted on a selected core. This type of method is similar to descriptions in the field of outcrops, except that it is done on drill cores. Geologists use this method to make a detailed, qualitative description of the rock types with arguments and discussion.
- (ii) **Analytical logging** is a detailed logging method where rocks are characterized in categories (such as colour, grain size, macrotexture and minerals). This type of method can be used as proxy data in geometallurgical programs and easily recorded in computers for easy access. Data is presented in an easy and standardized format for anyone to understand. However, the information to be presented in this log is limited and lithological contacts cannot be shown.
- (iii) **Graphical logging** is a downscale representation of a core drawn to a paper as a stratigraphic column. The log is presented with data from analytical logging, including

depths and all the parameters that can be used to locate the core in-situ. In this type of logging method, depth, structures and lithological boundaries are shown; and can be used as direct indicators of the actual core. This method needs to be used in conjunction with other logging methods to present additional details.

For accurate and representative data, all three logging methods are employed in one project. However, conducting classifications with these simple techniques are dependent on human knowledge and what one can see with the naked eye. Human eyes are deceptive and limit the characterization of the samples. Accurate mineral identification is not necessarily possible since colour is generally one of the last attributes for positive mineral identification. However, it would be good at potentially identifying differences in macrotexture (such as shape and size) (Donskoi et al., 2016; Lund et al., 2015; Nguyen, 2013; Pérez-Barnuevo et al., 2018). The logging is usually conducted on half cores with the other half reserved for elemental or mineralogical analysis (covered in the following sections). The sampling for small scale analyses is influenced by visual observations during logging.

2.4 Automated Scanning electron microscopy with energy dispersive X-ray spectrometry (Auto-SEM-EDS)

The use of scanning electron microscopy (SEM) originated in the 1960s with many applications across numerous disciplines including earth, life and materials sciences (Fitzgerald et al., 1968). Shortly after, the potential of this technology for quantitative mineralogical analyses was recognised giving rise to the development of the automated SEM coupled with energy dispersive X-ray spectrometry (EDS) platforms. The currently used auto-SEM-EDS are QEMSCAN, MLA, TESCAN-TIMA and Mineralogic instruments (Fandrich et al., 2007; Gottlieb et al., 2000; Paradis et al., 2021). This review largely focuses on the specifics of the QEMSCAN instrument which is used in this study.

2.4.1 Principles of auto-SEM-EDS

The principle of scanning electron microscopy is the focusing of a high voltage electron beam on the sample. This electron beam interacts with the sample causing the emission of cathodoluminescence, Auger electrons, secondary electrons, backscattered electrons (BSE) and characteristic X-rays – each of which can be measured with different detectors. Backscattered electrons and X-rays are key to mineral identification with Auto-SEM-EDS. Backscattered electrons are generated when the electron beam collides with atoms of the sample that are elastically scattered forming electrons with energies close to that of the incident electron beam. The brightness of these backscattered electrons is related to the average atomic mass of the material analysed. X-rays are produced by electron transitions from the outer to inner shells of an atom causing the emission of an X-ray with characteristic wavelength and energy (Morrison and Gu, 2016; Prost, 2013). The X-ray energy and intensity are recorded and

quantified by energy-dispersive X-ray spectrometry (EDS) (Girão et al., 2017; Pownceby and MacRae, 2016).

2.4.2 Mineral identification

Every mineral has a density and a composition comprising a set of elements in different relative proportions. Upon interaction with the electron beam, a unique BSE grey level and X-ray energy spectrum are produced for every pixel analysed. The energy of the X-ray peaks defines the identity of the element and the intensity of the peak defines the relative concentration. With a user-defined database known as the species identification protocol (SIP) in QEMSCAN, each pixel analysed can thereafter be positively identified as a mineral. The SIP file is generally in continual development and will be refined from one project to the next catering to the differences in mineral assemblage between different specific ores. Complementary techniques such as optical microscopy and quantitative XRD prove useful in confirming the identity of minerals.

2.4.3 Scanning and data acquisition

Samples are prepared as polished thin sections or resin mounted ore blocks depending on the sample and data requirements. In some cases, samples may also be analysed in discrete size fractions. Before analysis, the polished samples are carbon-coated to prevent charge build-up during analysis. Samples are then presented to the microscope for scanning and analysis. The data acquisition is automated once the optimal beam current, BSE brightness and contrast and X-ray energies have been calibrated and the measurement conditions including magnification and step size (resolution) have been defined. However, conditions of the system need to be defined for individual samples to obtain quality data, e.g., electron beam conditions (i.e., current, and energy), magnification and the measurement step size (pixel spacing). Ultimately, the resolution of the auto-SEM is dependent on the size of the electron beam and its interaction volume (Gottlieb et al., 2000).

The common measurement modes during scanning are bulk minerals analysis, particle mineral analysis and field image mode. The bulk mineral analysis is a fast and statistically valid form of line scanning providing information on the bulk mineral assemblage. BSE and EDS data are collected in one direction at a predefined step size. Particle mineral analysis (also known as EDS mapping measurement) analyses the full area of the sample with the resolution of the mapping customised by the magnification and pixel size. A full mineralogical dataset can be obtained from this analysis mode providing information on mineral grades as well as textural measurements (e.g., grain size, mineral association data, liberation). The field image mode also uses area mapping but is based on the premise that the size of the 'particle' is greater than the field size, and successive fields are virtually stitched together after analysis. For all the measurements, BSE thresholding is used before EDS acquisition to distinguish the background (or resin) from the analysed particles. The BSE thresholding can be used to rapidly locate specific individual mineral grains that occur in low amounts or as trace phases (such as BMSs

and PGMs) which can then be X-ray mapped (Graham et al., 2015; Pirrie and Rollinson, 2011; Schulz et al., 2020).

2.4.4 Data processing and reporting.

All the software platforms follow similar processing steps such as having a reference library of mineral characteristics to compare the acquired BSE and EDS data for mineral identification. In the case of QEMSCAN, acquired data is processed through the species identification protocol (SIP) file. Once phases have been identified, each phase is given a unique composition and density from which its relative abundance can be quantified by weight percent. Other important steps in data processing include dealing with boundary phases, deagglomerating touching particles, producing simplified and meaningful mineral lists relevant to the ore deposit characteristics, comparison of the back-calculated elemental composition with a measured composition (by chemical assay for data validation), as well as the quantification of various textural parameters.

False-colour images with user-defined colours can also be generated as output products. These images qualitatively illustrate how minerals are associated with each other, which is essential for particle analysis. Figure 2.4 illustrates selected QEMSCAN false colour particle images of the feed of magmatic Ni-Cu-PGE sulphide ore, with specific reference to the relationship of the naturally floating talc with orthopyroxene. Compared to the traditional method of point-counting in optical microscopy, representation of mineral grades in auto-SEM is automated and presented in area, volume or weight percentages with lower relative errors given that a significantly greater number of particles can be analysed.

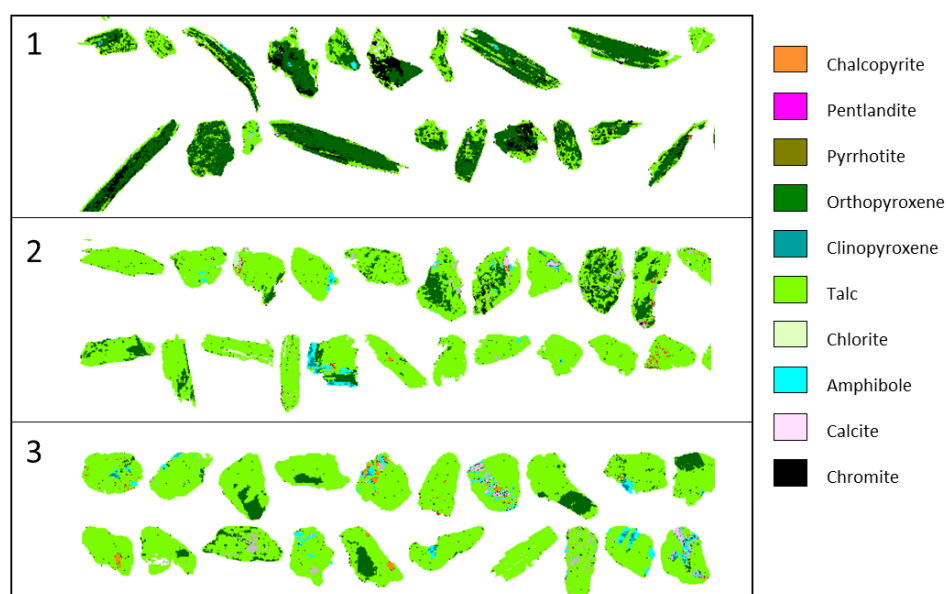


Figure 2.4: QEMSCAN false colour particle images in the $-75 +38$ mm fraction recovered in batch floatation tests of the Great Dyke magmatic Ni-Cu-PGE sulphide ore, Zimbabwe. Orthopyroxene and talc composites represent naturally floatable gangue in these ore types. Talc rims orthopyroxene in ore

1; orthopyroxene in ore 1 and 2 are pervasively altered talc, leaving relics of orthopyroxene (Dzingai et al., 2021).

2.4.5 Challenges and limitations

Auto-SEM-EDS can provide quantitative information of a variety of mineralogical parameters, especially of low-grade samples (e.g., precious metal bearing ores), although it should be recognised the results will always need validation with other complementary techniques. The EDS relies only on elemental composition for mineral identification and discrimination; posing a challenge in discriminating minerals with a similar chemical composition such as magnetite and hematite (Donskoi et al., 2016; Schulz et al., 2020). Auto-SEM techniques are one of the most expensive and time-consuming due to the requirements for high-quality sample blocks as well as the significant costs of the hardware and trained personnel operating the equipment. The user should not forget the very important role of sampling, to ensure that the small amounts of material presented to the auto-SEM-EDS are representative of the larger sample. However, due to the lack of a third dimension in the 2D image, auto-SEM-EDS data is subjected to stereological errors.

2.4.6 Applications in geometallurgy and the characterisation of magmatic Ni-Cu-PGE ores

Auto-SEM technologies can be used to quantify the mineral grades, element deportment, grain size distribution, mineral association and liberation characteristics of the samples, all of which are relevant in geometallurgy (Jardine et al., 2018; Tusa et al., 2019). The high resolution in auto-SEM allowed for the characterization of very fine-grained minerals that cannot be easily located and identified by optical microscopes, such as the identification of individual PGMs, especially in low grade (flotation tailings) samples. There are a host of case studies of southern African magmatic Ni-Cu-PGE ores where auto-SEM-EDS information has proved valuable to improving downstream flotation recovery of the valuable minerals, e.g. (Becker et al., 2009; Chetty et al., 2009; Lotter et al., 2011; Schouwstra and Rule, 2016). The Auto-SEM-EDS platform is generally considered the work-horse for process mineralogy in these types of applications (Becker et al., 2009; Graham et al., 2015; Molifie, 2021).

2.5 Hyperspectral imaging

The hyperspectral imaging spectrometer was introduced in the 1970s after the concept of spectroscopy was coupled with imaging in remote sensing in the 1950s (Goetz et al., 1985; Probst, 2013; Signoroni et al., 2019). Today, imaging spectrometry is used in laboratories, field, aircraft, and satellites which are either multispectral or hyperspectral imaging systems (Sriram et al., 2016). Currently, there are a variety of core scanners in the market: CSIRO – HyLogger3 systems; CORESCAN - Hyperspectral Core Imaging III (HCI-3); HyLogging system with Raman spectrometer and NEO Hypex hyperspectral

camera and TerraCore/Specim - SisuRock. A summary of these techniques is given by Harraden et al. (2019).

2.5.1 Principles of hyperspectral imaging

Infrared spectroscopy

Light illuminated onto the surface of a medium can either be reflected or absorbed (Clark, 1995). Hyperspectral imaging is based on reflectance spectroscopy and is associated with absorption characteristics depending on its chemical and physical properties (Lau, 2004). In general, electronic processes within the material result in broad absorption features compared to vibrational processes (bending and stretching of bonds) that result in sharp absorption features (Goetz et al., 1985; Raja et al., 2010). Spectral absorption can be described by the Beer-Lambert law. In hyperspectral imaging, the reflectance and absorption characteristics of a sample are monitored across a wavelength range (Table 2.2) that allows for direct identification of the material (Hunt, 1977).

Spectral regions

The wavelength ranges (also known as spectral regions) are needed to cover the range of wavelengths where the spectral absorption characteristic of many minerals occur (Table 2.2). In hyperspectral imaging, the common spectral ranges are (1) visible-near infrared (VNIR) typically characterised by electronic absorption processes, (2) short wave infrared (SWIR) characterized by vibrational overtones and combinations of fundamental vibrations related to water and O-H and C-O, and (3) long-wave infrared (LWIR) characterized by fundamental vibrations related to Si-O, O-H and CO₃²⁻. (Hunt, 1977; Prost, 2013; Ramanaidou et al., 2015). When interpreting the hyperspectral signatures, the focus is usually placed on the wavelengths of absorption in the VNIR and SWIR regions compared to the wavelengths of the peaks (also known as Reststrahlen bands) in the LWIR region (Lau, 2004; Linton et al., 2018).

Table 2.3: Wavelength ranges of the infrared regions' divisions with the spectral ranges commonly used for mineral identification. Table adapted from (Linton et al., 2018; Sriram et al., 2016).

EM Spectral regions	Remote sensing division	Mineral ID wavelengths	Wavelength (nm)	Cause of features
Visible infrared	Visible Infrared (VIR)	Visible near-infrared (VNIR)	0.7-1.0	Electronic processes-charge transfer and crystal field absorption
Near-infrared	Near-infrared (NIR)			
	Mid-infrared	Short-wave infrared (SWIR)	Short-wave infrared (SWIR)	1.0-2.5
Mid-wave infrared (MIR)			3.0-6.0	
Far infrared	Long-wave infrared (LWIR)	Longwave infrared (LWIR)	6.0-13.0	Fundamental vibrational processes
	Very long-wave infrared (VLWIR)	-	14-40	-
	Far infrared (FIR)			-

2.5.2 Mineral Identification

The hyperspectral signatures for a range of minerals were systematically measured by Graham Hunt and John Salisbury in the 1970s to create the first HSI mineral library covering silicates, carbonates, oxides, sulphides and salt. The response of each of the various minerals in the different spectral ranges is summarised in Table 2.3. Here it is evident that the response of the phyllosilicate minerals is good in the SWIR region and moderate in the LWIR, whereas the response of most anhydrous silicate minerals is good in the LWIR region. Also, the wavelength position of each spectrum is governed by chemistry. In some instances, absolute mineral abundance is not possible, especially for a mineral that is not detectable under a specific wavelength range (Tuşa et al., 2020). The close range HSI has the most significant potential to map and identify the mineral assemblage and lithology.

Table 2.4: Summary of hyperspectral imaging sensors and their abilities for mineral identification. Green-Good; Orange-Moderate; Red-Bad and White-Uncertain. Adapted from (Linton et al., 2018) 2018.). The yellow rectangle shows the assistance of HSI of problematic minerals in geometallurgy.

	Groups	Minerals	VNIR	SWIR	LWIR	
Silicates	Inosilicates	Amphibolite	Actinolite	Red	Green	Green
		Pyroxene	Diopside	Green	Yellow	Green
	Cyclosilicates	Tourmaline	Dravite	Red	Green	Yellow
	Nesosilicates	Garnet		Yellow	Red	Green
		Olivine	Forsterite	Green	Red	Green
		Zircon		Green	Red	Red
	Sorosilicates	Epidote		Red	Green	Green
	Phyllosilicates	Mica	Muscovite	Red	Green	Yellow
		Chlorite		Red	Green	Yellow
		Clay Minerals		Red	Green	Yellow
	Tectosilicates	Feldspars	Orthoclase	Red	Red	Green
			Albite	Red	Red	Green
Silica		Quartz	Red	Red	Green	
Non-silicates	Carbonates	Calcite		Red	Green	
		Dolomite		Red	Green	
	Hydroxides	Gibbsite		Red	Green	Yellow
	Sulphates	Alunite	Alunite	Red	Green	Yellow
			Barite	Red	Red	Green
	Borates		Borax	Red	Green	Yellow
	Halides	Chlorides	Halite	Red	Yellow	
	Phosphates	Apatite	Apatite	Yellow	Green	Green
			Amblygonite	Yellow	Green	Green
	Hydrocarbons		Bitumen	Red	Green	
	Oxides	Spinel	Haematite	Green	Red	Red
			Magnetite	Red	Red	Red
Sulphides	Pyrite		Yellow	Red	Red	
	Sphalerite		Red	Red	Red	

Causes for mineral spectral variation

Several factors are contributing to spectral variation influencing mineral detection. The absorption curves displayed in the spectra are caused by the presence of OH, H₂O, CO₃, SO₄, CH and Si-O (Prost, 2013). The spectral signature is dependent on various parameters: electronic and vibrational overtone processes, absorption confidence, reflective index, scattering effect and volume/surface scattering (Ramanaidou et al., 2015). Each of these parameters is influenced by the factors summarised in Table 2.5, which also affect the spectral variability in different minerals (Ramanaidou et al., 2015; Armengol, 2015).

Table 2.5: A summary of factors influencing spectral variation for mineral identification.

Parameter	Reason	Effect	Reference
Grain size	Changes in grain size affect the relative amount of reflection vs absorption.	Smaller grains have decreased absorption spectra and vice versa.	(Mathieu et al., 2017; Sriram et al., 2016)
Mineral composition	Changes in composition affect the wavelength position of specific absorption features i.e., a shift in a spectral band	The absorption minima can slightly shift with a change in elemental content. The significant minerals affected are the ones responsive to SWIR, like chlorite and micas.	(Pontual et al., 1997; Prost, 2013; Ramanaidou et al., 2015)
Mineral colour	Minerals have different colours influencing the amount of reflectance and absorption.	Darker minerals absorb too much light, and lighter grains tend to reflect more light.	(Salehi et al., 2020; Sriram et al., 2016)
Crystallinity	Change in crystal structure and order affects the shape of the absorption features (band strengths and widths).	A decrease in mineral crystallinity shallows and broadens the bands and vice versa.	(Pontual et al., 1997; Ramanaidou et al., 2015)
Mineral texture	The mineral mixture creates mixed spectral responses with a mixing of absorption features related to different mineral species present.	An intimate mineral mixture can mask the presence of certain minerals in the presence of others, creating mixed phases.	(Mathieu et al., 2017; Sriram et al., 2016)
Water	Water is responsive under NIR.	Wet samples tend to suppress the sample's reflectance value and water absorption bands tend to dominate and overpower mineral-related absorption.	(Jacq et al., 2019)

The advantage of using reflectance spectroscopy for sample analysis is that there is minimal sample preparation and because the analysis is non-destructive, the material can be used for other analyses after scanning. The only preparation required is to ensure that the surface of the core is clean and dry because the surface absorption is independent of the sample thickness.

2.5.3 Scanning and data acquisition

HSI provides both spectral and spatial information to produce spatial properties and compositional information (Gasser et al., 2019; Monali and Snehal, 2014; Signoroni et al., 2019). As the samples are captured with the cameras, the image is built consisting of pixels containing a complete spectral response to the spectral sensors. The system sampled light dispersed by a slit, either with a prism or grating (Figure 2.5). Therefore, for every wavelength sampled, energy is recorded for each pixel in the image to collect the spectrum (Bioucas-Dias et al., 2013; Mahajan and Kamalapur, 2016; McHugh et al., 2001). The images are collected using different hyperspectral sensors (Table 2.3); and each sensor is capable of identifying and quantifying minerals at a specific spectral range (Sharma, 2017; Sriram et al., 2016). Spectral sensors also play a significant role in determining the number of pixels captured (Mahajan and Kamalapur, 2016). For each wavelength band detected, the 2D spatial image is collected at the same time (Gasser et al., 2019; Mahajan and Kamalapur, 2016).

With spatial scanning, each of the outputs of the sensor represents a full slit spectrum. Various methods are used to acquire the HSI images. The whiskbroom (point to point) and push-broom (linear) scanners are the most common scanning methods differing in their acquisition approaches/procedures and the methods used to split the light (Gasser et al., 2019). Both scanning methods used have their advantages and disadvantages, making them suitable for use in space-borne analyses and laboratories. The push-broom is the commonly used method for drill core imaging and is the focus of this study. In the push-broom scanning method, samples move in the conveyor belt under stationary cameras (including spectral cameras) and illuminating sources (Fowler, 2014; Prost, 2013; Signoroni et al., 2019). The scanning system is dependent on a band filter, either fixed or tune-able. The samples are spectrally scanned by exchanging filters. The most commonly used are the turntable bandpass filter (see also Gasser et al. (2019)).

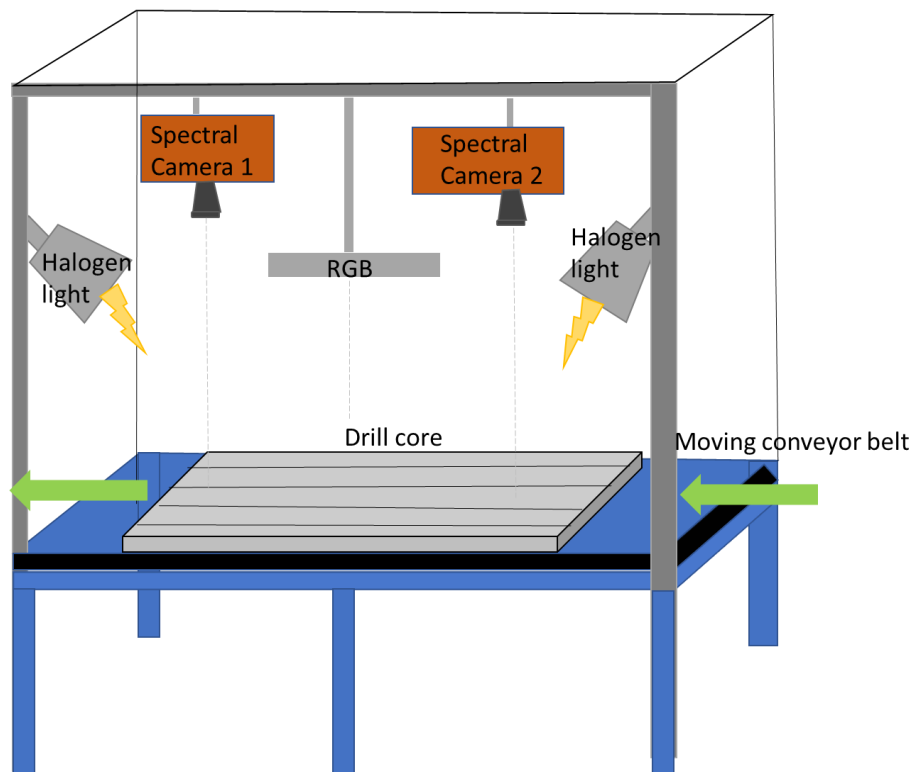


Figure 2.5: Schematic representation of the HSI acquisition (Adapted from Lorenz et al., 2019).

2.5.4 Data processing and analysis

The standard approach for HSI data processing and image analysis uses 3 steps (Kurz et al., 2013; Koerting et al., 2015; Kurz, 2017; Mohamed, 2018):

- a) Pre-processing and End-member extraction.

Pre-processing is for spectral calibration and image correction to remove or reduce artefacts such as noise and unnecessary vibrations (Mateen et al., 2018). End-member extraction is a collection of spectrally pure constituent spectra, having a range of compositions representing a series of minerals (Plaza et al., 2004). The end-member extraction identifies the hidden signals from the mixture and is the first approach to identify the spatial distribution of minerals and mineral assemblages. The mineral wavelengths mapped by different sensors are collected for more in-depth absorption features used as input classification (Mohamed, 2018). In this step, feature extraction is essential to minimize the spectral complexities and mixtures and capture all the possible absorption features in VNIR and SWIR, and peaks in LWIR (Linton et al., 2018). The 'Environment for Visualizing Images (ENVI, Exelis Visual Information Solutions Boulder, Colorado) software is often used in this step (Koerting et al., 2015; Tusa et al., 2019). The pre-processing includes removing anything (including trays) other than the drill core by applying a mask. Thereafter, readily automated mineral maps are generated using their spectral signatures obtained.

b) Hyperspectral classification.

The traditional mineral classification approach is conducted by comparing the spectral signature to the readily available spectral libraries such as the Johns Hopkins University (JHU), Geology, Geophysics, and Geochemistry Science Centre at the United States Geological Survey (USGS) libraries (Harraden et al., 2019; Kale et al., 2017; Ramakrishnan and Bharti, 2015; Tuşa et al., 2020). Spectral unmixing and non-linear classification are additional methods undertaken for mineral classification. However, these methods need expert knowledge and can be time-consuming, especially in complicated samples (Jacq et al., 2019; Kruse, 1996; Mohamed, 2018). Like any other mineralogical technique, HSI data also needs to be validated with other techniques such as auto SEM-EDS, XRD and optical microscopy. Making use of these supporting techniques allows for further mineral reclassification and identification of unclassified minerals (e.g., base metal sulphides, magnetite, chromite) with no responsive spectral signature in HSI. The end product is generated as drill cores with spatial mapping of different minerals with their corresponding spectral features (Figure 2.8).

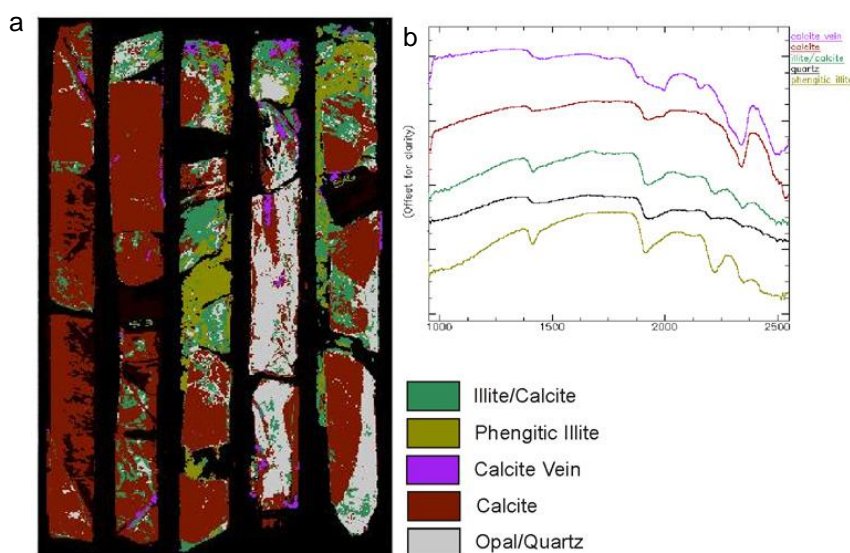


Figure 2.6: Output results of the processing stages of hyperspectral imaging. (a) Mineral map of drill core; (b) Spectral signature of the mineral map (From ALS and Terracore international).

c) Quantification

Successful spectral and mineral classification can provide a relative mineral abundance of minerals present by calculating pixel percentages over an area of interest in the drill core (Harraden et al., 2019). Quantitative data for absorption features and wavelength can also be extracted using calibration methods such as Hull correction. Hull correction normalises the reflectance spectrum to 100%. After the correction with this feature, the depth of absorption and peak heights can be calculated, related to the mineral abundance. Also, the wavelength position of each spectrum is governed by chemistry (Linton et al., 2018). In some instances, absolute mineral abundance is not possible, especially for the

mineral that is not detectable under a specific wavelength range (Tuşa et al., 2020). However, mineral association and quantification in complex ores can be challenging due to the nature of hyperspectral data and minerals having spectral properties that can be diagnosed by more than one spectral sensor (Table 2.3). Recently, various researchers have made use of artificial intelligence to overcome this challenge, particularly for data quantification (Johnson et al., 2019; Okada et al., 2020; Selci, 2019).

2.5.5 Challenges and limitations

Although hyperspectral imaging can rapidly acquire extensive datasets, the processing and interpretation of these data may be challenging due to the nature of hyperspectral data and minerals having spectral properties that can be diagnosed by more than one spectral sensor, particularly in complex ores. HSI may suffer from spectral mixing and mineral overlapping from different spectral sensors. The issues seem to be common in dark coloured minerals and for samples with a high degree of alteration. For example, in the work conducted by Duee et al. (2019), HSI showed weak reflectance on darker rocks and detected a high abundance of serpentine (due to its strong spectral feature in SWIR) masking other minerals present. These issues may lead to overestimations in the attempt to extract quantitative data (Tuşa et al., 2020). Therefore, extensive data interpretations and reclassification coupled with complementary mineralogical knowledge of the deposit may be required. The mineral reclassification may require specialists such as mineralogists or geologists. Identification of minerals by hyperspectral imaging is limited to silicate, carbonate, sulphates and certain phosphate minerals with sulphide mapping remaining an ongoing challenge (Armengol, 2015; Paradis et al., 2021). Like any other 2D technique, HSI also suffers from stereology.

2.5.6 Applications in geometallurgy and the characterisation of magmatic Ni-Cu-PGE ores

The HSI technique produces large volumes of datasets rapidly, which are well suited for geometallurgical applications (Johnson et al., 2019). Obtaining HSI data is fast and easy and can be used as input data for rock type recognition and ore type indicators for mineral processing. Ore bodies are characterised by variable rock types constituting rock-forming minerals that can be readily identified by HSI (e.g., silicate minerals). For some ore bodies, gangue minerals may be used directly to define the ore type; especially where silicate minerals have a strong impact on mineral processing, the use of hyperspectral imaging can be useful to identify and semi-quantify the mineral abundance. Another valuable application in geometallurgy is the ability to produce high-resolution images that allow the mapping of problematic minerals into the ore body block model, such as the phyllosilicates across different horizons or domains of an ore deposit (e.g., Porphyry, Sedimentary, Hydrothermal and Orogenic deposits) (Kruse et al., 2012; Mathieu et al., 2017; Mauger et al., 2007; Pan et al., 2019; Son et al., 2021). Phyllosilicate alteration minerals can cause numerous challenges in flotation and leaching, and their early identification can allow for appropriate mitigation strategies to be put in place (Cracknell et al., 2018). Merrill et al. (2018) outlined and proposed the methodology to use HSI to predict copper's flotation performance in the presence of gypsum and kaolinite minerals; and the aluminium content

(from white mica and gypsum) effect upon slag quality. The carbonate mineral content can also be measured for predicting acid consumption in both hydrometallurgy and environment acid mine drainage applications (Cracknell et al., 2018).

Mineral texture has been identified as an important attribute for predicting the behaviour in mineral processing. HSI was adopted to map and identify geological structures such as veins and faults (Tusa et al., 2019; Tuşa et al., 2020). Since quantitative textural information is required, different algorithms and methods have been implemented to characterize and quantify these features to assist HSI's ability to be further used for other mineralogical related parameters constituting the rock type (Liu et al., 2019; Signoroni et al., 2019; Okada et al., 2020). HSI was used to develop a methodology to extract geotechnical data (rock mass rating and quality index) from drill core at the Cadia East Au-Cu porphyry deposit, Australia using mineralogical data from HSI in combination with fracture orientation and spacing (Harraden et al., 2019). Johnson et al. (2019) used VNIR and SWIR to predict Au-Cu recovery and throughput at the Au-Cu porphyry-related skarn deposit, Phoenix Mine, Nevada, where chlorite and actinolite identified by HSI showed a positive association with increased recovery and throughput.

Although numerous applications of hyperspectral remote sensing in magmatic Ni-Cu-PGE ores have been reported (e.g., Bedini, 2017) no work seems to have been published on drill cores. In the conducted studies, the application of HSI remote sensing focused mostly on mapping mafic and ultramafic rocks. Mafic or ultramafic rocks often contain abundant alteration minerals such as serpentine, talc, chlorite, etc that have a strong spectral signature under VN-SWIR (Ramakrishnan and Bharti, 2015). However, the direct detection of Ni-Cu-PGE mineralization in these rocks is challenging since these minerals do not have a distinctive spectral response (Paradis et al., 2021). Some of the examples of remote sensing applications in these ores included the mapping of the ultramafic rocks of the Aynak-Logar Valley, Afghanistan using Hymap data. The rocks of the deposits have been mapped as ferrous (Fe^{2+}) and ferric (Fe^{3+}) iron-rich serpentine-bearing rocks using the spectral absorption features. Salehi et al. (2020) also used VNIR and SWIR to measure the content of iron (Fe^{2+} and Fe^{3+}) and Mg-OH, respectively, in the minerals of the mafic and ultramafic rocks. The Mg-OH rich spectra were associated with serpentine and iron features were associated with olivine and pyroxenes. Using these absorption features it was observed that mafic rocks have greater reflectance than ultramafic rocks. Mielke et al. (2014) analysed mafic and ultramafic mine waste materials with VNIR and SWIR to measure the area covered by the mine wastes and their mineral assemblage such as possible detection of acid rock drainage neutralising minerals being carbonates in this case.

2.6 X-ray computed tomography

X-ray computed tomography is a non-destructive rapid scanning technique developed in the 1960s for medical studies to examine the human body's internal structure (Bhide et al., 2019; Banholzer et al., 1987). The XCT application of XCT is currently being used both in geoscience research and industry (e.g., oil and diamond industries) to identify valuable minerals and valuable textures in 3D.

2.6.1 Principles of X-ray computed tomography

X-ray computed tomography images are built with multiple X-rays illuminated from the source through the sample over a range of angular orientations on a rotating stage to the detector. The X-rays from the incident source are focused onto a rotating sample to produce grey-scale values reflecting the density, thickness and atomic number variation of materials, equivalent to brightness and proportional to increasing sufficient attenuation (Kyle et al., 2008). The attenuation is the response of the material to whether it absorbs or scatters the incident X-rays. The interactions (physical processes) responsible for X-ray behaviour (attenuation) are photoelectric absorption, Compton scattering and pair production. The photoelectric absorption effects are dependent on the effective atomic numbers at low energies and dominant for geological samples, Compton scattering is dependent on density at high energies and pair production. These interactions of the X-ray with the samples are described by the Beer-Lambert Law (Godel, 2013) for homogenous samples. For heterogeneous samples, Beer's Law was modified to account for each voxel (volumetric pixel) taken at a specific angle along different X-ray paths (Godel, 2013; Wang and Miller, 2020). The X-ray responses are also influenced by the material's size, shape, and composition (Bam et al., 2016; Kyle et al., 2008).

2.6.2 Mineral identification

The relative mineral assemblage is characterized by the effective X-ray attenuation coefficient for each phase, represented by its grey-scale value. These grey-scale values reflect the relative effective attenuation and not the absolute attenuation coefficients, and absorption abilities of elements at a specific wavelength (Kyle et al., 2008; Morrison and Gu, 2016). The linear attenuation coefficient is a function of density and effective atomic number; it can be influenced by the X-ray beam energy, size and composition of the sample. Minerals have variable densities which will have different attenuation coefficients. Therefore, minerals with greater density contrast can be discriminated from one another, however, if density variation between minerals is small, it may be difficult to discriminate between the minerals due to similar grey values. To get good discrimination between minerals of interest, the optimal energy needs to be selected. This can be observed before scanning by plotting the linear attenuation coefficient of all minerals over the X-ray spectrum/energy (Figure 2.9). Several databases are available to determine linear attenuation coefficients: XCOM database used by Kyle and Ketcham (2015) as well as Bam et al. (2020) that developed a user-friendly excel spreadsheet to calculate X-ray attenuation that can be used off-line. This spreadsheet was advantageous as it considers the effective energy of the X-ray beam.

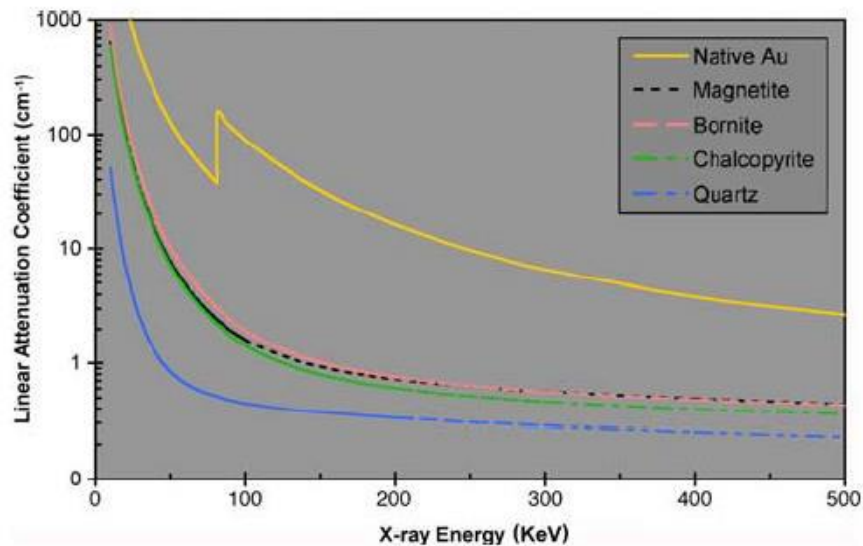


Figure 2.7: Linear attenuation coefficient of various minerals as a function of X-ray energy (Kyle, 2015).

2.6.3 Scanning parameters and data acquisition

The main components in XCT scanning are a focused X-ray source, a rotating sample stage and the detector. All the components of the XCT system are enclosed in a well-shielded cabinet, preventing the escape of any harmful X-rays (Morrison and Gu, 2016). Samples need to be prepared to a suitable size and geometry that can fit the sample stage, be within the field of view, and allow penetration of X-rays. Images produced are slices/projections captured at 360 degrees on the rotating stage at a constant set of intervals. Different kinds of XCT configurations have been employed, although cone-beam tomography is most commonly used (Kyle and Ketcham, 2015) (Figure 2.10). The focal spot size defines the resolution by determining the possible path rays to intersect the object. The diameter of the focused beam X-ray size handles the image qualities, by emitting stronger or softer X-ray energies depending on the sample the data required. For a large or compositionally complicated sample, the use of lower energy X-rays may not penetrate the sample, and high-energy X-rays may scatter (Kyle and Ketcham, 2015). The X-ray beam is generally pre-filtered by passing it through thin metal filters (e.g., copper, brass, and aluminium) used during scanning to minimize the possible artefacts such as beam and ring hardening. Batch scanning can be performed for small samples such as mini cores. Other X-ray parameters that need to be optimised in the acquisition are the number of projections and exposure time since a high number of projections and exposure time improves the discrimination in the grey value phase and minimises noise and artefacts (Bam et al., 2016) although at the expense of increasing the total scanning time.

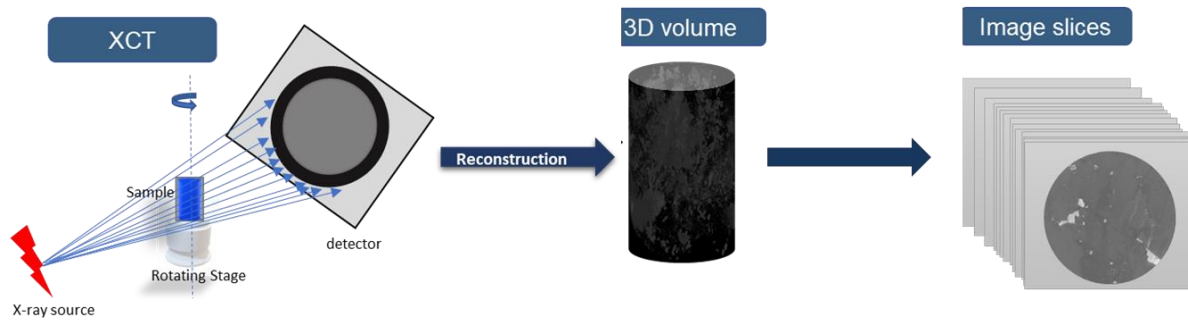


Figure 2.8: Schematic diagram of the XCT cone-beam configuration.

2.6.4 Data Processing

The extent of XCT data processing is ultimately dependent on what is required from the data. Guntoro et al., (2019) reviewed XCT data analysis specifically for mineral characterization. The typical steps for data analysis are summarised in Figure 2.11:

a) Reconstruction, stacking and pre-processing

The process involves converting the 2D projections into a virtual 3D volume and the raw intensities are converted into the CT values (Ketcham and Carlson, 2001). The reconstruction process is digital, using a mathematical algorithm filter that optimizes contrast and the sharpness of the images (Bam et al., 2016; Godel, 2013; Guntoro et al., 2019; Mees et al., 2003). There are various filters used for reconstruction. The most common analytical reconstruction procedure, especially for cone-beam XCT scanning, is filtered back projection. The filtered back projection is based on random transformation to cover the original object of interest by simply deconvoluting the back-projected images with the inverse of the impulse response (Wang and Miller, 2020).

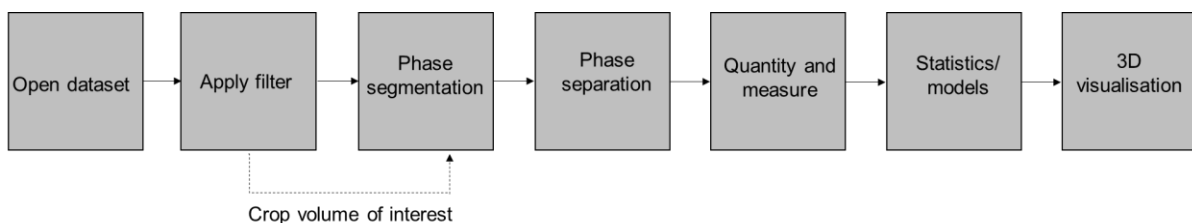


Figure 2.9: Schematic diagram for a generic XCT data processing (Adapted from Godel, 2018).

The reconstructed 3D volume may require further processing before interpretation to remove any artefacts from the sample that may have resulted from scanning. Many reconstruction system software platforms have beam hardening correction factors incorporated within them. Other filters also come in handy, like digital filters for denoising and blurring, or sharpening and edge detection (Godel et al.,

2019; Guntoro et al., 2019). These filter applications also have their limitations, such that the blurring filter tends to blur the image and other features which may be crucial in segmentation. This step is conducted to obtain quality data and prepare images for further processing. After reconstruction, the produced data is a 3D volume (Godel, 2013) that is cropped for further processing.

b) Segmentation and classification

Segmentation is a feature extraction process conducted by grouping grey-scale values into several segments or windows by identifying and isolating voxels with the same grey levels into a single phase. Segmentation forms an essential first step in isolating grey levels of interest representing different mineral groups so that their features may be extracted and quantified (e.g., grain size distribution, volume %) (Godel, 2013; Guntoro et al., 2019; Wang and Miller, 2020). The simplest and most common segmentation methods are histogram and thresholding analysis. The histogram method is used in less complicated samples although it may not be as effective in overlapping phases (such as finer mineral inclusions) and those affected by the partial volume effect. Using this method may overestimate the region of interest, resulting in inaccurate data quantifications. The thresholding method may be used to overcome these challenges by manually selecting the grey values to create a region of interest by applying a region growing functionality. This is usually applied to minerals that cannot be discriminated due to similar attenuation. The segmentation can also be carried out using a 3D growing method based on grain textural features such as shape and association (Godel, 2013). However, this method is time-consuming because the grains are manually selected. The accuracy of the segmentation needs to be verified and supported by other techniques such as auto-SEM-EDS before separation and phase quantification.

c) Separation and phase quantification

Segmented phases can be colour-coded for ease of differentiation. Most XCT software (such as VG Studio used in this study) has the erode and dilate functionality to separate the touching grains from one another. Following successful segmentation and separation where needed, quantitative data (such as mineral volume %, grain size and shape) can be extracted. The data can be computed for the entire sample or a specific region of interest.

2.6.5 Challenges and limitations

The XCT system operation and processing are highly dependent on operator expertise, especially when scanning heterogeneous geological samples. Achieving good quality results from heterogeneous ores depends on the sample size, scanning parameters and the need to minimize any possible artefacts. XCT does not provide the mineral assemblage independently, so supporting mineralogical techniques are needed for positive mineral identification and discrimination.

Cnudde and Boone (2003) reviewed the physical and scanning limitations associated with XCT: sample size, heterogeneous samples and artefacts (e.g., beam hardening, ring artefacts, star artefacts and metal artefacts). XCT artefacts degrade image quality and may omit information from images. Ring

artefacts are a result of unresponsive or calibrated detector pixels that appear as concentric rings around the axis of rotation. Star artefacts are a result of large high-density phases occurring during back-projection reconstruction. Beam hardening is the most common artefact caused by excessive attenuation of low energy X-rays from a polychromatic beam on high-density materials, preventing X-ray penetration. This affects the quality of data and leads to inconsistency in analysis (Carlson 2006). Beam hardening is most commonly seen in large and high-density samples (Kyle et al., 2008; Kyle and Ketcham, 2015). More on beam hardening can be found in Bam et al. (2020).

Additionally, sample size plays a significant role in X-ray penetration and the size of the voxel obtained for good quality images (Bam et al., 2016). Furthermore, XCT application in complex ore is challenging (Kyle et al., 2008; Kyle and Ketcham, 2015). Heterogeneous samples with variable attenuation coefficients (density phase associated with less density phase) may suffer from the partial volume effect where the boundaries of high-density phases become blurred affecting the actual XCT values of the neighbouring phases by averaging the CT values of different phases. This effect compromises the information to be extracted, including the quantitative data since segmentation might not work properly. The partial volume effect can be minimized by interpolation using higher spatial resolution (Guntoro et al., 2019).

Also, compositionally similar minerals and smaller attenuation coefficient difference (< 6%) can be poorly identified and misinterpreted using XCT if the mineral grains have roughly similar density values and X-ray attenuation coefficient (Bam et al., 2020). For example, many mineral grains may have varying natural characteristics: zoning alteration, micro-porosity, alteration, etc., which may have similar CT values and various beam spectrum and hardness (Bam et al., 2020). Thus, the use of XCT to identify such minerals may lead to erroneous determination. Identifying such minerals is possible but is time-consuming and may require the use of dual-energy scanning (Bam, et al., 2020; Wang et al., 2014) and prior mineralogical knowledge.

2.6.6 Applications in geometallurgy and the characterisation of magmatic Ni-Cu-PGE ores

The ability of X-ray computed tomography, as a rapid scanning system, to produce high-resolution images even on small samples for 3D internal characterization has seen a widespread application of the technology in geometallurgy (Godel, 2013; Wang and Miller, 2020), especially because it is not subject to stereological effects. These studies have primarily focused on the quantification of textural parameters relevant to the valuable mineral(s) – including quantification of grain size distribution, liberation, characterisation of porosity or crack networks, and determination of the theoretical mineral-grade recovery.

XCT has been used by various researchers to identify and characterise the grain size distribution of valuable minerals such as gold, mineral sands, sulphides and iron-bearing minerals in particles with unbroken textures (Bam et al., 2019; Dominy et al., 2011; Kyle et al., 2008; Nwaila et al., 2013; Yang et al., 2017). The determination of the 3D grain size distribution allows the definition of appropriate

grinding targets for valuable mineral liberation suitable for downstream separation and recovery by either flotation (Miller et al., 2009) or physical separation (including gravity concentration, magnetic concentration etc. (McGrath et al., 2015; Rozendaal et al., 2017). This can be investigated to determine how grinding targets vary between different geometallurgical end members of the ore body. Other grain characteristics have been evaluated, such as the sphericity which may also affect the recovery, for example, low sphericity elongated minerals are often lost in the screening and other processes, resulting in low-grade recoveries in mineral sands (Rozendaal et al., 2017).

For milled, particulate samples the XCT analysis has been used for an 'exposure analysis' that represents valuable mineral liberation in 3D (Lin et al., 1991; Miller et al., 2009, 2003; Ramos Oliveira et al., 2021; Wang and Miller, 2020). This can be further manipulated to calculate a theoretical grade-recovery curve, density-recovery curve and washability curves which represent the potential of the ore for separation and is only based on the recovery of particles containing the valuable mineral. For example, Miller et al., (2003) determined the fraction of mineral exposed and thus the ultimate recovery for copper through heap leaching using mineral exposure analysis. Using the Bauxite ore, Ramos et al., (2021) determined the 3D liberation of aluminium-ore bearing minerals in comparison to the 2D analysis that overestimates the degree and surface exposure. The phosphate liberation-limited grade/recovery in the flotation feed was determined using the number of grains generated from XCT (Miller et al., 2009). The theoretical recovery/gangue and density-recovery curves were obtained for sulphide minerals in the gangue minerals rejected by gravity preconcentration (Bacchuwar et al., 2020). In addition, coal washability has also been determined using the exposure analysis from XCT by identifying and measuring the particle density of each particle to construct a washability curve (Lin et al., 1991).

Fractures/cracks and porosity play an important role in mineralisation, valuable mineral liberation and metal recovery during leaching. The primary porosity, crack distribution and orientation across the ore have been studied by various researchers in different deposits (Deng et al., 2016; Kaufhold et al., 2016; Ketcham and Carlson, 2001).

Several geometallurgical studies have used XCT to evaluate the effectiveness of different comminution devices by characterising the development of a crack network and subsequent penetration of the leach solution into coarse particles for the recovery of Zn in sphalerite (Ghorbani et al., 2011), gold (Nwaila et al., 2013) and copper-bearing minerals (Dhawan et al., 2012; Yang et al., 2017).

In the case of magmatic Ni-Cu-PGE ores, XCT has also been used for identifying valuable minerals and characterising mineral texture (e.g., grain size distribution and their association). The high spatial resolution and 3D properties of the technique have proven beneficial for easily locating high-density phases, including the platinum-group minerals within the Bushveld Complex and other magmatic Ni-Cu-PGE ores (Basson and Miller, 2014; Godel, 2013; Kyle and Ketcham, 2015; McCall, 2016). Once located in 3D, the samples can readily be sectioned at the appropriate position for analysis with 2D auto-SEM-EDS for more information on PGM speciation (Godel, 2013). The focus of the abovementioned studies has been on understanding PGM grain size distributions and 3D mineral

association; to better understand the processes of mineralisation, understanding the types of particles to be recovered by flotation, and the required grinding for the liberation. Using the Nkomati magmatic Ni-Cu-PGE ore, Becker et al. (2016) went further to demonstrate the potential of using grey level co-occurrence matrices, a form of advanced image analysis for quantitative textural classification of drill core. In many of these studies, the presence of PGMs is assumed based on its grey level, but this needs verification or the use of appropriate filters to avoid misclassification of other high-density minerals such as galena (Wang et al., 2014).

2.7 Supporting techniques

Optical microscopy is one of the traditional techniques used at the initial stage of geometallurgical programs as well as a supporting technique to validate results obtained through other methods of mineral and textural analysis (Donskoi et al., 2016). This method is dependent on human knowledge and limited to qualitative and semi-quantitative data.

Quantitative X-ray diffraction (QXRD) is an inexpensive method to identify and quantify minerals. The analysis is based solely on the crystallographic properties of the sample with each crystalline solid having a unique diffraction pattern that can be used for mineral identification. Phase quantification is performed using the Rietveld method (Young 1995,2000). The Rietveld method uses fundamental calculations by inputting all the crystal structural parameters of the phases present and calculating a diffractogram. (Brown, 1966; de Villiers, 2016; Speakman, 1902). The detection limit is between 0.5-3 wt.% depending on the minerals and complexity of the samples. This analysis is suitable for major mineral identification within the rock.

Another commonly used chemical analytical technique is fire assays. Fire assays have been practised since ancient times to determine precious metal content such as gold and PGEs. In this method, a Pb or Ni collector is used to scavenge the precious metals from the larger sample mass in a series of pyrometallurgical steps resulting in the formation of a PGE-prill. Thereafter, the prill is dissolved in acid and the solution is analysed with ICP-OES or ICP-MS to identify and quantify the different precious metals such as Pt and Pt (Kable and Becker, 2016; Matsau, 2003).

2.8 The knowledge of contribution and research gap.

The magmatic Ni-Cu-PGE ore of the Bushveld complex is associated with silicate minerals, including alteration minerals that pose challenges in downstream processing. These alteration minerals can be rapidly and readily detected by HSI before mineral processing on the drill core. The Pseudo Reef constitutes about 50% of these alteration minerals. To avoid and manage the project and operational risks associated with these ores, detailed information regarding the mineral assemblage and texture at an early operational stage is crucial. Various methods have been applied to characterize and quantify these parameters ranging from simple manual descriptions to sophisticated automated analytical techniques. However, every method has its advantages and limitations in determining this type of information. 2D hyperspectral imaging for drill core scanning has gained much acceptance in geosciences and is viewed as an essential component in geometallurgy. HSI has been applied in various ores, mostly felsic deposits such as sedimentary, porphyry and orogenic deposits. However, the application of 3D XCT imaging has primarily remained a research tool in geosciences, even though it may be used to quantify the mineral assemblage and texture of drill core. Although these techniques have individually been used successfully, an opportunity exists to see whether further information can be obtained by combining these techniques. Such an approach has been investigated for other instrument combinations, e.g., XCT and Auto-SEM-EDS or HSI and Auto-SEM-EDS (Johnson et al., 2019; Tuşa et al., 2020; Voigt et al., 2019). The coupling of XCT and HSI appears to have not yet been systematically studied in a geometallurgical context for drill core scanning, although these techniques have been applied to predict soil structural properties with VNIR HSI coupled with XCT (Katuwal et al., 2017). For accurate mineral and texture characterization, for all applications of different methods of analysis, it is always advisable to have prior and complementary mineralogical information to support the interpretations. In this study, manual logging, QEMSCAN and QXRD will be used to obtain complementary information.

Table 2.6: Summary of XCT and Hyperspectral imaging technologies from the literature.

Parameters		Scanning Techniques	
		XCT	HSI
Performance	Speed	Batch scanning	Rapid continuous scanning
	Sample preparation	None is required, but for best results, a uniform geometry is favoured (e.g., cylinder)	Dust removal.
	Data processing	(1) Volume reconstruction. (2) Feature extraction. (3) Segmentation, separation and quantification.	(1) Pre-processing. (2) End-member extraction. (3) Hyperspectral mineral and spectral reclassification, and quantification.
	Electromagnetic spectrum (acquisition tool)	X-ray	Infrared + visible light.
Type of images acquired	Dimensions and colour	Produce 3D greyscale volumes.	Produce 2D false colour images.
Image analysis	Mineral identification and quantification	Minerals are identified by the linear attenuation coefficient. Discrimination of phases is dependent on sufficient difference in attenuation coefficient and on other techniques.	Mineral spectral signature detected with infrared microscopy. Mineral assemblage is limited to silicates and carbonates. Mineral quantification is complex.
	Texture	Simple quantitative textural parameters such as grain size distribution, liberation and porosity can be readily extracted. Complex quantitative textural parameters require the adaptation of image analysis methods.	Simple quantitative textural parameters can be extracted (although not routinely)—textural information is heavily dependent on resolution and pixel size.
	Common artefacts	Partial volume effect, beam hardening, ring artefacts	Spectral mixing and mineral overlapping

Chapter 3: Materials and methods

This chapter describes the materials and methods used in this research for mineralogical characterization of the drill core. The research approach is carried out in four steps: (i) sample preparation, (ii) image acquisition, (iii) data processing, and (iv) outputs, synthesis and interpretation. Figure 3.1 below demonstrates the summary approach.

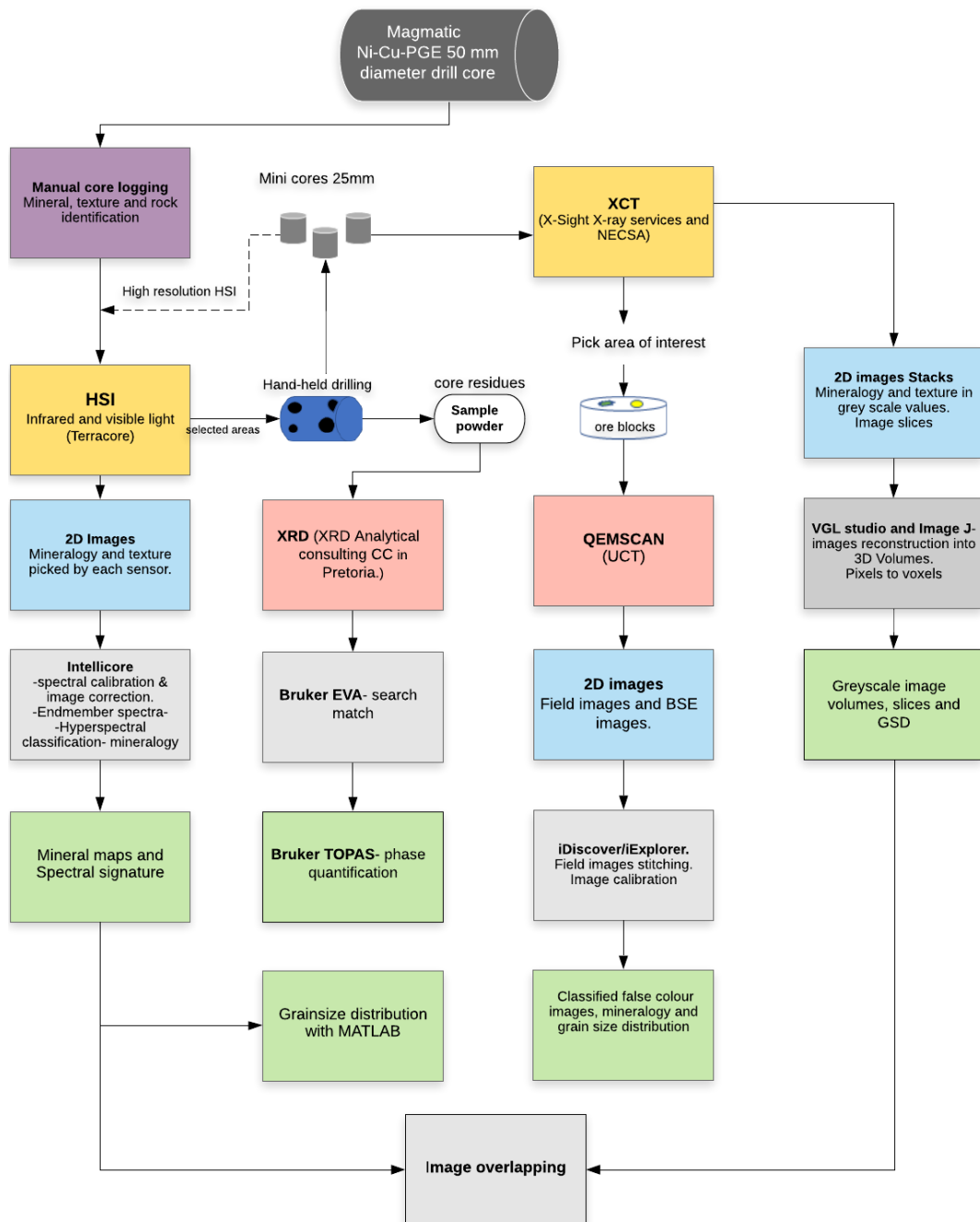


Figure 3.1: Schematic flow diagram summarizing the methodology of the project. Yellow indicates the major scanning techniques; pink – the supporting techniques; blue - 2D images; grey - processing systems and software; green - outputs from each technique.

3.1 Case study

3.1.1 Core/sample collection

Two trays of drill core from boreholes RD015 and TU277 with a length of 5.28 m and 5.33 m, respectively, were acquired from the Sedibelo Platinum Mine, Swartklip facies, Western Limb of Bushveld Complex in the North West Province of South Africa. Cores were received as 50 mm diameter half cores, along with the site logging details. The drill cores intersected the Merensky Reef through the Pseudo Reefs to the upper UG2 Chromitite Reef on the Tussenkomst (TU277) and Rooderant farms (RD015), respectively.

3.1.2 Manual core logging and petrography

Drill cores were manually logged on receipt at the University of Cape Town (UCT), Chemical Engineering Building, in the Centre for Minerals Research (CMR) Laboratory. Both analytical and graphical logging procedures were conducted to acquire detailed information on rock types, the mineral assemblage and texture.

3.2 Sample preparation

Twenty-three mini-cores, 25 mm in diameter, were extracted from the standard drill cores by Hardcore Drilling CC (South Africa). Table 3.1 below shows the mini-core labelling per drill hole. Five areas of interest from each core were selected for QXRD analysis (Figure 3.2).

Table 3.1: Mini core sampling and labelling from each borehole.

RD015			TU277		
	Sample ID (SED-)	Rock type		Sample ID (PPM-)	Rock type
1	55114	Anorthosite	1	129686	Anorthosite
2	5513	Altered harzburgite	2	129687	
3	5318		3	129687	Upper pegmatoidal pyroxenite
4	5319		4	129694	Pegmatite
5	5320		5	129699	Altered harzburgite
6	5321		6	129700	
7	5322		7	129702	
8	5325	Lower pegmatoidal pyroxenite	8	129704	Lower pegmatoidal pyroxenite
9	5327		9	129709	
10	5329		10	2x129710	
11	5331	Feldspathic pyroxenite	11	129713	Feldspathic pyroxenite



Figure 3.2: Selected areas for mini core extraction (circles), XQRD samples (blue rectangles), and rescanned HSI core (marked with X).

3.3 Hyperspectral imaging

Three rounds of hyperspectral imaging were performed. The first and second rounds were performed under standard conditions using the Terracore facilities in Johannesburg. The second run focused on re-scanning selected areas of interest where smearing was suspected. The third round for high-resolution scanning of mini cores was performed by the Terracore team at the Terracore facilities in Reno, USA.

3.3.1 Data acquisition

a) System calibration

The systems were calibrated before and during scanning to ensure that no wavelength shifts occurred and to monitor the position of the dead pixels in all the cameras. A standard reference board comprising minerals and materials with known spectra was used to calibrate each camera (Figure 3.3). The colour balance, aspect ratios and camera focus were also tested using this calibration.



Figure 3.3: Calibration board for the HSI system calibration. The calibration board is placed under the system cameras, moving in the conveyor belt. A: anodized aluminium squares are used to ensure image completeness and correct aspect ratio. B: examples of standard materials used to ensure spectral calibration, the centre object being a slab of styrofoam. C: reference glass and plastic are used to ensure camera calibration. D: Kodak colour and focus sheets to ensure correct colour balance, focus, and aspect ratio (Photo courtesy of Terracore).

Every camera was monitored differently. The VNIR sensor was monitored using commercial filter glass calibration standards on the reference panel. The SWIR sensor wavelength was calibrated with a styrofoam measurement reference. The LWIR was calibrated using transparent polypropylene plastic on the LWIR white reference standard. All the measurement reference data is captured in the same way that a typical sample measurement would be undertaken; by scanning the calibration board. The material was placed on the translation table, ready for measurement. Mineral samples on the reference panel also provided spot checks of the wavelength calibration, specifically quartz and carbonate. The spectral wavelengths obtained from the calibration methods were compared with the standard wavelengths provided by the manufacturer; the measured peaks and absorption position values matched with standard manufactured values with less than one spectral bandwidth spacing. Routine acquisition measurement procedures were conducted after the wavelength calibration method.

b) Standard drill core scanning

Drill cores trays were scanned at ALS in Johannesburg on a SisuRock core imaging system run by Terracore. The system was fitted with three cameras: Red-Green-Blue (RGB) high-resolution, FENIX camera with co-registered VNIR and SWIR sensors, and OWL camera equipped with LWIR spectral sensor (Figure 3.4). The system specifications are summarised in Table 3.2.

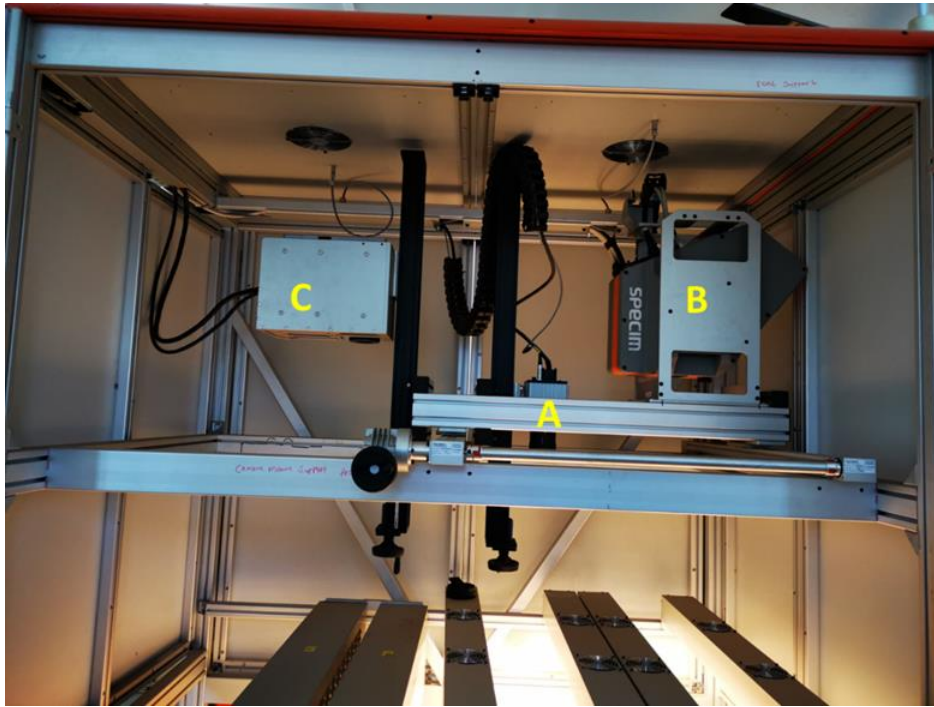


Figure 3.4: Interior of the SisuRock Gen2 Hyper-logger system showing the camera setup. A- RGB camera, B- FENIX (co-registered VNIR and SWIR), and C- OWL camera (LWIR). (Photo courtesy of Terracore).

The drill core trays were placed under the HSI cameras in a moving conveyor belt and scanned using the push-broom (Line Scanner) scanning method to collect and build frames (Figure 3.5). Images were captured with the two spectral cameras, both operating at 1.64 mm pixel size and a high-resolution RGB camera with 0.15 mm pixel size. The scanning parameters for the drill cores are summarised in Table 3.2, and the full system specification is provided in Appendix A.

Table 3.2: Camera specifications of the SisuRock Gen2 core scanning system used for standard drill core scanning.

System Specification	HSI cameras
Wavelength range	VNIR-SWIR (FENIX): 400-2500 nm LWIR (OWL): 7500-1200 nm. RGB: Not applicable
Spectral bands and bandwidth	VNIR: 174 bands; 3.4 nm SWIR: 274 bands; 6 nm LWIR: 96 bands; 48 nm
Spatial resolution (Pixel size)	Spectral sensors: 1.64 mm RGB: 0.15 mm
Acquisition speed	170 mm/s @ 1mm pixel size

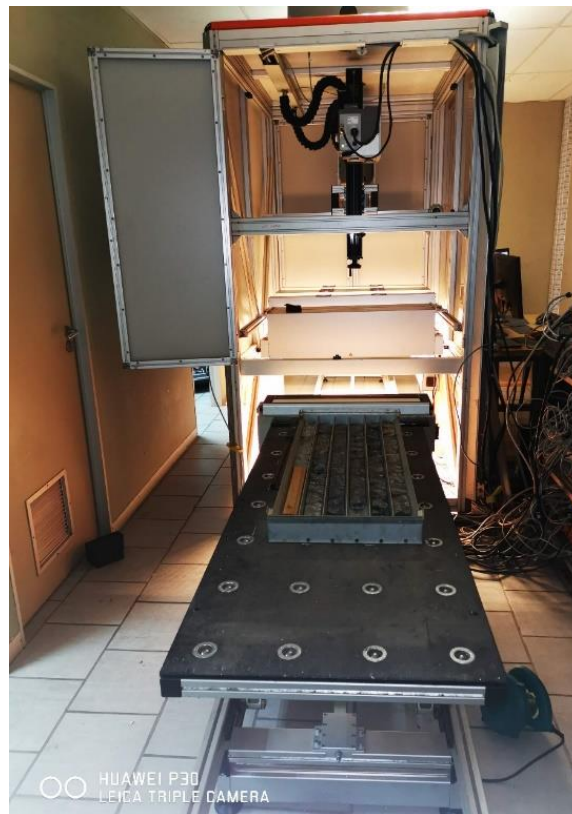


Figure 3.5: Illustration of the HSI scanning a tray of drill core moving in a conveyor belt under the system cameras (FENIX, OWL and RGB).

During the post-analysis data processing of the mineral maps, possible smearing was suspected. Therefore, selected drill cores were identified, washed carefully with tap water, and dried for round two of scanning using the above-mentioned parameters.

c) Mini core scanning

Twenty-three mini cores were scanned in Reno, the USA, by Terracore with a SisuRock Gen 2 hyperspectral scanner. Only the LWIR and SWIR hyperspectral sensors were used because FENIX does not have a lens suitable for the high-resolution work required for this phase of the study. Mini cores of the same borehole were aligned according to their stratigraphic positions and imaged simultaneously. Their scanning parameters are summarised in Table 3.3.

Table 3.3: Camera specifications of the SisuRock Gen2 Hyper logger system used for mini cores core scanning.

System Specification	HSI cameras
Wavelength range	SWIR: 8-12 μm LWIR: 1000 -2500 nm
Spectral bands and bandwidth	SWIR: 228 bands; 6 nm LWIR: 96 bands; 48 nm
Spatial resolution (Pixel size)	0.40 mm 0.16 mm (RGB)
Acquisition speed	90 mm/s @ 1 pixel size

3.3.2 Data processing and analyses

All the data processing steps were similar for the different HSI datasets. The first stage was preprocessing, undertaken on-site using the Environment for Visualizing Images (ENVI) data viewing software to check if the image dimensions were correct. Data viewing was followed by processing in TerraCore's proprietary software to correct the data and remove noise and dead pixels. Further QAQC was conducted at the Terracore offices in Johannesburg, South Africa.

The impurities other than the core were extracted including the exposed tray, channels and material balancing the core (such as wood) (Figure 3.2). The process was conducted using Intellicore V0.9.3.82 software. Further data processing and analysis were conducted at the University of Cape Town using a software application provided by Terracore. The readily automated mineral spectral and mineral maps were reclassified. The reclassification was done by matching and comparing the mineral spectra with other libraries, such as JHU and USGS, and using information derived from the supporting mineralogical techniques (QEMSCAN, QXRD). Spectra that remained unclassified were interpreted as representative of minerals without a definitive spectral response. Additionally, the mineral assemblage was pulled out for the mineral maps. Other post-processing, such as the determination of mineral grades and grain size distribution, was conducted using MATLAB 2021a with specially developed scripts.

3.4 X-ray computed tomography

3.4.1 X-ray computed tomography data acquisition

All 23 mini cores were scanned with a NIKON XTH 225 ST scanning system at XSight X-ray services in Somerset West, South Africa to produce XCT images. Before scanning, a test for a suitable scanning potential was conducted on sample DM-04. The drill core was scanned at 180 kV using a 1 mm Cu filter and 140 kV using a 0.5 mm Cu filter. The energy that allowed for the best penetration was 140 kV. After determining the optimum scanning parameters, batch scanning was conducted using the parameters given in Table 3.4.

Table 3.4: XCT scanning parameters.

Scanning parameters	Measurements
Drill core diameter	25 mm
Potential (kV)	140 kV
Current	120 μ A
Voxel size (μ m)	20
Frames averaging	One frame per sec.
Number of images per rotation increment	1000
Filter	0.5 mm Cu
Measurement time per drill core	50 min.

3.4.2 Data processing and analyses

The XCT scan data was reconstructed using the CT Pro 3D software at X-Sight X-ray Services. Further data processing and feature extraction was conducted using VG Studio Max version 3.2 software at X-Sight X-ray services and South African Nuclear Energy Corporation (NECSA). Data processing included the surface determination to outline (cover) the sample and the background creating a region volume. The phase segmentation process conducted further processing on mineral phases to extract the region of interest (ROI) using the histogram (grey value method) rendering and region-growing methods. The segmentation allowed for porosity/inclusion analysis to generate the defect analysis report. The defect analysis was conducted on the ROI, containing different grey values, using the 'only threshold' algorithm. The only- threshold algorithm considers all phases a defect if the grey values are below the specified threshold.

3.5 Supporting techniques

Quantitative Evaluation of Minerals by Scanning Electron Microscopy (QEMSCAN) and Quantitative X-ray diffraction (QXRD) were used as complementary techniques supporting the mineralogical interpretation of the HSI and XCT data. The sample selection from each core is given in Table 3.5.

Table 3.5: Summary table for rock types sampled from drill core (RD015 and TU277) for QXRD and QEMSCAN analyses.

Rock type	TU277		RD015	
	QEMSCAN	QXRD	QEMSCAN	QXRD
Feldspathic Pyroxenite	PPM 129713	PPM 129711	SED 05331	SED 05331
Pegmatoidal olivine-pyroxenite	PPM 129687	PPM 129687	SED 05325&27	SED 05327
Pegmatoidal pyroxenite	PPM 129709&10	PPM 129710	SED 05329	SED 05329
Altered harzburgite	PPM 129699	PPM 129699	SED 05319	SED 05319&20
Anorthosite	PPM 129687	PPM 129686	SED 05514	SED 05514

3.5.1 Quantitative Evaluation of Minerals by Scanning Electron Microscope

After HSI and XCT scanning, a sub-selection of mini cores was submitted for QEMSCAN analysis in the Department of Chemical Engineering at the University of Cape Town. Twelve mini-cores were chosen from the 23 mini-cores spanning some of the sample set's variability in mineral assemblage and texture. The selected samples were sawed to produce a thin slice, ideally containing the same surface scanned with HSI. These mini-drill core slices were made into 30 mm diameter resin blocks. After mounting with resin, samples were placed in a pressure pot to remove excess bubbles and, after that, into an oven overnight at 30°C for curing. Resin blocks were then subjected to a series of grinding and polishing steps to produce a high-quality surface finish suitable for QEMSCAN analysis. Samples were carbon-coated prior to QEMSCAN analysis on an FEI QEMSCAN 650F instrument with two Bruker 6130 EDS detectors. Using the field image analysis mode, samples were scanned at 25 kV, 10 nA, and 357 fields/frames at 15 µm pixel spacing. The resultant data was processed using QEMSCAN iDiscover V5.3 software. Images were stitched and particulated (removed from background) and filtered by size (>1000) to remove any extraneous pixels. A simple mineral list was created to represent the bulk mineral assemblage by grouping minerals and phases from the primary list. The granulator was applied to the field images to allow the quantification of grain size distribution.

3.5.2 Quantitative X-ray diffraction (QXRD)

The residual sample from the mini cores' extraction was analysed for QXRD as another independent means of quantifying the mineral grades. Five to six areas (of ~5cm of drill core length) of interest per drill core were analysed. The selected regions of samples are noted in Table 3.5. Each piece was crushed using a hammer and pulverized for 30 seconds in a Sieb swing mill. After that, the mill products were split into 3.5-4 g aliquots using a rotary microfilter. One of these aliquots was then micronized for 10 minutes in a McCrone micronizing mill. The micronized samples were dried, packaged and couriered to XRD Analysis and Consulting in Pretoria.

The XRD analyses were used to identify the crystalline phases present in the sample. Sample powders were backloaded into the sample holder. The powder was analysed with a Panalytical Aeries diffractometer with a PIXcel detector and fixed slits with Fe filtered Co-K α radiation. Phase identification was performed using the Bruker Eva V4.1 software. This was followed by phase quantification using the Bruker Topas V4.1 software, based on the Rietveld method described in Young (2000). The lower detection limit of this method is typically between 0.5–3 wt. %, depending on the minerals, their crystallinity and the complexity of the sample.

3.6 Image overlapping

The overlapping procedure aimed to overlap HSI and XCT information produced from the same surfaces of the mini cores (Figure 3.6). Since HSI is a surface scanning technique, the uppermost XCT slices were extracted with VG Studio V3.2.2 software to match the HSI surface. Images were overlapped manually due to a lack of suitable orientation markers visible in both output images, and some areas of cores were not scanned by HSI due to core tilting and irregular surfaces which resulted in fragments during drilling. XCT image slices were used as the image base due to their high resolution. The overlapping was done on PowerPoint using the visual cores for references by observing the edge fragments for orientation. Since XCT scanned the entire core surface, HSI mineral maps were overlapped on RGB images to identify point references and areas covered by HSI on XCT slices.

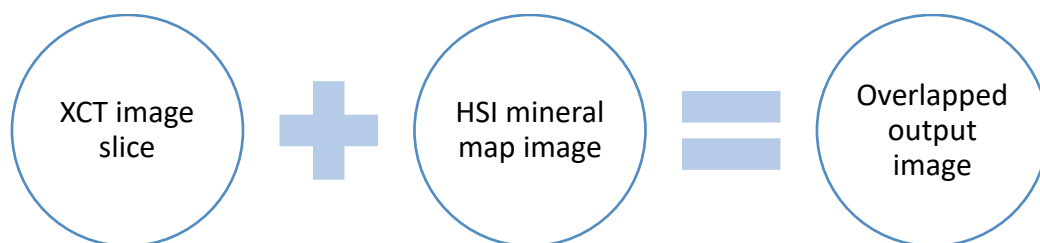


Figure 3.6: Schematic diagram for HSI and XCT image overlapping.

Chapter 4: Sample characterization

This chapter presents the results of the standard manual core logging coupled with QXRD and QEMSCAN to obtain an overall understanding of the mineral assemblage of the drill cores (RD015 and TU277) used in this study. Two drill cores were used to explore differences related to mineralogical characteristics such as the modal composition, alteration, texture and their scanning techniques. Firstly, manual core logging was conducted to identify different rock types, the minerals present and textures in the cores. A full description of rocks in the drill cores is given in Appendix-Table B1 and B2. The nomenclature of the rocks used here is based on their primary mineral assemblage that allows their location within the stratigraphic sequence. Secondly, a detailed mineralogical and textural characterization was conducted for different lithologies, and textural variations were observed across the stratigraphy during manual logging (Figure 4.1). For detailed mineral grades and texture, selected cores were analysed using QXRD and QEMSCAN.



Figure 4.1: Photographs of TU277 and RD015 drill cores investigated with the selected marked areas for QEMSCAN (circles) and QXRD (rectangle) analyses sampled on the drill cores. Core depths are indicated with green lines marking the change in lithologies with associated changes in mineral assemblage and texture. TU277 core depths are labelled from 82 m to 86 m and RD015 from 25 m to 29 m.

Rock-forming minerals occur in different proportions and were grouped as major (> 5 wt.%), minor (< 5 wt.%) and trace (< 1 wt.%) minerals. The quantification of mineral grades provided by QEMSCAN field images and QXRD may differ due to the sampling effect. The QXRD samples were subsampled from a larger volume that is more representative of the bulk composition. In contrast, QEMSCAN only quantifies the composition of a single surface and minerals occurring in trace amounts in QEMSCAN may occur in concentrations below the detection limit in QXRD. For example, QXRD and QEMSCAN sampling for pyroxenites in both cores was conducted in different areas (Figure 4.1). These minerals may also have different shapes and sizes, and they may be associated (intergrown) differently from other minerals in the rock, which may produce textures that are quite complex. In this study, however, the textural characterization is limited to quantifying grain size distribution, with more complex textures only being qualitatively described. The grain size distribution (GSD) computed by QEMSCAN represents the equivalent spherical diameter, calculated on the grain surface. Only minerals with a distinct hyperspectral signature were used for the GSD determination to allow for later comparison in Chapter 5. The mineral grain size classification in each rock is defined as very fine (< 1000 μm), fine (1000-2000 μm), medium (2000-5000 μm), coarse (5000-10000 μm) and very coarse (or pegmatitic) (>10000 μm).

4.1 Drill core TU277

This borehole was 5.33 m long, collected from a depth of 86.50 m to 81.54 m (Figure 4.2) and represents the stratigraphic intersection from the UG2 Hanging wall to the Merensky Reef Footwall. Drill core TU277 was intact with no fractures. The base of the drill core starts with a thin 0.1 m pyroxenite of the UG2 Footwall. The pyroxenite gradually changes to a pegmatoidal olivine pyroxenite of the Lower Pseudo Reef (LPR). The LPR pegmatoidal olivine pyroxenite is terminated by a 0.5 cm thick chromitite stringer which marks the start of the harzburgitic Upper Pseudo Reef (UPR). The harzburgite was the most extensive layer and the highly altered unit of the borehole. The UPR pegmatoidal pyroxenite hosts a 1 cm chromite stringer at 0.35 cm before erosionally changing to the upper pegmatoidal pyroxenite that marks the end of the UPR. The pegmatoidal pyroxenite also terminates to a thin Merensky Footwall mottled anorthosite. The QXRD determined mineral grades are given in Table 4.1, selected QEMSCAN field images (Figure 4.3), bulk mineral assemblage (Figure 4.4) and grain size distribution of selected minerals in Figure 4.5.

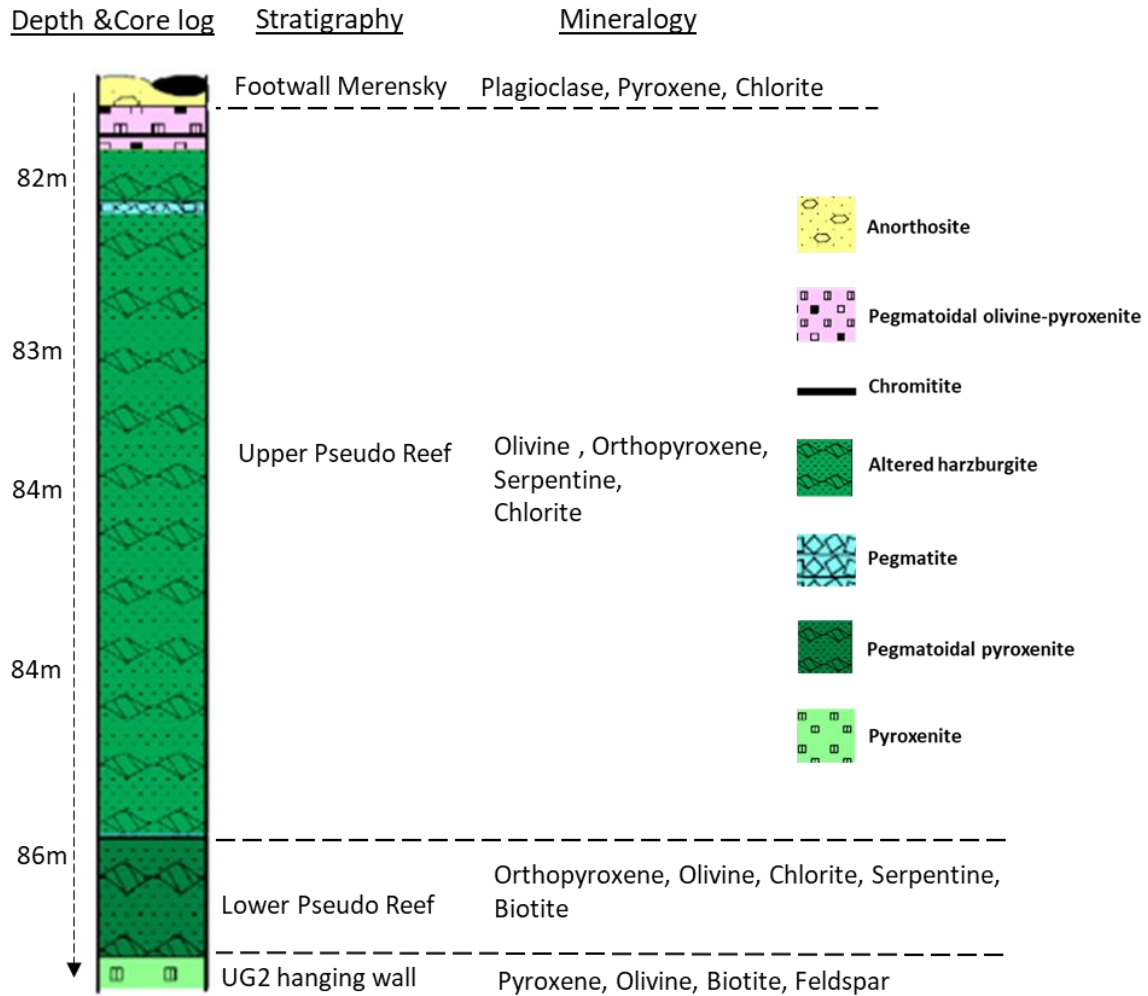


Figure 4 2: Stratigraphic column for drill core TU277 from the UG2 Hanging wall to the Merensky Reef Footwall. The column shows the major minerals in the rock types under each stratigraphy.

4.1.1 Mineral assemblage and texture of drill core TU277

a) Footwall Merensky anorthosite

This layer is locally composed of gabbronorite, mottled anorthosite and leucogabbro (going up stratigraphy) (Figure 4.1). These rock types are made up of pyroxenes and plagioclase and darker rocks indicate a high abundance of pyroxenes (Figure 4.1). On a larger scale, this rock is the anorthosite. Other minor minerals identified by QXRD in these rocks include mica, amphibole, chlorite and talc. The area sampled for QEMSCAN analysis was gabbronorite (Figure 4.3a and Figure 4.4) within the anorthosite package.

The gabbronorite comprises very fine to medium-grained plagioclase (Figure 4.5a). The plagioclase is associated with medium-grained cumulate grains of clinopyroxene and orthopyroxene, with disseminated pentlandite and chalcopyrite. Figure 4.3a shows the alteration of plagioclase by epidote.

Also, epidote and biotite seem to be transforming into chlorite. Chlorite also occurs as veinlets in plagioclase and is associated with fine-grained biotite at the rims of clinopyroxene. The larger area of clinopyroxene is not altered, and in some areas, it is sandwiched between chlorite with fine-grained biotite and orthopyroxene. The orthopyroxene median grain size falls within the fine-grained range (Figure 4.5a). The grain size and proportion of pyroxenes decrease, and plagioclase increase to the mottled anorthosite. The mottled texture is created by the aggregated orthopyroxene and clinopyroxene forming lumps in the plagioclase. The plagioclase in the mottled anorthosite is coarse-grained and medium-grained in the leuconorite. The leuconorite is characterized by spotted semi-rounded to rounded clinopyroxene and orthopyroxene throughout the plagioclase.

*Table 4.1: QXRD bulk mineral grades for different rock types sampled in drill core TU277 (in wt. %). Minerals indicated with a hyphen were not detected in the selected sample. *Spinel covers chromite and Fe-oxides. Base metal sulphides were below the detection limit.*

Rock names Minerals	Footwall Merensky anorthosite	UPR pegmatoidal Pyroxenite	UPR altered harzburgite	LPR pegmatoidal pyroxenite	UG2 feldspathic pyroxenite
Olivine		<lld	<lld	<lld	
Orthopyroxene	-	-	2	25	48
Clinopyroxene	6	6	3	16	10
Amphibole	4	4	-	15	7
Serpentine	-	25	61	1	-
Talc	3	20	11	17	9
Chlorite	5	18	-	11	15
Plagioclase	78	10	5	10	5
Calcite	2	2	0	-	0
Mica	1	4	3	2	5
*Spinel	-	11	14	3	-

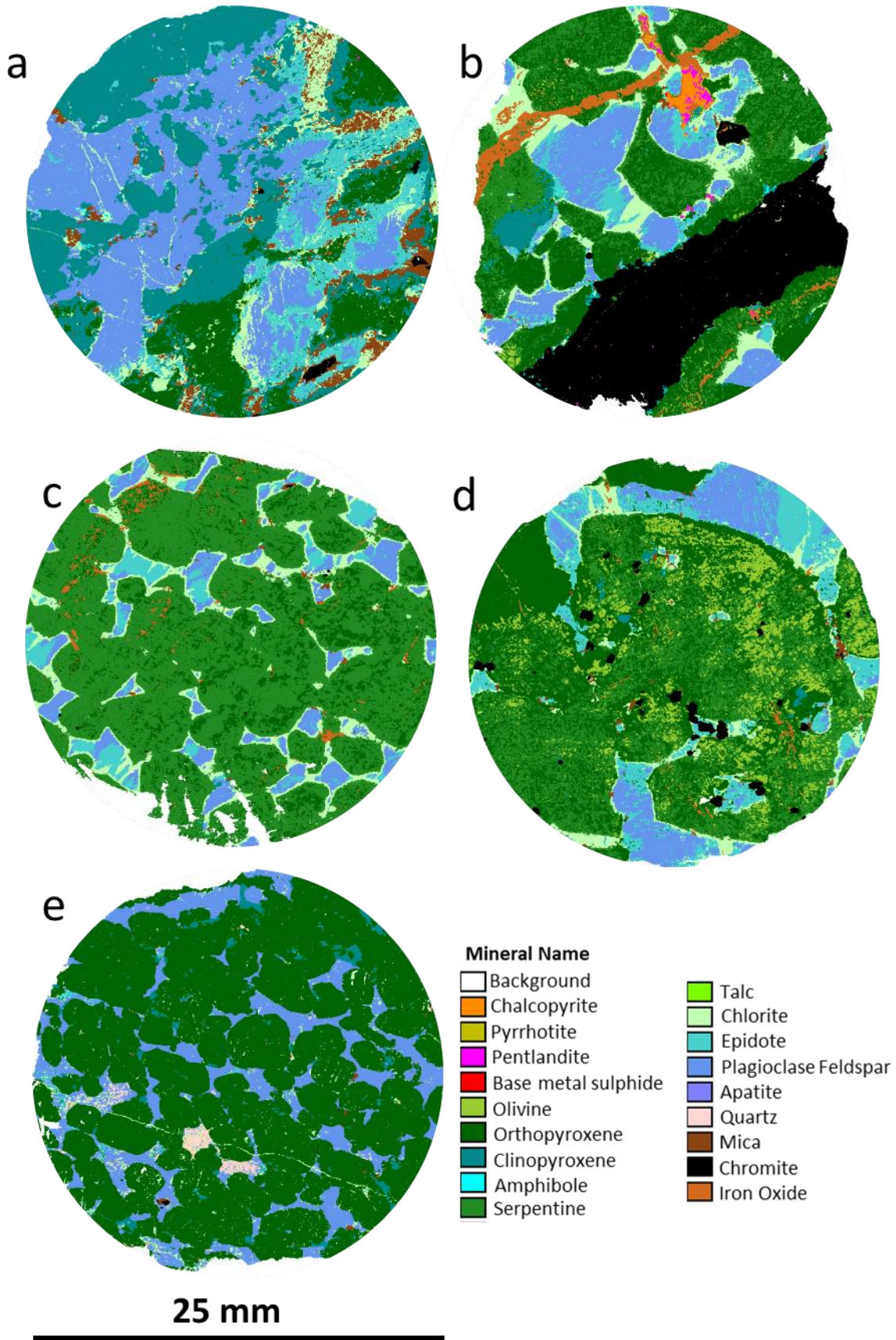


Figure 4.3: QEMSCAN field images for TU277, stratigraphically from (a) Gabbronorite, (b) Altered harzburgite, (c) Pegmatoidal-olivine pyroxenite, (d) Pegmatoidal pyroxenite and (e) Pyroxenite.

b) Upper Pseudo Reef pegmatoidal pyroxenite

The pegmatoidal olivine-pyroxenite has coarse cumulate grains of olivine and medium-grained pyroxenes with intercumulus chlorite. This rock is dominated by alteration minerals that make up 63 wt.% of the rock: serpentine, talc and chlorite at a ratio of 1.4:1.1:1 (Table 4.1). Plagioclase, clinopyroxene and spinel were identified as major rock-forming minerals. In this rock, amphibole, mica and calcite were classified as minor minerals. Compared to any other rock in this core, the upper pegmatoidal pyroxenite contains more calcite (carbonate) at 2 wt.%.

The orthopyroxene is medium to very coarse-grained and pervasively altered to serpentine forming a mesh texture (Figure 4.3b). The relicts of fine-grained olivine are associated with orthopyroxene and serpentine grains. The orthopyroxene and serpentine grains are set in a plagioclase-epidote-chlorite alteration assemblage. Chlorite rims the plagioclase, whereas epidote alteration is more pervasive through the grain (Figure 4.3b). Although a significant amount of talc (20 wt. %) has been detected by QXRD, its association cannot be seen in QEMSCAN field images. Talc is very fine-grained (likely < 20 µm) in QEMSCAN.

Evident from manual logging (Figure 4.1) and QEMSCAN (Figure 4.4), this rock contains abundant BMS and chromite (Table 4.1). It hosts a 5 mm thin chromite stringer and other individual chromitite grains associated with plagioclase-epidote-chlorite assemblage. The chromitite stringer contains inclusions of very fine-grained BMS (Appendix B- Table B1 -upper pegmatoidal pyroxenite). Very fine to medium-grained BMSs are also associated with chlorite and magnetite. The sulphide domains observed in this rock suggest a chalcopyrite-pentlandite-pyrrhotite assemblage. In other cases, magnetite appears to rim the pyrrhotite or crosscut the sample as a vein. Magnetite grains are also found within chlorite grains.

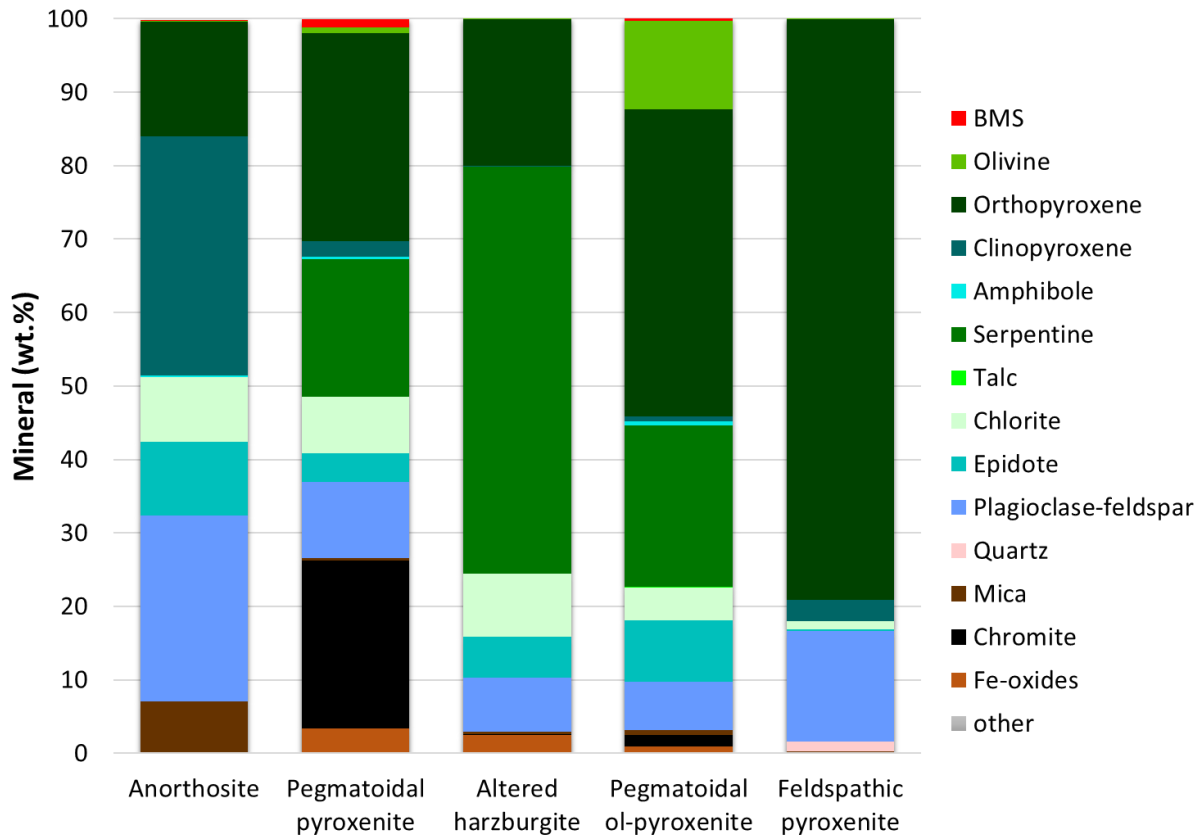


Figure 4.4: Bulk mineral grades obtained from (QEMSCAN analyses for the different lithologies for drill core TU277. Differences in mineral grades between QEMSCAN and QXRD analyses (Table 4.1) are considered to be due to sampling effects.

c) Upper Pseudo Reef harzburgite

The Upper Pseudo Reef harzburgite (referred to as altered harzburgite) is the most extensive layer of this core is dark green to black, with some of the interstitial spaces being a creamy-white colour. Various layers of harzburgites are differentiated by differences in grain size and alteration minerals, for example, the very coarse grains of chlorite, very fine-grained serpentine, and variable orthopyroxene grain sizes (Figure 4.1). These layers are characterised by abundant serpentine, spinel, talc and plagioclase (in their increasing order of abundance) (Table 4.1). Orthopyroxene, clinopyroxene and mica are present as minor minerals. However, the very fine-grained layers found between the altered harzburgite only comprise serpentine, magnetite and minor clinopyroxene (Appendix-Table D2).

The alteration of orthopyroxene and olivine to serpentine is almost complete with only very fine-grained (<800 μm) relict orthopyroxene present (Figure 4.5 c). Orthopyroxene-serpentine grains are interconnected, also connecting the intercumulus plagioclase-chlorite minerals (also evident in the hand samples-Appendix B). Like the pegmatoidal pyroxenite rocks, plagioclase-epidote-chlorite alteration forms the matrix. However, the plagioclase in this rock type is very fine to fine-grained (Figure 4.5c). Chlorite and epidote were not detected by QXRD but rather the abundance of talc. The presence of

minor mica (3 wt.%) has been detected by both QXRD and QEMSCAN (Table 4.1 and Figure 4.4). In this core, too, very fine-grained mica is associated with chlorite.

Figure 4.3c shows very fine grains of magnetite aligned with one another, in some areas forming veins whilst in others occurring only as individual grains. Only minor euhedral fine-grained chromite grains are found in this lithology. Multiple amphiboles and magnetite veins characterize the very fine-grained layers between the altered harzburgite (1 mm- 5 mm) (Appendix B- Table B1). The pegmatite vein crosscutting the harzburgite is very coarse-grained, white, and grey (Table 4.1). It comprises quartz, plagioclase, amphibole veins and flake-like phlogopite minerals.

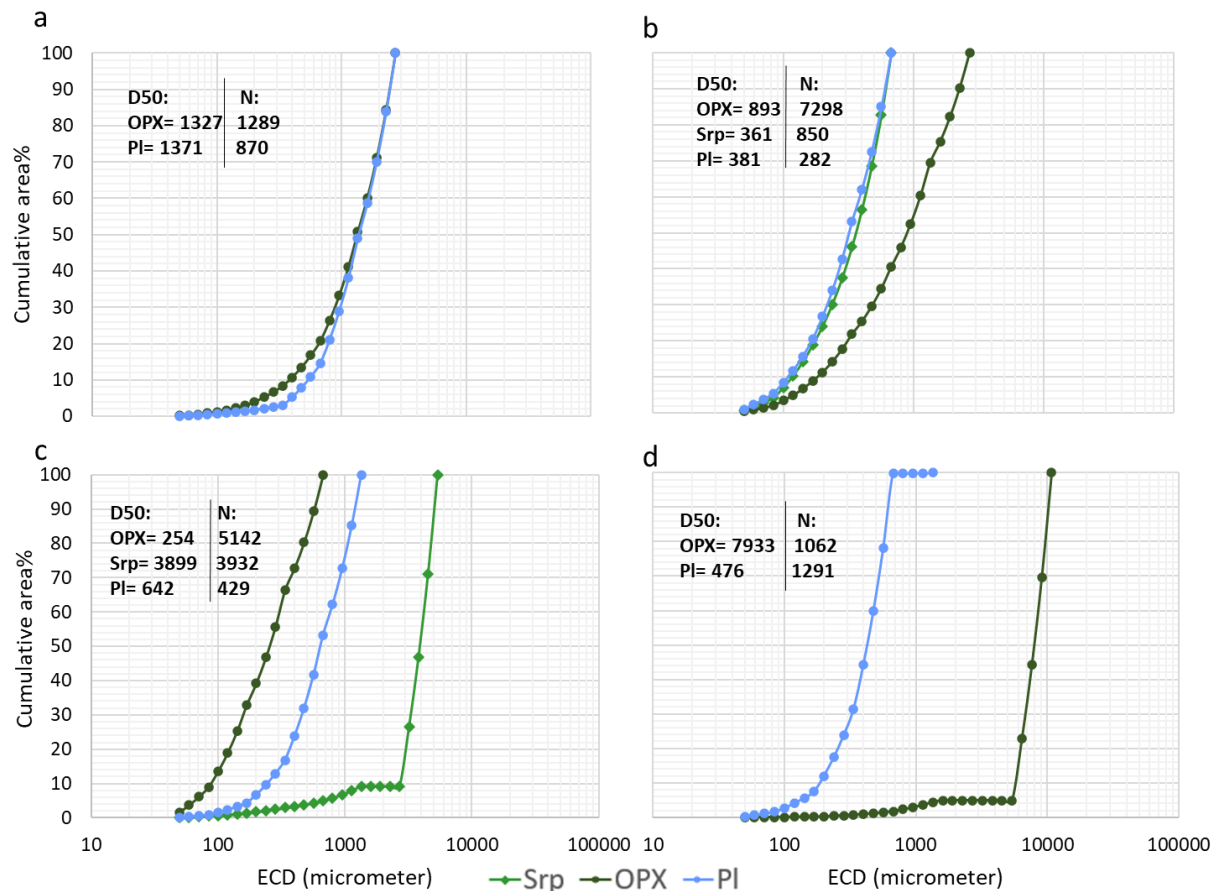


Figure 4.5: QEMSCAN determined grain size distribution for selected minerals in drill core TU277: serpentine (Srp), orthopyroxene (OPX) and plagioclase (PI) in the (a) anorthosite, (b) pegmatoidal olivine-pyroxenite, (c) altered harzburgite and (d) feldspathic pyroxenite. The pegmatoidal pyroxenite and pegmatoidal-olivine pyroxenite constitute similar minerals, and only one was chosen for GSD analysis. The d50 in microns is also given.

d) Lower Pseudo Reef pegmatoidal pyroxenite

This layer retains the colour of the underlying pyroxenite and gradually changes to a darker green-black colour. This is visually characterized by coarse-grained net-textured olivine and pyroxenes (Figure 4.3d). According to QXRD analysis, orthopyroxene, clinopyroxene, amphibole, and plagioclase are the rock's predominant minerals. This rock contains a significant amount of alteration minerals: chlorite and

talc (11 and 17 wt.%) with minor serpentine (Table 4.1). Spinel (magnetite and chromite) and mica were also identified as minor minerals.

Orthopyroxene and olivine are pervasively altered to serpentine although there are still some very coarse orthopyroxene grains that are not altered (Figure 4.3d)—leading to the orthopyroxene grain size ranging from very fine to very coarse-grained. However, olivine was not detected by QXRD, most likely due to its extensive replacement by serpentine. The plagioclase-epidote-chlorite alteration assemblage, identified in QEMSCAN field images, forms the intercumulus phase matrix of the rock, whilst QXRD identified only plagioclase and chlorite. The plagioclase is very fine-grained due to its intensive alteration by epidote and chlorite.

Angular and euhedral medium chromite grains are disseminated throughout the rock, associated with either an orthopyroxene-olivine-serpentine assemblage or plagioclase-epidote-chlorite assemblage with biotite. Very fine-grained magnetite is disseminated (especially in chlorite) and sometimes forms veinlets (Figure 4.3d). Relicts of mica are also associated with chlorite. The LPR pegmatoidal olivine pyroxenite is terminated by a 0.5 cm thick chromitite stringer which marks the start of the Upper Pseudo Reef (UPR) (Figure 4.1).

e) UG2 Hanging wall feldspathic pyroxenite.

The feldspathic pyroxenite of the UG2 hanging wall is the lightest layer of the mafic igneous rocks in the drill core. It is greenish and characterized by semi-rounded to elongated pyroxene grains and euhedral fine-grained mica (observed from hand specimen—Figure 4.1). This rock is composed of orthopyroxene, clinopyroxene, amphibole, plagioclase and mica (as the predominant primary minerals). Alteration minerals occurring as major constituents are talc and chlorite (at a ratio of 1:2) (Table 4.1). QXRD and QEMSCAN indicated orthopyroxene (orthopyroxene) as the predominant pyroxene. The orthopyroxene is medium to coarse-grained (Figure 4.5d), hosting a very fine-grained clinopyroxene (clinopyroxene) (Figure 4.5e). These pyroxenes (orthopyroxene and clinopyroxene) are set amongst very fine to fine-grained plagioclase (Figure 4.5d). Plagioclase also appears to be associated with quartz, amphibole, and biotite. Very fine-grained chlorite is distributed throughout the rock and appears as veinlets crosscutting the orthopyroxenes (Figure 4.3e). There are very few disseminated and very fine-grained chromite grains present.

4.2 Drill core RD015

This borehole was 5.28 m long, collected from a depth of 29.1 m to 23.82 m (Figure 4.6) and similarly represents the stratigraphic intersection from the UG2 hanging wall to the Merensky Reef Footwall. Overall, the drill core is more altered than borehole TU277. Borehole RD015 starts with a 0.2 m medium-grained pyroxenite of UG2 hanging wall from the bottom. The pyroxenite layer terminates erosionally at 28.9 m to a pegmatoidal olivine orthopyroxenite of the Lower Pseudo Reef. The layer sharply

changes to pegmatoidal pyroxenite. The pegmatoidal pyroxenite is bounded by pegmatoidal olivine-orthopyroxenite at 28.2 m. The pegmatoidal olivine orthopyroxenite changes gradationally to upper Pseudo Reef harzburgite. Harzburgite is the dominant layer, 3.98 m long, and the borehole's pervasive altered and mineralised lithology. The harzburgite changed gradationally to anorthosite of the Footwall Merensky Reef. The QXRD determined mineral grades given in Table 4.1. Selected QEMSCAN field images in Figure 4.7 and mineral grades in Figure 4.8. The grain size distribution of selected minerals is present in Figure 4.9.

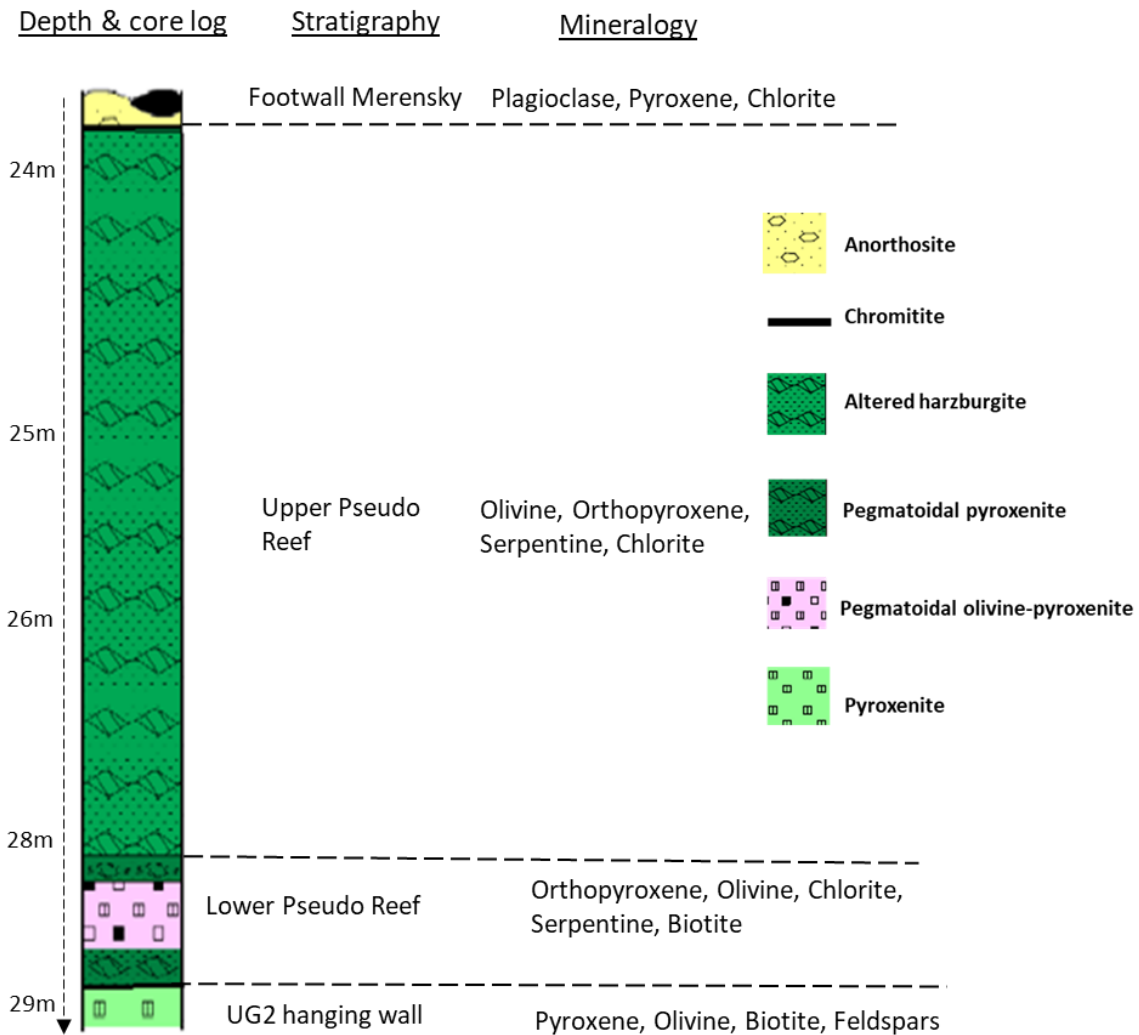


Figure 4.6: Stratigraphic column for Drill core RD015 from the UG2 hanging wall (bottom) to the Merensky Reef Footwall (top) with minerals identified in each rock type during manual core logging.

4.2.1 Mineral assemblage and texture of drill core RD015

a) Footwall Merensky anorthosite

The anorthosite is a thin layer, red-stained due to sulphide oxidation and it is medium-grained dominated by plagioclase and pyroxenes (Figure 4.1). QXRD detected more clinopyroxene than orthopyroxene. Epidote and talc have also been identified as major minerals. Chlorite, mica, and spinel are also present as minor minerals (Table 4.2). In some areas, plagioclase is more abundant with fewer pyroxenes. The plagioclase is fine to coarse-grained (Figure 4.9a). The plagioclase in this core has been least altered, by epidote and chlorite compared to other rocks in the core. Epidote altered the area of plagioclase, and chlorite appears as veinlets on the rock. Chlorite also alters the very fine-grained orthopyroxene either around the or within the grains (Figure 4.7a). The chromite and BMS were detected by QEMSCAN (Figure 4.8). The anorthosite hosts individual chromite grains aligned to form a stringer crosscutting the rock at 45 degrees (tray used as the reference point, channels at 90 degrees). Some of these stringers contain visible BMS. These BMS are very fine-grained chalcopyrite-pyrrhotite-pentlandite base metal sulphide domains that occur disseminated throughout the core (Figure 4.7a). The carbonate veins are also dominant in this layer, acting as the zones of weakness (Figure 4.1b).

Table 4.2: QXRD bulk mineral grades for different rock types sampled in drill core RD015 (in wt. %). Minerals indicated with a hyphen were not detected in the selected sample. *Spinel covers chromite and Fe-oxides. Base metal sulphides were below the detection limit.

Rock names Minerals	Footwall Merensky anorthosite	UPR altered harzburgite	LPR pegmatoidal pyroxenite	LPR pegmatoidal pyroxenite	UG2 feldspathic pyroxenite
Olivine	-	<lld	<lld	<lld	-
Orthopyroxene	9	-	40	58	77
Clinopyroxene	15	2	5	4	3
Amphibole	2	-	2	2	2
Serpentine	1	69	22	3	1
Talc	5	11	9	18	4
Chlorite	3	-	-	5	1
Plagioclase	47	7	16	5	10
Epidote	13	-	-	-	-
Calcite	-	1	2	-	<0.1
Mica	1	2	1	3	1
*Spinel	4.7	8.8	3.9	3.3	1.9

b) Upper Pseudo Reef altered harzburgite

A dominant layer, 3.98 m long, dark green to black with interconnected white interstitial spaces and white euhedral grains in some areas. There are four layers of harzburgite observed, either granular or poikilitic textural harzburgite separated by crystalline serpentinite with abundant magnetite mineralization. This is a highly altered rock type with different types of altered harzburgites with various textures and the degree of alteration: chloritized harzburgite, serpentinised harzburgite and very fine-grained dunite.

This rock is dominated by serpentine (65-70 wt.%), plagioclase and talc, dominant in some core areas (SED 05319-Appendix B, Table B1). More magnetite has been detected compared to other rock types. Mica and calcite were detected as minor minerals (Table 4.2). As evidenced from the QEMSCAN field image (Figure 4.7b), olivine is the primary source of serpentine. Serpentine is altering the area of olivine and rims the orthopyroxene grains. Sample SED 05319 (appendix-Figure) clearly shows the alteration rim of serpentine around orthopyroxene. The serpentine grains range from very fine to coarse-grained depending on the degree of alteration (Figure 4.9b). The plagioclase-epidote-chlorite alteration is also present but not extensive. Traces of mica and very fine-grained magnetite are associated with serpentine. The carbonate veins are most common towards the anorthosite (Figure 4.1-hand sample). The magnetite mineralization is dominant throughout the drill core and occurs as veins, which are displaced by the second generation of amphibole in some areas (observed in hand samples- Appendix B, Table B2).

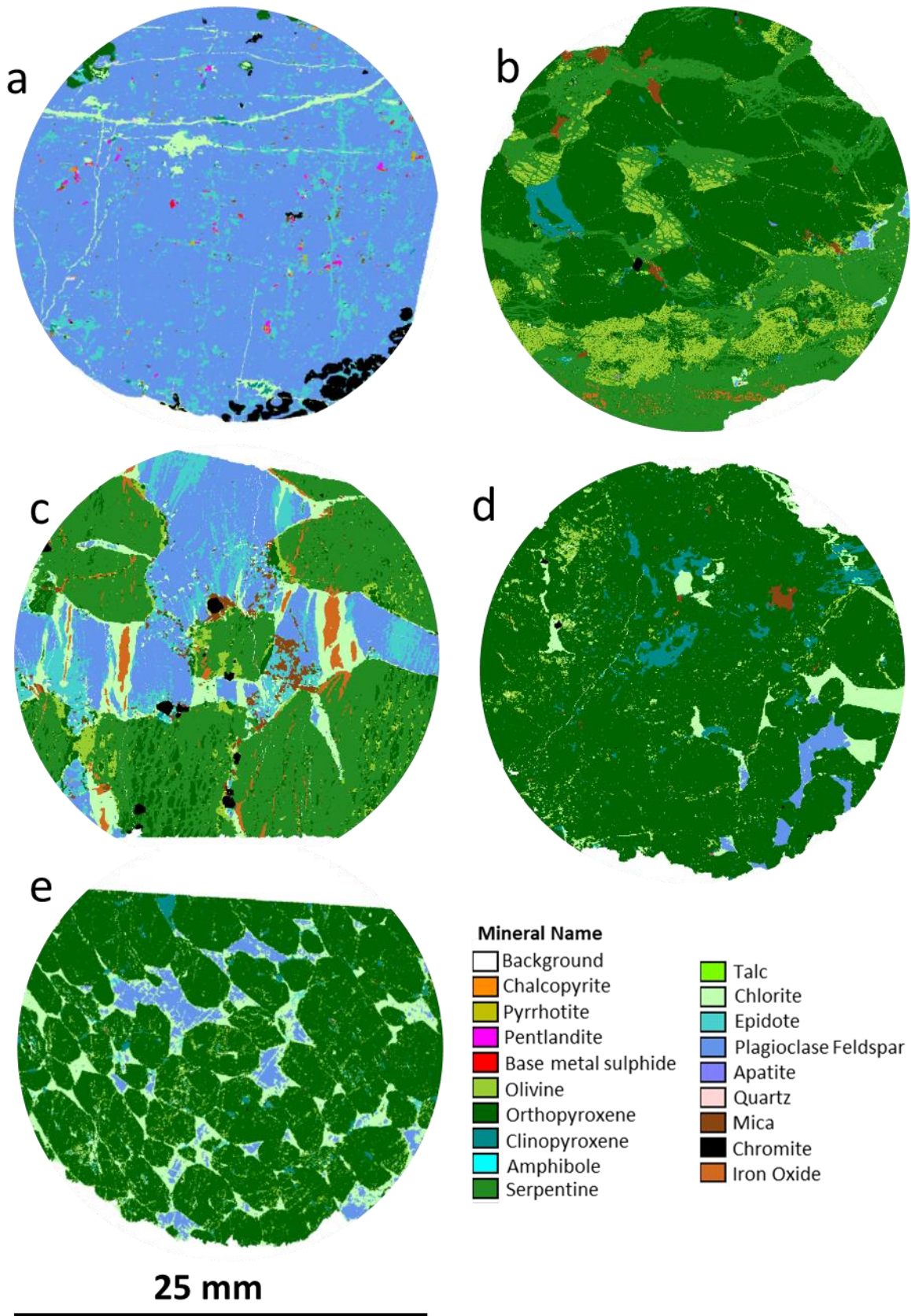


Figure 4.7: QEMSCAN field images for TU277, stratigraphically from (a) Anorthosite, (b) Altered harzburgite, (c) Pegmatoidal-olivine pyroxenite, (d) Pegmatoidal pyroxenite and (e) Pyroxenite.

c) Lower Pseudo Reef pegmatoidal olivine-pyroxenite and pegmatoidal pyroxenite

This layer is a very coarse-grained, dark grey to green mafic layer. It is characterized by nodular olivine grains (dark grey) set in very coarse subhedral grains of orthopyroxenes and euhedral mica (observed from the hand samples-Figure). According to QXRD analysis, this rock is dominated by orthopyroxene, plagioclase and clinopyroxene as primary minerals. Serpentine and talc are the predominant alteration minerals at a ratio of 3:1 (Table 4.2). The presence of calcite is also detected as a trace mineral.

Orthopyroxenes and olivine present are altered to serpentine- supported by the abundance of serpentine detected by both QXRD and QEMSCAN (Table 4.2 and Figure 4.8). The alteration is also evident in the QEMSCAN field images by the very fine to fine-grained relicts of olivine and orthopyroxene (Figure 4.9c). The olivine abundance increases towards the plagioclase-epidote-chlorite alteration, prominent as the matrix. Also, very fine-grained and irregularly shaped micas are set within the plagioclase-epidote-chlorite assemblage. Lense-shaped magnetite grains are only set in chlorite and on serpentine as the veinlets. Irregular fine-grained chromite grains are primarily associated with mica and a few with serpentine (Figure 4.7c).

The pegmatoidal pyroxenite is also very coarse-grained and lighter green than the pegmatoidal olivine-pyroxenite (Figure 4.1b). It is characterized by the dominance of very coarse-grained orthopyroxene and chlorite. QXRD detected more talc than chlorite, with minor serpentine at a ratio of 7:2:1 (Table 4.2). There is minor plagioclase detected in this rock, including clinopyroxene, mica, spinel and amphibole. Orthopyroxene grains seem to be interconnected with relicts of clinopyroxene and biotite (Figure 4.7d). Chlorite is altering the plagioclase-feldspar set in as a matrix hosting the orthopyroxene grains. In some areas, chlorite is also altering biotite and clinopyroxene, which also appear as relicts and the grain boundaries of orthopyroxene.

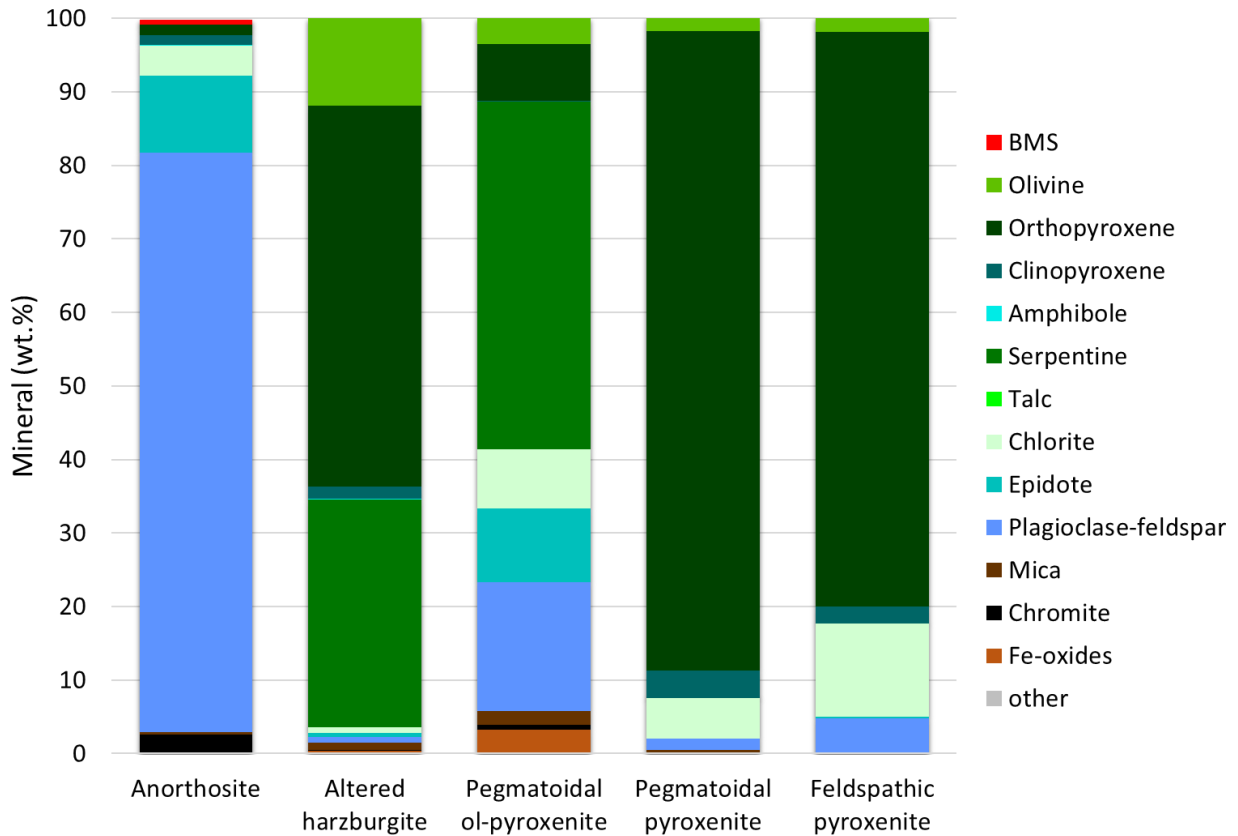


Figure 4.8: Bulk mineral grades obtained from QEMSCAN analyses for different lithologies in drill core RD015. Differences in mineral grades between QEMSCAN and QXRD analyses (Table 4.2) are considered to be due to sampling effects.

d) UG2 Hanging wall feldspathic pyroxenite

The feldspathic pyroxenite is greenish with medium elongated pyroxenes grains, mica, and fine-grained feldspar (Figure 4.1). Orthopyroxene was detected as the predominant pyroxene with plagioclase. The alteration minerals (chlorite and talc) constitute less than 5 wt.%. Amphibole, clinopyroxene, and spinel are minor minerals (Table 4.2).

Chlorite and plagioclase make up the groundmass of the rock, with chlorite altering plagioclase from the rims of grains (Figure 4.7e). The median grain size of plagioclase falls within the range of fine-grained (Figure 4.9d). Chlorite is also partly altering areas of orthopyroxene grains. The orthopyroxene grains range from very fine-grained to coarse grains (Figure 4.9d). These grains were interconnected but separated where grain boundaries were visible. However, from the manual logging, individual orthopyroxene grains could not be seen with the naked eye. Only the spinifex chlorite grains were observed. The rims of orthopyroxene grains are associated with very fine-grained clinopyroxene.

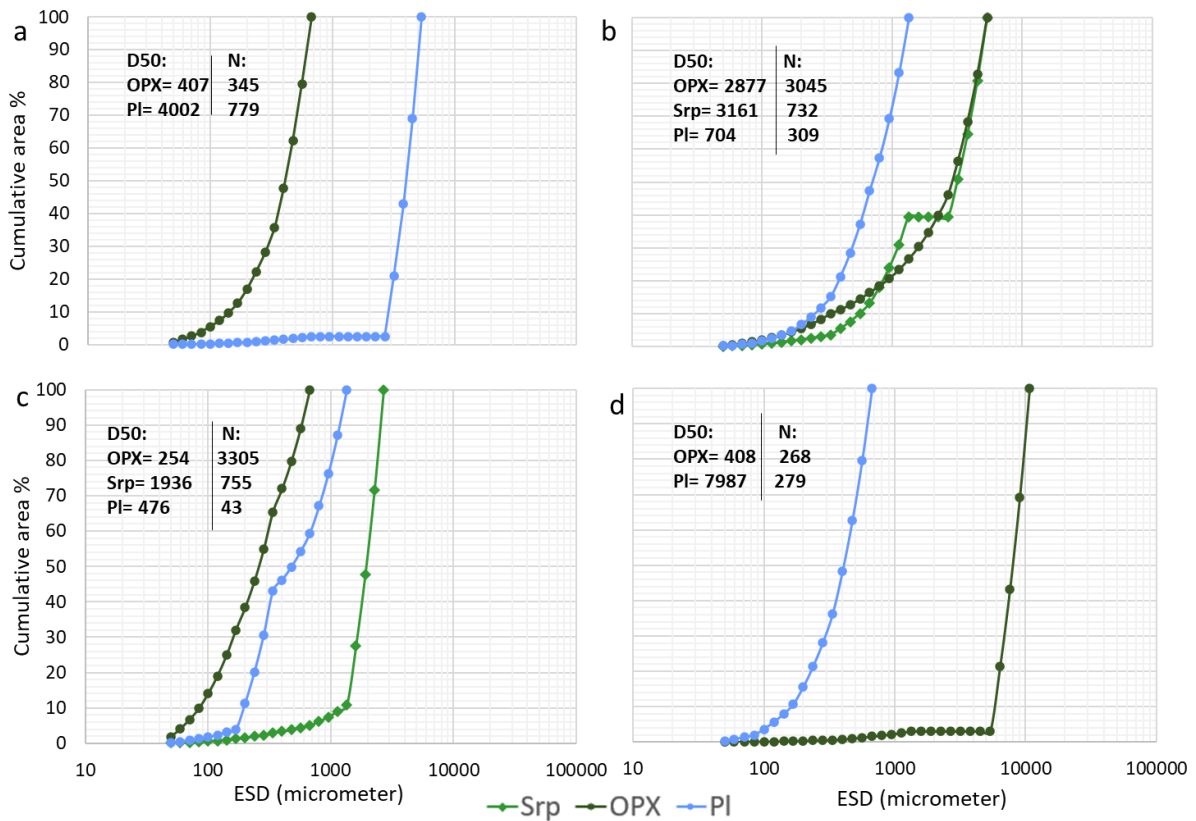


Figure 4.9: Grain size distribution for selected minerals in drill core RD015: serpentine (Srp), orthopyroxene (orthopyroxene (OPX)) and plagioclase (PI) in (a) anorthosite, (b) pegmatoidal pyroxenite, (c) altered harzburgite and (d) feldspathic pyroxenite. The pegmatoidal pyroxenite GSD was excluded due to intensive interconnected grains that could not be separated. The number of grains is given in Appendix C (Table C3).

4.3 Department of base metal sulphide minerals

The assay results provided by the mine detected the element abundance of Nickel (Ni) and Copper (Cu) (Appendix B, Table B3a and B3b). According to QEMSCAN results, pentlandite is the main host of Ni and chalcopyrite of Cu. Pyrrhotite is associated with pentlandite and chalcopyrite occurring in sulphide blebs or domains (Figure 4.11). The highest grades are associated with the chromite grains and stringers; the more abundant BMS is detected on the anorthosite, altered (in drill core RD015), pegmatoidal olivine pyroxenite and pegmatoidal pyroxenite in both drill cores (TU277 and RD015) (Figure 4.10). Platinum and palladium grades are directly proportional; the highest grades are associated with rock types hosting the chromite stringer or the neighbouring rock types (0.1-0.2 m from the chromite stringer). In this study, the QEMSCAN field image analyses did not identify any discrete platinum group minerals (PGM), most likely due to the resolution at which the measurements were conducted (15 μm per pixel). The success in identifying discrete PGM is a function of scanning at the correct resolution (pixel size) and analysing sufficient mass. If the focus of this study had been on the PGM, multiple surfaces would have been scanned at a higher resolution, for example, in the work conducted by Molifie (2021) that characterised a run of mine flotation feed sample from Pilanesburg

Platinum Mine, over eighty 30 mm diameter block surfaces were analysed at 1 µm pixel spacing to obtain around 100 PGM particles.

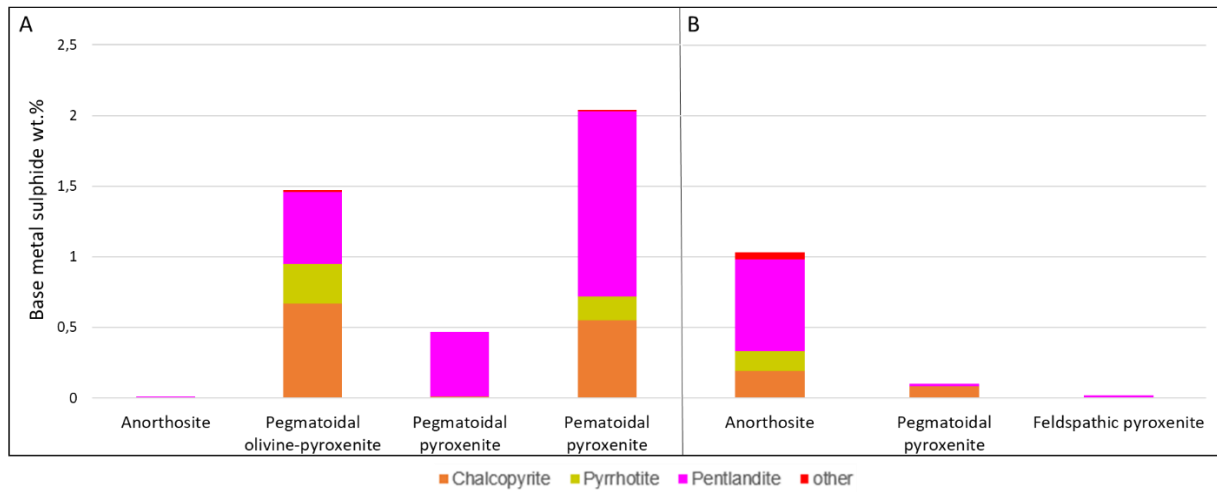


Figure 4.10: Base Metal sulphides quantified from QEMSCAN field images for different rock types in (A) drill core TU277 and (B) drill core RD015. Other represent sulphide minerals not mentioned above.

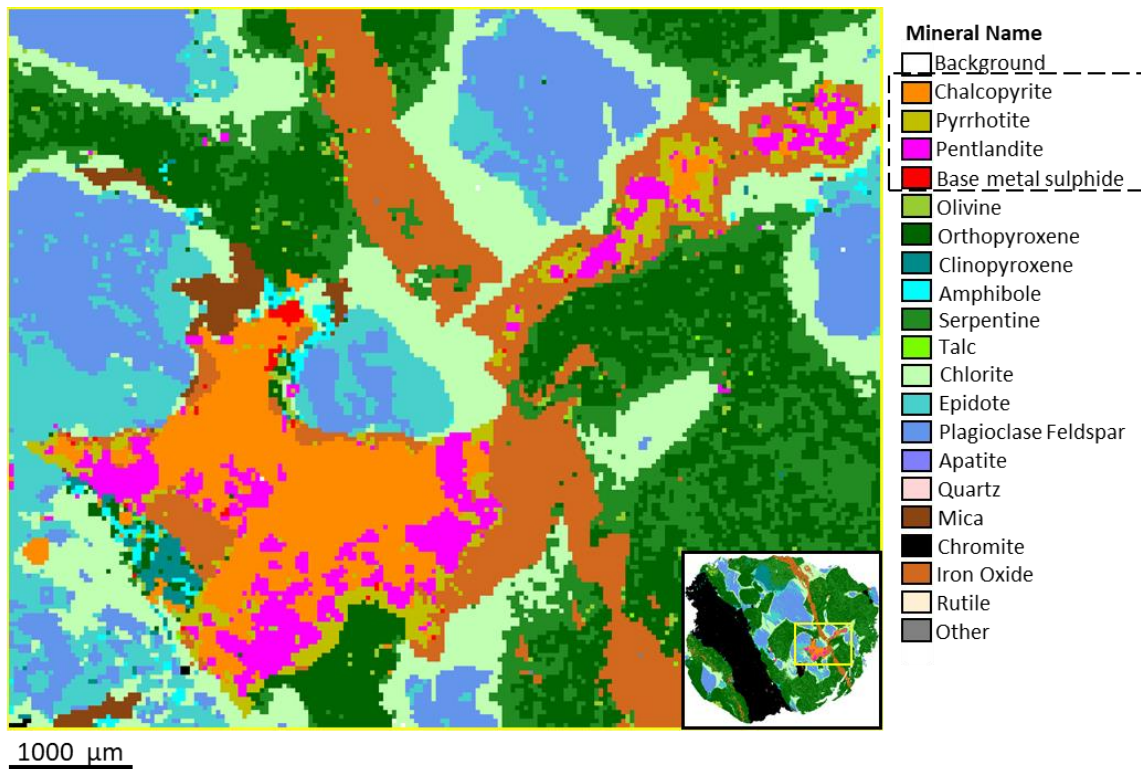


Figure 4.11: Selected area from the olivine pegmatoidal pyroxenite of the drill core TU277 showing the textural association of the base metal sulphide.

Chapter 5: Scanning technologies

The main objective of this project was to investigate how X-ray computed tomography complements the routinely applied hyperspectral imaging in drill core. Therefore, this chapter focuses on the main scope of this project to address the outlined objective and key questions. The chapter is divided into three parts: part I presents the results for hyperspectral imaging; part II presents X-ray computed tomography results and part III presents the image overlapping results. The results presented in Chapter 4 will form an integral part of the mineral identification and interpretation of the HSI and XCT datasets.

5.1 Hyperspectral imaging

5.1.1 Standard core scanning

The drill cores: TU277 and RD015 were scanned with HSI and produced readily automated hyperspectral minerals. The cores were scanned with both the FENIX (combined VNIR-SWIR) and OWL (LWIR) sensors. The minerals that were readily identified by each of the sensors are summarized in Table 5.1. Some of the minerals identified are unexpected and not consistent with a magmatic Ni-Cu-PGE deposit. Therefore, an important aspect of the investigation recognises that not all readily identified minerals are necessarily present. To gain confidence in the datasets, each of the minerals needed to be validated and confirmed. The sections below describe how this is achieved. The summary table provides the default (readily identified) mineral assemblage in the rock types throughout the stratigraphy in Appendix D- Table D1 and D2.

Table 5.1: Readily identified mineral assemblage detected under VNIR-SWIR and LWIR sensors before data validation and interpretation. The green-highlighted minerals annotated are the predominant minerals detected by each spectral sensor.

Mineral group	VN-SWIR		LWIR	
	Major	Minor	Major	Minor
Silicates	Amphibole	Buddingtonite	Epidote Quartz	Orthopyroxene
	Epidote	Chloritoid		Clinopyroxene
	Prehnite	Topaz		Anorthite
Phyllosilicates	Illite	Muscovite	Chlorite Biotite	Illite
	Serpentine	Montmorillonite		Andradite
	Talc	Pyrophyllite		Muscovite
	Chlorite	Dickite		
	Saponite	NH4 illite		
Carbonates	Carbonate			Carbonate
Phosphate			Apatite	Gypsum
Sulphates				Barite Alunite
Hydrocarbon	Bitumen			

Some of the minor minerals listed in Table 5.1 detected a flat spectral response with no absorption features or tiny pixels, which could not be real. For example, bitumen, barite and gypsum are minerals commonly associated with sedimentary rocks. These minerals appear to be uncommon and unlikely in the Bushveld Igneous Complex. Therefore, they were not considered and immediately reclassified as null.

TU277 Spectral mineral assemblage

VN-SWIR and LWIR scans initially produced the mineral maps in Figure 5.1. The anorthosite is dominated by illite associated with prehnite and muscovite, and serpentine, epidote, chlorite, amphibole and saponite detected by VN-SWIR. Under LWIR, minor pixels of gypsum, anorthite, alunite, orthopyroxene, epidote and apatite were detected.

The pegmatoidal pyroxenite of the Upper Pseudo Reef is mapped with chlorite associated with amphibole and talc. Serpentine was detected as the dominant mineral within the 'unclassified' chromite stringer under VN-SWIR. However, under LWIR, the chromite stringer was not readily visible and mapped as apatite and chlorite (Figure 5.1). The LWIR detected abundant apatite and chlorite associated with minor biotite and orthopyroxene overlapping with serpentine in VN-SWIR.

Serpentine fully maps the harzburgite of the Pseudo Reef in VN-SWIR, with minor pixels of chlorite, epidote, and amphibole. Under LWIR, chlorite was more dominant than apatite. Also, it overlaps with serpentine in VN-SWIR (Figure 5.1). However, VN-SWIR has detected more chlorite in the pegmatite cross-cutting the harzburgite. This chlorite is associated with amphibole at the boundaries of prehnite with saponite. Quartz and biotite are detected under LWIR in the pegmatite, overlapping with prehnite and chlorite in VN-SWIR. LWIR has mapped the chromite stringers as apatite with chlorite at its boundaries. Most areas of the pegmatoidal pyroxenite of the lower Pseudo Reef under VN-SWIR were also mapped with serpentine with minor chlorite, talc, epidote and prehnite. Talc, amphibole and chlorite increase in content going down to the pyroxenite. Areas unclassified in VN-SWIR are mapped as apatite under LWIR (Figure 5.1). Like the upper pegmatoidal pyroxenite in this core, biotite mapped in LWIR overlaps with talc and amphibole in VN-SWIR. Also, chlorite appears as the predominant mineral in this rock under LWIR. Ninety percent of the pyroxenite of the UG2 Reef is unclassified in VN-SWIR, and talc is only detected. However, in LWIR, apatite is abundant with minor epidote and orthopyroxene (Figure 5.1).

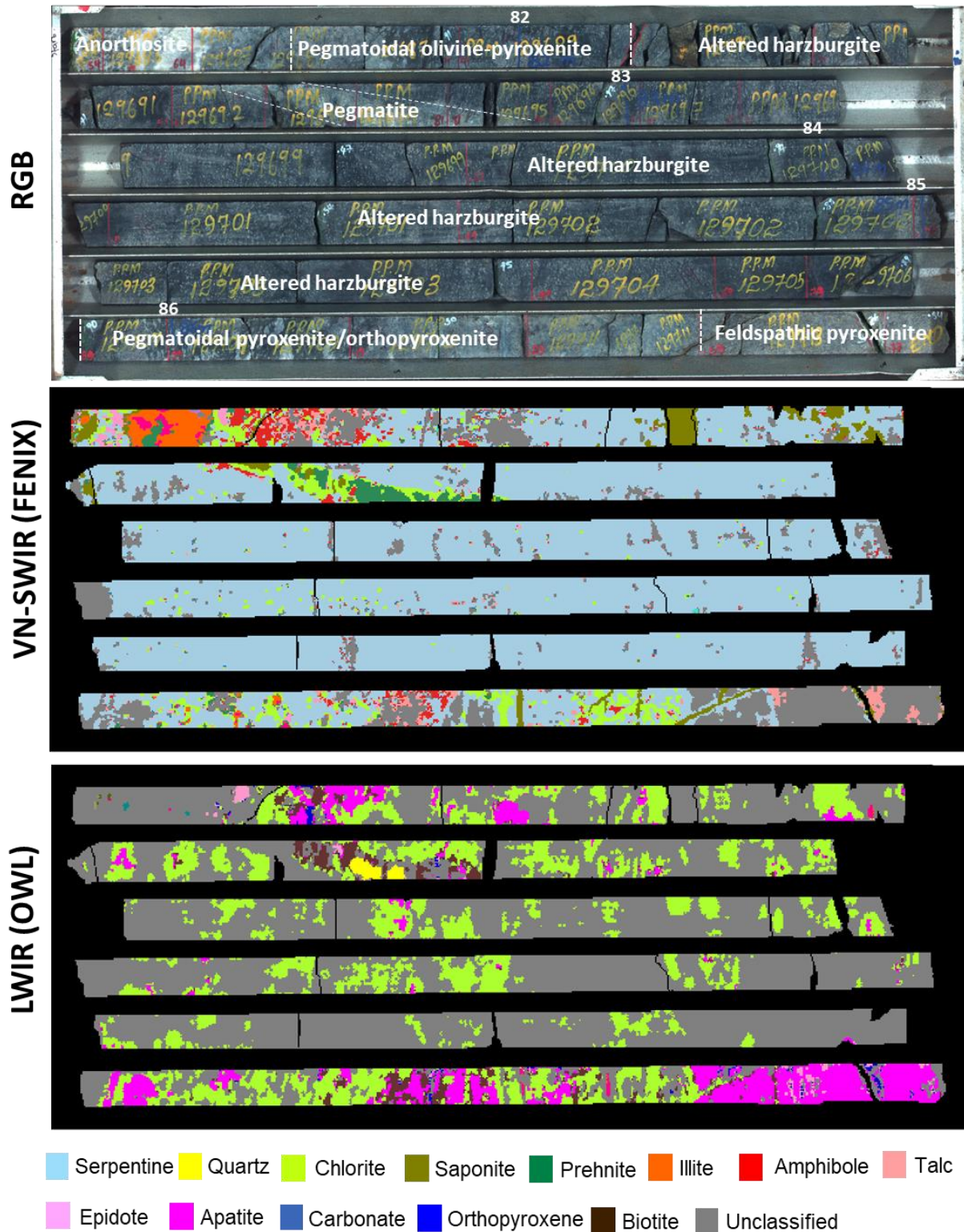


Figure 5.1: Drill core TU277-Mineral maps for the readily identified mineral assemblage (before data validation and interpretation) detected with the VNIR-SWIR and LWIR sensors scanned at 1.64 mm pixels; and RGB images at 0.16 mm pixel. 50 mm core diameter.

RD015 Spectral mineral assemblage

Hyperspectral imaging detected saponite and illite as the predominant mineral assemblage in the anorthosite under VN-SWIR (Figure 5.2). Illite and prehnite appear as co-existing minerals, both associated with small pixels of muscovite. Calcite veins mapped in the manual core logging of the anorthosite (SED 05315) were detected as carbonate-saponite veining by VN-SWIR. Under LWIR, most of the anorthosite was unclassified, with only apatite, chlorite and minor orthopyroxene being identified. Only minor overlapping of pixels occurred between the two sensors in the anorthosite, with serpentine identified under VN-SWIR compared to epidote and chlorite with LWIR.

The presence of apatite was dominant in the harzburgite of the Upper Pseudo Reef under LWIR (Figure 5.2). Apatite is associated with chlorite, epidote, and minor biotite under LWIR. Most areas of the harzburgite were unclassified with LWIR but mapped by VN-SWIR as serpentine with veins of carbonate and amphibole along with very-fine grained chlorite amphibole and epidote pixels.

Serpentine, as detected by VN-SWIR, was still dominant in pegmatoidal olivine-pyroxenite of the Lower Pseudo Reef. Abundant talc associated with minor pixels of amphibole was also detected with VN-SWIR and saponite and minor chlorite (Figure 5.2). In contrast, the LWIR camera detected abundant apatite associated with chlorite and biotite. In this case, extensive mineral overlapping was recognised in this lithology with pixels mapped as serpentine, saponite, talc and amphibole, with VN-SWIR and mapped as apatite chlorite and biotite with LWIR. Only a few areas were unclassified with both sensors.

The pegmatoidal pyroxenite has a similar mineral assemblage to that detected in the olivine pegmatoidal pyroxenite. However, saponite and amphibole become more dominant in the pegmatoidal pyroxenite with VN-SWIR and chlorite more dominant with LWIR. The mineral overlapping between the sensors is also extensive.

The felspathic pyroxenite of the UG2 was mapped with apatite and fine pixels of epidote and orthopyroxene by LWIR and minor traces of epidote under VN-SWIR (Figure 5.2). Like the anorthosite, most areas of this rock were unclassified under VN-SWIR. The mineral overlapping between the sensors is not extensive in the lighter rocks of the core.

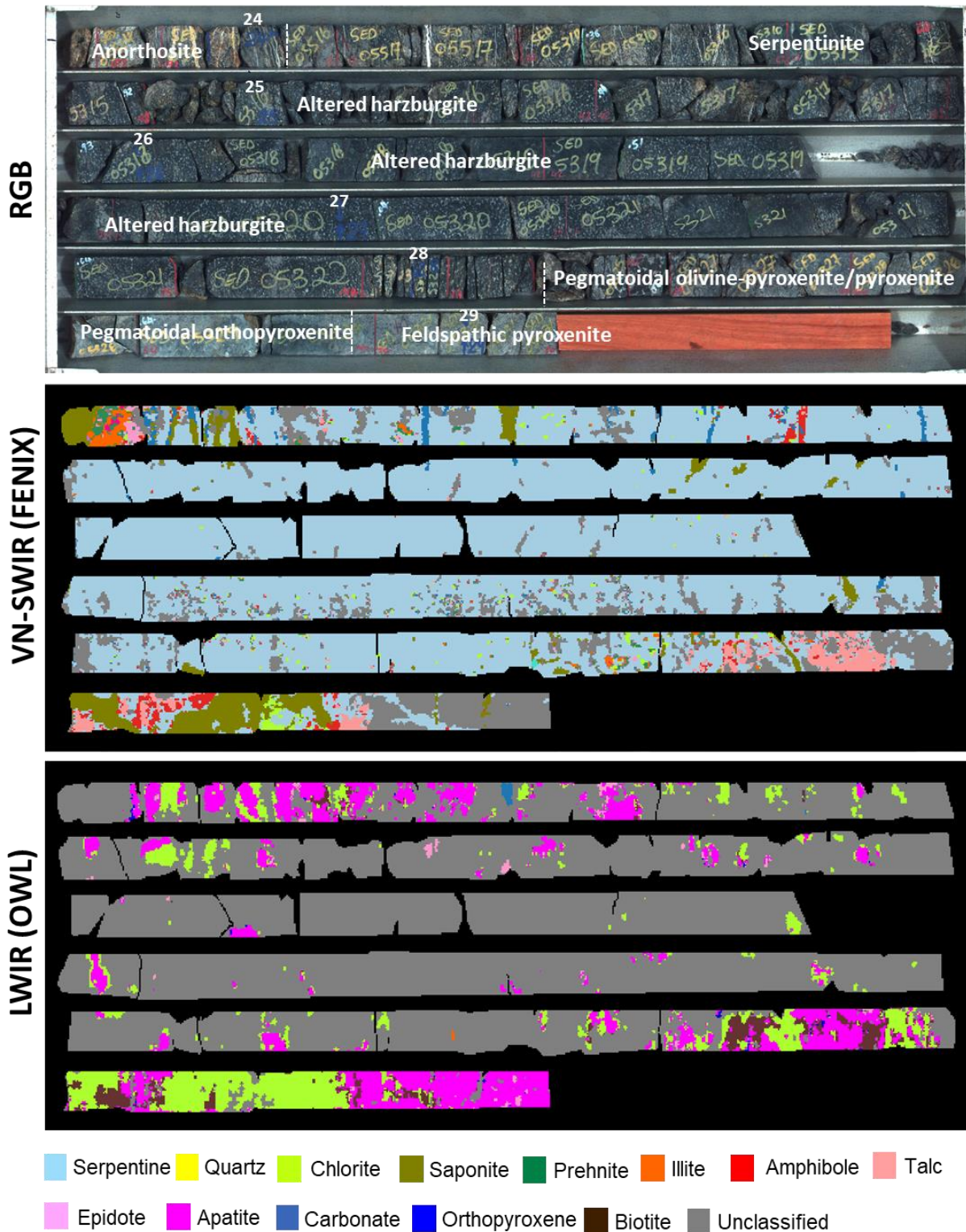


Figure 5.2: Drill core RD015-Mineral maps for the readily identified mineral assemblage (prior to data validation and interpretation) detected with the VNIR-SWIR and LWIR sensors scanned at 1.64 mm pixels; and RGB images at 0.16 mm pixel. 50 mm core diameter.

Possible smearing was suspected; therefore, selected sections of cores were rescanned (Figure 5.3) after washing with tap water. After rescanning, serpentine is still a dominant mineral detected by VN-

SWIR, although contained slightly less amphibole and talc than in the original scan (Figure 5.3a and a*). Under LWIR, more chlorite and apatite are detected compared to the original scans (Figure 5.3b and b*).

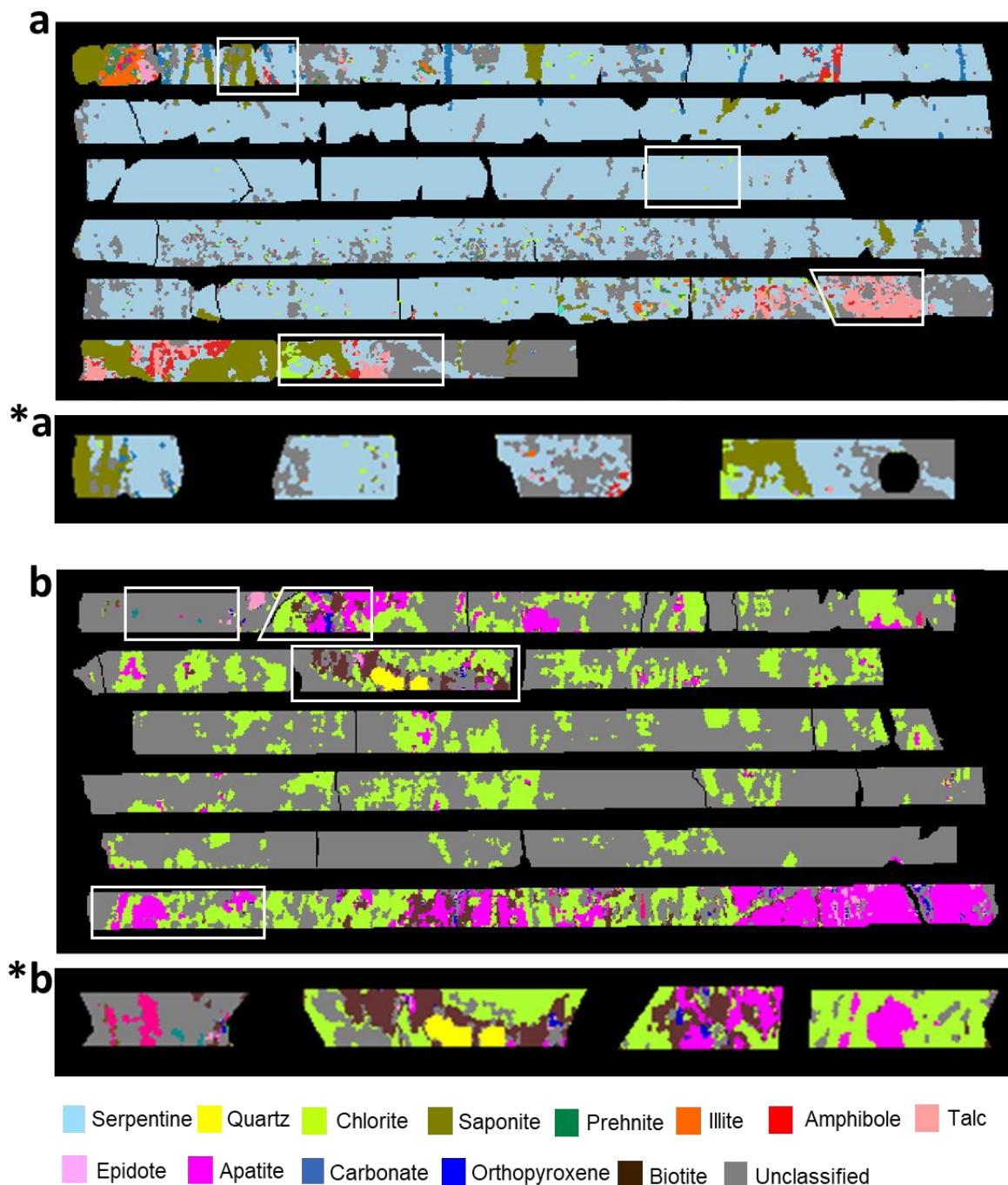


Figure 5.3: Comparisons between mineral maps of the standard scanning (a and b) with selected rescanned cores (*a and *b). The selected cores are illustrated with white boxes sampled from standard drill cores. VN-SWIR mineral maps for (drill core RD015) standard cores (a) with selected rescanned cores (*a), and LWIR mineral maps (for drill core TU277) standard cores (b) with selected rescanned cores (*b). 50 mm core diameter.

To allow for more precise comparison and validation, the surfaces of the mini core scanned with XCT and QEMSCAN were also scanned at high resolution with HSI (Section 3.5).

5.1.2 Mini core scanning

The readily identified mineral assemblage (prior to data validation and interpretation) of the mini cores scanned at high resolution with SWIR and LWIR is summarized in Table 5.2. The VNIR sensor was not used in mini cores due to its inability to focus at the required resolution. Some cores dipped due to the curvature and fragmentation that occurred during drilling; therefore, there were unscanned areas on some surfaces and some unintentional scanning of the sides of the cores (Appendix D, Figure D1 and D2, in the appendix).

Table 5.2: Readily identified HSI mineral assemblage (prior to data validation and interpretation) of the mini cores scanned at high resolution (0.15 mm pixel size). Minerals in green are the predominant minerals under each spectral sensor.

Mineral group	SWIR		LWIR	
	Major	Minor	Major	Minor
Silicates	Amphibole	Prehnite	Epidote	Orthopyroxene
	Epidote		Quartz Anorthite	Clinopyroxene
Phyllosilicates	Illite	Muscovite	Chlorite	Illite
	Serpentine	Montmorillonite	Biotite	Muscovite
	Talc			
	Chlorite Saponite			
Carbonates	Carbonate		Carbonate	
Phosphate			Apatite	Gypsum
Sulphates				Alunite
Hydrocarbon		Bitumen		

The readily identified mineral assemblage of the mini cores is similar to the minerals detected in the standard cores (Table 5.2). However, the LWIR detected clinopyroxene in the anorthosite of drill core TU277. Also, the serpentine is not as abundant in the harzburgite compared to the standard cores, and carbonate is more abundant in the SWIR of the mini cores. Orthopyroxene was also more abundant in LWIR (Figure 5.4). However, some core areas were unclassified, such as the anorthosite in drill core TU277; see Figure D1 and D2 in the appendix. The mineral maps show the unclassified areas (Figure 5.4 and Figure 5.5).

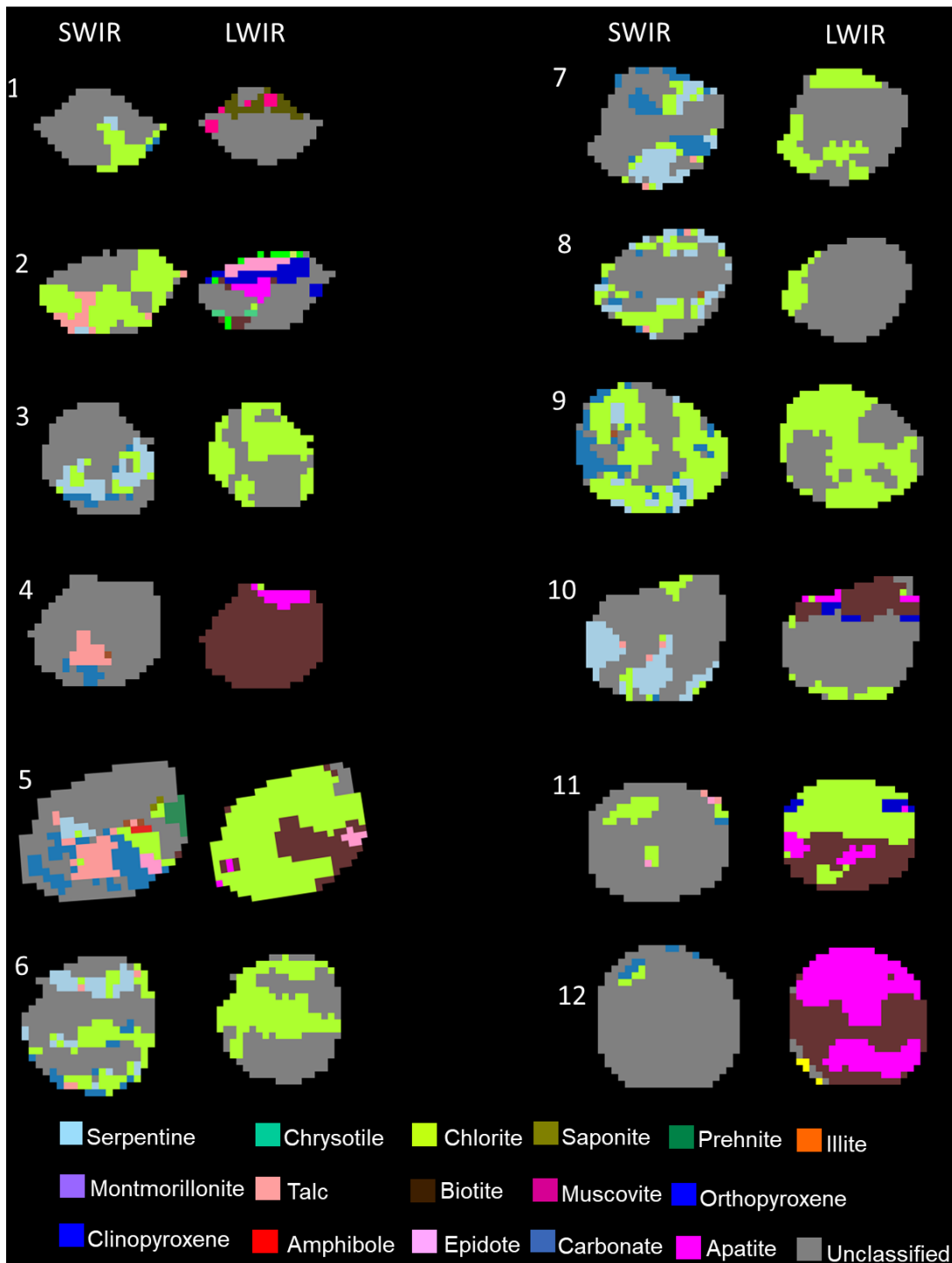


Figure 5.4: Drill core TU277 (mini cores)-Mineral maps for the readily identified mineral assemblage (prior to data validation and interpretation) detected with the VNIR-SWIR and LWIR sensors scanned at 0.4 mm pixels. Sample 1 to 2 represents the anorthosite, sample 3 is upper pegmatoidal pyroxenite, sample 6 to 7-represents altered harzburgite, samples 8 to 10 represents pegmatoidal pyroxenite, and sample 11 and 12 represents feldspathic pyroxenite. Mini cores are 25 mm in diameter.

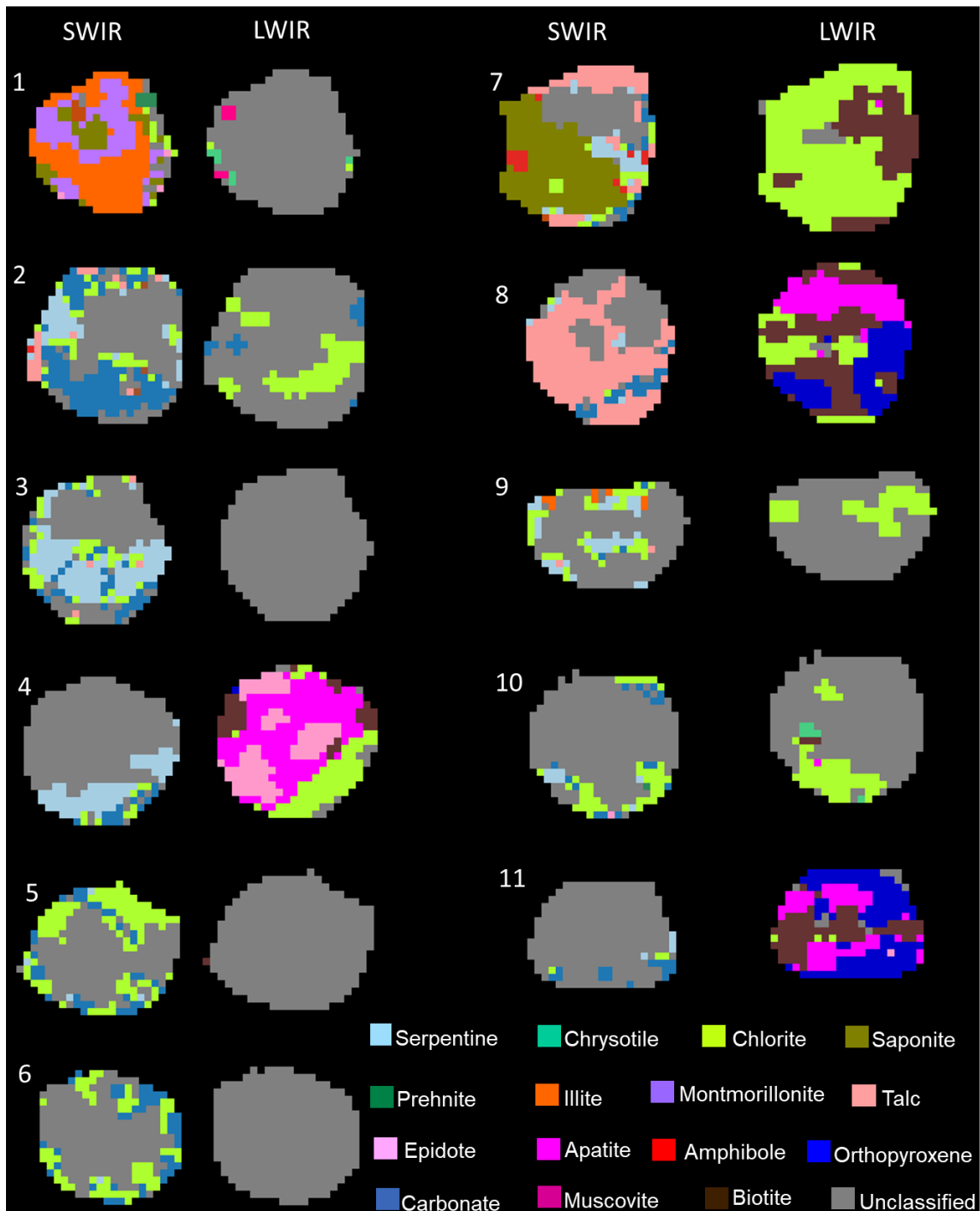


Figure 5.5: Drill core RD015 (mini cores)-Mineral maps for the readily identified mineral assemblage (prior to data validation and interpretation) detected with the VNIR-SWIR and LWIR sensors scanned at 0.4 mm pixels. Sample 1 represents the anorthosite, samples 2 to 7 represent altered harzburgite, samples 8 to 10 represent pegmatoidal pyroxenite, and sample 11 represents feldspathic pyroxenite. Mini cores are 25 mm in diameter.

5.1.3 Spectral and mineral reclassification

Spectral reclassification was needed because of the discrepancies in the mineral identification from the automated mineral identification datasets as outlined above. The mineral reclassification was initially conducted on the mini cores where complementary QEMSCAN and QXRD data were available to support the interpretation. The spectral reclassification used the USGS, JHU and TC libraries to match, validate and reclassify the mineral spectra. Table 5.3 summarises the different minerals detected with QEMSCAN, QXRD and HSI sensors (SWIR and LWIR), and Table 5.4 shows how selected spectra were reclassified and grouped.

Table 5. 3: Detected mineral assemblage in QEMSCAN, QXRD and HSI mini cores (before the spectral reclassification).

Mineral groups		Minerals	Minerals detected				
			QEMSCAN	QXRD	SWIR	LWIR	
Silicates	Inosilicates	Amphibole	Amphibole	Amphibole	Amphibole	Amphibole	
		Orthopyroxene	Orthopyroxene	Orthopyroxene	-	±Orthopyroxene	
		Clinopyroxene	Orthopyroxene	Orthopyroxene	-	±Clinopyroxene	
		Other	-	-	Prehnite	-	
	Nesosilicates	Olivine	Olivine	< lld	-	-	
	Tectosilicates	Feldspar	Plagioclase-feldspar	Plagioclase	-	±Plagioclase	
		Quartz	±Quartz	-	-	Quartz	
	Sorosilicates	Epidote	Epidote	Epidote	Epidote	Epidote	
	Phyllosilicates	Serpentine	Serpentine	Serpentine	Serpentine	Serpentine	-
		Talc	±Talc	Talc	Talc	Talc	-
		Chlorite	Chlorite	Chlorite	Chlorite	Chlorite	Chlorite
		Mica	Biotite± Muscovite	Biotite/phlogopite	Muscovite	Muscovite Biotite	
		Others	-	-	Illite Saponite	Illite	
	Other					Andradite	
	Non-silicates		Carbonates		Carbonate	Carbonate	Carbonate
		Phosphate	±Apatite	-	-	Apatite Gypsum	
		Sulphate	-	-	-	Barite Alunite	
		Hydrocarbon	-	-	Bitumen	-	
		Oxides	Fe-Oxide Chromite	Magnetite Chromite	-	-	
		Sulphide	Pentlandite Chalcopyrite Pyrrhotite	< lld	-	-	

Table 5.4: Summary table for HSI mineral reclassification from readily identified (before) to reclassified (after). Minerals in green are the predominant minerals under each spectral sensor.

Mineral group	SWIR		LWIR	
	Before	After	Before	After
Silicates	Amphibole	Amphibole	Amphibole	Amphibole
	-	-	±Orthopyroxene	Orthopyroxene
	-	-	±Clinopyroxene	Clinopyroxene
	Prehnite	Plagioclase-prehnite	-	-
	-	-	-	-
	-	-	±Anorthite	Plagioclase
	-	-	Quartz	Sulphate
	Epidote	Epidote	Epidote	Orthopyroxene-Epidote
	Serpentine	Serpentine-olivine	-	-
	Talc	Talc or Talc-chlorite	-	-
	Chlorite	Chlorite	Chlorite	Plagioclase-chlorite
	Muscovite	Prehnite	Muscovite	Plagioclase
	-	-	Biotite	Chlorite-biotite
	Illite	Prehnite	Illite	null
	Saponite	Saponite-Clinopyroxene	Andradite	null
Non-silicates	Carbonate	Carbonate	Carbonate	Carbonate
	-	-	Apatite	Orthopyroxene
	-	-	Gypsum	null
	-	-	Barite	null
	-	-	Alunite	Plagioclase
	Bitumen	null	-	-

Drill core TU277

The LWIR detected apatite in the anorthosite, which was reclassified as orthopyroxene using the spectral libraries (Appendix D, Figure D4) and the presence of orthopyroxene was supported by QEMSCAN and QXRD (Table 4.1 and Figure 4.4). The results also match with the standard cores; however, the majority of the area remains unclassified. The LWIR detected the presence of plagioclase-feldspar as anorthite. Minor pixels of anorthite were detected in the standard cores (Figure 5.4). There is also talc detected in the SWIR and epidote with fine pixels of biotite and clinopyroxene. Like the scanned standard cores, the upper pegmatoidal pyroxenite (Figure 5.4: number 3) is mapped with serpentine, which was later reclassified as serpentine-olivine due to the presence of olivine detected by QEMSCAN (Figure 4.3 and Figure 4.4). In this core, there is carbonate detected in SWIR confirmed by QXRD as calcite.

Compared to the standard cores, mini core samples 7 to 9 representing altered harzburgite (Figure 5.6) had comparatively less serpentine and more talc and chlorite alteration in SWIR; however, most of the areas in these cores are unclassified. Only chlorite was identified in the LWIR and some areas are

unclassified. These areas covered by chlorite are classified as plagioclase-feldspar in QEMSCAN (Figure 4.3). Therefore, chlorite in the LWIR was reclassified as the mixed phase, plagioclase-chlorite. Carbonate and talc were also detected under SWIR. There was less mineral overlapping in these cores.

Chlorite continues to be dominant in the lower pegmatoidal pyroxenite (Figure 5.6: number 10 and 11) detected both by SWIR and LWIR. In this core, there is also less serpentine alteration detected under SWIR. Like the previous cores, a large area of the cores remained unclassified. The LWIR only mapped the presence of biotite and chlorite. Pyroxenite is mapped with orthopyroxene, biotite and finer pixels of clinopyroxene and orthoclase detected by LWIR (Figure 5.4). The abundance of biotite detected from the LWIR was not supported by QXRD and QEMSCAN data and has been reclassified as mixed-phase chlorite-biotite because biotite was intimately associated with chlorite (Figure 4.3d).

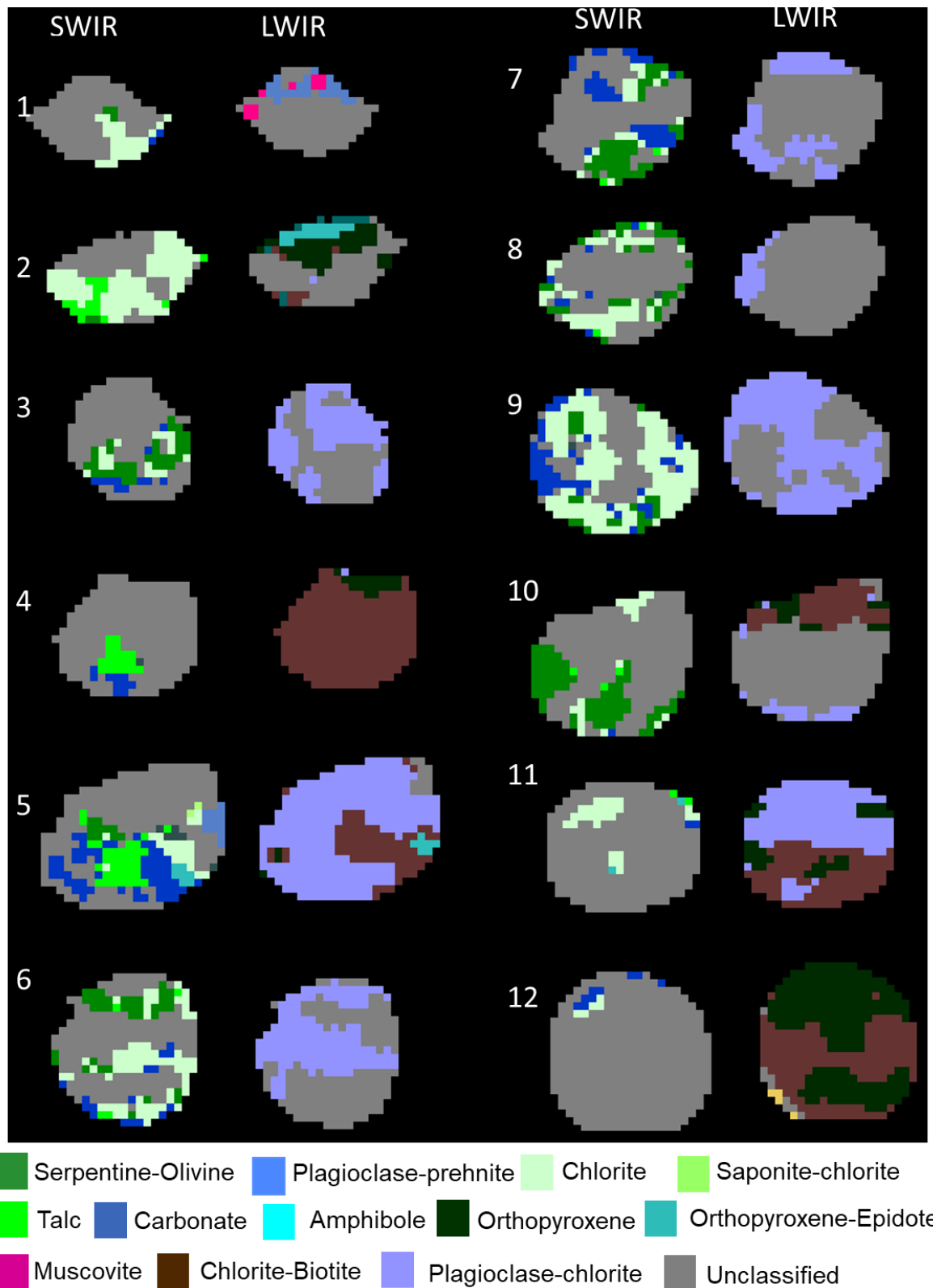


Figure 5.6: Reclassified mineral maps for drill core TU277 scanned at high resolution. Sample 1 to 2 represents the anorthosite, sample 3 is upper pegmatoidal pyroxenite, sample 6 to 7-represents altered harzburgite, samples 8 to 10 represent pegmatoidal pyroxenite, and sample 11 represents feldspathic pyroxenite. The mineral false colours were changed from those initially represented in Figure 5.4 and 5.5 to match with the QEMSCAN field images data in Figure 4.3. Mini cores are 25 mm in diameter.

Drill RD015

In the anorthosite, saponite (a smectite group mineral) was detected as an uncommon mineral that matched the clinopyroxene spectra. Neither the XRD nor QEMSCAN detected the presence of saponite, and consequently, these pixels were reclassified as saponite-clinopyroxene (Figure 4.7). Although QEMSCAN detected the presence of chlorite, it was not as dominant as quantified from the SWIR HSI data. Prehnite, illite and muscovite have matching spectra and the absorption between wavelengths of 1400-1500 nm (double absorption) and single absorption between 1800-2000 nm and 2200-2400 nm and were grouped as prehnite (Figure 5.7). However, QXRD and QEMSCAN did not show any indication of such minerals but only plagioclase feldspar and clinopyroxene were identified as the dominant minerals (Table 4.2 and Figure 4.8). Which then changed the reclassification to prehnite-plagioclase, suggesting the sericitic alteration of plagioclase. Supported by the abundance of plagioclase identified by QEMSCAN and QXRD (Figure 5.7). The carbonate veins in HSI were detected as calcite in the QXRD.

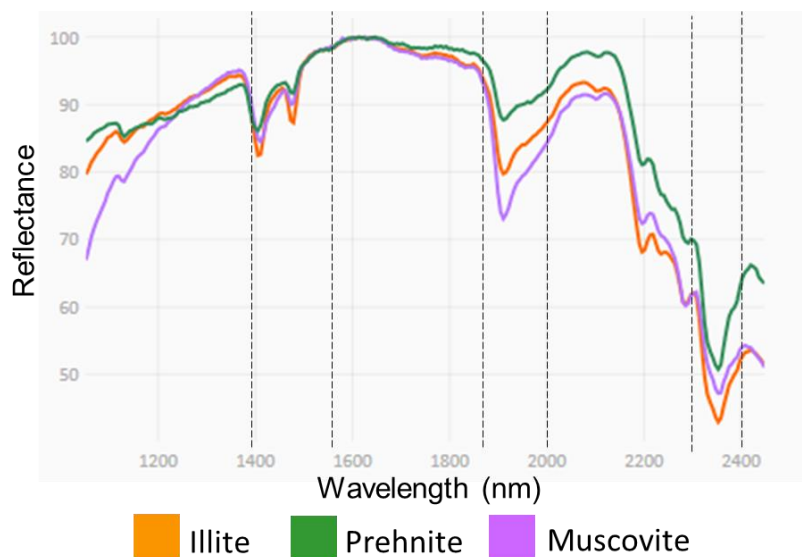


Figure 5.7: Spectral absorption features for illite, prehnite and muscovite.

For the harzburgite of the Upper Pseudo Reef (UPR), apatite detected in standard cores by LWIR matched the orthopyroxene spectra from the libraries. It was subsequently reclassified as orthopyroxene (Figure 5.8-number 4) (confirmed by QEMSCAN and QXRD). The QEMSCAN blocks showed the alteration of orthopyroxene to serpentine and the presence of olivine (Figure 4.7b), where HSI only detected serpentine in VN-SWIR (Figure 5.5). The serpentine was, therefore, reclassified as serpentine-olivine. Also, chlorite detected in the mini cores by LWIR was identified as serpentine, olivine, and minor plagioclase and chlorite in QEMSCAN (Figure 4.7b) and was subsequently reclassified as plagioclase-chlorite. However, the epidote detected in the mini cores is mapped as

orthopyroxene in the standard cores, confirmed in QEMSCAN. The spectra signature for chlorite, talc and amphibole are difficult to distinguish (Appendix D, Figure D5).

In the pegmatoidal pyroxenites, talc is abundant in standard and mini cores (Figure 5.2 and Figure 5.5), supported by the QXRD results (Table 4.1). However, there is less talc detected in QEMSCAN. Saponite detected by SWIR in the pegmatoidal pyroxenite was identified as orthopyroxene with clinopyroxene in QEMSCAN, and there is no talc detected. In the LWIR data, more biotite has been detected for standard and mini cores than in QEMSCAN and QXRD. This biotite overlaps with chlorite in the SWIR. Due to spectral overlapping, the biotite spectra were reclassified as a mixed spectrum comprising chlorite-biotite.

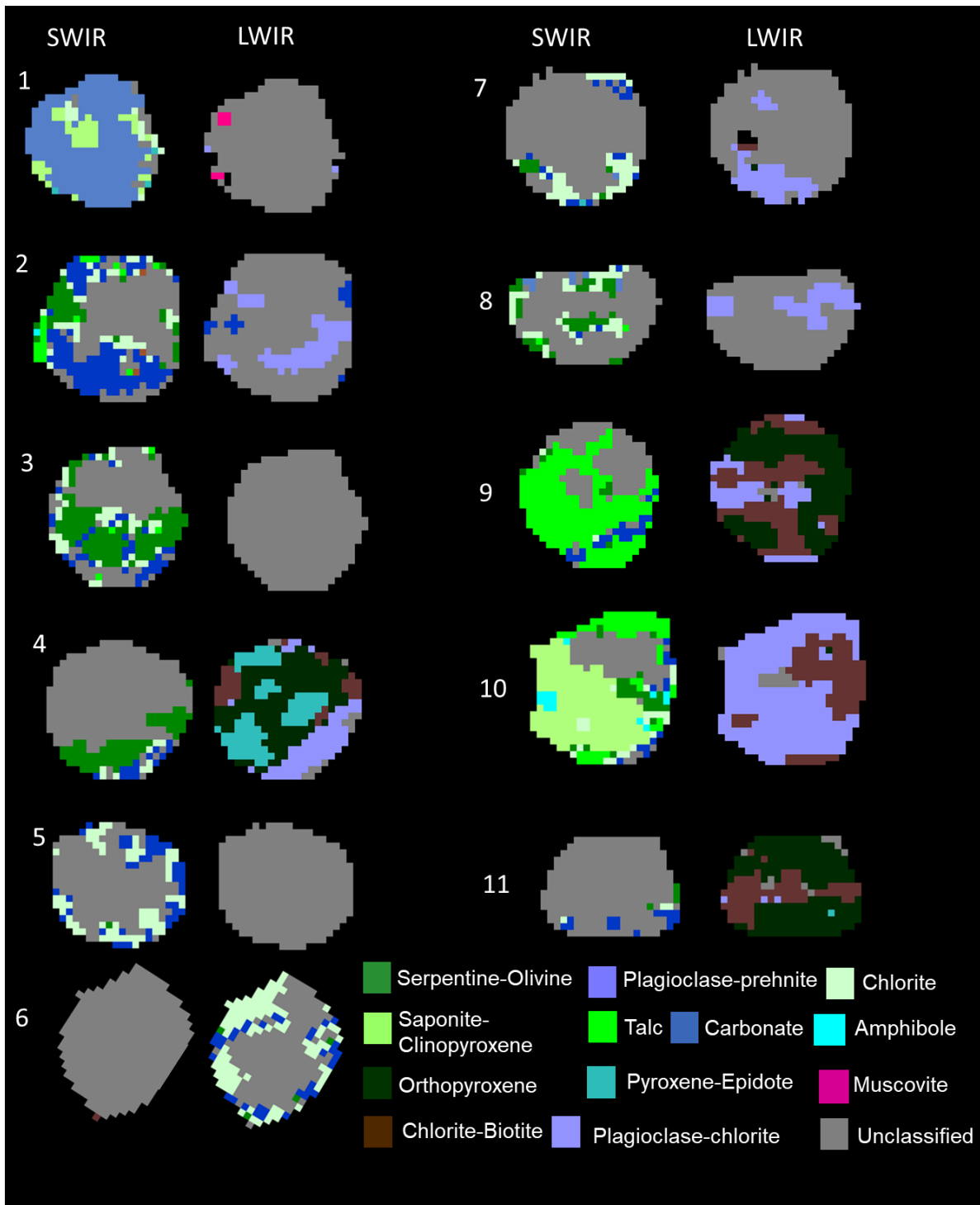


Figure 5.8: Reclassified mineral maps for drill core RD015 scanned at high resolution. Sample 1 represents the anorthosite, samples 2 to 7 represent altered harzburgite, samples 8 to 10 represent pegmatoidal pyroxenite, and sample 11 represents feldspathic pyroxenite. The mineral false colours were changed from those initially represented in Figure 5.4 and 5.5 to match with the QEMSCAN field images data in Figure 4.3. Mini cores are 25 mm in diameter.

QEMSCAN mineral data were normalized to match the HSI data to facilitate comparison from the HSI mini cores with the QEMSCAN blocks characterised in Chapter 4. In this case, opaque minerals that do not respond with HSI (i.e., base metal sulphides, magnetite and chromite) are reported as

'unclassified' (Figure 5.9 and Figure 5.10). The relative error at 95% interval was calculated using the equation defined by Van der Plas and Tobi, (1950); which considers the number of mineral observations and the proportion of the mineral of interest. The relative error tables are in Appendix D, Table D5 and D6. Direct comparison of the reclassified HSI data against the QEMSCAN data shows that the data is comparable in terms of the minerals present, but not necessarily their modal abundance. HSI produced less information regarding the mineral assemblage compared to QEMSCAN, even when minerals from SWIR and LWIR are combined. The smaller error bars in QEMSCAN suggest that the data is more precise than HSI data having larger error bars. However, in the standard cores, precision is expected to be much better because more pixels are analysed at a larger surface area than in mini cores.

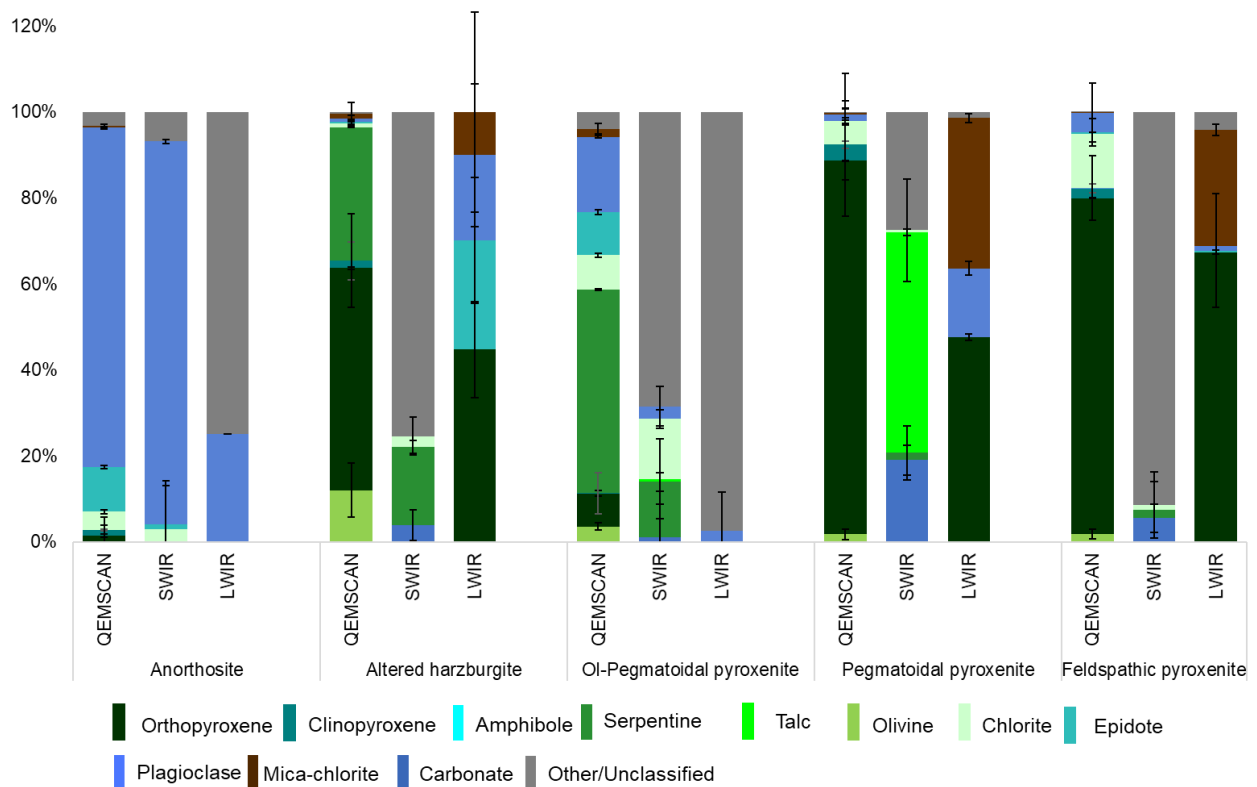


Figure 5.9: Mineral grades for the selected RD015 mini cores scanned with QEMSCAN and HSI after the spectral reclassification. QEMSCAN mineral grades for those minerals with no spectral response (base metal sulphides, magnetite and chromite) are shown as 'other/unclassified'. The errors bars represent the relative error at 2σ standard deviation.

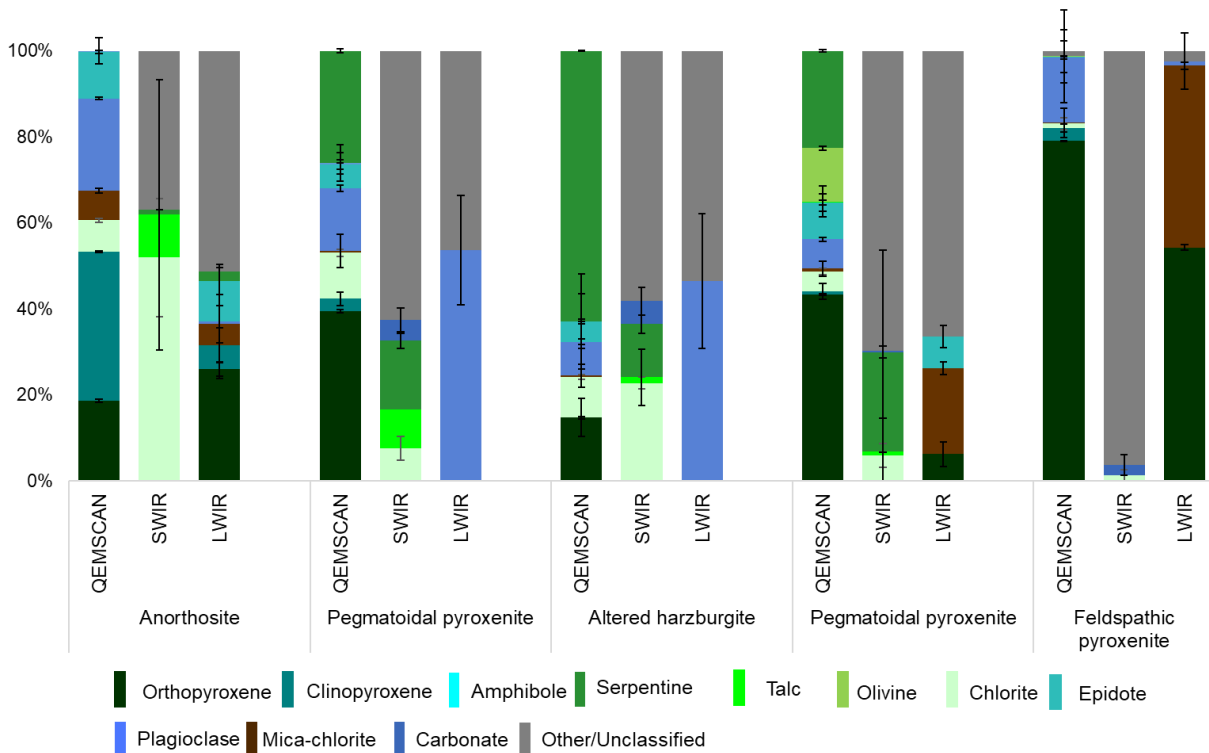


Figure 5.10: Mineral grades for the selected TU277 mini cores scanned with QEMSCAN and HSI after the spectral reclassification. QEMSCAN mineral grades for those minerals with no spectral response (base metal sulphides, magnetite and chromite) are shown as 'other/unclassified'. The errors bars represent the relative error at 2σ standard deviation.

Reclassified standard drill cores

The mini cores reclassification procedures used were then projected to the standard core to produce the reclassified mineral maps for drill core TU277 (Figure 5.11) and drill core RD015 (Figure 5.12). However, the difference in scanning parameters and minerals detected between the standard and mini cores resulted in some uncertainty for the reclassification in standard cores. The mini cores only represented a small area of the standard drill cores and were only scanned with SWIR and LWIR, compared to the standard cores that were scanned with VNIR-SWIR and LWIR. For example, most mini cores under SWIR are unclassified and less serpentine detected than in the standard cores.

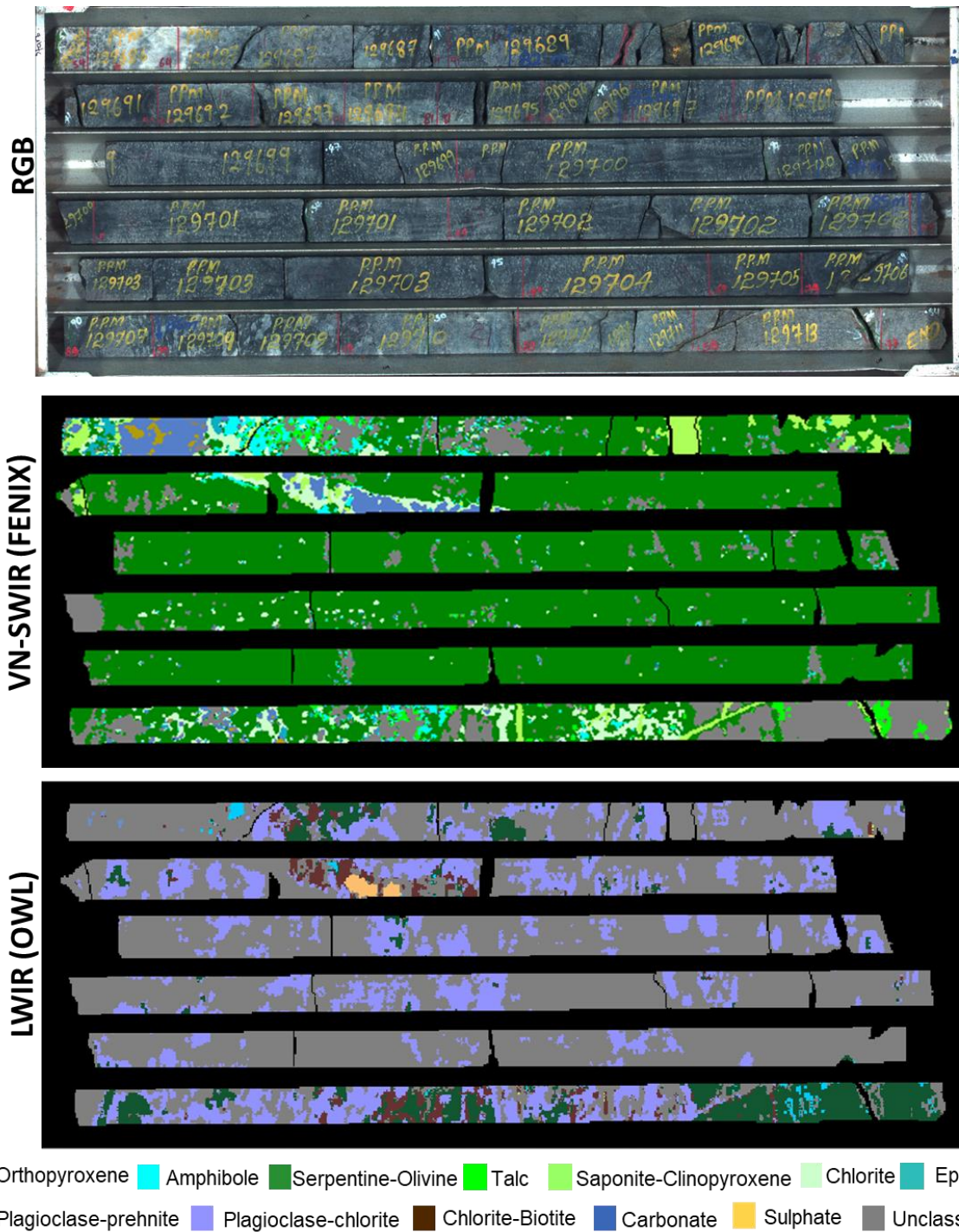


Figure 5.11: Drill core TU277- Reclassified hyperspectral mineral maps for VN-SWIR and LWIR spectral sensors scanned at 1.64 mm pixels. There is a lot of spectral mixing in LWIR. The mineral false colours were changed from those initially represented in Figure 5.1 and 5.2 to match with the QEMSCAN field images data in Figure 4.3. 50 mm core diameter.

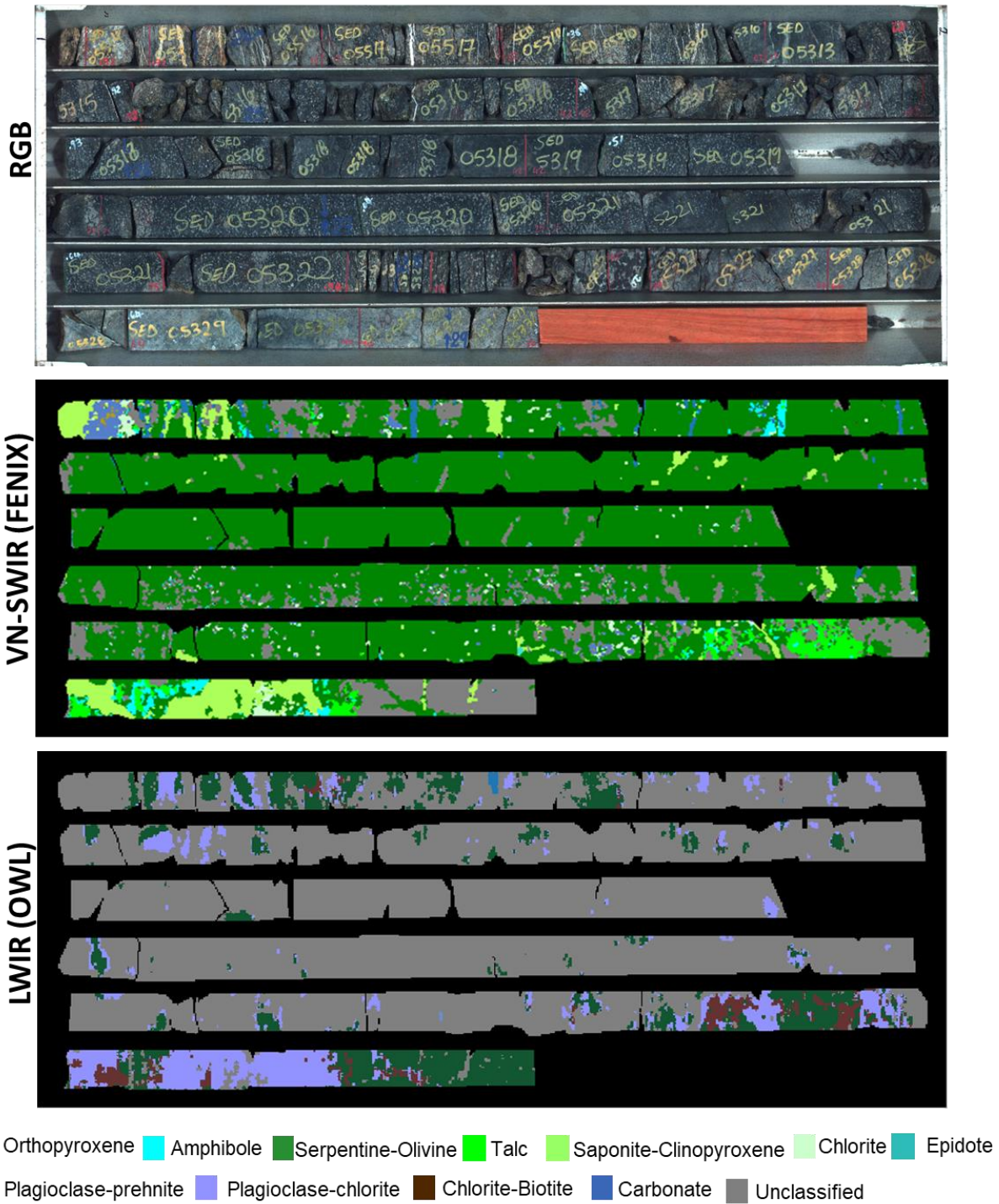


Figure 5.12: Drill core RD015- Reclassified hyperspectral mineral maps for VN-SWIR and LWIR spectral sensors scanned at 1.64 mm pixels. There are a lot of mixed phases in LWIR, e.g., chlorite-biotite. The false mineral colours have been changed from those initially represented in Figure 5.1 and 5.2 to match the QEMSCAN data. 50 mm core diameter.

5.1.4 Mineral texture

The HSI grain size data could not be automatically extracted from the hyperspectral software, like the QEMSCAN processing software. Therefore, the grain size distribution for HSI mineral maps was quantified using a script written for MATLAB (Appendix D, Figure D6 and D7). For direct comparisons, only cores where QEMSCAN data was available are shown here. Similarly, only the dominant minerals in the cores are presented in this section. For plagioclase, the GSD was extracted from the mixed-phase prehnite-plagioclase by SWIR and chlorite-plagioclase by LWIR spectra since HSI indirectly identified plagioclase (Figure 5.6 and Figure 5.8). Based on the resolution of the HSI scans, the minimum grain size was 1050 μm . Many interconnected grains could not be separated since mineral grain boundaries were not visible in the HSI maps. Therefore, only a few grains were generated with larger grain size values, resulting in the actual grain size being overestimated. Some grain sizes were not entirely representative of the entire core surface because they were not scanned due to curvature or tilting. i.e., only a limited area of the anorthosite and pegmatoidal pyroxenite were scanned (Figure 5.6 and Figure 5.8). The grain size distribution of the major minerals in different lithologies in drill cores TU277 and RD015 is given in Figure 13 and Figure 14, respectively. All the mineral grain size distributions presented are negatively skewed like the QEMSCAN derived grain size distribution (Figure 4.5 and Figure 4.9). The d50 for every mineral grain is also summarised in Tables 5.5 and 5.6; see Appendix D, Table D3 and D4 for more d50 tables.

For drill core TU277, the overall grain size distribution for olivine-serpentine in the altered harzburgite (Figure 5.14b and Table 5.6) and pegmatoidal pyroxenite matched the QEMSCAN data with medium and coarse-grain sizes, respectively. Also, orthopyroxene in the pegmatoidal pyroxenite and feldspathic pyroxenite was comparable to QEMSCAN data (fine and coarse-grained, respectively). However, the plagioclase in the anorthosite (Table 5.6) and chlorite-plagioclase are not comparable to QEMSCAN data, likely due to underestimation and overestimation of the minerals in the rock. The unscanned areas contribute to this matter.

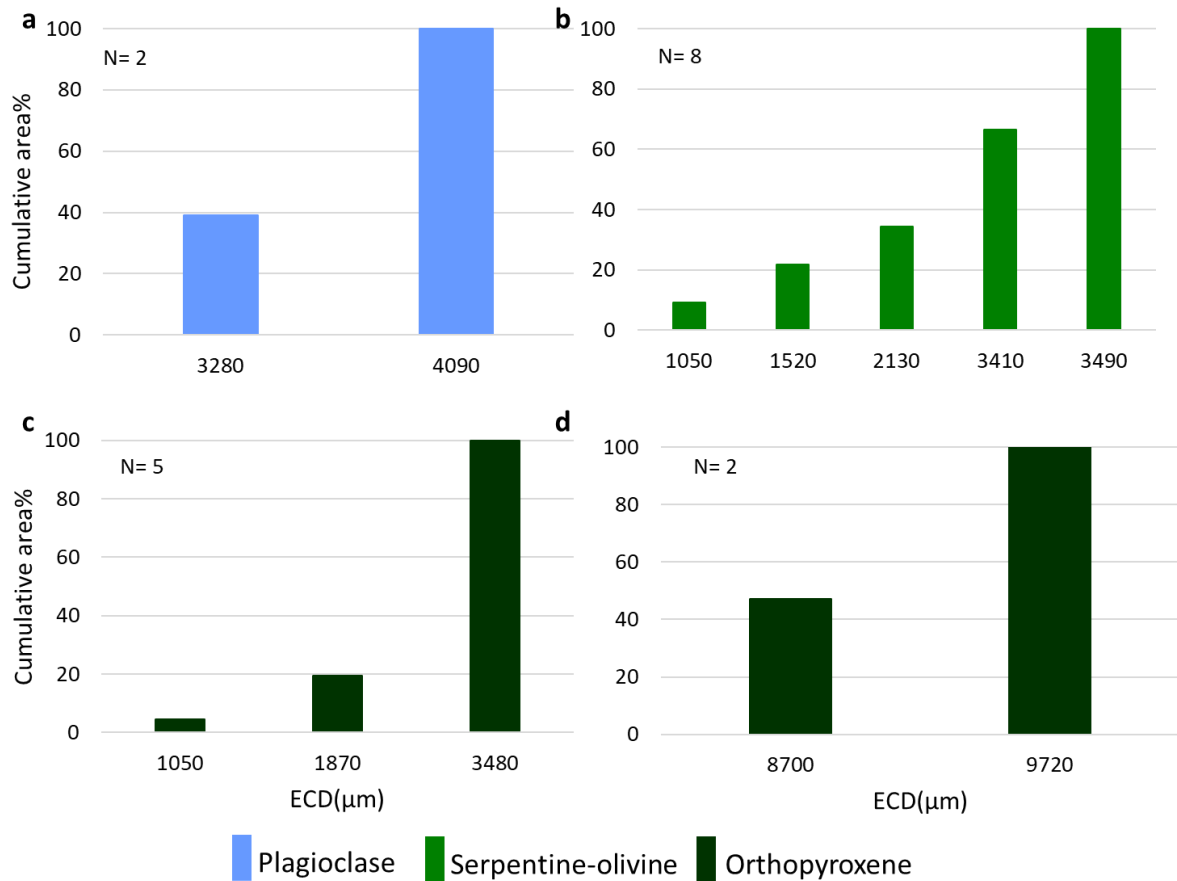


Figure 5.13: Grain size distribution for predominant minerals identified by HSI in drill core TU277. Selected minerals are presented: (a) Anorthosite, (b) Altered harzburgite, (c) Pegmatoidal olivine-pyroxenite and (d) Pyroxenite.

Table 5. 5: Summary table of the mineral median grain size (d_{50} , μm) determined using both SWIR and LWIR data from HSI compared with QEMSCAN for drill core TU277. The selected minerals are the common (predominant) minerals identified by both techniques. Minerals that do not respond under the specific sensor or interconnect minerals that gave only one value are annotated with a hyphen (-).

Rock type	Minerals	SWIR	LWIR	QEMSCAN N
Anorthosite	Prehnite-plagioclase	-	-	4526 (medium)
Altered harzburgite	Serpentine-olivine	5598 (coarse)	-	3806 (medium)
Pegmatoidal pyroxenite	Serpentine-olivine	2002 (medium)	-	2263 (medium)
	Prehnite-plagioclase	1434 (fine)	-	951 (very fine)
Pyroxenite	Orthopyroxene	-	9255 (coarse)	9051 (coarse)

For drill core RD105, the overall grain size classification for serpentine-olivine in the altered harzburgite, pegmatoidal pyroxenite, and orthopyroxene in the feldspathic pyroxenite matched the QEMSCAN data in terms of general grain size category but not the absolute value (medium and coarse-grained) (Figure 5.13b and d, Table 5.5). However, the HSI data likely overestimated the grain size for prehnite-plagioclase in the anorthosite and pegmatoidal pyroxenite (Figure 5.13a and c). The differences are likely due to intensive grain connectivity and the mixed mineral phases in HSI maps.

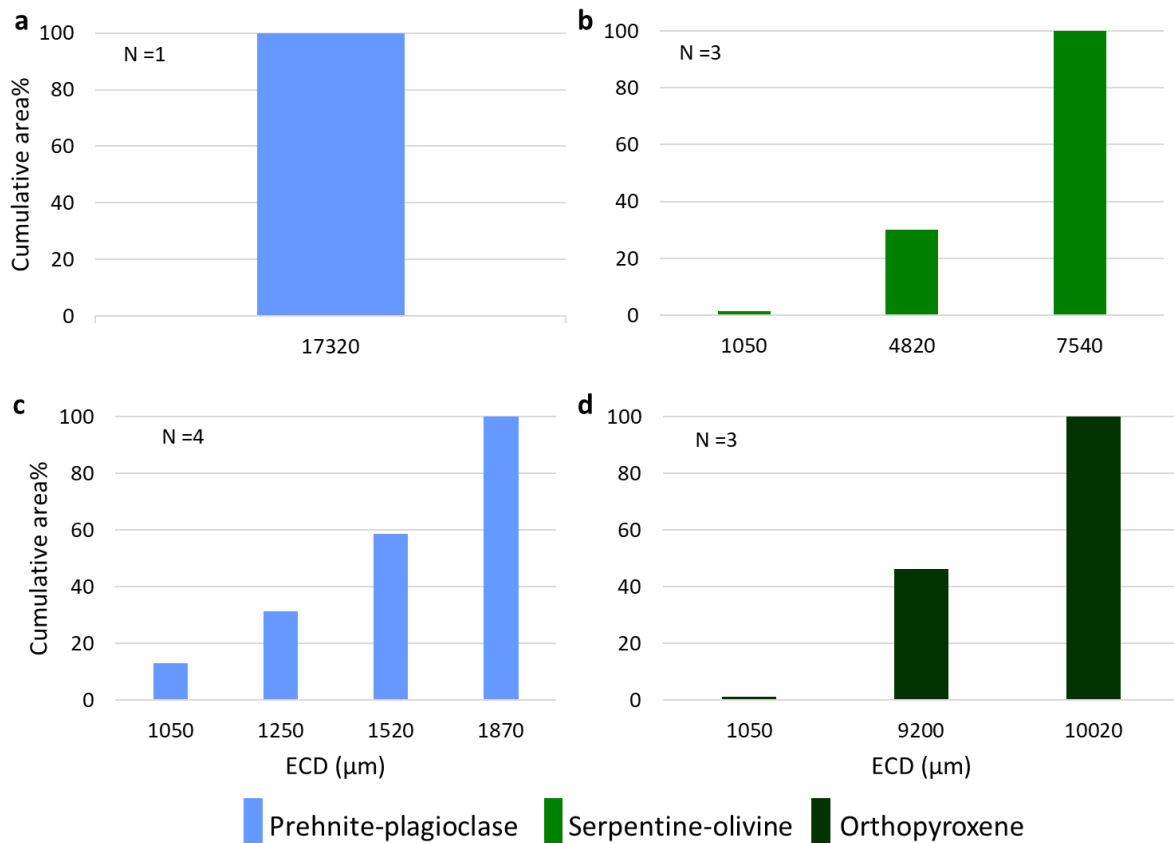


Figure 5.14: Grain size distribution for major minerals detected by HSI across various lithologies for drill core RD015. Selected minerals (or mixed mineral phases) are presented for the (a) Anorthosite, (b) Altered harzburgite, (c) Pegmatoidal olivine-pyroxenite and (d) Pyroxenite. The number of grains (N) analysed is also given.

Table 5.6: Summary table of the mineral median grain size (d_{50} , μm) determined using SWIR and LWIR data from HSI compared with QEMSCAN for drill core RD015. The selected minerals are the common (predominant) minerals identified by both techniques. Minerals that do not respond under the specific sensor or interconnected grains that gave only one value are annotated with a hyphen (-).

Rock type	Minerals	SWIR	LWIR	QEMSCAN
Anorthosite	Plagioclase (Anorthite)	-	3425 (medium)	1371 (fine)
Altered harzburgite	Serpentine-olivine	2754 (medium)	-	3805 (medium)
Pegmatoidal pyroxenite	Orthopyroxene	-	1904 (fine)	893 (very fine)
Pyroxenite	Orthopyroxene	-	8754 (coarse)	7933 (coarse)

5.2 X-ray computed tomography.

The mini cores scanned with HSI and QEMSCAN were also scanned with XCT. Previous studies have shown information provided by XCT to be insufficient to discriminate detailed the mineral assemblage, especially for minerals with similar or small attenuation coefficient differences. Therefore, mineral data obtained in chapter four were used to assist with the mineral identification and discrimination for XCT data. The summary of the minerals present in each lithology is given in Table 5.7.

Table 5.7: Summary of major minerals detected by QEMSCAN for each lithology in the drill cores.

Lithology	Silicates	Phyllosilicates	BMS and Oxides
Anorthosite	Plagioclase Clinopyroxene Orthopyroxene Epidote	Chlorite Biotite	Chromite BMS
Altered harzburgite	Orthopyroxene ±Clinopyroxene Olivine Plagioclase Epidote	Serpentine Chlorite ±Talc	Magnetite Chromite
Pegmatoidal pyroxenite	Orthopyroxene ±Clinopyroxene Plagioclase Epidote	Serpentine Chlorite Talc	Magnetite
Pegmatoidal olivine pyroxenite	Orthopyroxene Olivine Plagioclase Epidote	Serpentine Chlorite Biotite Talc	Magnetite Chromite BMS
Feldspathic pyroxenite	Orthopyroxene ±Clinopyroxene Plagioclase Olivine	Chlorite ±Talc	Chromite

The mini cores were scanned with XCT to produce grayscale volumes. This section presents the mini cores representing the lithologies observed in each standard core (Figure 4.1). Only a few mini cores are presented in the thesis and data for the rest are given in the appendix.

The effective linear coefficient was calculated for the major minerals identified in Chapter 4 (Table 5.2.1). The mineral effective linear attenuation coefficient was calculated based on ideal mineral chemical formulae and densities. These linear attenuation coefficients were calculated at an X-ray energy of 63.10 KeV from an input of 140 kV as used during scanning (see Section 3. 6) using the spreadsheet developed by Bam et al. (2020). Table 5.8 presents the calculated mineral attenuation coefficient for various mineral groups arranged according to their density.

Table 5.8: The simplified QEMSCAN bulk mineral assemblage is grouped based on the relative mineral densities to calculate the attenuation coefficient using Bam et al., 2020. Density information was obtained from various (Bam et al. 2020; <http://www.webmineral.com/>; Bartheemy, 2019; Molifé, 2021).

Mineral Groups		Minerals	Density (g/cm ³)	Attenuation coefficient (cm ⁻¹)
		Plagioclase	2.56	0.70
		Quartz	2.65	0.62
		Calcite	2.71	0.92
Silicates	Phyllosilicates	Serpentine	2.57	0.60
		Talc	2.75	0.63
		Chlorite	2.95	0.71
		Mica	3.09	0.94
		Orthopyroxene	3.27	0.75
		Clinopyroxene	3.40	0.99
		Olivine	3.32	1.52
		Apatite	3.19	1.36
		Amphibole	3.20	1.12
		Epidote	3.45	1.43
BMS		Chalcopyrite	4.20	3.78
		Pyrrhotite	4.61	3.56
		Pentlandite	4.80	4.40
Oxides		Chromite	4.79	3.32
		Magnetite	5.18	4.14
PGMs		Sperrylite	10.58	31.65
		Ferroplatinum	14.3	45.12

Both drill cores have similar minerals in their different rock types; therefore, both cores' grey value discrimination and validation will be similar. All the rock types represented in these cores contain about nineteen minerals detected by QEMSCAN, and only three to four grey value ranges have been observed in the XCT volumes. Most minerals have similar grey values resulting in poor discrimination. The most reflecting minerals are usually the high-density phases (Stapley et al., 2016; Voigt et al., 2020), which is evident by the differences in attenuation coefficient calculated in Table 5.8.

5.2.1 Phase segmentation

Mineral phases with different grey values and attenuation coefficients in Table 5.8 from each drill core were segmented using histogram and region growing in VG Studio 3.3.2 to select the region of interest (ROI). The segmentation method varied for each core and sometimes for phases in the same core. A histogram provides a distribution of grey values and their frequency (counts) constituting the core (Figure 5.15). The phases with similar grey values (attenuation coefficient) were selected and segmented to create regions using volume rendering. However, some cores could not be segmented properly due to the partial volume effect. The effect is caused by the high-density minerals being

favoured over the less density minerals. This creates a high attenuating blended phase between the two minerals, marked as an issue during segmentation due to the overestimation of grey values. The 'region growing' is one of the segmentation methods applied using a point selection (on the phase of interest) to grow boundaries around phases of similar grey values. This method allowed for mineral separation and limited the overestimation of regions. False colours were applied to differentiate between the segmented phases (Figure 5.16).

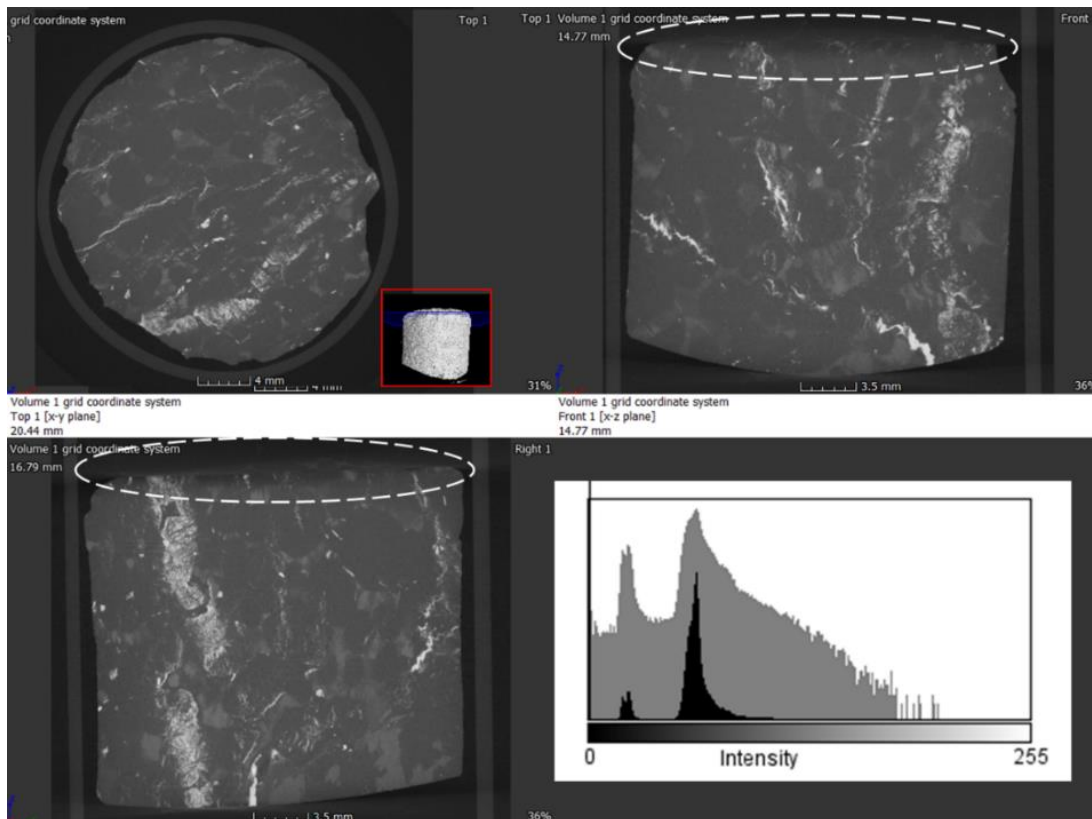


Figure 5.15: Different views of the core in VG studio, showing the uppermost slices exposed to air and touched by styrofoam in the 3D volume scanned with XCT. Stippled lines indicated the section that was exposed to air. The mini core is 25 mm in diameter.

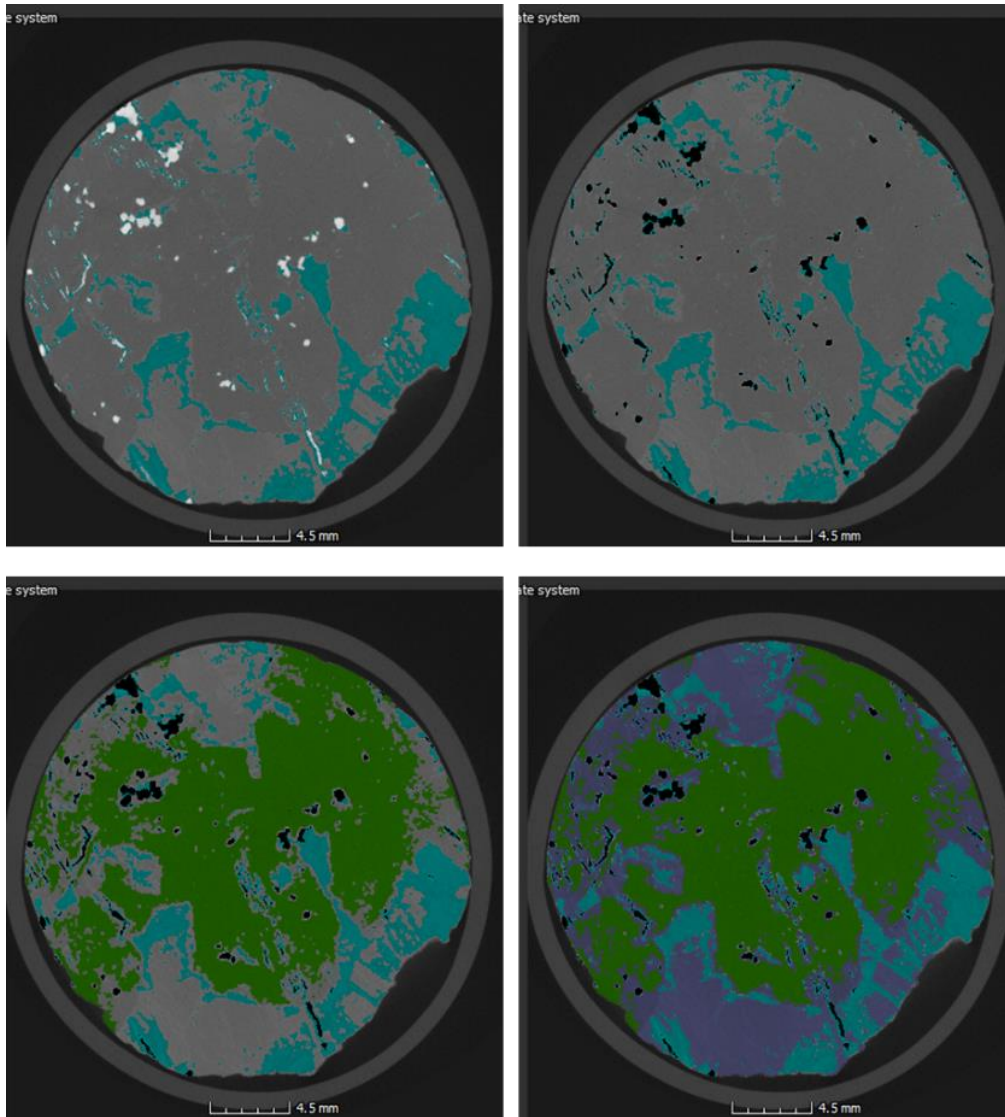


Figure 5.16: An illustration of phase-to-phase segmentation in the core with different regions colour coded for easier discrimination (pegmatoidal olivine-pyroxenite-TU277). The images illustrate the segmentation from one grey value range (top left) to the next until all phases (bottom right) in the cores are segmented. The mini core is 25 mm in diameter.

For accurate segmentation and comparison purposes with the same surface characterised with QEMSCAN, the uppermost slices from the XCT volumes were targeted. This entailed removing the first few XCT slices of the cores due to their interaction with the air (Figure 5.15). The effective comparison started with slices 99 to 200 from a total of 1100-1400 image slices (each slice was 20 μm thick), depending on the rock type and volume. Given the coarser nature of the mineral grains in these cores (Figure 4.5 and 4.9), similar slices matching the QEMSCAN images were observed.

5.2.2 Mineral Identification

The rock-forming minerals in these cores are similar but differ in their association, abundance, and grain sizes. The order in which the minerals are grouped (from lowest to highest grey value) is similar, although the grey value ranges and cut points vary in each rock type. The backscattered electron (BSE) images from QEMSCAN (see Appendix E-Figure E2 and E3) also assisted with the identification.

Drill core TU277

Three to five grey value ranges were observed in the mini cores of the drill core TU277. The anorthosite had few disseminated brighter phases (at a grey value range of 165 to 252) and an abundance of silicate minerals characterised by different shades of darker phases indicating alteration. In QEMSCAN field images, these layers indicate the alteration assemblage of orthopyroxene-clinopyroxene-chlorite (Figure 4.3 and Figure 5.17a). Plagioclase and orthopyroxene have the darkest grey value (ranging from 52 to 103). Clinopyroxene was differentiated from orthopyroxene and epidote with an attenuation coefficient difference of 28 and 31%, respectively (Table 5.8). However, looking closely at Figure 5.17a, epidote and clinopyroxene have similar grey values and this required an extensive segmentation process to discriminate these minerals. According to Bam et al. (2020), minerals with an attenuation coefficient difference greater than 6% can be discriminated.

Figure 5.17b displays a chromite stringer and the Fe-oxide veins cross-cutting the rock. According to the attenuation coefficient calculated in Table 5.8, magnetite was expected to attenuate brighter than chromite with an attenuation difference of 22%. However, due to partial volume effects caused by the presence of variable high attenuating minerals these minerals could not be properly differentiated. The vein or mineral crosscutting the magnetite shows a similar grey value to magnetite but with high attenuating rims (Figure 5.17b). According to QEMSCAN, this vein is composed of variable BMS; the high attenuating BMS with a maximum grey value of 255 at the rims is pentlandite with the attenuation coefficient of 4.0 cm^{-1} . However, the fine-grained pentlandite inclusions in the chromite cannot be identified even with a 28% attenuation difference (Figure 5.17b).

The abundance of high-density phases: chromite stringer, magnetite and BMS, blurs the low density (silicate) minerals present in the core, affecting their grey values and leading to poor discrimination. For example, plagioclase and chlorite grey values overlapped with serpentine-orthopyroxene; although, they were expected to be differentiated as in the altered harzburgite (Figure E2 in the appendix). Only epidote was discriminated from plagioclase-chlorite and serpentine-orthopyroxene due to its higher attenuation coefficient (Figure 2.17b). However, the plagioclase-chlorite and epidote association were not visible when they were in close contact with BMS, usually pentlandite (Figure 2.17b). The fine-grained orthopyroxene associated with serpentine appears darker within the grey value range of 52 to 76. Away from the high-density phases, serpentine-orthopyroxene was differentiated from pure orthopyroxene (Figure 5.17b).

Like other cores, epidote was discriminated from plagioclase and chlorite in the pegmatoidal olivine-pyroxenite (Figure 5.17c), while chlorite and plagioclase were grouped within the grey value range of 94 to 114. The larger grains in the middle of the sample are set within the grey value range of 52 to 94— the grains identified are composed of fine-grained orthopyroxene-olivine-serpentine assemblage by QEMSCAN (Figure 4.3d). QEMSCAN field images showed serpentine to be intimately associated with fine-grained olivine and orthopyroxene. The attenuation difference between serpentine and orthopyroxene was 79% and between serpentine and olivine was 27% (Table 5.8) although, they could not be discriminated. However, the pure-coarser orthopyroxene appears lighter and was discriminated from the orthopyroxene-olivine-serpentine assemblage (Figure 5.17c). The high attenuating sub-rounded grains distributed within the dark phase (orthopyroxene-olivine-serpentine) with grey values between 140 to 255 were identified as chromite.

The feldspathic pyroxenite is composed of abundant darker grey values and very few high attenuating grains (Appendix E, Figure E2). The elongated minerals are orthopyroxene, hosted within a darker matrix (ranging between grey values of 55 and 83). QEMSCAN has reported the presence of quartz. The attenuation coefficient difference between quartz and plagioclase is 31% but only one grey value is observed since quartz is minor in abundance relative to the plagioclase.

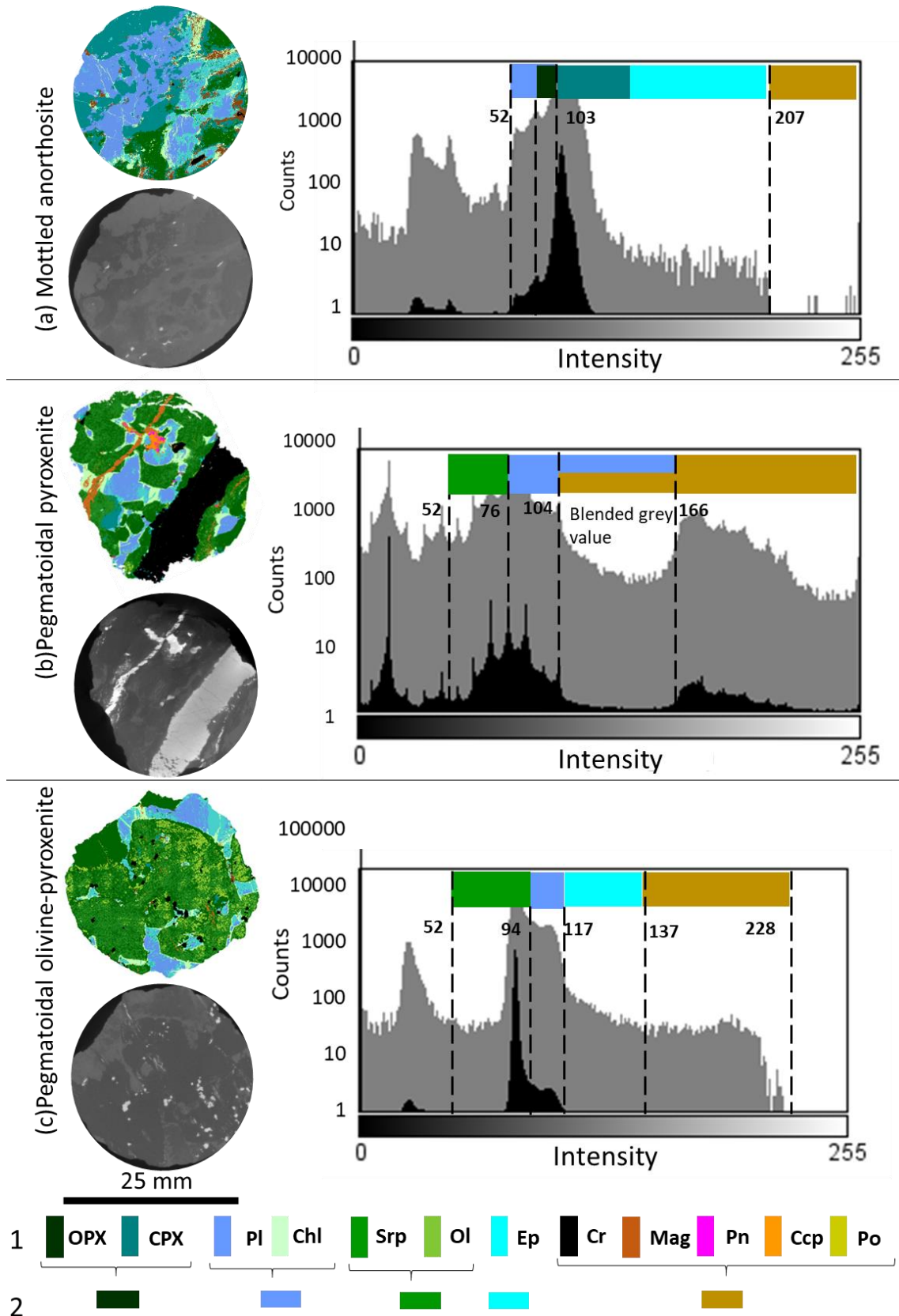


Figure 5.17: The illustration of XCT image slices with corresponding grey value range histogram for selected rock types: (a) Pegmatoidal pyroxenite and (b) pegmatoidal olivine-pyroxenite, from drill core TU277. QEMSCAN false colour compositional field images for similar slices are used for direct mineral identification in each slice. 1-QEMSCAN legend and 2- XCT grouping. Mineral abbreviations from Whitney and Evans, (2010).

Drill core RD015

Similar to drill core TU277, three to five grey value ranges were observed in the mini cores of this drill core. The anorthosite of the drill core RD015 is dominated by a darker grey value phase (at a range of 50-78) with high attenuating grains (grey values > 175) appearing in a linear form (Figure 5.18a). These grains were identified as chromite stringers by QEMSCAN. The fine grains in the centre of the image slice that attenuate more than the chromite were identified as disseminated BMS (pentlandite, chalcopyrite and pyrrhotite) with QEMSCAN. Pentlandite has the highest attenuation coefficient of 4.40 cm^{-1} (with a difference of 21-30 % from other BMS and chromite) (Table 5.8), suggesting the higher attenuating grains to be pentlandite. Also, plagioclase is associated with chlorite and epidote, according to the QEMSCAN field images (Figure 4.3). Plagioclase and chlorite have similar grey values within the range 50 and 78. The grey phase (at a range of 78-138) seen in the XCT histogram (Figure 5.18a) is interpreted as epidote because the attenuation coefficient is almost twice the value of other silicates present (plagioclase, chlorite, and orthopyroxene).

The feldspathic pyroxenite (Figure 5.18b) and pegmatoidal pyroxenite (Appendix E, Figure E3) resemble similar grouping to anorthosite due to minor alterations (i.e., limited serpentine and talc present). The plagioclase and chlorite are grouped together but at different cut points because of the difference in the mineral's abundance (i.e., more plagioclase and chlorite in the feldspathic pyroxenite). These rock types contain orthopyroxene grains (according to QEMSCAN and XRD) that can be differentiated from plagioclase and chlorite with an attenuation coefficient difference of 9-22%. The grey value range for orthopyroxene varies from 85-101 in feldspathic pyroxenite to 64-92 in pegmatoidal pyroxenite. In both cores, highly attenuating minerals are very fine-grained and disseminated throughout the core, interpreted as chromite according to QEMSCAN.

In the altered harzburgite, serpentine takes the first range of grey values of 47 to 93. Due to the intimate association olivine was not differentiated from serpentine. Similar to the pegmatoidal olivine pyroxenite (Figure 5.17c), the less altered coarse-grained orthopyroxene was discriminated from the serpentine-olivine group. Also, the fine grained-plagioclase, chlorite and biotite were grouped with serpentine and olivine. Observed from QEMSCAN field images (Figure 4.7), biotite is fine-grained and associated with chlorite and plagioclase having an attenuation coefficient difference of 10 and 28%, respectively. The orthopyroxene and clinopyroxene in the altered harzburgite have a grey value range of 93 to 156 (Figure 5.18c) and could not be separated due to the less abundant and fine-grained nature of clinopyroxene compared to the anorthosite of drill core TU277 (Figure 5.17a). Compared to any other rock, this rock contains a high abundance of serpentine as the major mineral. The high attenuating mineral associated with the serpentine has a maximum grey value of 224, similar to feldspathic pyroxenite. This mineral is either magnetite or chromite, depending on the texture. The vein-like minerals are usually magnetite, and irregular grains are chromite.

The dominant grey value range in the pegmatoidal olivine pyroxenite is between 46 – 80 and represents the minerals serpentine, olivine and orthopyroxene. Like the altered harzburgite, serpentine can be differentiated from orthopyroxene but not olivine. Similar to other rocks, epidote was differentiated from

plagioclase-chlorite. However, plagioclase-chlorite and epidote were grouped during segmentation due to their association with high-density minerals that caused the partial volume effect. The high attenuating minerals (at a grey value range of 150 to 243) appear as lenses, veinlets and irregular to sub-rounded grains distributed in the sample, identified as chromite and magnetite. These minerals can be discriminated against, but their grey values overlap. i.e., chromite grey level ranges from 106 to 170 and magnetite from 150 to 243.

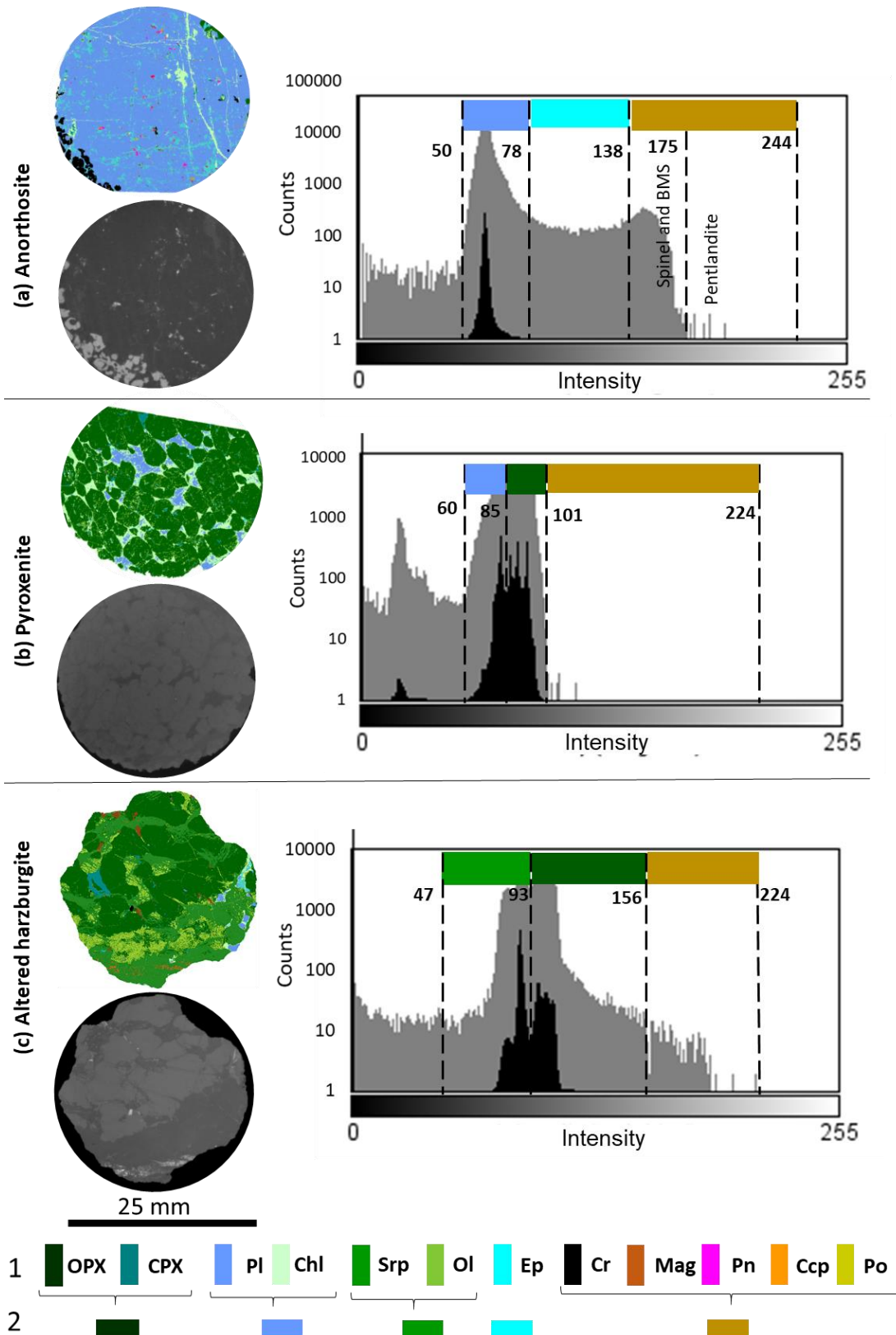


Figure 5.18: The illustration of XCT image slices with corresponding grey value range histogram for selected rock types in drill core RD 015: (a) Anorthosite, (b) Pyroxenite, and (c) Altered harzburgite. QEMSCAN false colour compositional field images for similar slices are used for direct mineral identification in each XCT slice. The y-axis is plotted with actual numbers (black) and a log scale (grey). 1-QEMSCAN legend and 2- XCT grouping. Mineral abbreviations from Whitney and Evans, (2010)

Mineral groupings after segmentation and identification were colour coded to match with QEMSCAN field images. Figure 5.19 and Figure 5.20 are the images obtained after applying the object rendering colour-changing window using volume rendering. See appendix E for colour-coded volumes.

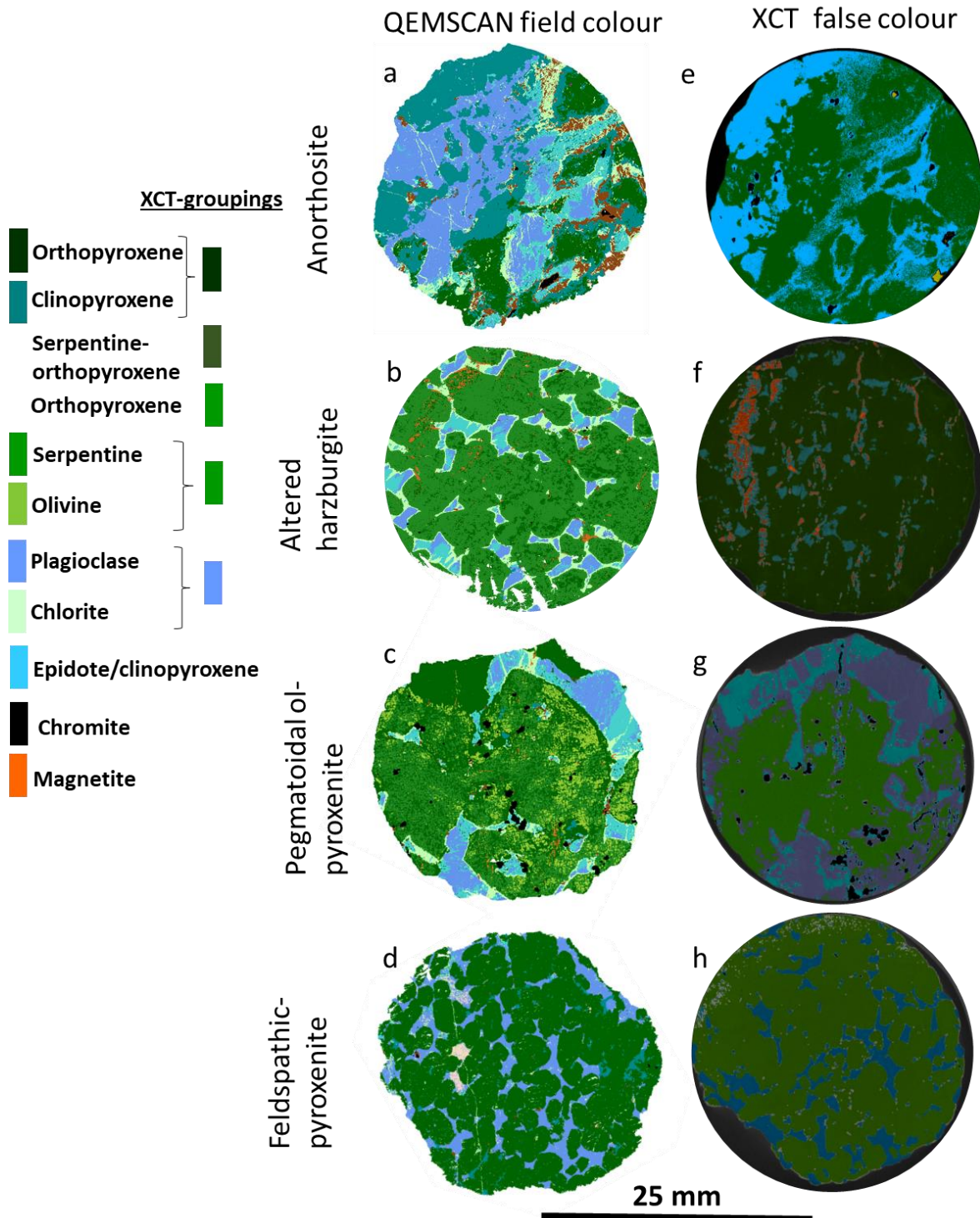


Figure 5.19: Drill core TU277-The comparison between the false-colour XCT image slices (e-h) after mineral segmentation with QEMSCAN false colour field images (a-d). NB. Mineral colours in XCT are not constant.

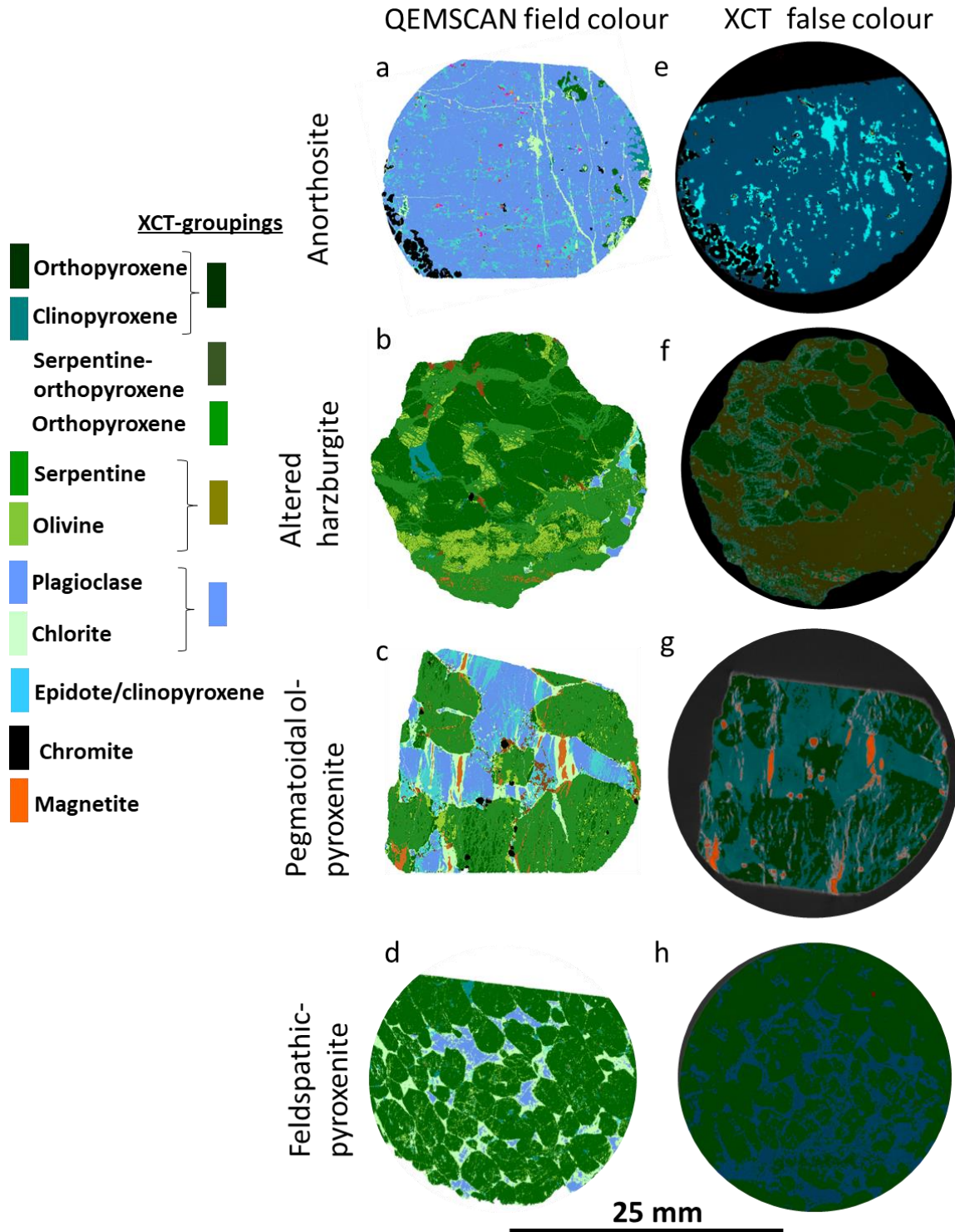


Figure 5.20: Drill core RD015-The comparison between the false-colour XCT image slices (e-h) after mineral segmentation and identification with QEMSCAN false colour field images (a-d). NB. Mineral colours in XCT are not constant.

5.2.3 Mineral grades and texture

The mineral segmentation enabled the extraction of the volume percentage for all the grouped minerals. The volume percentages for each phase were extracted and plotted against the QEMSCAN area

percentage (Figure 5.21 and 5.22) for drill cores RD015 and TU277, respectively. The QEMSCAN mineral grades were regrouped and normalized according to the XCT mineral groupings to facilitate the comparison. In some instances, comparison of the mineral assemblage from XCT with QEMSCAN is good (Figure 5.21a and 5.22a), and for others, less so (Figure 5.21c and 5.22c). This degree of agreement in the comparison was due to the sampling effect (i.e., comparing a volume to a surface) likely due to the coarse-grained nature of the samples and lithology dependent, e.g., comparisons are suitable for the anorthosite but not for mafic rocks (altered harzburgite, pegmatoidal pyroxenite and pyroxenite). The difference in the mafic rocks is due mainly to the degree of mineral alteration present in these rocks; for example, olivine-serpentine, orthopyroxene-serpentine and plagioclase-chlorite-epidote alteration. QEMSCAN was able to differentiate between the individual altered and unaltered minerals present in the core. However, the percentage of the more attenuating phases (i.e., oxides and BMS) was directly comparable across the two methods. The relative error bars for QEMSCAN are larger compared to the number of voxels obtained in XCT data because the number of pixels in QEMSCAN slices were less compared to the XCT data conducted on the entire volume. This implies that XCT mineral grades are more precise.

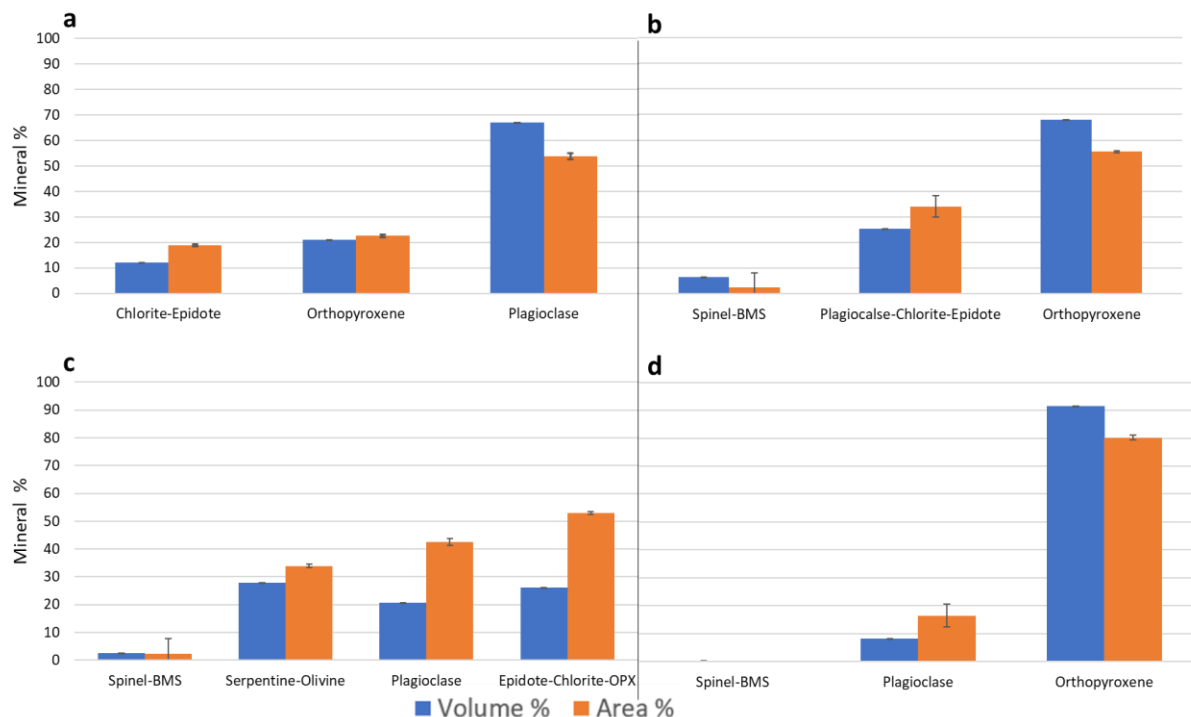


Figure 5. 21: Drill core TU277-QEMSCAN mineral grades grouped according to the XCT mineral grouping obtained by mineral segmentation. QEMSCAN data reported is area percent and XCT in volume percent. All rock types are presented: (a) anorthosite, (b) altered harzburgite, (c) pegmatoidal pyroxenite and (d) feldspathic pyroxenite. The graphs are plotted with relative error at a 95% confidence interval.

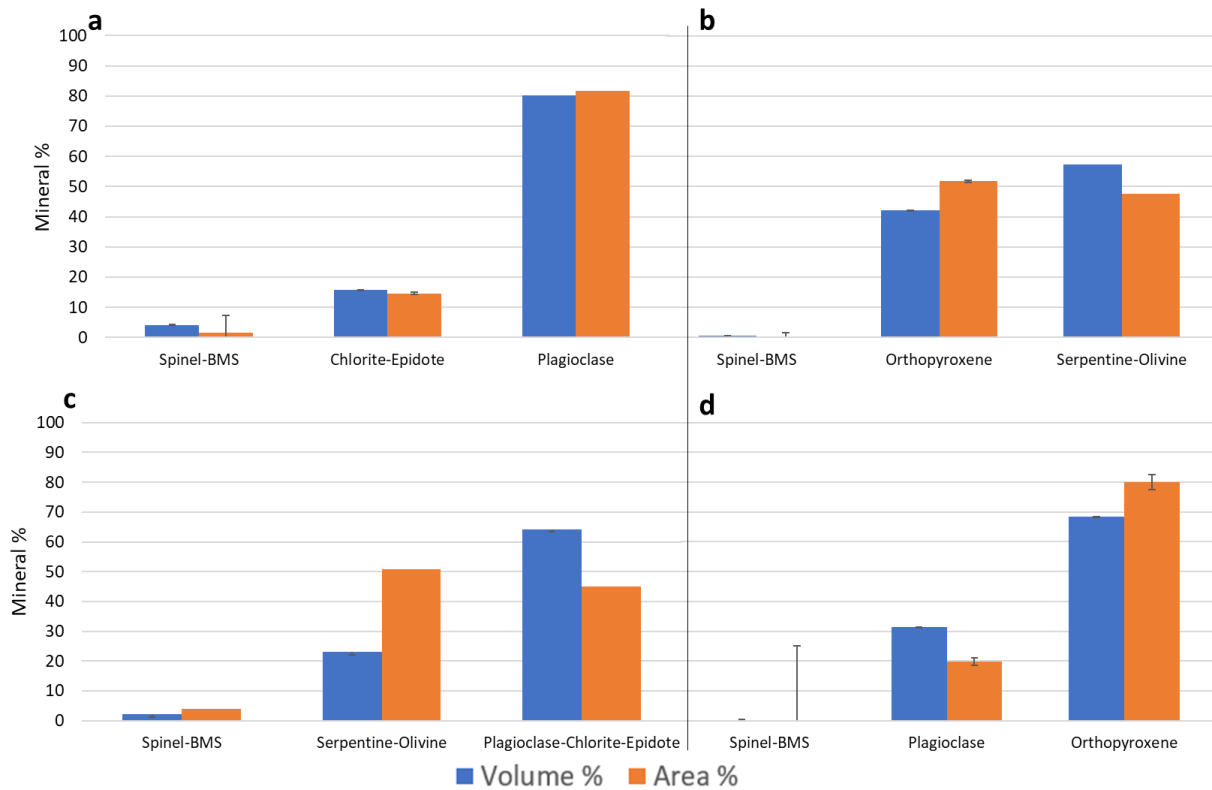


Figure 5.22: Drill core RD015-QEMSCAN mineral grades grouped according to the XCT mineral grouping obtained by mineral segmentation. QEMSCAN data reported is area percent and XCT in volume percent. All rock types are presented: (a) anorthosite, (b) altered harzburgite, (c) pegmatoidal pyroxenite and (d) feldspathic pyroxenite. The graphs are plotted with relative error at a 95% confidence interval.

Mineral texture

Besides the well-defined internal structure provided by XCT images, the phase segmentation allowed for the simple textural analysis of the GSD. The defect analysis function was applied to each segmented phase to extract additional information using VG Studio software. The parameters extracted included: volume, maximum diameter, voxel, and greyscale for every grain in the sample. The extracted volume was used to calculate the equivalent diameter for each grain present in the core. The volumes are grouped according to a colour scale from the smallest to the largest in the image viewer (Figure 5.23, Appendix E, Figure E7). The 3D grain size distribution obtained with the XCT was compared with 2D QEMSCAN determined grain size distribution (Figure 5.24 and Figure 5.25).

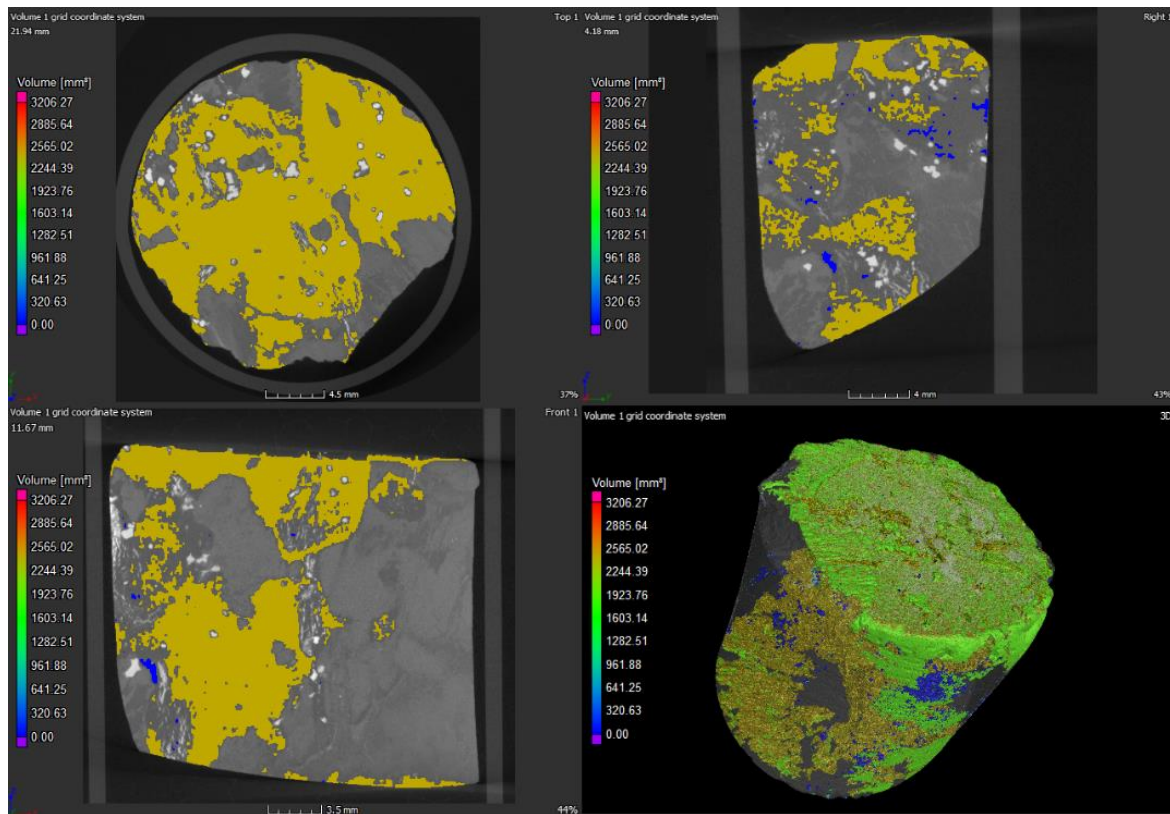


Figure 5. 23: The serpentine grain sizes in pegmatoidal olivine pyroxenite grouped according to a volume colour scale, demonstrated in 3 sections and volume. The volume is calculated in mm^3 .

Grain sizes obtained from 3D volumes are coarser than the grain size obtained from 2D QEMSCAN (Figure 5.24 and 5.25). The latter is different when the erode and dilate function was applied to separate interconnected grains, for example, orthopyroxene (Figure 5.24b). Using this function, grains were successfully separated on the orthopyroxenes hosted by the altered harzburgite and feldspathic pyroxenite. However, the function cuts over the grain boundaries and excluding some grains led to over underestimation (Appendix E-Figure E4). The grain separation was also conducted on the orthopyroxenes in the QEMSCAN field images. Both curves show a smooth curve (Figure 5.24 and Figure 5.25). 2D QEMSCAN results are underestimated because of stereology and do not reflect the true grain size because of the grain size and shape variations throughout the drill core; 3D XCT results are more representative since the analysis is performed on the volume and more grains are considered.

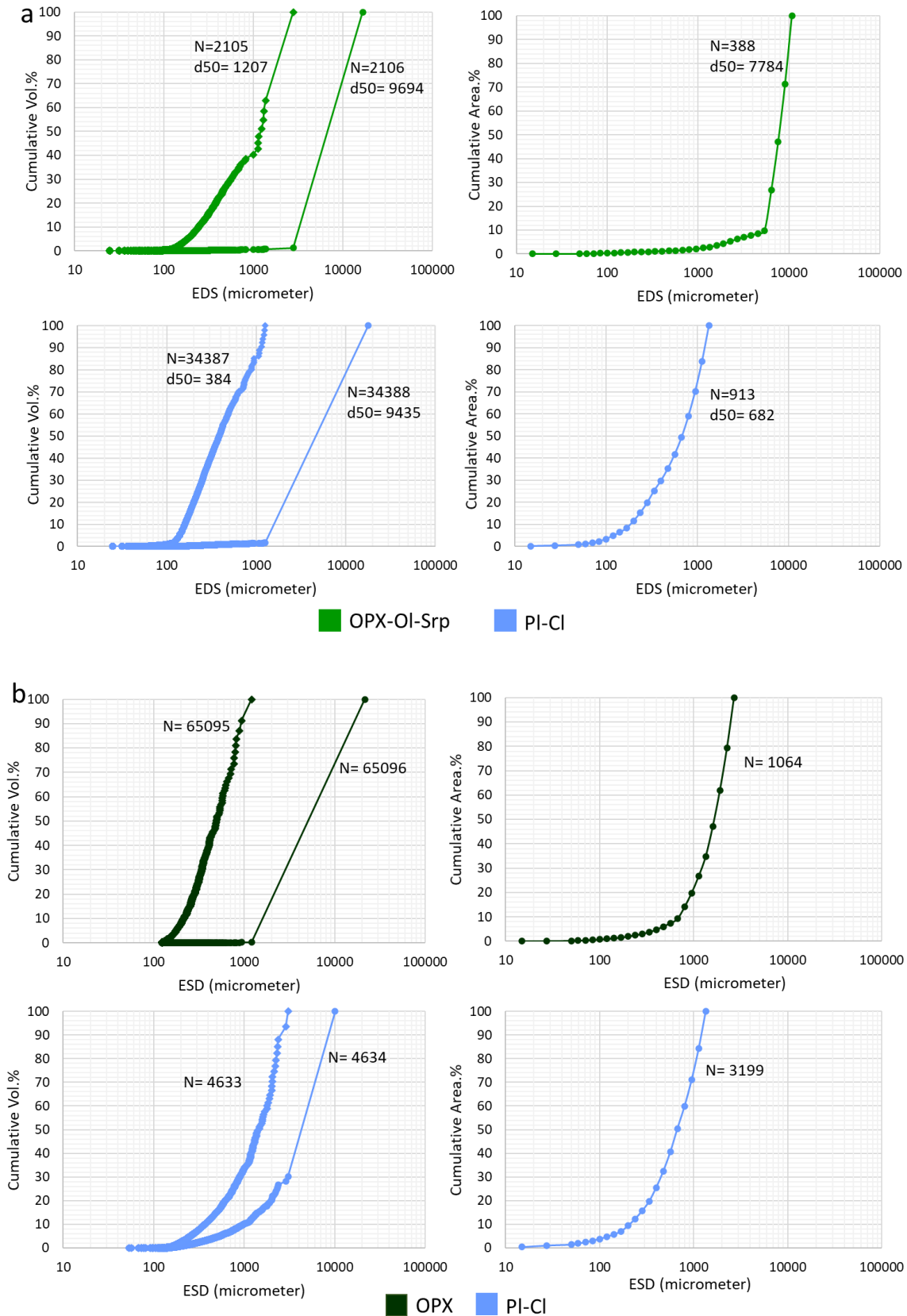


Figure 5.24: Grain size distribution of 3D XCT ESD (left) and 2D QEMSCAN ESD (right) for rocks types in drill core TU277: (a) Pegmatoidal pyroxenite and (b) Feldspathic pyroxenite grain distribution. ESD-Equivalent spherical diameter. The XCT is plotted with (circular-shaped) and without (diamond-shaped) the maximum grains.

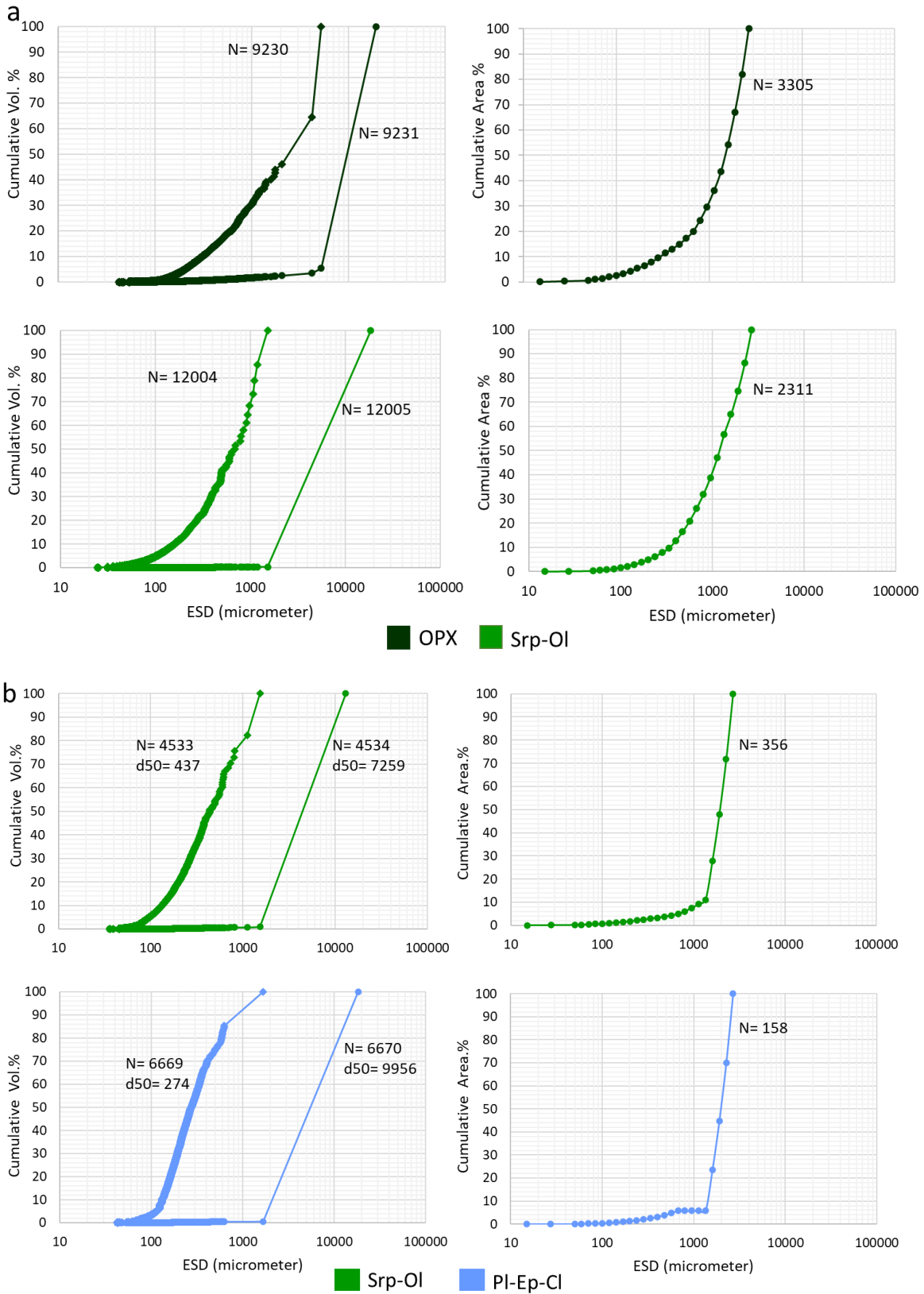


Figure 5.25: 3D XCT and 2D QEMSCAN minerals grain size distribution for rocks types in drill core RD015. (a) altered harzburgite, the erode-dilate function was applied to serpentine-olivine grains. (b) Pegmatoidal pyroxenite. ESD-Equivalent spherical diameter. The XCT is plotted with (circular-shaped) and without (diamond-shaped) the maximum grains.

5.2.4 3D Volume visualization

The 3D volume visualization allows for characterization from different views and the sample's internal structure to eliminate stereological errors associated with 2D surfaces. This allowed for 2D slice images matching with QEMSCAN to be extracted for direct mineral identification. However, minerals for grey values in XCT slices were identified on the 2D slices using QEMSCAN as the supporting technique. The fact that XCT is a 3D volume technique cannot be ignored.

The 2D surface visualization does not always represent a 3D volume unless in homogenous or less complicated samples. Cores in this study are heterogeneous; especially given the coarser nature of their mineral grains as determined in chapter four. Nevertheless, the surface slices were projected a few slices down (depending on the core) into a volume for a rough 3D representation. However, the projection was somewhat easier for high-density minerals, primarily where ore minerals are disseminated or have variable textures throughout the core. Identifying high-density minerals 2D auto-SEM-EDS techniques may be time-consuming, requiring multiple slice selection and preparation. Also, since HSI is also a 2D and high-density minerals do not show spectral features, PGMs cannot be identified. In this case, the use of X-ray CT can be time effective. Highly attenuating minerals can be targeted and located on 3D-XCT volumes for auto-SEM-EDS slice preparations and mineral identification (Butcher, 2020; Godel, 2013; Wang et al., 2014).

Figure 5.26 shows the core volume (pegmatoidal pyroxenite) used to determine the appropriate scanning parameters. The core displayed a few highly attenuating minerals brighter than BMS, chromite or magnetite. These brighter grains were segmented from BMS and other minerals present. The grains (in red) are nugget shaped and disseminated in the BMS and may potentially represent valuable PGMs (Ballhaus and Sylvester, 2000; McCall, 2016).

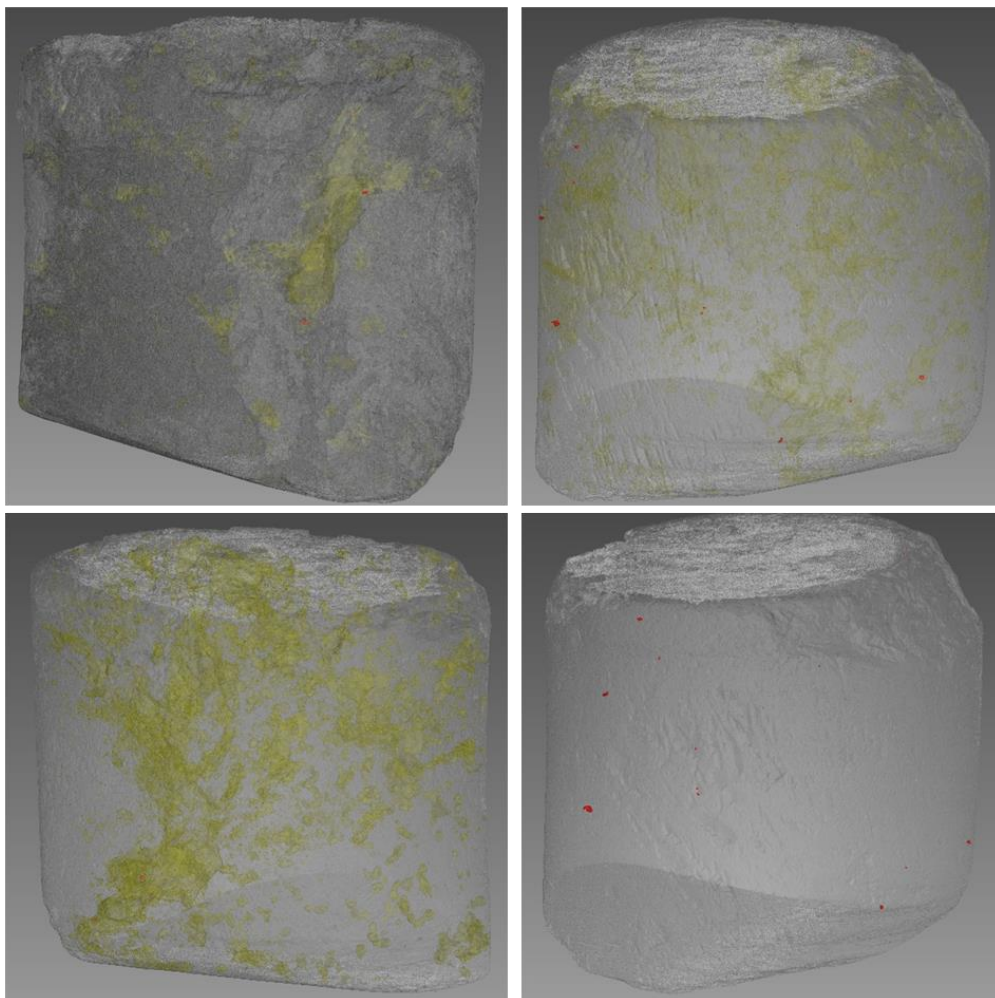


Figure 5.26: 3D view of the LPR pegmatoidal pyroxenite of (Drill core TU277) with segmented BMS (yellow) and possible PGM (red).

5.3 Image overlapping

Extended image overlapping was conducted on the output images from HSI and XCT slices. The overlap was conducted for different sensors on HSI with XCT slices. Since HSI scans the core surface, the uppermost XCT slices were targeted (see section 5.2). As outlined in chapter 5.1, it was apparent that HSI identified only silicates and carbonates, whereas silicates and BMSs were identified by XCT (with poor discrimination). Conceptual examples for possible overlapping outcomes were determined based on each technique's mineral responses—three scenarios for overlapping HSI on XCT and one for XCT on HSI were identified.

Possible overlapping scenarios:

1. Good grey values discrimination in XCT with poor mineral discrimination (mixed phases) in HSI.
2. Poor discrimination in XCT due to less than 6% difference in attenuation with good minerals discrimination in HSI.
3. Similar attenuation coefficient in XCT and mixed spectral phases in HSI.

The first scenario was using the XCT data to assist in distinguishing between the mixed spectra in HSI. The example demonstrating this scenario was the unclassified areas in HSI with minerals having variable grey values in XCT. In this case, XCT will provide more information in terms of minerals present and mineral texture such as mineral association, particularly between sulphides and silicates (Figure 5.27A, B and C).

Figures 5.27B and 5.27C illustrate scenario two. The second scenario is the opposite of scenario one in the case where BMS have been identified in XCT. The ideal example is the core with chromitite stringers. The poor discrimination of silicate minerals was influenced by the abundance of high-density phases (chromite, magnetite and BMS) in XCT, and HSI identified the silicate minerals (orthopyroxene, serpentine and plagioclase-chlorite). However, the stringers were not detected in HSI because it does not have any spectral response. The second possible example would be net textured orthopyroxene and serpentine. In XCT, these minerals cannot be discriminated but are identified separately in SWIR (serpentine) and LWIR (orthopyroxene) (Figure 5.27C).

The latter can also be the third scenario when there is unaltered orthopyroxene with serpentine (forming from olivine). In this case, orthopyroxene, serpentine and talc can be distinguished in XCT and HSI (Figure 5.27D and E). The mixed spectra identified in HSI and the mineral grouping in XCT are mostly similar. For example, olivine was not detected in HSI but serpentine. QEMSCAN field images identified the pervasive alteration of olivine by serpentine. Also, serpentine and olivine cannot be discriminated against in XCT. This is a similar case with plagioclase-chlorite, grouped in XCT and identified as mixed spectra in HSI.

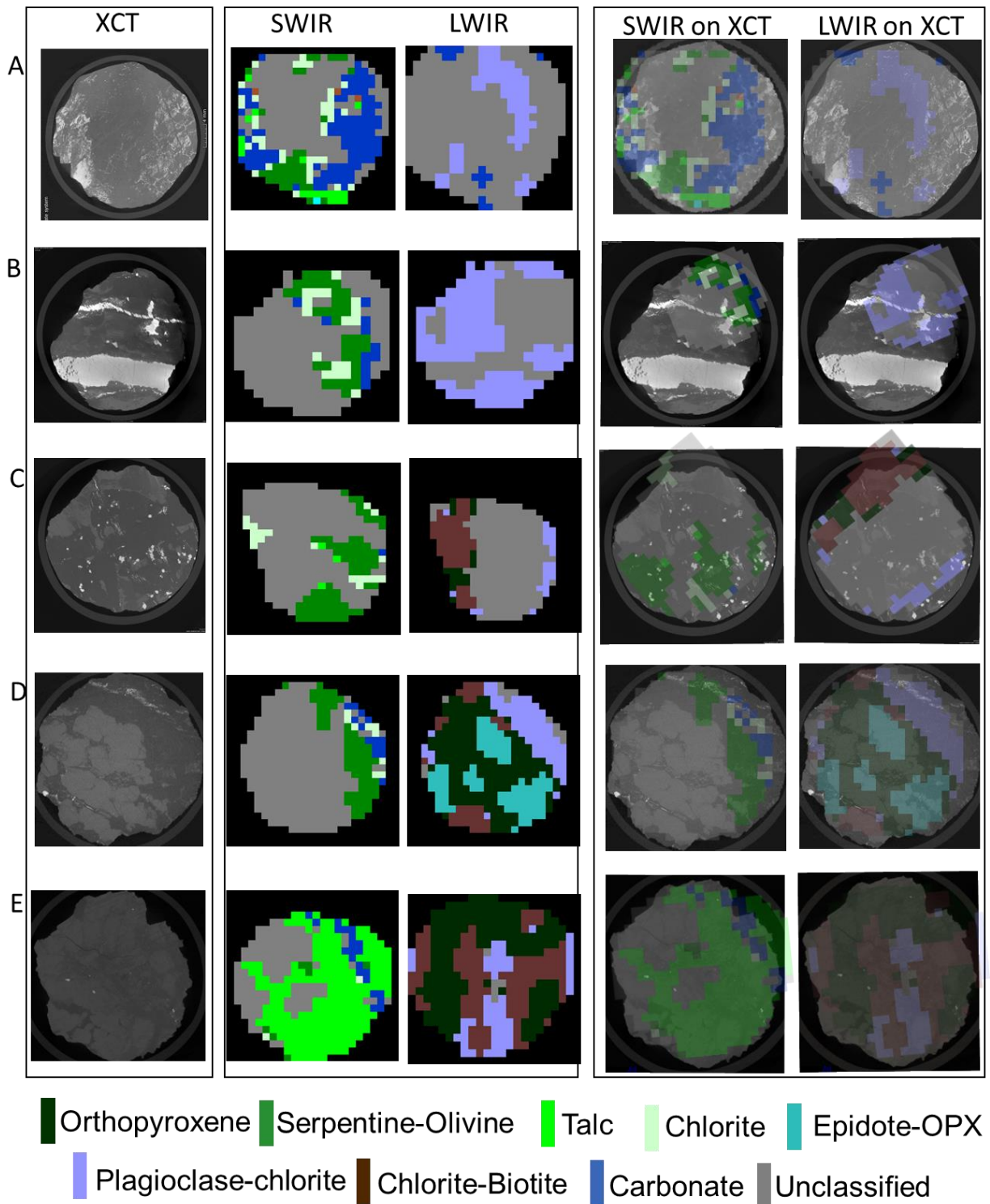


Figure 5.27: Manual image overlapping for HSI mineral maps on XCT greyscale slices. All the unclassified areas represent scenario one (well demonstrated in A). B and C illustrate scenario two (high attenuation minerals in XCT and grey value overlap due to partial volume effect). D and E demonstrate scenario 3 (where minerals can be discriminated both in HSI and XCT). Mini cores are 25 mm in diameter.

Chapter 6: Discussion

This chapter discusses the results presented in chapters 4 and 5, aiming to address the outlined objectives by answering the key questions posed in section 1.3. The first part of the discussion will focus on each technique's practical steps to obtain mineralogical and textural information. Then the discussion focuses on the benefits and limitations of each technique in characterising the mineral assemblage and texture. A summary of the mineralogical and textural information obtained from XCT and HSI is also provided. Lastly, the approach to overlapping the two output images from HSI and XCT will be discussed, highlighting its practicality.

6.1 A systematic workflow for extraction of mineralogical and textural characteristics in drill cores

HSI and XCT were used to capture mineralogical and textural information of two magmatic Ni-Cu-PGE ore drill cores. This section provides a narrative of the parameters that influenced the extraction of data regarding the mineral assemblage and texture from each technique without any critical evaluation (which is considered in section 6.2). Figure 6.1 provides a summary of the procedures required to acquire quality data.

Hyperspectral imaging and X-ray computed tomography did not require extensive sample preparation, other than dust removal for HSI and reducing the sample size to a 25 mm diameter drill core for optimal scanning in the XCT system. HSI scanning is sensitive to small changes (such as serpentine smearing) and absorption is dependent on the surface depth; hence, clean cores are a preference (Jacq et al., 2019). Specific procedures were carried out for each technique, from acquisition to product generation. The systems were calibrated and set up for optimal scanning for both HSI and XCT. These setups and calibrations included monitoring the scanning source, detector, and sample field of view to minimise and manage the possible artefacts (such as beam and ring artefacts in XCT, and wavelength shifts in HSI) and to achieve an excellent signal to noise ratio (for both XCT and HSI).

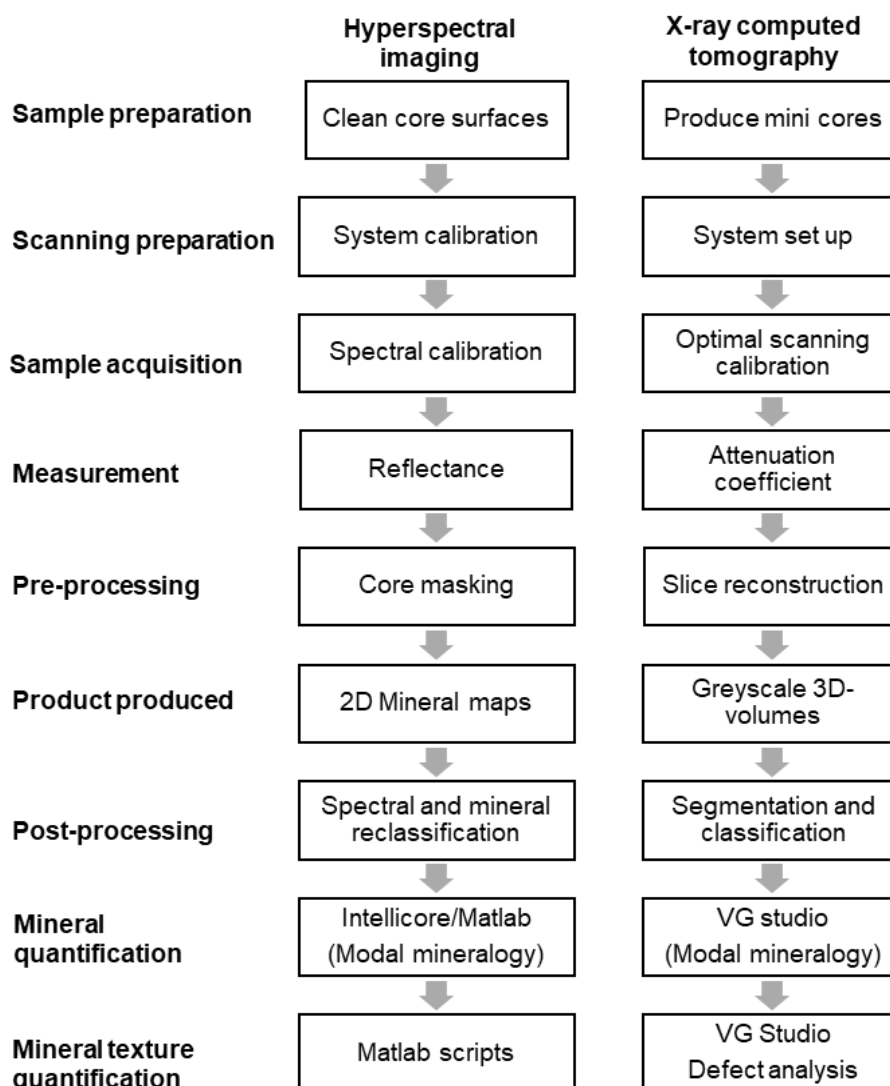


Figure 6.1: Flow chart for acquiring mineralogical and textural information from the two scanning techniques (HSI and XCT).

Before the actual scanning, XCT scanning parameters were optimised using a single mini core selected as a reference that visibly contained high-density phases such as base metal sulphides and chromite as well as the array of ferromagnesian silicate minerals. The reference mini core was scanned at different X-ray energies using different combinations of copper filters, beam current, and the number of projections. The optimal input energy that allowed penetration with good discrimination was 140 kV. Although sample size can be investigated in determining the optimal scanning parameters, based on prior work (Bam et al., 2019; Ghent and Mol, 2019; Guntoro et al., 2019; Voigt et al., 2020), a diameter of 25 mm with a 20 μm voxel size was chosen to distinguish silicates from sulphides and chromite. For hyperspectral imaging, the system calibration was conducted before and during the sample scanning (for standard, selected and mini cores) to monitor the wavelengths in the cameras. The white and black reference was used for reflectance and image calibration (Johnson et al., 2019; Qiu et al., 2017). The calibrations were performed for every spectral camera. Before any scanning could proceed, spectral

calibrations needed to undergo quality control to monitor the wavelength shifts from different sensors (Kurz et al., 2017). Depending on the specific mineral targeted, mineral characterisation before scanning is essential to obtain the desired mineral assemblage such as using the attenuation coefficient spreadsheet by Bam et al., (2020) and mineralogical supporting techniques (this helps to understand the type of ore you are working with and what minerals to expect).

Minerals were measured for their reflectance in HSI and attenuation coefficient in XCT producing mineral spectral signatures and grey value histograms, respectively. All the datasets produced after the acquisition were monitored and modified using various filters to enhance the images by reducing physical and scanning artefacts/effects such as noise (Bam et al., 2019; Cnudde and Boone, 2013; Guntoro et al., 2019; Mohamed, 2018; Tusa et al., 2019). HSI pre-processing was performed on a standard computer (with 8.0 GB and 1.80 GHz) whereas XCT needed a supercomputer with large memory (32.0 GB) and a processor (2.3 GHz). For both techniques (HSI and XCT), accurate mineral identification and texture were only possible after careful reclassification and segmentation, using the supporting methods of QXRD and QEMSCAN. QEMSCAN was used for direct comparison since the same surfaces were also scanned with HSI and XCT, whereas QXRD was used for the determination of mineral grades due to its sample representativeness (the QXRD represented the analysis of a greater sample mass). Post-processing of the output image files was critical to ultimately obtain the desired mineralogical and textural information. Batch processing was performed on the HSI data (on a whole tray), whereas for XCT, each mini core needed to be processed individually due to the overlapping of grey values.

Spectral and mineral reclassification was key to generating meaningful information on the mineral assemblage in the core. This was achieved by spectral matching from other libraries such as USGS and JHU (Kale et al., 2017; Mohamed, 2018; Raja et al., 2010). Usually, the spectral shape gives an idea of what kind of mineral it might be e.g., the readily identified apatite spectra matched with orthopyroxene spectra from the libraries-section 5.1. In some instances, a shift in wavelength may indicate a change in the mineral's composition (Linton et al., 2018). A supporting mineralogical validation technique was used for the mineral and spectral reclassification. The key step to XCT post-processing was phase segmentation for every grey value range present in the core. The segmentation varied for every core, influenced by a mineral's presence (or absence) and association with each other. The choice of segmentation was also dependent on the range of grey value phases present in the core. In the case where high-density phases were associated with low-density phases, careful segmentation (region growing) needed to be carried out to minimise grey value overlapping (Godel, 2013). The final mineral maps were generated as 2D output images in PNG format for both HSI and XCT, as well as 3D volumes in AVI file format.

After successful mineral identification and classification, mineralogical and textural data quantification was performed on each output image. In XCT, the mineral grades (in volume percent) were quantified using VG studio's 'sample properties' functionality for every segmented phase in the core. The HSI mineral grades (in area percent) was generated for every mineral detected under each sensor (VNIR,

SWIR and LWIR) using both the Intellicore and MATLAB software. MATLAB data was also used to validate the mineral grades extracted in Intellicore, and MATLAB results were used instead.

The effect of HSI grain size distribution had to be quantified using MATLAB since Intellicore did not provide this functionality. The grain size distribution was extracted on HSI mineral maps using specially developed MATLAB scripts. The scanning resolution mainly influenced the quantification of grain size, resulting in the apparent interconnectivity of mineral grains lacking grain boundaries that could not be segmented properly. Also, the spectral absorption favours larger grains over smaller grains resulting in the overestimation and underestimation of larger and smaller grains, respectively (Clark 1999; Mathieu et al., 2017). In XCT, the texture quantification was obtained in VG studio by applying the defect analysis functionality to the segmented phase to extract volumes of each grain present in the core. In some cases, grain separation needed to be carried out using the erode and dilate functionality.

6.2 Benefits and limitations for mineralogical and textural characterisation (from acquisition to processing)

Table 6.1 summarises the benefits and limitations of HSI and XCT to obtain accurate mineralogical and textural information based on the results from this study.

The HSI system operation can be run by anyone after a few training sessions, especially when the setup has already been done. System calibration is required between the scanning of multiple trays of the core. The HSI system allowed the scanning of the standard core at low resolution and the mini cores at high resolution rapidly, in less than 2 minutes for each tray. At high resolution, the spectral sensors of the device used were limited to only SWIR and LWIR. Limited areas (in the mini cores) were scanned due to irregular surfaces and tilting which resulted from samples not being fixed on a stage during scanning. The determination of the mineral assemblage in HSI is dependent on the typical mineral's spectral response under each sensor, therefore, more than one spectral sensor is required for representative data unless targeting specific minerals. The HSI data processing was mainly automated using the available spectral libraries. However, in some cases, spectral and mineral reclassification were needed as well as the relevant geological and mineralogical knowledge (e.g., expected mineral association from hydrothermal alteration, (Becker et al., 2014, 2012; Hey, 1999; Molifie, 2021) (Section 5.1.2 and 5.2.1). In complex ores, with pervasive alteration, mineral discrimination between the primary and secondary minerals was challenging due to spectral mixing and mineral overlapping, restricting the extraction of mineral texture such as grain sizes and shapes (e.g., pervasive alteration of serpentine in Figure 5.6, 5.8, 5.11 and 5.12). On the other hand, HSI is limited to identifying silicates (including alteration silicates) and carbonates (Table 5.3)

In comparison, XCT systems require geological and technical knowledge (particularly with a strong physics background) to run and monitor the system. The XCT scanning resolution is higher, producing well defined internal structure, grain sizes, shapes, and attenuation. The scanning time of XCT is

considerably longer than HSI, running at 50 minutes/core. The XCT resolution though is dependent on sample size and the distance between the sample and the detector (Ketcham and Carlson, 2001). Compared to HSI mini core scanning, XCT samples were fixed during scanning minimising unnecessary artefacts. The cylindrical shapes of the mini cores extracted allowed consistent X-ray penetration to acquire good quality data facilitating discrimination of high density from low-density phases. XCT lends itself to processing for the extraction of mineral grades and texture, including their quantification (Ketcham and Carlson, 2001; Kyle and Ketcham, 2015). The only extensive processing was phase segmentation since it was carried out manually for each core. In addition, all XCT processing and pre-processing were carried out on one software suite, using greater computing powers compared to the standard computers used for HSI. Using the grey values, high-density phases (such as BMS) can be differentiated from the lower density phases (silicates and carbonates) without a supporting technique (Figure 5.17b and c and Figure 5.18a). However, XCT fully depends on the supporting techniques for proper mineral identification and sufficient difference in attenuation coefficient for mineral discrimination. However, the BMS and oxides could not be discriminated under the conditions that the samples were scanned.

Table 6.1: Summary table of the benefits and limitations for HSI and XCT for mineralogical and textural information as relevant to the measurements in this study.

Parameter	Benefits		Limitations	
	HSI	XCT	HSI	XCT
System operation	It does not require specialist knowledge to run	The system can run with interference	Calibrations between the scanning of multiple cores	Requires geological and technical knowledge to operate the system
Scanning parameters	Rapid scanning time (90 mm/s)	High scanning resolution (20 μm)	Scanned at a lower resolution	The scanning time was long (50 minutes for each sample)
Core size and shape	All sizes can be scanned (mm-m)	A cylindrical shape of the mini cores allows consistent penetration	Dipping and irregular surface limited the captured area	A cylinder with a small diameter (25 mm) is required for optimal imaging
Pre and Post Processing	Mineral data is mainly automated and reclassified using available spectral libraries	All processing runs on one software suite	Requires spectral and geological knowledge for data processing	Requires high computing power for data processing
Mineral assemblage discrimination	Identification of individual alteration silicates	Able to obtain information on high-density phases not recognised by HSI	Inability to identify BMS, chromite and magnetite. Spectral mixing Minerals correlation from sensors	Dependent on other techniques for mineral discrimination
Texture discrimination	Mineral association and structures can be obtained with LWIR	Well defined structures can be obtained and quantified within the core (grain size, shape, and association)	Limited textural information (GSD)	Scanning parameters such as resolution influence mineral grouping

6.3 Extent of data automation

Post-processing was dependent chiefly on human knowledge. Little can be said about XCT because the system lends itself to processing and was computed on one software suite. However, the XCT post-processing was extensive and time-consuming due to the manual segmentation that was performed for each mini core. Following segmentation, both the mineral grades and grain size distribution were readily quantified. HSI software went as far as producing mineral grades although limited by the pixel size resolution and the grain size distribution was extracted using MATLAB. Even though the use of HSI and XCT in this study was fairly intensive on manual processing, for repeat samples with similar mineral assemblages, it would be possible to develop macros or software scripts to automate these processes.

6.4 Comparisons in characterisation of the mineral assemblage and texture from HSI and XCT

A summary table of the minerals identified by HSI (SWIR and LWIR) and XCT is given in Table 6.3. HSI identified silicate minerals, particularly alteration minerals such as serpentine, chlorite and talc in VN-SWIR and primary minerals such as orthopyroxenes in LWIR (Table 5.4, Figure 5.6, 5.12). In comparison, XCT identified low- and high-density minerals in their corresponding attenuation coefficient and grey values (Figure 5.17 and 5.18). The high-density phases were classified as BMS, chromite and magnetite by QEMSCAN and QXRD. However, none of the BMS, chromite and magnetite were identified by HSI since they do not have spectral features and they could not be differentiated in XCT (Table 6.4) due to negligible attenuation coefficient difference (Figure 5.8). The most highly attenuating minerals were pentlandite (particularly in the anorthosite in Figure 5.18a) and a few other small grains in the pegmatoidal pyroxenite that may potentially be valuable PGM (Figure 5.26).

Table 6.2: A summary of the minerals/mineral groups identified in HSI (SWIR and LWIR) and XCT in this study. Minerals highlighted in green are phyllosilicates.

Mineral Groups	Minerals	SWIR	LWIR	XCT
Silicates	Plagioclase	Prehnite-Plagioclase	Plagioclase-Chlorite	Plagioclase-Chlorite-Biotite-Talc
	Chlorite	Chlorite Saponite- Clinopyroxene		
	Biotite	-		
	Talc	Talc-Chlorite	-	
	Serpentine	Serpentine-Olivine	-	Serpentine-Olivine
	Olivine		-	
	Calcite	Carbonate	Carbonate	orthopyroxene-clinopyroxene-Amphibole
	Orthopyroxene	-	orthopyroxene-clinopyroxene	
	Clinopyroxene	-	-	
	Amphibole	Amphibole	-	
	Epidote	Epidote	Epidote	Epidote
BMS	Chalcopyrite	-	-	Base metal sulphides and Oxides
	Pyrrhotite	-	-	
	Pentlandite	-	-	
Oxides	Chromite	-	-	
	Magnetite	-	-	
PGMs*	Braggite	-	-	PGMs
	Ferro platinum	-	-	

*PGMs were not positively identified, but high-density phases that were found are likely to represent PGMs.

The ability to differentiate between minerals was evaluated using QEMSCAN data, and most minerals, including silicate minerals, posed a challenge, especially where there was extensive alteration (as in the altered harzburgite). Due to spectral mixing in HSI, and overlapping grey values in XCT, various minerals had to be grouped. The mixed-phases occur as a result of intimately associated minerals due to alteration (Mathieu et al., 2017; Sriram et al., 2016). In both techniques, the serpentine-olivine and chlorite-plagioclase pairs were grouped (Table 6.3, Figure 5.6, Figure 5.8, Figure 5.11 and Figure 12). Although olivine and plagioclase were expected to have a strong, distinctive spectral response in LWIR, these minerals were not identified; instead, serpentine and chlorite were identified in SWIR. In XCT, serpentine and olivine could not be discriminated with an attenuation difference of 25%, even though they were expected to be differentiated, according to Bam et al. (2020). QEMSCAN data indicates the presence of these minerals but olivine and plagioclase have been extensively altered to serpentine and chlorite, respectively (Figure 4.3, Figure 4.7). The extent of alteration was also supported by the QXRD data (Table 4.1 and Table 4.2). In some instances (like in the altered harzburgite), orthopyroxene only experienced incipient alteration to serpentine and talc. However, orthopyroxene, serpentine and talc were identified by HSI (responding under different sensors), and orthopyroxene was discriminated from

serpentine in XCT. The same was observed with epidote, which appears as the alteration product of plagioclase. Epidote was identified under VN-SWIR and could be distinguished from plagioclase and chlorite in XCT (Table 6.3).

Other minerals such as chlorite and biotite were detected under LWIR, and plagioclase was identified in VN-SWIR as a mixed phase (prehnite-plagioclase) in the anorthosite and pegmatite vein (Figure 5.6 and Figure 5.8). Chlorite and biotite were expected to be more responsive under SWIR than LWIR. The effect could be due to the spectral mixing due to the presence of fine alteration minerals. The QEMSCAN field images showed chlorite to be the alteration product of plagioclase and biotite. This was observed in all the cores scanned with HSI (standard, selected and mini cores).

6.4.1 Quantitative mineralogical characterisation

The output images were analysed, and the mineral grades was calculated. The mineral grades obtained from both XCT and HSI were generally comparable to QEMSCAN. The comparison was made by normalising the QEMSCAN data according to the minerals identified under each technique. The HSI-derived mineral grade of the mini cores was complementary to QEMSCAN data in terms of minerals present (excluding minerals that did not respond under HSI) and roughly similar in their abundance (Figure 9 and 5.10). The comparison between HSI and XCT was on surface to volume, and the observed minor differences are largely considered due to the sampling effect (Figure 5.21 and Figure 5.22). The relative error of the precision of each technique was also calculated and compared (Table 6.4 and Table E2, Appendix E). The relative errors increased from XCT to HSI. It appears that the errors are dependent on sampling; a small area of core was scanned in HSI compared to QEMSCAN and XCT (representing the entire volume). In this case, XCT mineral grades was the most precise and representative of the cores with an error range of <0.1-0.1%. Although the precision was best, the accuracy for silicates and carbonates was not necessarily the best due to poor discrimination in minerals with similar attenuation differences such as olivine-serpentine and plagioclase-chlorite (Figure 5.17, and Figure 5.18). Additionally, the accuracy of HSI cannot be directly compared to QEMSCAN since slightly different areas of cores were analysed (due to tilting, see section 3.6 and 5.1.4. In addition, the accuracy of HSI compared to QEMSCAN is also difficult to interrogate due to spectral mixing and mineral overlapping between different spectral sensors.

Table 6.3: Relative error at the 95% confidence interval for mineral grades (of drill core RD015) obtained in QEMSCAN, HSI and XCT, reported by area % (QEMSCAN and HSI) and volume % (XCT).

Rock type	Grouped Minerals	Error %			
		XCT	QEMSCAN	SWIR	LWIR
Anorthosite	Spinel-BMS	0.1	7.9	-	-
	Epidote	0.1	5.9	7.7	-
	Plagioclase-Chlorite	<0.1	0.4	-	47.1
Altered harzburgite	Spinel-BMS	0.1	7.4	-	-
	Orthopyroxene	<0.1	1.2	-	10.65
	Serpentine-Olivine	<0.1	0.4	1.5	-
Pegmatoidal olivine-pyroxenite	Spinel-BMS	<0.1	2.8	-	-
	Serpentine-Olivine	<0.1	6.3	2.1	-
	Plagioclase-Chlorite-Epidote-orthopyroxene	<0.1	2.5	-	20.5
Pyroxenite	Spinel-BMS	0.1	17.0	-	-
	Plagioclase	<0.1	1.2	-	7.7
	Orthopyroxene	<0.1	2.4	-	0.6

6.4.2 Mineral texture characterisation

The scanning resolution of the XCT was between 82 and 22 times larger than the HSI scanning resolution of standard and mini cores, respectively. Therefore, qualitative mineral textural characteristics (mineral association and structure) were well defined in XCT, for example, the cleavage planes and shapes of orthopyroxene, the finer inclusions, veinlets, and grain boundaries (e.g., elongated grains in feldspathic pyroxenite) (Figure 5.17 and 5.18). These structures are limited in HSI with the only structures observed being 0.5-1 cm wide carbonate or pegmatoidal veins in the standard core due to the larger surface area exposed to the resolution (Figure 5.11 and Figure 5.12). Vein structures were identified by Mathieu et al., (2017) and Tusa et al., (2019), with Tusa developing a methodology to extract them from the mineral maps. The evidence suggests that veins are one of the structures that can be readily identified by HSI. Due to the scanning resolution in HSI, the mineral association and grain boundaries were not visible. In these cores, there are chromite stringers mapped both in HSI and XCT. However, these stringers were misidentified in LWIR as orthopyroxene and serpentine and unclassified under VN-SWIR. In contrast, the pegmatite vein structure was well mapped in both VN-SWIR and LWIR because it is the lighter rock with minimum alteration (Figure 5.11).

6.4.3 Quantitative textural characterisation

The lack of mineral structures (such as grain boundaries) in HSI, especially in mini cores, resulted in the identification of limited grains (seven grains maximum) due to their interconnectivity, thereby likely overestimating the actual grain sizes (Section 5.1.3). The absolute grain sizes obtained in HSI were not comparable to QEMSCAN or XCT grain sizes. QEMSCAN and XCT were both scanned at high resolution and identified very-fine grains (<1000 µm). The minimum grain size obtained was 1904 µm,

falling within the fine grain range (1000-2000 μm). However, some of the HSI and QEMSCAN median values fell within similar ranges in terms of fine, medium, and coarse-grained categories (Table 5.4 and Table 5.5). The XCT grain size comparison was conducted on the grouped mineral pairs serpentine-olivine and chlorite-plagioclase (Section 5.2.3). Grain size distributions were computed in equivalent spherical diameter. The 2D QEMSCAN grain size distributions were finer than the 3D XCT as expected due to stereological error (Gu et al., 2012; van Dalen and Koster, 2012). The comparable dataset in XCT and QEMSCAN was also achieved by the ability to separate interconnected grain separation.

6.5 Effects of rock types and hydrothermal alteration on HSI and XCT

The mineral assemblage determined from QEMSCAN (Figure 4.4 and Figure 4.8) and QXRD (Table 4.1 and Figure 4.2) indicated that these rocks underwent hydration reactions that formed alteration minerals such as serpentine, chlorite and talc. The presence of alteration minerals is important in geometallurgy because they have been noted to affect mineral processing in these ores, e.g., the flotation recovery of valuable PGEs (Becker et al., 2012; Molifie, 2021; Smith et al., 2013). The abundance of serpentine in the olivine-bearing rocks such as altered harzburgite and pegmatoidal olivine pyroxenite was directly identified by QEMSCAN, QXRD and HSI, and indirectly identified in XCT. Orthopyroxene was only altered to serpentine in the presence of olivine supported by very fine-grained relics of olivine and orthopyroxene (Figure 4.3.b, c, d and Figure 4.7c) and thread-like serpentine branching from olivine (Figure 4.7b) indicating an early stage of serpentinization (Ningthoujam et al., 2012). Figures 4.3c and 4.7d suggest that olivine was the first to be altered before orthopyroxene as evidenced by relics or intact orthopyroxene with the minimal presence of olivine. Talc is present and more abundant in altered harzburgite, pegmatoidal pyroxenite and pegmatoidal olivine pyroxenite. In most cases, talc is known to be forming from orthopyroxene of the serpentinised rocks (Iyer et al. 2008; Salem, 1992).

The plagioclase in the interstitial spaces of most rock types underwent a second event of alteration forming an alteration assemblage of plagioclase-epidote-chlorite. It is only in the feldspathic pyroxenite, where the plagioclase was only altered to chlorite (Figure 4.3e and Figure 4.7e). According to Li et al. (2004) epidote is commonly associated with secondary plagioclase appearing as patchy, in smaller sizes and with lower anorthite content (Figure 4.3a, b, c and d and Figure 4.7a, c). There are also biotite pseudomorphs altered by chlorite (Figure 4.3a) and associated with serpentine and plagioclase (Figures 4.7 c and d). The interstitial spaces and induced cracks appear to be the channels that allowed fluids into the rocks. For example, the presence of veins of chlorite (Figure 4.7a), carbonates (Figure 5.2) and magnetite (Figure 5.3b) appear to serve as the direct evidence for hydrothermal fluid circulation. The results obtained (e.g., presence of alteration minerals) fully suggest the interaction of these rocks with hydrothermal fluids and weathering.

Several factors seem to have influenced the extraction of data on the mineral assemblage and texture in HSI and XCT. However, the most noted factors were the effect caused by different rock types (i.e.,

compositional relation) and the degree of alteration in minerals (Duée et al., 2019; Tuşa et al., 2020). The scanned cores intentionally constituted different rock types composed of variable minerals with distinct colours (Figure 5.1 and 5.2). The anorthosite and feldspathic pyroxenites are the light rocks in the cores compared to the altered harzburgite and pegmatoidal pyroxenite (Figure 6.2) Also, the altered harzburgite and pegmatoidal pyroxenite were highly altered with serpentine formed at the expense of olivine and orthopyroxene.

Furthermore, the rock types constitute plagioclase-epidote-chlorite alteration, except in the feldspathic pyroxenite, where there is only plagioclase-chlorite alteration. Both HSI and XCT seem to depend on the mineral colour and texture (ideally alteration). In HSI, the mineral colour influences the rate of reflectance and absorption. The pixel overlapping in VNIR, SWIR and LWIR is less in the light rocks (being the anorthosite and feldspathic pyroxenite-Section 5.1) than dark coloured more altered rocks. The mineral grouping in lighter rocks is similar— the grey value and minerals overlapping were less due to incipient alteration of plagioclase and orthopyroxene. In contrast, the overlapping was more intensive on the darker rocks where there was pervasive mineral alteration (Figure 5.11 and Figure 5.12). For example, olivine and serpentine are grouped, both in HSI and XCT. The pervasive alteration of olivine by serpentine complicates the mineral association in that serpentine mineral spectra and attenuation coefficient overpowered the olivine spectra and grey value. The pervasive alteration was challenging for HSI mineral identification due to complex mineral associations –in general, the more abundant minerals, with larger grain sizes and strong spectral signatures are favoured and likely overestimated. For example, serpentine detected with SWIR was extensive, whereas olivine was not detected in any sensor as it was expected to respond in LWIR. Serpentine and olivine are chemically similar, and olivine is present in both the altered harzburgite and olivine-pegmatoidal pyroxenite— the darker rocks in the core. This may be evidence that HSI does not do very well in darker rocks because darker minerals absorb more light (showing weaker reflectance) and lighter minerals reflect more light (Mathieu et al., 2017; Salehi et al., 2020; Sriram et al., 2016). However, orthopyroxene is also chemically similar to its alteration product (talc), but both minerals were detected by VN-SWIR (talc) and orthopyroxene (LWIR). This can be influenced by the minimal alteration of orthopyroxene by talc; also, the identification of these minerals was on light rocks (pegmatoidal pyroxenite and feldspathic pyroxenite). In addition, talc is lighter than orthopyroxene, although, it was detected as very fine-grained (< 20 µm) by QEMSCAN, in HSI, talc mapping is extensive in VNIR and SWIR (Figure 5.8 and Figure 5.12). This observation shows that lighter minerals are favoured, irrespective of their grain sizes. However, grain size does play a significant role in HSI (Mathieu et al., 2017; Sriram et al., 2016). According to Clark, (1999) larger grains are favoured in HSI since they have greater path lengths where more light can be absorbed, decreasing the reflectance according to Beer's law. This may also account for why olivine was not detected in LWIR. Olivine appeared to be very fine-grained than serpentine and orthopyroxene in QEMSCAN field images because it was pervasively altered leaving only relics (Figure 4.3 and Figure 4.7). Also, olivine, orthopyroxene, and serpentine are all dark minerals and talc is naturally lighter. However, the BIC talc is discoloured possibly due to the abundance of iron content in the ore (PERS. COMM. Becker, 2021). The effect of mineral abundance, grain size, colour and alteration are issues that still need to be further investigated and determine their correlation to HSI. The degree of mineral

alteration and variability throughout the cores resulted in the different grey value cut-off points during segmentation (Figure 5.17 and Figure 5.18) and mineral grouping for every mini core. For, example the net textured orthopyroxene, olivine and serpentine are grouped in altered harzburgite and pegmatoidal pyroxenite. The unaltered (or less altered) orthopyroxene can be discriminated from serpentine-olivine (Figure 5.18c). This issue could have been avoided if the grey level ranges were standardised using standards (e.g., pure copper or tungsten (Voigt et al., 2021).

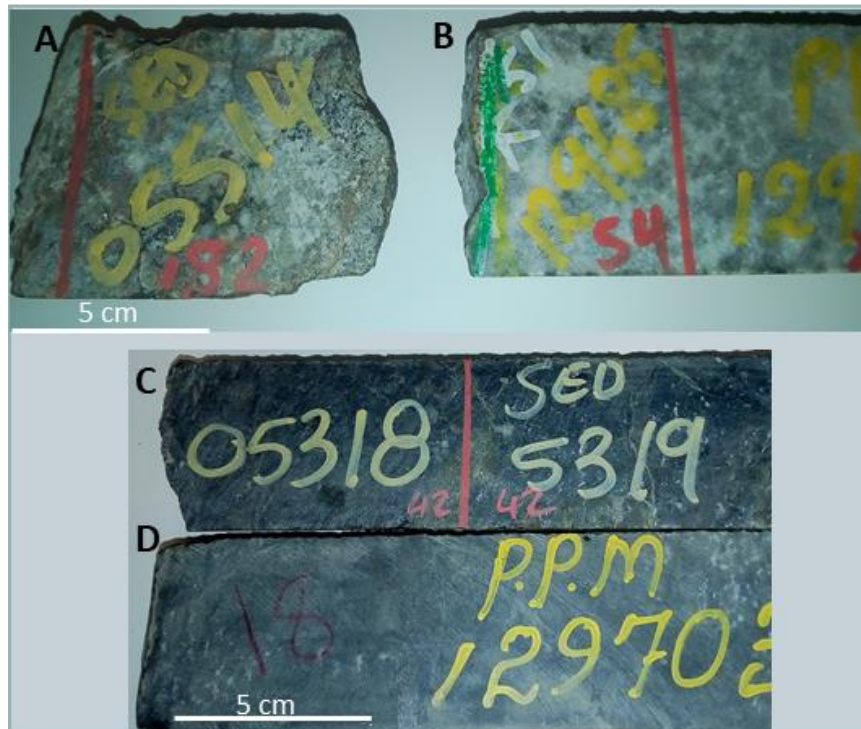


Figure 6. 2: Segments of rock types from the drill cores illustrating lighter and darker rocks. A and B are anorthosites from drill core RD015 and TU277, respectively. C and D are the altered harzburgite from RD015 and TU277, respectively.

The plagioclase-epidote-chlorite alteration also influenced the mineral assemblage detected in HSI and the discrimination in XCT. Due to the scanning parameters used, the difference in the attenuation coefficients between plagioclase and chlorite was $< 6\%$ and could not be differentiated. Plagioclase was expected to respond in LWIR and chlorite to react better in SWIR than LWIR. However, plagioclase spectra were not detected, and chlorite responded in both SWIR and LWIR although it was more abundant in LWIR (Figure 5.1, Figure 5.2, Figure 5.4 and Figure 5.5). According to the QEMSCAN field images, chlorite is the alteration product of plagioclase. This implies that the change in crystallinity due to alteration has affected the plagioclase absorption features (Linton et al., 2018). The presence of biotite with chlorite and plagioclase suggests a type I and type II chlorite is when the biotite is retained as Pseudomorphs (Wu et al., 2019). Type I is formed directly from biotite and type II is formed from

feldspars (Wu et al., 2019). This alteration process may also be a contribution to why biotite was detected with chlorite under LWIR.

6.6 Image overlapping

One of the objectives of this study was to investigate the potential of overlapping the output images from HSI and XCT (section 5.3), which will be further discussed here.

The rock types of these drill cores constitute silicates, carbonate, oxides, and base metal sulphide minerals (Table 6.3). Figure 6.3 is a conceptual diagram illustrating all the possible scenarios observed from overlapping information provided by each technique. The first three possible scenarios overlapping HSI on XCT were successfully demonstrated (Section 5.3-Figure 5.3). Scenario four illustrates the possible outcome of overlapping XCT on HSI images. However, due to lower resolution, HSI as a base image would have limited the information in overlapped images. Therefore, XCT was immediately identified as a suitable base due to its high resolution.

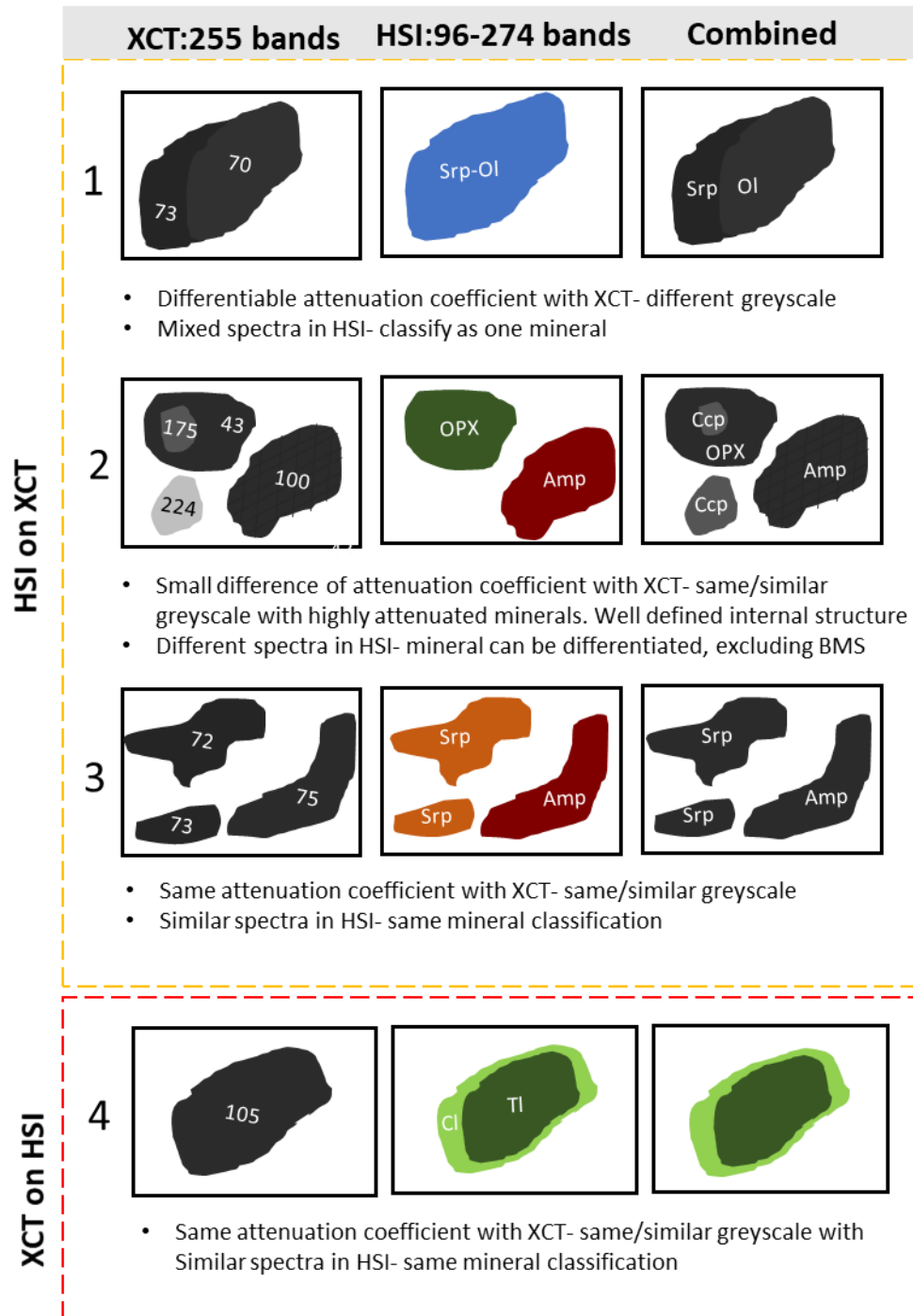


Figure 6.3: A conceptual diagram illustrating the possible overlapping scenarios. The scenarios are illustrated with the data obtained from HSI and XCT for this study. *Numbers are grey values.

The two techniques provide complementary information, silicates in HSI and BMS, chromite and magnetite in XCT. More information can be extracted from the overlapped images; however, a supporting technique will be required, i.e., QEMSCAN (Table 6.3). For example, scenario one is primarily dependent on XCT, which is also dependent on other techniques for mineral identification. In that case, a supporting technique will be required to identify certain missed areas in HSI (Figure 5.3). Scenario two is the ideal scenario where different silicate minerals are identified in HSI, with mineral

grey value variation in XCT but prominent high-density phases. The highly attenuating phases are already known to be high-density phases but could not be discriminated in this case. A supporting technique will be required for their discrimination. Also, the mineral identification with different sensors in HSI can assist with the mineral grouping in the XCT, ideally for silicates. The example for this scenario was demonstrated by the net-textured serpentine and orthopyroxene assemblage that could not be discriminated in XCT but responded very well in SWIR (serpentine) and LWIR (orthopyroxene) (Figure 5.3d). More information can be acquired if more than one sensor is used since the primary minerals responded well in LWIR and secondary alteration minerals responded well in VN-SWIR.

It has been noted that both techniques cannot discriminate between certain minerals. Mineral grouping in XCT is due to a similar or small difference in attenuation coefficient (grey value), and in HSI is due to mixed (similar) spectra. This qualified as the third scenario, the examples being the grouping of plagioclase-chlorite, chlorite-biotite and serpentine-olivine (Table 6.3, Figure 5.6 and Table 8). The same applied to the serpentine-olivine. The serpentine-olivine assemblage was illustrated by the QEMSCAN field images, showing the alteration of olivine and orthopyroxene to talc (Figure 4.3 and Figure 4.7). Without the QEMSCAN as the supporting technique, the presence of olivine would not have been known, even though olivine is one of the major minerals in peridotites. This also brings forward the necessity to have the supportive technique. However, serpentine and orthopyroxene as the predominant minerals were identified by HSI without the supporting technique but through spectral matching. This information can be useful for mineral identification in XCT; given that the mineral shape and structure are defined e.g., serpentine vein-like structure and orthopyroxene blobs in HSI (Figure 5.3D). The latter goes back to XCT being the key to defining both simple (grain size distribution) and complex (liberation and association) textural attributes. Complex mineral textures (mineral association and shape) were key to the success of the overlapping technique. XCT contributed more to the mineral texture (due to high resolution) with well-defined internal structures and minerals association. An example was the well-defined structure of elongated orthopyroxene grains in feldspathic pyroxenite, chromite stringers, chromite grains, magnetite veins, BMS grains, and mineral alteration assemblage (Figure 5.19 and Figure 5.20).

6.6.1 Challenges associated with data processing and analysis from overlapping technique

These techniques provided complementary mineralogical and textural information. The implementation of this technique has the potential to reduce the acquisition and processing periods. However, the effectiveness of this technique is dependent on other techniques for mineral identification since HSI and XCT are not entirely automated techniques (Section 6.3). In addition, the unscanned areas in HSI due to sample movements and tilting posed a challenge during overlapping, leaving pixels in those areas unidentified. Therefore, in a case where there are no supporting techniques, minerals cannot be fully identified in the drill core and the technique will not be helpful. For this technique to be carried out, the same surface areas needed to be scanned. Due to a smaller stage in XCT and a requirement for quality data, mini cores (25 mm in diameter) were produced and were also scanned with HSI. This meant that

the HSI scanning parameters needed to be optimised to scan smaller samples than standard practice. However, the change in resolution and sample size resulted in pixelated HSI maps which limited mineral texture characterization such as grain shapes and boundaries (Figure 5.6, Figure 5.8, Figure 5.13 and Figure 5.14). The overlapping was conducted manually due to a lack of suitable orientation markers visible in both HSI and XCT (Figure 5.27). Each spectral sensor identified different minerals according to their spectral properties (Table 5.4). Overlapping mineral maps of the mini cores from SWIR and LWIR were unsuccessful due to the common pixels mapped as different minerals with no defined mineral texture. Compared to mini cores, standard core shapes that overlapped were visible in both VN-SWIR and LWIR because more pixels have been analysed, although the mineral assemblage was also different (Figure 5.11 and Figure 5.12). Therefore, each pixel from each spectral sensor needed to be overlapped separately with XCT which was time-consuming. Since, HSI is a surface scanner, similar slices from XCT were extracted. Due to the coarse nature of the cores used in this case study, extracting similar slices was not a problem. However, conducting this technique on fine-grained cores may be challenging.

Chapter 7: Conclusion and recommendations

7.1 Conclusion

This study was conducted with the overarching aim of investigating how the use of 3D XCT scanning complements more routine site-based 2D hyperspectral core scanning for practical geometallurgical applications, using a magmatic Ni-Cu-PGE ore case study. To achieve this aim, the following objectives were outlined: (1) *investigating the practical parameters influencing the extraction of mineralogical and textural information on each technique*, (2) *comparing mineral assemblage and texture obtained from each technique*, and (3) *investigating the potential for overlapping the output images to generate a third image with combined information from both techniques*. The conclusion of this research is focused on the integration of the objectives and proposed key questions in section 1.3 and following their discussion in chapter 6.

The ore characterization was firstly conducted by the three commonly used techniques for ore characterisation that were applied before scanning, namely, manual core logging, QEMSCAN and QXRD to understand this ore deposit. In the previous studies, these techniques provided mineralogical and textural information used as proxies for constructing geometallurgical block models. The high abundance of silicate minerals, including alteration minerals (e.g., serpentine and talc) which are problematic to downstream mineral processing and valuable-bearing minerals (e.g., chromite, magnetite and BMS) were identified by these techniques. Although the mineral assemblage was roughly similar throughout the core, the degree of alteration differed depending on the rock type and minerals present. The degree of alteration was measured using the extensiveness of minerals alteration, identified by fully, partially or completely replacement of primary minerals by alteration minerals. The partial replacement was indicated by the presence of relict minerals (such as olivine and orthopyroxene). Of the three techniques, QEMSCAN was the only technique to provide the simple quantitative texture of grain size distribution, which is crucial to understanding the mineral association and mineral liberation. The effect of mineral texture plays a significant role in mineral processing, particularly quantitative texture. QEMSCAN reflected the nature of this ore to be medium to coarse-grained. Using only these techniques, it was evident that obtaining accurate ore characterisation requires more than one technique.

Hyperspectral imaging and X-ray computed tomography were the primary techniques viewed in this study. These techniques were reviewed for their practicality from data generation, output images and results based on the cores scanned in this study. *The steps for determining the mineral assemblages were first discussed in section 6.1 and summarised in a systematic workflow (Figure 6.1)*. To obtain good quality data, specifications and requirements under each category were crucial (e.g., system and data calibration). All steps permitted the extraction of valuable information (mineral assemblage and mineral texture) to produce decent quality images (mostly on the standard cores for HSI) to understand ore variability and achieve the goal of the research. The steps included the calibrations conducted

before and during scanning and data processing for quality data extraction, such as the HSI spectral and mineral reclassification and segmentation and classification for XCT data. Hyperspectral data post-processing required the use of MATLAB to generate quantitative texture and mineral grades.

These two techniques were evaluated based on their performance in acquiring mineralogical and textural information. *This was achieved by highlighting each technique's benefits and limitations based on the steps taken to acquire data in this research* (in section 6.1). This study proved HSI to be a more rapid scanning technique than XCT, given that HSI only captures the surface and XCT scans the entire volume of the core. However, the HSI data processing appeared to be more complex and extensive than XCT, which lends itself to processing in one software suite although the computing hardware requirements for XCT were significantly more advanced than HSI. XCT mineral identification and discrimination were dependent on other techniques (QEMSCAN and XRD in this case). Due to the complexities of this ore, the data processing for HSI was extensive and the determination of the mineral assemblage was complex because of mineral overlapping between different sensors (VN-SWIR/SWIR and LWIR). However, in less complicated ores, most minerals can be readily identified, and reclassification could be conducted with readily available spectral libraries and with QEMSCAN and QXRD used for validation.

Mineral and textural characterisation are one of the crucial primary parameters for determining the effects of ore variability ahead of mining and processing. These parameters are central to developing the geometallurgical block models. One of the objectives of this study was to *compare the mineralogical and textural data obtained from HSI and XCT*. HSI provided good discrimination of primary minerals under LWIR, and alteration minerals such as serpentine, chlorite and talc under SWIR. The identification of these alteration minerals is important in geometallurgy since they provide advanced knowledge of minerals problematic to mineral processing, such as affecting the recovery and concentration grade of the PGMs. For XCT, identifying high-density phases (such as BMS, chromite and magnetite) that have been viewed to be associated with PGMs or identifying possible PGMs. In addition, the XCT volumes provided quality data that allowed the extraction of quantitative data (both mineral grades and grain sizes distribution) generally comparable to QEMSCAN data. The HSI scanning resolution too low for obtaining representative quantitative mineral texture, but the mineral grades obtained were comparable to QEMSCAN. For comparison purposes, the QEMSCAN mineral grades was normalised to represent minerals detected under each technique, and XCT upper slices were targeted to match with QEMSCAN and HSI surfaces. The relative error in precision for mineral grades was calculated at the 95% confidence interval. The relative error precision was lowest for XCT with the range of (<0.1-4.4%), followed by QEMSCAN (0.1-17%) and HSI (0.6-42%). However, the accuracy between the techniques could not be directly compared since slightly different surfaces of cores were analysed (i.e., representative sample surfaces were not identical) and pervasive mineral alteration. The information obtained in this study suggests that these techniques are complementary. However, both techniques suffered mineral discrimination issues due to the extensive mineral alteration and colour of the rock types.

The supporting techniques identified a high degree of alteration in this core involving the minerals serpentine, and chlorite talc. These minerals are the results of hydrothermal alteration and weathering. The degree of alteration is dependent on the rock types. Darker and more Fe-Mg rocks (altered harzburgite, pegmatoidal pyroxenite) are extensively altered compared to lighter rocks (anorthosite and pyroxenite) that are less altered. The HSI results were more affected by the change in rock mineral composition with more spectral overlapping observed in mafic rocks than felsic rocks due to an unparalleled reflectance level. Also, the extensive degree of alteration caused spectral mixing and grey value overlapping in XCT. This resulted in the grouping of primary minerals with their alteration products such as the serpentine-olivine and plagioclase-chlorite mineral pairs. In some instances, LWIR and VN-SWIR or SWIR successfully distinguished between the primary and secondary minerals, such as orthopyroxene (identified by LWIR) and talc (identified by SWIR); although this was because orthopyroxene was not pervasively altered, and its grain shape was still retained.

The last key question *investigated the possibility of overlapping the output images from XCT and HSI to obtain a third image with added information*. This method was achieved by moving the HSI from its routine application on standard drill cores to producing 25mm diameter mini cores. Four possible scenarios were hypothesised, three of which were investigated, i.e., overlapping the HSI output images onto the XCT image slices. The fourth scenario overlapping XCT image onto HSI was not fully investigated, XCT was immediately the 'base' image for overlapping because of its high resolution. The overlapping was successful, given that the two techniques provided complementary information such as silicate minerals from HSI and BMS and oxides in XCT. However, this overlapping could not be achieved without the use of an intermediate technique (such as QEMSCAN). In addition, the overlapping was challenging due to numerous factors such as some unscanned areas of the core by HSI and a lack of defined grain structures.

Concluding remark

This research investigated the coupling of hyperspectral imaging and X-ray computed tomography in drill core for geometallurgical application, using a South African magmatic Ni-Cu-PGE ore as the case study. The summary conclusion is that *HSI scanning on the PGE drill core was challenging* because of the dark colour of the core, however, useful information on the alteration mineral assemblage can still be extracted. HSI core scanning needed to be *moved to a higher resolution* than standard practice in order to scan mini cores for comparative scanning. XCT scanning provided information on *valuable minerals and mineral texture in 3D*. Therefore, the two scanning techniques will likely offer complementary information, although *applying this combined technique for routine work will be limited in practice*.

7.2 Recommendations

This study investigated the use of HSI and XCT in geometallurgy using drill cores. This work was the first approach to investigating the integration of HSI and XCT using a case study from a South African magmatic Ni-Cu-PGE ore from the Bushveld Complex. The following are some recommendations for future study:

- Since there is no published work on mafic and ultramafic rocks using HSI in the drill core, more studies need to be conducted on other mafic and ultramafic deposits to compare with the results obtained in this study. Possibly, further investigation on the effect of colour may be carried out.
- The level of automation in HSI needs to be investigated and improved, especially for the extraction of textural information using machine learning.
- For XCT, grey value calibration and the use of dual-energy could be considered to create consistency in grey value distribution for different rock types to provide better discrimination of minerals with overlapping grey values (Wang et al., 2014).
- The overlapping technique can be further investigated and improved. Other techniques such as LIBS and micro-XRF that can identify high-density minerals can be used in integration with XCT and HSI to develop a practical technique at a broader scale.
- Mineral texture in HSI needs to be further investigated and one could consider coupling the information with other techniques such as grey level co-occurrence matrices (GLCM) for advanced texture quantification (Guntoro et al., 2019; Jardine et al., 2018).

References

- Agangi, A., Hofmann, A., Rollion-Bard, C., Marin-Carbonne, J., Cavalazzi, B., Large, R. and Meffre, S. 2015. Gold accumulation in the archaean Witwatersrand basin, South Africa-evidence from concentrically laminated pyrite. *Earth-Science Reviews*. 140:27–53. DOI: 10.1016/j.earscirev.2014.10.009.
- Alexandre, H.. 2018. Portable X-Ray Fluorescence Spectrometry: Principles and Applications for Analysis of Mineralogical and Environmental Materials. *Aspects in Mining and Mineral Science*. 1:6. DOI: 10.31031/amms.2018.01.000506.
- Armengol, A.A. 2015. Towards Automated Logging of Ore. MSc Thesis. Lulea University of Technology. 96.
- Bacchuwar, S.S., Mkandawire, N.P., McGrath, T., Lin, C.L. and Miller, J.D. 2020. X-Ray computed tomography for 3D analysis of gangue mineral rejection by gravity preconcentration of sulfidic gold ores. *Mineral Processing and Extractive Metallurgy: Transactions of the Institute of Mining and Metallurgy*. 129:49–63. DOI: 10.1080/25726641.2019.1643133.
- Ballhaus, C. and Sylvester, P. 2000. Noble metal enrichment processes in the Merensky Reef, Bushveld Complex. *Journal of Petrology*. 41:545–561. DOI: 10.1093/petrology/41.4.545.
- Bam, L.C. 2020. Developing protocols for XCT scanning of density mineral ore samples with applications to geology and minerals processing. PhD Thesis. Stellenbosch University. 72.
- Bam, L.C., Miller, J.A., Becker, M., Beer, F.C. De and Basson, I. 2016. X-ray Computed Tomography – Determination of Rapid Scanning Parameters for Geometallurgical Analysis of Iron Ore. In *Proceedings of the 3rd International Geometallurgy Conference*. S.C. Dominy and L. O`Connor, Eds. Perth, Western Australia: The Australasian Institute of Mining and Metallurgy. 209–219.
- Bam, L.C., Miller, J.A., Becker, M. and Basson, I.J. 2019. X-ray computed tomography: Practical evaluation of beam hardening in iron ore samples. *Minerals Engineering*. 131:206–215. DOI: 10.1016/j.mineng.2018.11.010.
- Bam, L.C., Miller, J.A. and Becker, M. 2020. A Mineral X-ray Linear Attenuation Coefficient Tool (MXLAC) to Assess Mineralogical Differentiation for X-ray Computed Tomography Scanning. *Minerals*. 10:8–11. Available: doi:10.3390/min10050441.
- Basson, I. and Miller, J.A. 2014. Application of XCT in determining the 3-D environment of PGM and sulphide minerals in Merensky and UG2 Reefs, Bushveld Complex. (September):2–4.
- Baum, W. 2014. Ore characterization, process mineralogy and lab automation a roadmap for future mining. *Minerals Engineering*. 60:69–73. DOI: 10.1016/J.MINENG.2013.11.008.
- Becker, M., Harris, P.J., Wiese, J.G. and Bradshaw, D.J. 2009. Mineralogical characterisation of

naturally floatable gangue in Merensky Reef ore flotation. *International Journal of Mineral Processing*. 93:246–255. DOI: 10.1016/j.minpro.2009.10.004.

Becker, M., Ramonotsi, M. and Petersen, J. 2012. Proceedings of the 10th International Congress for Applied Mineralogy (ICAM). In *Proceedings of the 10th International Congress for Applied Mineralogy (ICAM)*. Maarten A.T.M. Broekmans, Ed. Trondheim, Norway: Springer, Berlin, Heidelberg. 9. DOI: 10.1007/978-3-642-27682-8.

Becker, M., Wiese, J. and Ramonotsi, M. 2014. Investigation into the mineralogy and flotation performance of oxidised PGM ore. *Minerals Engineering*. 65:24–32. DOI: 10.1016/j.mineng.2014.04.009.

Becker, M., Jardine, M.A., Miller, J.A. and Harris, M. 2016. X-ray Computed Tomography: A geometallurgical tool for 3D textural analysis of drill core? In *Proceedings of the 3rd AusIMM International Geometallurgy Conference*. Perth, Western Australia. 231–240.

Bhide, A., Datar, S. and Stebbins, K. 2019. *Case Histories of Significant Medical Advances: Development of Computed Tomography*. (20). Cambridge, MA, United State of America. DOI: 10.2139/ssrn.3429976.

Bioucas-Dias, J.M., Plaza, A., Camps-Valls, G., Scheunders, P., Nasrabadi, N.M. and Chanussot, J. 2013. Hyperspectral remote sensing data analysis and future challenges. *IEEE Geoscience and Remote Sensing Magazine*. 1:6–36. DOI: 10.1109/MGRS.2013.2244672.

Van den Boogaart, K. and Tolosana-Delgado, R. 2018. Predictive Geometallurgy: An Interdisciplinary Key Challenge for Mathematical Geosciences. In *Handbook of Mathematical Geosciences: Fifty Years of IAMG*. S.B.S. Daya, Q. Cheng, and F. Agterberg, Eds. Springer International Publishing. 673–686. DOI: 10.1007/978-3-319-78999-6.

Brammall, A. 1936. Mineral transformation and their equations. *Science progress-Sage journals*. 30:616–627.

Butcher, A. 2020a. Upscaling of 2D mineralogical information to 3D volumes for geoscience applications using a multi-scale, multi-modal and multi-dimensional approach Upscaling of 2D mineralogical information to 3D volumes for geoscience applications using a multi-scale, *IOP Conference Series: Materials Science and Engineering*. 891:7. DOI: 10.1088/1757-899X/891/1/012006.

Butcher, A.R. 2020b. When Scientists and Engineers Talk – Lessons from the Oil Industry and Applications to Mining.

Byrne, K., Lesage, G., Gleeson, S.A., Piercey, S.J., Lypaczewski, P. and Kyser, K. 2020. Linking mineralogy to litho-geochemistry in the Highland Valley Copper District: Implications for porphyry copper footprints. *Economic Geology*. 115:871–901. DOI: 10.5382/ECONGEO.4733.

Carlson, W.D. 2006. Three-dimensional imaging of earth and planetary materials. *Earth and Planetary Science Letters*. 249:133–147. DOI: 10.1016/j.epsl.2006.06.020.

- Cawthorn, R.G. and Webb, S.J. 2001. Connectivity between the western and eastern limbs of the Bushveld complex. *Tectonophysics*. 330:195–209. DOI: 10.1016/S0040-1951(00)00227-4.
- Chauhan, S., Rühaak, W., Khan, F., Enzmann, F., Mielke, P., Kersten, M. and Sass, I. 2016. Processing of rock core microtomography images: Using seven different machine learning algorithms. *Computers and Geosciences*. 86:120–128. DOI: 10.1016/j.cageo.2015.10.013.
- Chayes, F. 1955. Potash Feldspar as a by-product of the biotite-chlorite transformation. *The University of Chicago Press journal*. 63:75–82.
- Chetty, D., Gryffenberg, L., Lekgetho, T. and Molebale, I.. 2009. Automated SEM study of PGM distribution across a UG2 concentrate bank: implications for understanding PGM flotability. *The Journal of The Southern African Institute of Mining and Metallurgy*. 109:587–593.
- Cloete, L.M. and Slabbert, W. 2018. Current Geometallurgical initiatives at the Siguiri Gold Mine, Guinea. In *Proceedings of the SAIMM Geometallurgy Conference Proceedings*. Cape Town, South Africa: The South African Institute of Mining and Metallurgy. 133–150.
- Cnudde, V. and Boone, M.N. 2013. High-resolution X-ray computed tomography in geosciences: A review of the current technology and applications. *Earth-Science Reviews*. 123:1–17. DOI: 10.1016/j.earscirev.2013.04.003.
- Coward, S., Vann, J., Dunham, S. and Stewart, M. 2009. The Primary-Response Framework for Geometallurgical Variables. In *Seventh International Mining Geology Conference*. Perth, Western Australia. 109–113.
- Cracknell, M.J., Parbhakar-Fox, A., Jackson, L. and Savinova, E. 2018. Automated acid rock drainage indexing from drill core imagery. *Minerals*. 8:1–11. DOI: 10.3390/min8120571.
- Deng, H., Fitts, J.P. and Peters, C.A. 2016. Quantifying fracture geometry with X-ray tomography: Technique of Iterative Local Thresholding (TILT) for 3D image segmentation. *Computational Geosciences*. 20:231–244. DOI: 10.1007/s10596-016-9560-9.
- Deschamps, F., Godard, M., Guillot, S. and Hattori, K. 2013. Geochemistry of subduction zone serpentinites: A review. *Lithos*. 178:96–127. DOI: 10.1016/j.lithos.2013.05.019.
- de Villiers, J. 2016. X-ray diffraction in mineralogy. In *Process Mineralogy: JKMRRC Monograph Series in Mining and Mineral Processing*, No 6. M. Becker, E.M. Wightman, C.L. Evans, Eds. Brisbane, Australia: Julius Kruttschnitt Mineral Research Centre. 67–78.
- Dhawan, N., Safarzadeh, M.S., Miller, J.D., Moats, M.S., Rajamani, R.K. and Lin, C.L. 2012. Recent advances in the application of X-ray computed tomography in the analysis of heap leaching systems. *Minerals Engineering*. 35:75–86. DOI: 10.1016/j.mineng.2012.03.033.
- Dominy, S.C., Platten, I.M., Howard, L.E., Elangovan, P., Armstrong, R., Minnitt, R.C.A. and Abel, R.L. 2011. Characterisation of gold ores by X-ray computed tomography - Part 2: Applications to the determination of gold particle size and distribution. In *The first AusIMM International Geometallurgy*

- Conference. D. Dominy, Ed. Brisbane, Qld: Carlton South, Vic. : AusIMM. 293–309.
- Donskoi, E., Poliakov, A., Holmes, R., Suthers, S., Ware, N., Manuel, J. and Clout, J. 2016. Iron ore textural information is the key for the prediction of downstream process performance. *Minerals Engineering*. 86:10–23. DOI: 10.1016/j.mineng.2015.11.009.
- Duée, C., Orberger, B., Maubec, N., Laperche, V. and Capar, L. 2019. Impact of heterogeneities and surface roughness on pXRF, pIR, XRD and Raman analyses: Challenges for online, real-time combined mineralogical and chemical analyses on drill cores and implication for “high speed” Ni- laterite exploration. *Journal of Geochemical Exploration*. 198:1–17. DOI: 10.1016/j.gexplo.2018.12.010.
- Dzingai, T., McFadzean, B., Tadie, M. and Becker, M. 2021. Decoupling the effects of alteration on the mineralogy and flotation performance of Great Dyke PGE ores. *Journal of the Southern African Institute of Mining and Metallurgy*. 121:475–485.
- Fandrich, R., Gu, Y., Burrows, D. and Moeller, K. 2007. Modern SEM-based mineral liberation analysis. *International Journal of Mineral Processing*. 84:310–320. DOI: 10.1016/j.minpro.2006.07.018.
- Fitzgerald, R., Keil, K. and Heinrich, K.F.J. 1968. Solid-state Energy-Dispersion Spectrometer for Electron-Microprobe X-ray Analysis. *Science*. 159(3814):528–530. DOI: <https://doi.org/10.1126/science.159.3814.528>.
- Fowler, J.E. 2014. Compressive pushbroom and whiskbroom sensing for hyperspectral remote-sensing imaging. In *International Conference on Image Processing (ICIP)*. Mississippi State University, USA: IEEE. 684–688.
- Gasser, C., González-Cabrera, M., Ayora-Cañada, M.J., Domínguez-Vidal, A. and Lendl, B. 2019. Comparing mapping and direct hyperspectral imaging in stand-off Raman spectroscopy for remote material identification. *Journal of Raman Spectroscopy*. 50:1034–1043. DOI: 10.1002/jrs.5607.
- Ghent, B.- and Mol, B.-. 2019. Applications of X-ray computed tomography in the geosciences. 21:1–6.
- Ghorbani, Y., Becker, M., Petersen, J., Morar, S.H., Mainza, A. and Franzidis, J.P. 2011. Use of X-ray computed tomography to investigate crack distribution and mineral dissemination in sphalerite ore particles. *Minerals Engineering*. 24:1249–1257. DOI: 10.1016/j.mineng.2011.04.008.
- Girão, A.V., Caputo, G. and Ferro, M.C. 2017. Application of Scanning Electron Microscopy–Energy Dispersive X-Ray Spectroscopy (SEM-EDS). *Comprehensive Analytical Chemistry*. 75:153–168. DOI: 10.1016/bs.coac.2016.10.002.
- Godel, B. 2013. High-resolution X-ray computed tomography and its application to ore deposits: From data acquisition to quantitative three-dimensional measurements with case-studies from Ni-Cu-PGE Deposits. *Economic Geology*. 108:2005–2019. DOI: 10.2113/econgeo.108.8.2005.
- Godel, B., Engineering, R. and Resources, A. 2019. High-Resolution X-ray Computed Tomography and Its Application to Ore Deposits: From Data Acquisition to Quantitative Three-Dimensional

- Measurements with Case Studies from Ni-Cu-PGE Deposits. *Society of Economic Geologists, Inc. Economic Geology*. 108:2005–2019.
- Goetz, A.F.H., Vane, G., Solomon, J.E. and Rock, B.N. 1985. Imaging spectrometry for earth remote sensing. *Science*. 228:1147–1153. DOI: 10.1126/science.228.4704.1147.
- Gottlieb, P., Wilkie, G., Sutherland, D., Ho-Tun, E., Suthers, S., Perera, K., Jenkins, B., Spencer, S., et al. 2000. Using quantitative electron microscopy for process mineralogy applications. *Journal of the Minerals, Metals and Materials Society (JOM)*. 52:24–25. DOI: 10.1007/s11837-000-0126-9.
- Graham, S.D., Brough, C.P. and Cropp, A. 2015. An introduction to ZEISS Mineralogic Mining and the correlation of light microscopy with automated mineralogy: a case study using BMS and PGM analysis of samples from a PGE-bearing chromitite prospect. In *Precious Metals '15*. 10.
- Gribble, C.D. 1993. *Optical Mineralogy*. 3rd ed. DOI: 10.1201/b12647.
- Gu, Y., Schouwstra, R. and Wang, D. 2012. A comparison between 2D and 3D particle size measurements. In *Process Mineralogy '12*. Cape Town, South Africa: Minerals Engineering International (MEI). 1–4.
- Guntoro, P.I., Ghorbani, Y., Koch, P.H. and Rosenkranz, J. 2019. X-ray microcomputed tomography (μ ct) for mineral characterization: A review of data analysis methods. *Minerals*. 9:20–26. DOI: 10.3390/min9030183.
- Haavisto, O., Kauppinen, T. and Hakkanen, H. 2013. Laser-induced breakdown spectroscopy for rapid elemental analysis of drillcore. In *16th IFAC Symposium on Automation in Mining, Minerals and Metal Processing: IFAC Proceedings Volumes (IFAC-PapersOnline)*. V. 46. San Diego, California, USA. 87–91. DOI: 10.3182/20130825-4-US-2038.00047.
- Harraden, C.L., Cracknell, M.J., Lett, J., Berry, R.F., Carey, R. and Harris, A.C. 2019. Automated core logging technology for geotechnical assessment: A study on core from the Cadia East porphyry deposit. *Economic Geology*. 114:1495–1511. DOI: 10.5382/econgeo.4649.
- Hey, P. V. 1999. The effects of weathering on the UG2 Chromitite Reef of the Bushveld Complex, with special reference to the platinum-group minerals. *South African Journal of Geology*. 102:251–260.
- Howard, L.E., Elangovan, P., Dominy, S.C., Armstrong, R., Hezel, D. and Abel, R.L. 2011. Characterisation of gold ores by X-ray computed tomography - Part 1: Software for calibration and quantification of mineralogical phases. In *GeoMet 2011 - 1st AusIMM International Geometallurgy Conference 2011*. D. Dominy, Ed. Brisbane, Qld: Carlton South, Vic. : AusIMM. 321–330.
- Hunt, G.R. 1977. Spectral signatures of particulate minerals in the visible and near-infrared. *Geophysics*. 42:501–513. DOI: 10.1190/1.1440721.
- Hunt, J., Berry, R., Becker, M. and Baumgartner, R. 2019. A special issue dedicated to geometallurgy: Preface. *Economic Geology*. 114:1473–1479. DOI: 10.5382/econgeo.4688.

- Iyer, K., Austrheim, H., John, T. and Jamtveit, B. 2008. Serpentinization of the oceanic lithosphere and some geochemical consequences: Constraints from the Leka Ophiolite Complex, Norway. *Chemical Geology*. 249:66–90. DOI: 10.1016/j.chemgeo.2007.12.005.
- Jacq, K., Giguët-Covex, C., Sabatier, P., Perrette, Y., Fanget, B., Coquin, D., Debret, M. and Arnaud, F. 2019. High-resolution grain size distribution of sediment core with hyperspectral imaging. *Sedimentary Geology*. 393:10. DOI: 10.1016/j.sedgeo.2019.105536.
- Jardine, M.A., Miller, J.A. and Becker, M. 2018. Coupled X-ray computed tomography and grey level co-occurrence matrices as a method for quantification of mineralogy and texture in 3D. *Computers and Geosciences*. 111:105–117. DOI: 10.1016/j.cageo.2017.11.005.
- Johnson, C.L., Browning, D.A. and Pendock, N.E. 2019. Hyperspectral imaging applications to geometallurgy: Utilizing blast hole mineralogy to predict Au-Cu recovery and throughput at the Phoenix mine, Nevada. *Economic Geology*. 114:1481–1494. DOI: 10.5382/econgeo.4684.
- Kable, E.J.D. and Becker, M. 2016. Chemical assays. *In Process Mineralogy: JKMRRC Monograph Series in Mining and Mineral Processing, No 6*. M. Becker, E.M. Wightman, and C.L. Evans, Eds. Brisbane, Australia: Julius Kruttschnitt Mineral Research Centre. 36-50.
- Kale, K. V., Solankar, M.M., Nalawade, D.B., Dhumal, R.K. and Gite, H.R. 2017. A Research Review on Hyperspectral Data Processing and Analysis Algorithms. *Proceedings of the National Academy of Sciences India Section A - Physical Sciences*. 87:541–555. DOI: 10.1007/s40010-017-0433-y.
- Kaufhold, A., Halisch, M., Zacher, G. and Kaufhold, S. 2016. X-ray computed tomography investigation of structures in Opalinus Clay from large-scale to small-scale after mechanical testing. *Solid Earth*. 7:1171–1183. DOI: 10.5194/se-7-1171-2016.
- Keeney, L. and Walters, S.G. 2008. *JK Mineral Research Centre, University of Queensland ARC Centre of Excellence in Ore Deposits, University of Tasmania*.
- Ketcham, R.A. and Carlson, W.D. 2001. Acquisition, optimization and interpretation of x-ray computed tomographic imagery: Applications to the geosciences. *Computers and Geosciences*. 27:381–400. DOI: 10.1016/S0098-3004(00)00116-3.
- Koch, P. and Rosenkranz, J. 2020. Sequential decision-making in mining and processing based on geometallurgical inputs. *Minerals Engineering*. 149. DOI: 10.1016/j.mineng.2020.106262.
- Koch, P.H., Lund, C. and Rosenkranz, J. 2019. Automated drill core mineralogical characterization method for texture classification and mineral grades estimation for geometallurgy. *Minerals Engineering*. 136:99–109. DOI: 10.1016/j.mineng.2019.03.008.
- Koerting, F., Rogass, C., Kaempfer, H., Lubitz, C., Harms, U., Schudack, M., Kokaly, R., Mielke, C., et al. 2015. Drill core mineral analysis by means of the hyperspectral imaging spectrometer HySpex, XRD and ASD in the proximity of the Mýtina Maar, Czech Republic. *International Archives of the Photogrammetry, Remote Sensing and Spatial Information Sciences - ISPRS Archives*. 40:417–424.

DOI: 10.5194/isprsarchives-XL-1-W5-417-2015.

Kruse, F.A. 1996. Identification and mapping of minerals in drill core using hyperspectral image analysis of infrared reflectance spectra. *International Journal of Remote Sensing*. 17:1623–1632. DOI: 10.1080/01431169608948728.

Kruse, F.A., Bedell, R.L., Taranik, J. V., Peppin, W.A., Weatherbee, O. and Calvin, W.M. 2012. Mapping alteration minerals at the prospect, outcrop and drill core scales using imaging spectrometry. *International Journal of Remote Sensing*. 33:1780–1798. DOI: 10.1080/01431161.2011.600350.

Kurz, T.H., Buckley, S.J. and Becker, J.K. 2017. Hyperspectral imaging: a novel geological mapping technique for subsurface construction sites. In *World Tunnel Congress 2017 – Surface challenges – Underground solutions*. 1–10.

Kyle, J.R. and Ketcham, R.A. 2015. Application of high-resolution X-ray computed tomography to mineral deposit origin, evaluation, and processing. *Ore Geology Reviews*. 65:821–839. DOI: 10.1016/j.oregeorev.2014.09.034.

Kyle, J.R., Mote, A.S. and Ketcham, R.A. 2008. High-resolution X-ray computed tomography studies of Grasberg porphyry Cu-Au ores, Papua, Indonesia. *Mineralium Deposita*. 43:519–532. DOI: 10.1007/s00126-008-0180-8.

Lamberg, P., Rosenkranz, J., Wanhainen, C., Lund, C., Minz, F.E., Mwanga, A. and Amiri Parian, M. 2013. Building a Geometallurgical Model in Iron Ores using a Mineralogical Approach with Liberation Data. In *2nd AusIMM International Geometallurgy Conference*. Brisbane, Australia. 317–324.

Lau, I.. 2004. Regolith-landform and mineralogical mapping of the White Dam Prospect, eastern Olary Domain, South Australia, using integrated remote sensing and spectral techniques. PhD Thesis. University of Adelaide Australia.49-109.

Lechuti-Tlhalerwa, R.. and Gilika, O. 2018. Modelling Geometallurgical variability of comminution parameters in Orapa kimberlite ore. In *Proceedings of the SAIMM Geometallurgy Conference Proceedings*. Cape Town, South Africa: The South African Institute of Mining and Metallurgy. 253–264.

Li, C., Ripley, E., Merino, E. and Maier, W.D. 2004. Replacement of base metal sulphides by actinolite, epidote, calcite, and magnetite in the UG2 and Merensky Reef of the Bushveld Complex, South Africa. *Economic Geology*. 99:173–184. DOI: 10.1016/S0361-1124(78)80358-X.

Lin, C.L., Miller, J.D., Cortes, A.B. and Galery, R. 1991. Coal washability analysis by x-ray computed tomography. *Coal preparation*. 9:107–119. DOI: 10.1080/07349349108960560.

Lindholm, R.C. 1987. Mineral identification using X-ray diffraction. In *A Practical Approach to Sedimentology*. Springer, Dordrecht. 124–153. DOI: 10.1007/978-94-011-7683-5_6.

Linton, P., Browning, D., Pendock, N., Harris, P., Donze, M., Mxinwa, T. and Mushiana, K. 2018. Hyperspectral data applied to geometallurgy. In *Proceedings of the SAIMM Geometallurgy Conference Proceedings*. Cape Town, South Africa: The South African Institute of Mining and Metallurgy. 109–120.

- Lishchuk, V. and Pettersson, M. 2021. The mechanisms of decision-making when applying geometallurgical approach to the mining industry. *Mineral Economics*. 34(1):71–80. DOI: 10.1007/s13563-020-00220-9.
- Lishchuk, V., Lamberg, P. and Lund, C. 2015. Classification of Geometallurgical Programs Based on Approach and Purpose. In *13th Biennial SGA Meeting*. Nancy, France. 1431–1434.
- Lotter, N.O., Bradshaw, D.J., Becker, M., Parolis, L.A.S. and Kormos, L.J. 2008. A discussion of the occurrence and undesirable flotation behaviour of orthopyroxene and talc in the processing of mafic deposits. *Minerals Engineering*. 21:905–912. DOI: 10.1016/j.mineng.2008.02.023.
- Lotter, N.O., Kormos, L.J., Oliveira, J., Fragomeni, D. and Whiteman, E. 2011. Modern process mineralogy: Two case studies. *Minerals Engineering*. 24:638–650. DOI: 10.1016/j.mineng.2011.02.017.
- Lotter, N.O., Baum, W., Reeves, S., Arrué, C. and Bradshaw, D.J. 2017. The business value of best practice process mineralogy. *Minerals Engineering*. (May):0–1. DOI: 10.1016/j.mineng.2017.05.008.
- Lund, C., Lamberg, P. and Lindberg, T. 2015. Development of a geometallurgical framework to quantify mineral textures for process prediction. *Minerals Engineering*. 82:61–77. DOI: 10.1016/j.mineng.2015.04.004.
- Mateen, M., Wen, J., Nasrullah and Akbar, M.A. 2018. The role of Hyperspectral Imaging: A literature review. *International Journal of Advanced Computer Science and Applications*. 9:51–62. DOI: 10.14569/ijacsa.2018.090808.
- Mathieu, M., Roy, R., Launeau, P., Cathelineau, M. and Quirt, D. 2017. Alteration mapping on drill cores using a HySpex SWIR-320m hyperspectral camera: Application to the exploration of an unconformity-related uranium deposit (Saskatchewan, Canada). *Journal of Geochemical Exploration*. 172:71–88. DOI: 10.1016/j.gexplo.2016.09.008.
- Matsau, E.N. 2003. Determination of platinum, palladium, rhodium and gold in platiniferous ores using ICP-MS and microwave dissolution. MSc Thesis. University of Stellenbosch.140.
- Mauger, A.J., Keeling, J.L. and Huntington, J.F. 2007. Alteration mapping of the Tarcoola Goldfield (South Australia) using a suite of hyperspectral methods. *Transactions of the Institutions of Mining and Metallurgy, Section B: Applied Earth Science*. 116:2–12. DOI: 10.1179/174327507X167028.
- McCall, M.J. 2016. Mineralogical and geochemical variations in the UG2 Reef at Booyendal and Zondereinde mines, with implications for beneficiation of PGM. MSc Thesis. Stellenbosch University.140.
- McCullom, T.M. and Bach, W. 2009. Thermodynamic constraints on hydrogen generation during serpentinization of ultramafic rocks. *Geochimica et Cosmochimica Acta*. 73:856–875. DOI: 10.1016/j.gca.2008.10.032.
- McCoy, J.T. and Auret, L. 2019. Machine learning applications in minerals processing: A review. *Minerals Engineering*. 132:95–109. DOI: 10.1016/j.mineng.2018.12.004.

- McGrath, T.D.H., O'Connor, L. and Eksteen, J.J. 2015. A comparison of 2D and 3D shape characterisations of free gold particles in gravity and flash flotation concentrates. *Minerals Engineering*. 82:45–53. DOI: 10.1016/j.mineng.2015.04.022.
- McHugh, E., Girard, J. and Denes, L. 2001. Simplified hyperspectral imaging for improved geologic mapping of mine slopes. In *the Third International Conference on Intelligent Processing and Manufacturing of Materials*. 143–152. Available: <https://www.cdc.gov/niosh/mining/UserFiles/works/pdfs/shifig.pdf>
<http://www.cdc.gov/niosh/mining/pubs/pdfs/shifig.pdf>.
- McMillan, N.J., Harmon, R.S., De Lucia, F.C. and Miziolek, A.M. 2007. Laser-induced breakdown spectroscopy analysis of minerals: Carbonates and silicates. *Spectrochimica Acta - Part B Atomic Spectroscopy*. 62:1528–1536. DOI: 10.1016/j.sab.2007.10.037.
- Mees, F., Swennen, R., Van Geet, M. and Jacobs, P. 2003. Applications of X-ray Computed Tomography in the Geosciences. *Geological Society, London, Special Publications*. 215:1–6. Available: www.geolsoc.org.uk.
- Merrill, J., Diaz, E., Voisin, L. and Townley, B. 2018. Mineral and textural classification from Hyperspectral data for geometallurgical approach. In *Resources for Future Generations*. Chile: ResearchGate. 34.
- Mielke, C., Rogaß, C., Broadhurst, J.L., Becker, M., Franzidis, J. and Wit, M.J. De. 2010. Hyperspectral Remote Sensing of mine tailings in South Africa. (June):2010.
- Mielke, C., Boesche, N.K., Rogass, C., Kaufmann, H., Gauert, C. and de Wit, M. 2014. Spaceborne mine waste mineralogy monitoring in South Africa, applications for modern push-broom missions: Hyperion/OLI and EnMAP/Sentinel-2. *Remote Sensing*. 6:6790–6816. DOI: 10.3390/rs6086790.
- Miller, J.A. 2014. The Application of XCT in Determining the 3-D Environment of In-Situ PGM Grains and Associated Minerals from the Bushveld Complex, South Africa. (August):1–2.
- Miller, J.D., Lin, C.L., Garcia, C. and Arias, H. 2003. Ultimate recovery in heap leaching operations as established from mineral exposure analysis by X-ray microtomography. *International Journal of Mineral Processing*. 72:331–340. DOI: 10.1016/S0301-7516(03)00091-7.
- Miller, J.D., Lin, C.L., Hupka, L. and Al-Wakeel, M.I. 2009. Liberation-limited grade/recovery curves from X-ray micro CT analysis of feed material for the evaluation of separation efficiency. *International Journal of Mineral Processing*. 93:48–53. DOI: 10.1016/j.minpro.2009.05.009.
- Mohamed, S.B. 2018. Characterizing The Surface Mineralogy in the Aggeneys Sedex System with Hyperspectral Imagery. MSc Thesis. University of Twente. 61. Available: https://webapps.itc.utwente.nl/librarywww/papers_2018/msc/aes/mohamed.pdf.
- Molifie, A. 2021. Investigating the use of sodium metasilicate to improve the flotation performance of altered PGE ores. PhD Thesis. University of Cape town.

- Monali, P., and Snehal, M.. 2014. Hyperspectral imaging. *Food Engineering Series*. 2:199–216. DOI: 10.1007/978-1-4939-0311-5_9.
- Morrison, R. and Gu, Y. 2016. X-ray Computed Microtomography. In *Process Mineralogy: JKMRM Monograph Series in Mining and Mineral Processing, No 6*. M. Becker, E.M. Wightman, C.L. Evans, Eds. Brisbane, Australia: Julius Kruttschnitt Mineral Research Centre. 133–148.
- Ndlovu, B., Forbes, E., Farrokhpay, S., Becker, M., Bradshaw, D. and Deglon, D. 2014. A preliminary rheological classification of phyllosilicate group minerals. *Minerals Engineering*. 55:383–389. DOI: 10.1016/j.mineng.2013.06.004.
- Nguyen, K. 2013. A New Texture Analysis Technique for Geometallurgy. In *The second AUSIMM International Geometallurgy Conference*. Brisbane, Qld: The Australasian Institute of Mining and Metallurgy. 187–190.
- Nwaila, G., Becker, M., Ghorbani, Y., Petersen, J., Reid, D.L. and Bam, L.C. 2013. A Geometallurgical Study of the Witwatersrand Gold Ore at Carletonville, South Africa. In *The second AUSIMM International Geometallurgy Conference*. Brisbane, Qld: The Australasian Institute of Mining and Metallurgy. 75–83.
- Okada, N., Maekawa, Y., Owada, N., Haga, K., Shibayama, A. and Kawamura, Y. 2020. Automated identification of mineral types and grain size using hyperspectral imaging and deep learning for mineral processing. *Minerals*. 10:1–22. DOI: 10.3390/min10090809.
- Pacey, A., Wilkinson, J.J. and Cooke, D.R. 2020. Chlorite and epidote mineral chemistry in porphyry ore systems: A case study of the northparkes district, New South Wales, Australia. *Economic Geology*. 115:701–727. DOI: 10.5382/econgeo.4700.
- Pan, Z., Liu, J., Ma, L., Chen, F., Zhu, G., Qin, F., Zhang, H., Huang, J., et al. 2019. Research on hyperspectral identification of altered minerals in Yemaquan West Gold Field, Xinjiang. *Sustainability (Switzerland)*. 11:20. DOI: 10.3390/su11020428.
- Paradis, M.C.M., Doucet, F.R., Rifai, K., Özcan, L., Azami, N. and Vidal, F. 2021. Ecore: A new fast automated quantitative mineral and elemental core scanner. *Minerals*. 11:16. DOI: 10.3390/min11080859.
- Parbhaker-Fox, A., Lottermoser, B. and Bradshaw, D.J. 2013. Cost-Effective Means for Identifying Acid Rock Drainage Risks – Integration of the Geochemistry- Mineralogy-Texture Approach and Geometallurgical Techniques. In *Proceedings of the Second AusIMM International Geometallurgy Conference*. Brisbane, Qld: The Australasian Institute of Mining and Metallurgy. 143–154.
- Pérez-Barnuevo, L., Lévesque, S. and Bazin, C. 2018. Automated recognition of drill core textures: A geometallurgical tool for mineral processing prediction. *Minerals Engineering*. 118:87–96. DOI: 10.1016/j.mineng.2017.12.015.
- Pirard, E. 2016. Optical Microscopy. In *Process Mineralogy: JKMRM Monograph Series in Mining and*

- Mineral Processing, No 6*. M. Becker, E.M. Wightman, C.L. Evans, Eds. Brisbane, Australia: Julius Kruttschnitt Mineral Research Centre. 51–66.
- Pirrie, D. and Rollinson, G.K. 2011. Unlocking the applications of automated mineral analysis. *Geology Today*. 27:226–235. DOI: 10.1111/j.1365-2451.2011.00818.x.
- Plaza, A., Martínez, P., Pérez, R. and Plaza, J. 2004. A quantitative and comparative analysis of endmember extraction algorithms from hyperspectral data. *IEEE Transactions on Geoscience and Remote Sensing*. 42:650–663. DOI: 10.1109/TGRS.2003.820314.
- Pontual, S., Merry, N. and Gamson, P. 1997. Spectral Analysis Guides for Mineral Exploration. In *Vol 1 - Spectral Interpretation Field Manual*. V. 1. AusSpec International. 763–773. Available: <http://dx.doi.org/10.1016/j.ejwf.2014.03.001><http://dx.doi.org/10.1016/j.ajodo.2009.07.026><https://doi.org/10.1016/j.ortho.2019.11.003><https://doi.org/10.1016/j.ajodo.2018.04.023><http://dx.doi.org/10.1016/j.ajodo.2014.03.023>
- Pownceby, M. and MacRae, C. 2016. Electron probe microanalyser. In *Process Mineralogy: JKMRC Monograph Series in Mining and Mineral Processing, No 6*. M. Becker, E.M. Wightman, C.L. Evans, Eds. Brisbane, Australia: Julius Kruttschnitt Mineral Research Centre. 79–96.
- Prost, G.L. 2013. *Remote Sensing for Geoscientists*. Third ed. Boca Raton, Florida: CRC Press. DOI: 10.1201/b15638.
- Qiu, J.T., Qi, H. and Duan, J.L. 2017. Reflectance spectroscopy characteristics of turquoise. *Minerals*. 7:1–10. DOI: 10.3390/min7010003.
- Raja, S., Rajendran, S., G.B, P. and Thirunavukkarasu, A. 2010. Study on Hyperspectral Signatures for Magnetite Iron ore in Thattayengerpet region of Trichirappalli district in Tamil Nadu State. *International journal of geomatics and geoscience*. 1:188–196.
- Ramakrishnan, D. and Bharti, R. 2015. Hyperspectral remote sensing and geological applications. *Current science*. 108:879–891.
- Ramanaidou, E., Wells, M., Lau, I. and Laukamp, C. 2015. Characterization of iron ore by visible and infrared reflectance and, Raman spectroscopies. In *Iron Ore: Mineralogy, Processing and Environmental Sustainability*. Woodhead Publishing. 191–228. DOI: 10.1016/B978-1-78242-156-6.00006-X.
- Ramos Oliveira, G.J., Horta, D.G., da Silva, F.L., von Krüger, F.L., Araújo, F.G. da S. and Mazzinghy, D.B. 2021. Determination of Mineral Liberation of a Bauxite Ore Based on 3D Compositional and Textural Characteristics Using X-ray Microtomography. *Mineral Processing and Extractive Metallurgy Review*. 00:1–11. DOI: 10.1080/08827508.2021.1986707.
- Ross, P.S., Bourke, A. and Fresia, B. 2013. A multi-sensor logger for rock cores: Methodology and preliminary results from the Matagami mining camp, Canada. *Ore Geology Reviews*. 53:93–111. DOI: 10.1016/j.oregeorev.2013.01.002.

- Rozendaal, A., Roux, S.G. Le, Plessis, A., Philander, C. 2017. Grade and product quality control by microCT scanning of the world-class Namakwa Sands Ti-Zr placer deposit West Coast, South Africa : An orientation study. *Minerals Engineering*. 116:11. DOI: 10.1016/j.mineng.2017.09.001.
- Salehi, S., Mielke, C. and Rogass, C. 2020. Mapping ultramafic complexes using airborne imaging spectroscopy and spaceborne data in Arctic regions with abundant lichen cover, a case study from the Niaqornarsuit complex in South West Greenland. *European Journal of Remote Sensing*. 53:156–175. DOI: 10.1080/22797254.2020.1760733.
- Schulz, B., Sandmann, D. and Gilbricht, S. 2020. Sem-based automated mineralogy and its application in geo-and material sciences. *Minerals*. 10:1–26. DOI: 10.3390/min10111004.
- Schwarzenbach, E.M., Gazel, E. and Caddick, M.J. 2014. Hydrothermal processes in partially serpentinized peridotites from Costa Rica: evidence from native copper and complex sulfide assemblages. *Contributions to Mineralogy and Petrology*. 168:1–21. DOI: 10.1007/s00410-014-1079-2.
- Scoon, R.N. 1987. Metasomatism of cumulus magnesian olivine by iron-rich postcumulus liquids in the upper Critical Zone of the Bushveld Complex. *Mineralogical Magazine*. 51:389–396. DOI: 10.1180/minmag.1987.051.361.05.
- Sehoole, L.T.. 2019. Application of 3D seismics to enhance mapping of potholes in the western Bushveld Complex, South Africa. MSc Thesis. University of the Witwatersrand.169.
- Selci, S. 2019. The future of hyperspectral imaging. *Journal of Imaging*. 5:7. DOI: 10.3390/jimaging5110084.
- Shanks, W.C.P. 2012. Hydrothermal alteration: volcanogenic massive sulfide occurrence model. *US Geological Survey Scientific Investigations*. 165–180.
- Sharma, R.K. 2017. Various Spectroscopic Techniques. In *Environmental Pollution: Monitoring, Modeling and Control*. 181–206.
- Sharma, S.K., Misra, A.K., Lucey, P.G., Wiens, R.C. and Clegg, S.M. 2007. Combined remote LIBS and Raman spectroscopy at 8.6 m of sulfur-containing minerals, and minerals coated with hematite or covered with basaltic dust. *Spectrochimica Acta - Part A: Molecular and Biomolecular Spectroscopy*. 68:1036–1045. DOI: 10.1016/j.saa.2007.06.046.
- Shervais, J.W., Kolesar, P. and Andreasen, K. 2005. A Field and Chemical Study of Serpentinization—Stonyford, California: Chemical Flux and Mass Balance. *International Geology Review*. 47:1–23. DOI: 10.2747/0020-6814.47.1.1.
- Signoroni, A., Savardi, M., Baronio, A. and Benini, S. 2019. Deep learning meets hyperspectral image analysis: A multidisciplinary review. *Journal of Imaging*. 5. DOI: 10.3390/jimaging5050052.
- Smith, A.J.B., Viljoen, K.S., Schouwstra, R., Roberts, J., Schalkwyk, C. and Gutzmer, J. 2013. Geological variations in the Merensky Reef at Bafokeng Rasimone Platinum Mine and its influence on

- flotation performance. *Minerals Engineering*. 52:155–168. DOI: 10.1016/j.mineng.2013.05.015.
- Son, Y.-S., You, B.-W., Bang, E.-S., Cho, S.-J., Kim, K.-E., Baik, H. and Nam, H.-T. 2021. remote sensing Mapping Alteration Mineralogy in Eastern Tsogttsetsii, Mongolia, Based on the WorldView-3 and Field Shortwave-Infrared Spectroscopy Analyses. *MDPI remote sensing*. 13:34. DOI: 10.3390/rs13050914.
- Speakman, S.A. 1902. Introduction to X-Ray Powder Diffraction Data Analysis. Massachusetts Institute of Technology. Available: <https://www.researchgate.net/file.PostFileLoader.html?id=58d22df3dc332d06c7245969&assetKey=AS%3A474618730422273%401490169331513>.
- Sriram, B., Meier, P.M. and Reinagel, P. 2016. Temporal and spatial tuning of dorsal lateral geniculate nucleus neurons in unanesthetized rats. *Journal of Neurophysiology*. 115:2658–2671. DOI: 10.1152/jn.00812.2014.
- Stapley, T., Drennan, G.R., Tshibubudze, A., Nwaila, G.T. and Kirk, J.D. 2016. Computed tomographic analyses on gold occurrence and distribution in drill-core samples. 4.
- Sture, Ø., Snook, B. and Ludvigsen, M. 2019. Obtaining hyperspectral signatures for seafloor massive sulphide exploration. *Minerals*. 9:1–21. DOI: 10.3390/min9110694.
- Sutherland, D. 2007. Estimation of mineral grain size using automated mineralogy. *Minerals Engineering*. 20:452–460. DOI: 10.1016/j.mineng.2006.12.011.
- Thiele, S.T., Lorenz, S., Kirsch, M., Cecilia Contreras Acosta, I., Tusa, L., Herrmann, E., Möckel, R. and Gloaguen, R. 2021. Multi-scale, multi-sensor data integration for automated 3-D geological mapping. *Ore Geology Reviews*. 136:12. DOI: 10.1016/j.oregeorev.2021.104252.
- Tusa, L., Andreani, L., Khodadadzadeh, M., Contreras, C., Ivascanu, P., Gloaguen, R. and Gutzmer, J. 2019. Mineral mapping and vein detection in hyperspectral drill-core scans: Application to porphyry-type mineralization. *Minerals*. 9:1–23. DOI: 10.3390/min9020122.
- Tuşa, L., Khodadadzadeh, M., Contreras, C., Shahi, K.R., Fuchs, M., Gloaguen, R. and Gutzmer, J. 2020. Drill-core mineral abundance estimation using hyperspectral and high-resolution mineralogical data. *Remote Sensing*. 12:23. DOI: 10.3390/rs12071218.
- Tzamos, E., Bussolesi, M., Grieco, G., Marescotti, P., Crispini, L., Kasinos, A., Storni, N., Simeonidis, K., et al. 2020. Mineralogy and Geochemistry of Ultramafic Rocks from Rachoni Magnesite Mine, Gerakini (Chalkidiki, Northern Greece). *Minerals*. 9:34. DOI: 10.3390/min10110934.
- Vadivambal, R. and Jayas, D.S. 2015. Hyperspectral imaging. In *Bio-Imaging*. V. 2. 128–167. DOI: 10.1201/b18840-9.
- Van Dalen, G. and Koster, M.W. 2012. 2D and 3D particle size analysis of micro-CT images. *Bruker-microCT User Meeting*. 16. Available: <http://bruker-microct.com/company/UM2012/31.pdf>.

- Van der Plas, L. and Tobi, A.C. 1950. A chart for judging the reliability of point counting results. *American Journal of Science*. 263:87 LP – 90. DOI: 10.2475/ajs.263.1.87.
- Vezhapparambu, V., Eidsvik, J. and Ellefmo, S.. 2018. Rock Classification Using Multivariate Analysis of Measurement While Drilling Data : Towards a Better. *Minerals*. 384:23. DOI: 10.3390/min8090384.
- Viljoen, M.J. 1999. The nature and origin of the Merensky Reef of the western Bushveld Complex based on geological facies and geophysical data. V. 02. 221–239.
- Viring, R.G. and Cowell, M.W. 1999. The Merensky Reef on Northam Platinum Limited. *South African Journal of Geology*. 102:192–208.
- Voigt, M., Miller, J.A., Mainza, A.N., Bam, L.C. and Becker, M. 2020. The Robustness of the Gray Level Co-Occurrence Matrices and X-Ray Computed Tomography Method for the Quantification of 3D Mineral Texture. *Minerals*. 10:24–26. DOI: 10.3390/min10040334.
- Voigt, M.J., Miller, J., Bbosa, L., Govender, R.A., Bradshaw, D., Mainza, A. and Becker, M. 2019. Developing a 3D mineral texture quantification method of drill core for geometallurgy. *Journal of the Southern African Institute of Mining and Metallurgy*. 119:347–353. DOI: 10.17159/2411-9717/590/2019.
- Wang, Y. and Miller, J.D. 2020. Current developments and applications of micro-CT for the 3D analysis of multiphase mineral systems in geometallurgy. *Earth-Science Reviews*. 211:103406. DOI: 10.1016/j.earscirev.2020.103406.
- Wang, D., Yuan, X., Gu, Y., Case, T. and Feser, M. 2014. Investigation of MicroCT (Computed Tomography) for 3- Dimensional Mineral Characterization – A Dual Energy Approach. In *Minerals Engineering Conferences: Process Mineralogy '14*. Cape Town, South Africa. 8.
- Wells, M.A. 2013. Raman Spectroscopic Core Scanning for Iron Ore and BIF Characterization Raman Spectroscopic Core Scanning for Iron Ore and BIF Characterization. In *Proceedings of the 11th International Congress for Applied Mineralogy (ICAM), Springer Geochemistry/Mineralogy*. F. Dong, Ed. Mianyang, China: Springer, Cham. 387–396. DOI: 10.1007/978-3-319-13948-7.
- Wu, D., Pan, J., Xia, F., Huang, G. and Lai, J. 2019. The mineral chemistry of chlorites and its relationship with uranium mineralization from huangsha uranium mining area in the middle nanling range, SE China. *Minerals*. 9:23. DOI: 10.3390/min9030199.
- Yang, B. hua, Wu, A. xiang, Narsilio, G.A., Miao, X. xiu and Wu, S. yue. 2017. Use of high-resolution X-ray computed tomography and 3D image analysis to quantify mineral dissemination and pore space in oxide copper ore particles. *International Journal of Minerals, Metallurgy and Materials*. 24:965–973. DOI: 10.1007/s12613-017-1484-4.

Appendix

Appendix A: Scanning parameters

Table A1: Hyperspectral imaging system specifications





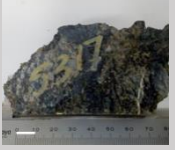





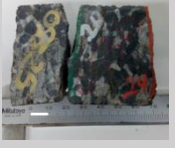


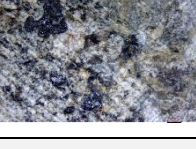
System Specifications	Hyperspectral Cameras	RGB Camera
Wavelength Range	380-2500nm (FENIX) 7700-12300nm (OWL)	Not Applicable
Infrared Zone Covered	VNIR/ SWIR (FENIX) LWIR (OWL)	Visible
Spectral Band Width	3.4/ 6/ 48nm	Not applicable
Spectral Resolution	3.5/ 12/ 100nm	Not applicable
Spectral Bands	174/ 274/ 96 bands	3 bands
Image Dimensions	384 pixels across the track	4000 pixels across the track
Pixel Size (Spatial Resolution)	±1mm@32.3° FOV*	±0.16mm@640mm FOV*
Camera Serial Number	350016 (FENIX) 920015 (OWL)	B04709
Camera Calibration	Spectral calibration, normalised	White balance
Scan Rate	170mm/ s @ 1mm pixel size	170mm/ s @ 0.10mm pixel size
Maximum Sample Size	1500mm (length) x 640mm (width) x 300mm (height), 50kg	
Operating Conditions	Enclosed facility (limited dust), 0 to +40°C, non-condensing	
Operating Voltage	220/ 240V; 50/ 60Hz	
System Dimensions	5.5m x 1.5m x 2.5m (l x w x h)	
Output File Format	BIL file format, ENVI compatible	

*FOV- Field of view

Appendix B: Core logging

Table B1 and B2: Summary table for the lithological description, mineral assemblage, and texture for drill core RD015 and TU277, respectively. Mineral abbreviations: plagioclase (Pl), pyroxene (pxn), orthopyroxene (Opx), clinopyroxene (Cpx), olivine (Ol), amphibole (Amp), serpentine (Srp), biotite (Bt), magnetite (Mag), Chromite (Cr), pentlandite (Pn), chalcopyrite (Ccp) and pyrrhotite (Pn). (Whitney and Evans, 2010)

Appendix

Width (m) (depth m)	Drill core RD015 Stratigraphy	Lithology	Rock images		Description	Minerals		
			Photograph	Micrographs		Major	Minor	Sulphides
0.1 (23.82 -23.92)	Merensky Footwall	Mottled Anorthosite			White and black medium-grained rock with red tints due to ccp oxidation. The rock is cross-cut by fine to medium cumulate chromitite grains some with Ccp inclusions and anastomosing calcite veins (1 mm to 6 mm) cutting across the rock sample at 25-30°. Cr grains form a linear shape (stringer). The rock gradually changes to harzburgite with increasing pyroxene abundance and grain size.	pl, pxn, ol	bt	pn, ccp
4.22 (23.92 – 28.14)	Pseudo Reef harzburgite	Calcitic harzburgite			Black and green medium to coarse-grained granular harzburgite with annealing cumulate grains of Opx giving the rock a light grey appearance with serpentine replacing opx and some olivine. Olivine (dark grey) are present are fine to coarse euhedral grains with the presence of serpentine with the interstitials of plagioclase. Calcite veins act as zones of weakness, fracturing the granular harzburgite. N.B Difference harzburgite are separated by mineralized serpentinite with magnetite veins	opx, ol, cpx	amp	Pn
		Micaceous Harzburgite			Dark green flaky rock with a defined eroded alteration of harzburgite with pronounced grains of biotite and chlorite set in aggregates medium grains of pyroxenes and olivine. Shows the presence of crystalline serpentinite (black and soupy texture)- hosting a BMS vein.	opx, ol, cl		pn
		Harzburgite			This layer shows a well-defined chloritization- chlorite reaction rim around pyroxenes (light-grey). Cumulate pyroxenes form white patches throughout the rock. The euhedral serpentine olivine (black) and chloritized olivine (green) grains are set in opx and plag interstitials. Gradational change to pegmatoidal ol-pyroxenite. Increased grain size of olivine and increase in the pyroxene abundance	opx, ol	cpx	pn po
		Mineralized Serpentinite			Black layer separating harzburgite cycles. It is a highly altered layer It is crystalline and slippery in texture. It hosts with BMS vein. In some area, magnetite crosscut and displaced by pale green vein (amphibole)	ol, opx, cl, srp	cpx, amp	pn
0.76 (28.14 – 28.90)	Lower Pseudo Reef	Pegmatoidal ol- pyroxenite			The layer starts as a 70 % light-grey opx oikocrysts hosting 20% euhedral olivine grains, to a very coarse euhedral and subhedral olivine grains, set in an opx-plagioclase matrix. Also, Euhedral grains of biotite (0.5 – 6 mm) Gradationally changes to pyroxenite- grading from coarse-grained pyroxene to small and medium-grained.	opx, ol	bt, pl	pn, ccp, po
0.2 (28.90 – 29.10)	UG2 Hanging wall	Pyroxenite			Pale green and medium-grained euhedral grains of pyroxenes and biotite. Disseminated grains of chalcocopyrite	opx, cpx, ol	bt	pn, ccp
Total length = 5.28 m	From top to bottom		Scale range: 60 -110 cm	— 500 µm	Fine grain = < 2mm Medium grain = 2-5 mm Coarse grain = 5mm – 1 cm Very coarse > 1 cm (mostly pegmatites)	Major > 5 area. %	Minor < 5 area %	

Appendix

Width (m) (depth m)	Drill core TU277 Stratigraphy	Lithology	Rock images		Description	Minerals		
			Photograph	Micrographs		Major	Minor	Sulphides
0.1 (81.54-81.64)	Footwall Merensky	Anorthosite			Start as the mottled anorthosite with coarse-grained and round of pyroxenes Decrease the content of pyroxenes and are aggregated and increase the content of plagioclase Gradational change to Pegmatoidal pyroxenite	pl, pxn	bt	pn, ccp Po
0.27 (81.64-81.94)	Pseudo Reef harzburgite	Pegmatoidal pyroxenite			A well-defined layer of grey-pale green layer of Poikilitic pegmatoidal pyroxenite. Large cumulus grains of orthopyroxene (light-grey) set in dark olivine altered to serpentine and plagioclase interstitial. This layer hosts 0.5 cm chromite stringer is and marks the change of mineral assemblage and colour. Disseminated chalcopyrite and pentlandite veins Towards the end, pyroxenes are aggregated form lumps ~ 3 mm	opx, cpx, cl	ol, bt	cr, pn, ccp
3.98 (82.11-85.89)		Chloritized harzburgite			Brown coloured fine-grained rock with large euhedral grains of chlorite, appearing as platy and shiny. This chlorite grains growing within the opx grains and form a flower shape.	opx, ol, cpx,	bt	pn
		pegmatite			Harzburgite x-cut by the pegmatite (white in colour) 3.8 cm thick. Pentlandite from the harzburgite flakes into the pegmatite. It is made up of large grains of quartz and plagioclase.	pl, qz	bt	pn po
		Chromite layer			This serves as a contact between harzburgite and pegmatoidal pyroxenite Hosts disseminated grains of chalcopyrite and pentlandite.	cr	Cl	pn, ccp, po
0.69 (85.89-86.58)	Lower Pseudo Reef	Pegmatoidal ol- orthopyroxenite			Light-grey rock comprising very coarse opx adcumulate texture and subhedral cpx and olivine grains set in dark serpentine matrix with plg interstitials. Plg also included in some opx. Fine to medium euhedral phlogopite grains are included in the serpentinized matrix.	opx, cpx, ol	bt, pl	pn, ccp po
0.19 (86.58-86.77)	UG2 hanging wall	Pyroxenite			Pale green in colour, medium grained pyroxenite with well-defined euhedral mica grains.	opx, cpx, pl	bt	pn, ccp, po
Total length = 5.23 m			Scale range: 60 -110 cm	= 500 µm	Fine grain = < 2mm Medium grain = 2-5 mm Coarse grain = 5mm – 1 cm very coarse > 1 cm (mostly pegmatites)	Major > 5 area %	Minor < 5 area %	Abundance

Table B3a: Fire Assay data for drill core TU277 provided by the mine.

Sample_ID	m_From	m_To	Width	Lithology	Stratigraphy	Pt_ppm	Pd_ppm	Au_ppm	Ni_ppm	Cu_ppm
PPM129686	81.54	81.64	0.10	Anorthosite	Merensky Reef Foot Wall	0.06	0.03	0.005	51	37
PPM129687	81.64	81.91	0.27	Pegmatoidal pyroxenite	Upper Pseudo Reef Pegmatoid	2.19	1.4	0.11	1810	530
PPM129689	81.91	82.11	0.20	Altered Harzburgite	Pseudo Reef Harzburgite (Tarentaal)	0.4	0.77	0.04	1550	140
PPM129690	82.11	82.31	0.20		Pseudo Reef Harzburgite (Tarentaal)	0.07	0.02	0.005	1390	8.4
PPM129691	82.31	82.51	0.20		Pseudo Reef Harzburgite (Tarentaal)	0.05	0.005	0.005	1380	33
PPM129692	82.51	82.61	0.10		Pseudo Reef Harzburgite (Tarentaal)	0.08	0.02	0.005	1500	49
PPM129693	82.61	82.71	0.10		Pseudo Reef Harzburgite (Tarentaal)	0.05	0.02	0.005	830	1
PPM129694	82.71	82.81	0.10		Pseudo Reef Harzburgite (Tarentaal)	0.07	0.02	0.005	440	1
PPM129695	82.81	82.91	0.10		Pseudo Reef Harzburgite (Tarentaal)	0.12	0.12	0.005	820	1
PPM129696	82.91	83.01	0.10		Pseudo Reef Harzburgite (Tarentaal)	0.14	0.06	0.005	1450	1
PPM129697	83.01	83.11	0.10		Pseudo Reef Harzburgite (Tarentaal)	0.11	0.05	0.005	1510	1
PPM129699	83.11	83.61	0.50		Pseudo Reef Harzburgite (Tarentaal)	0.08	0.03	0.005	1570	5.8
PPM129700	83.61	84.11	0.50		Pseudo Reef Harzburgite (Tarentaal)	0.06	0.03	0.005	1500	1

Appendix

PPM129701	84.11	84.49	0.38		Pseudo Reef Harzburgite (Tarentaal)	0.06	0.02	0.005	1530	1
PPM129702	84.49	84.99	0.50		Pseudo Reef Harzburgite (Tarentaal)	0.09	0.03	0.005	1380	1
PPM129703	84.99	85.49	0.50		Pseudo Reef Harzburgite (Tarentaal)	0.1	0.03	0.005	1610	1
PPM129704	85.49	85.69	0.20		Pseudo Reef Harzburgite (Tarentaal)	0.24	0.14	0.005	1600	1
PPM129705	85.69	85.79	0.10		Pseudo Reef Harzburgite (Tarentaal)	2.28	1.32	0.6	4550	130
PPM129706	85.79	85.89	0.10		Pseudo Reef Harzburgite (Tarentaal)	1.2	0.84	0.33	2720	180
PPM129707	85.89	85.99	0.10		Lower Pseudo Reef Pegmatoid	4.62	1.75	0.21	1640	670
PPM129709	85.99	86.19	0.20	Pegmatoidal olivine pyroxenite	Lower Pseudo Reef Pegmatoid	0.33	0.22	0.04	1210	150
PPM129710	86.19	86.39	0.20		Lower Pseudo Reef Pegmatoid	1.57	1.23	0.3	950	460
PPM129711	86.39	86.58	0.19		Lower Pseudo Reef Pegmatoid	0.13	0.05	0.02	350	100
PPM129713	86.58	86.77	0.19		Feldspatic Pyroxenite	UG2 Hanging Wall 4	0.67	0.24	0.05	310

Table B3b: Fire Assay data for drill core RD015 provided by the mine.

Sample_ID	m_From	m_To	Width	Lithology	Stratigraphy	Pt_ppm	Pd_ppm	Au_ppm	Ni_ppm	Cu_ppm
SED05514	23.82	23.92	0.10	Leuconorite	Merensky Reef Foot Wall 1	7.52	3.47	0.39	3990	1260
SED05516	23.92	24.12	0.20	Harzburgite	Pseudo Reef Harzburgite (Tarentaal)	0.09	0.09	0.005	1060	73
SED05517	24.12	24.32	0.20		Pseudo Reef Harzburgite (Tarentaal)	0.12	0.06	0.005	1310	71
SED05310	24.32	24.52	0.20		Pseudo Reef Harzburgite (Tarentaal)	0.12	0.08	0.005	1460	80
SED05311	24.52	24.62	0.10		Pseudo Reef Harzburgite (Tarentaal)	0.74	0.29	0.06	1600	220
SED05313	24.62	24.72	0.10		Pseudo Reef Harzburgite (Tarentaal)	0.07	0.03	0.005	1690	25
SED05314	24.72	24.82	0.10		Pseudo Reef Harzburgite (Tarentaal)	0.14	0.05	0.005	1310	49
SED05315	24.82	24.92	0.10		Pseudo Reef Harzburgite (Tarentaal)	0.11	0.03	0.005	1560	25
SED05316	24.92	25.42	0.50		Pseudo Reef Harzburgite (Tarentaal)	0.18	0.06	0.04	1470	36
SED05317	25.42	25.92	0.50		Pseudo Reef Harzburgite (Tarentaal)	0.05	0.02	0.005	1630	13
SED05318	25.92	26.42	0.50		Pseudo Reef Harzburgite (Tarentaal)	0.09	0.03	0.005	1720	6.5
SED05319	26.42	26.75	0.33		Pseudo Reef Harzburgite (Tarentaal)	0.06	0.02	0.005	1570	5.9

Appendix

SED05320	26.75	27.25	0.50		Pseudo Reef Harzburgite (Tarentaal)	0.06	0.03	0.005	1520	5.1
SED05321	27.25	27.75	0.50		Pseudo Reef Harzburgite (Tarentaal)	0.11	0.04	0.005	1700	8.7
SED05322	27.75	27.94	0.19		Pseudo Reef Harzburgite (Tarentaal)	0.57	0.18	0.005	1590	52
SED05323	27.94	28.04	0.10		Pseudo Reef Harzburgite (Tarentaal)	1.78	0.95	0.3	3070	1010
SED05324	28.04	28.14	0.10		Pseudo Reef Harzburgite (Tarentaal)	2.41	0.75	0.1	2070	240
SED05325	28.14	28.24	0.10	Pegmatoidal olivine pyroxenite	Lower Pseudo Reef Pegmatoid	1.55	0.77	0.07	1480	240
SED05327	28.24	28.44	0.20	Pegmatoidal pyroxenite	Lower Pseudo Reef Pegmatoid	1.03	0.74	0.21	920	220
SED05328	28.44	28.64	0.20		Lower Pseudo Reef Pegmatoid	0.26	0.08	0.04	280	98
SED05329	28.64	28.90	0.26	Pegmatoidal olivine pyroxenite	Lower Pseudo Reef Pegmatoid	0.38	0.16	0.1	540	130
SED05331	28.90	29.10	0.20	Pyroxenite	UG2 Hanging Wall 4	1.22	0.75	0.22	900	390

Appendix C: Bulk mineral grades.

Table C1: TU277 QEMSCAN bulk mineral grades in wt. %.

Minerals	Anorthosite	Peg. Pyroxenite	Altered harzburgite	Peg. ol-pyroxenite	Feldspathic pyroxenite
Quartz	-	-	-	-	1.3
Olivine	0.1	0.8	0.1	12.0	0.0
Orthopyroxene	15.7	28.3	20.0	41.9	79.0
Clinopyroxene	32.5	2.1	0.1	0.7	2.9
Amphibole	0.2	0.3	<0.1	0.5	0.1
Serpentine	-	18.7	55.4	21.9	-
Talc	-	-	-	0.2	-
Chlorite	8.8	7.7	8.6	4.5	1.1
Epidote	10.1	3.9	5.6	8.3	0.2
Plagio-feldspar	21.3	10.5	7.3	6.5	15.2
Mica	6.9	0.3	0.4	0.7	0.2
Chromite	<0.1	22.8	0.1	1.6	-
Fe-oxides	-	3.3	2.4	0.8	-
BMS	<0.1	1.2	-	0.3	-
other	0.1	<0.1	<0.1	0.2	0.1

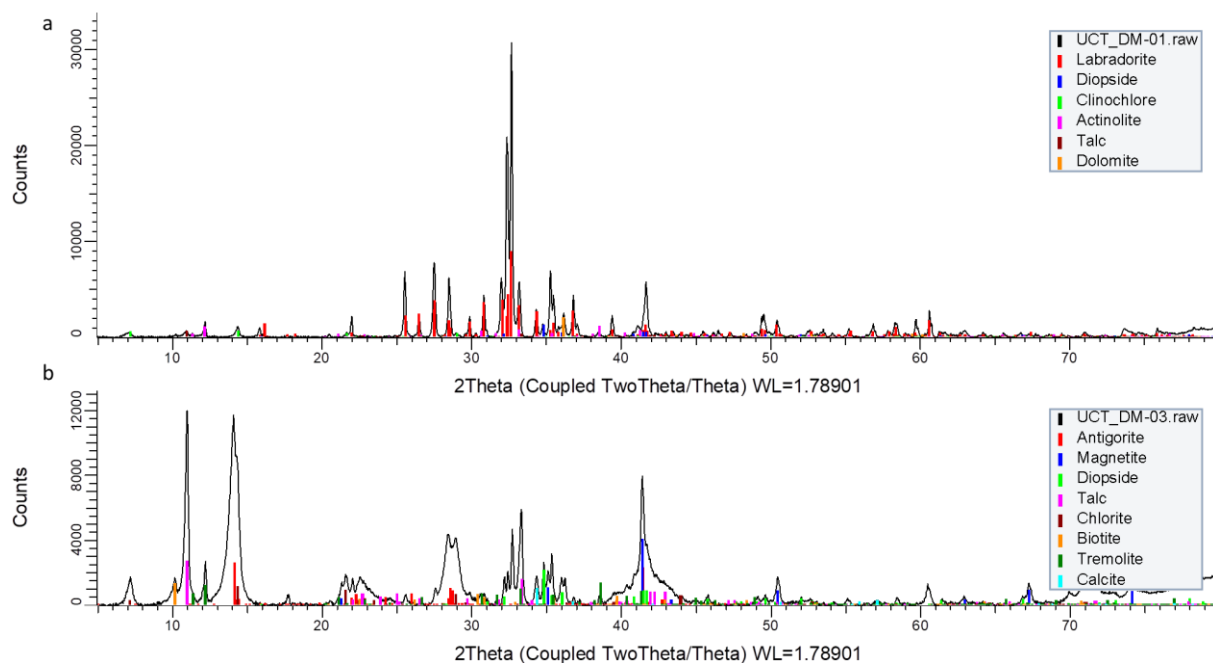
Table C2: RD015 QEMSCAN bulk mineral grades in wt. %.

Minerals	Anorthosite	Altered harzburgite	Peg. ol-pyroxenite	Peg. Pyroxenite	Feldspathic pyroxenite
Olivine	<0.1	11.9	3.6	1.8	1.8
Orthopyroxene	1.4	51.8	7.7	86.9	78.2
Clinopyroxene	1.4	1.7	0.1	3.7	2.3
Amphibole	<0.1	-	-	<0.1	0.1
Serpentine	-	31.1	47.3	-	-
Talc	-	-	-	0.01	-
Chlorite	4.2	0.8	8.1	5.5	12.7
Epidote	10.4	0.5	10.0	-	0.3
Plagio-feldspar	78.8	0.8	17.6	1.5	4.7
Mica	0.3	1.0	1.9	0.4	0.1
Chromite	2.4	0.1	0.7	0.2	0.0
Fe-oxides	0.1	0.3	3.2	<0.1	-
BMS	0.7	-	-	<0.1	<0.1
other	0.1	0.1	<0.1	<0.1	<0.1

Table C3: Number of grains analysed for QEMSCAN grain sizes distribution.

Rock type	Mineral	RD015	TU277
		Number of grains	Number of grains
Anorthosite	OPX	345	1289
	Plagioclase	479	870
Pegmatoidal pyroxenite	OPX	3045	5142
	Plagioclase	309	429
	Serpentine	732	3932
Altered harzburgite	OPX	3305	7298
	Plagioclase	43	282
	Serpentine	725	850
Feldspathic pyroxenite	OPX	268	1064
	Plagioclase	279	1291

X-ray diffractograms



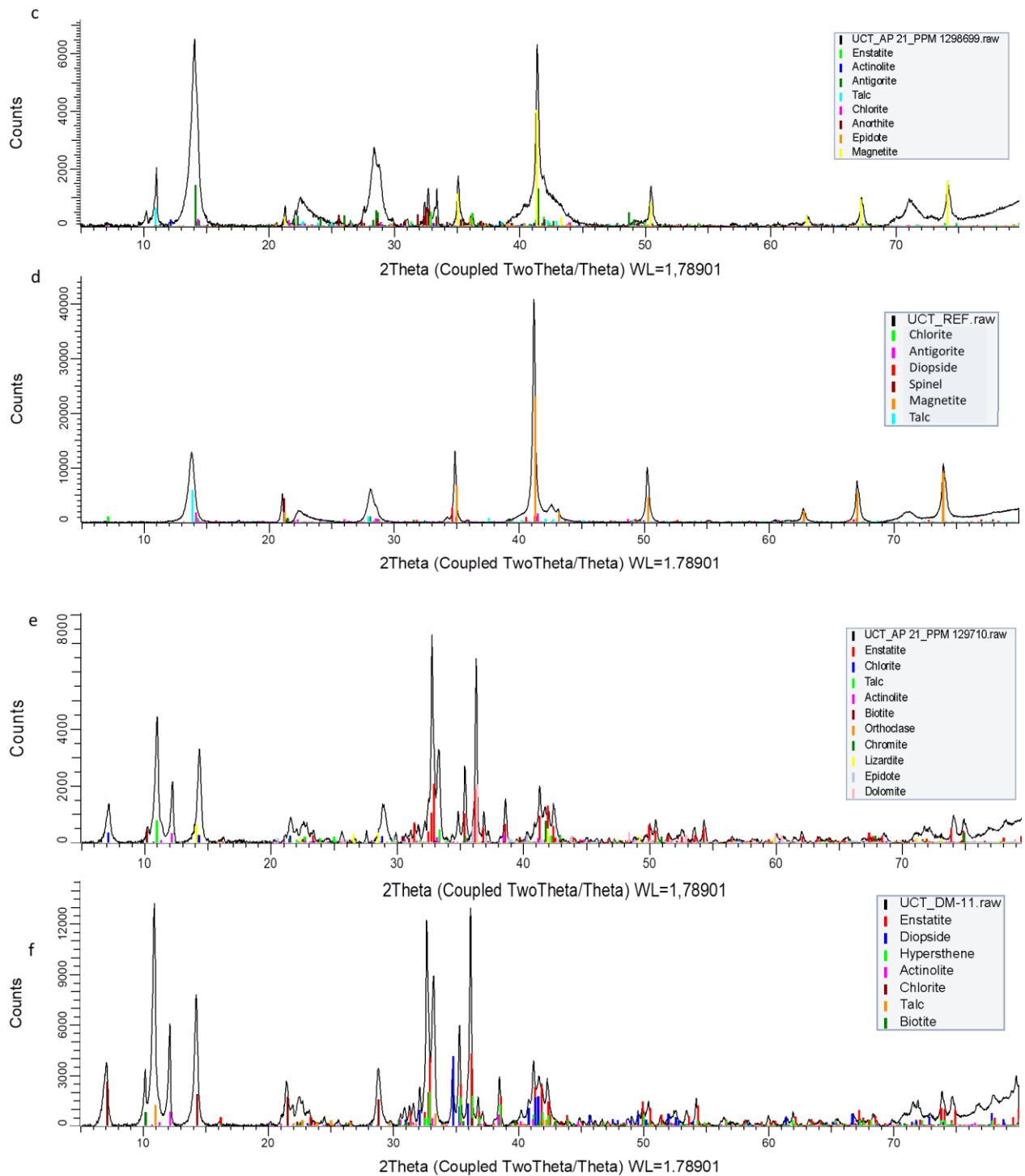
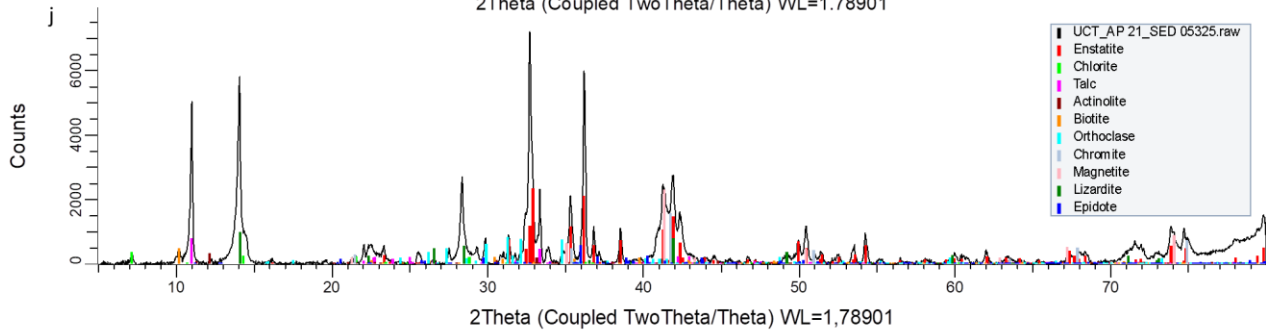
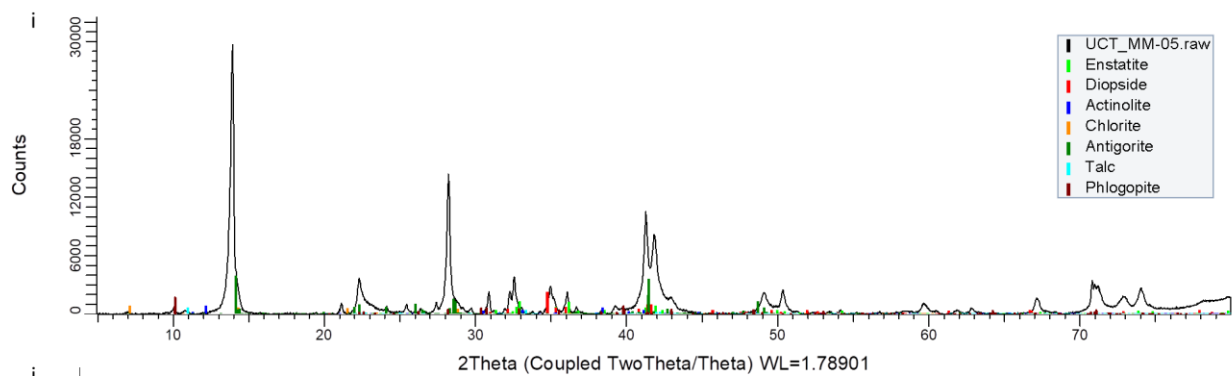
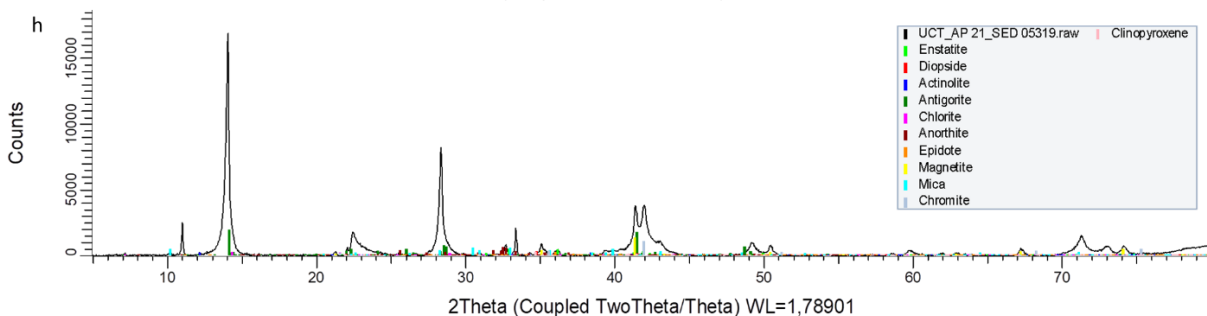
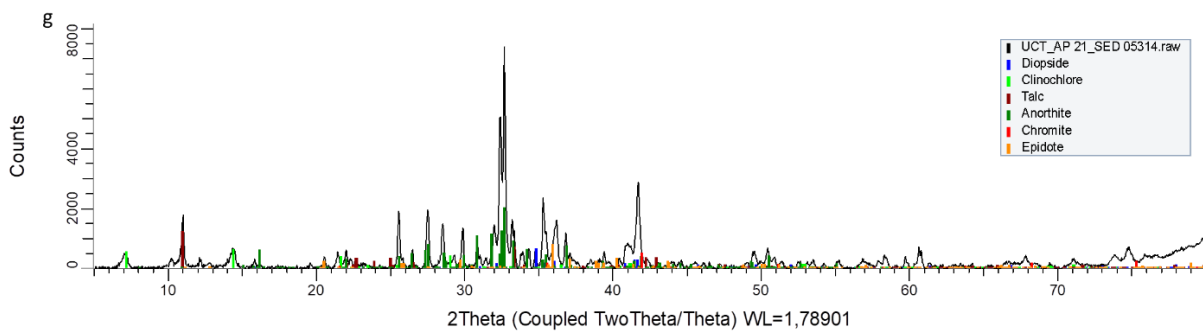


Figure C1: X-ray diffractogram for rock types in Drill core TU277. (a) Mottled anorthosite, (b) Pegmatoidal olivine-pyroxenite, (c) Altered harzburgite, (d) Serpentinite, (e) Pegmatoidal pyroxenite and (f) Feldspathic pyroxenite.

Drill core RD015



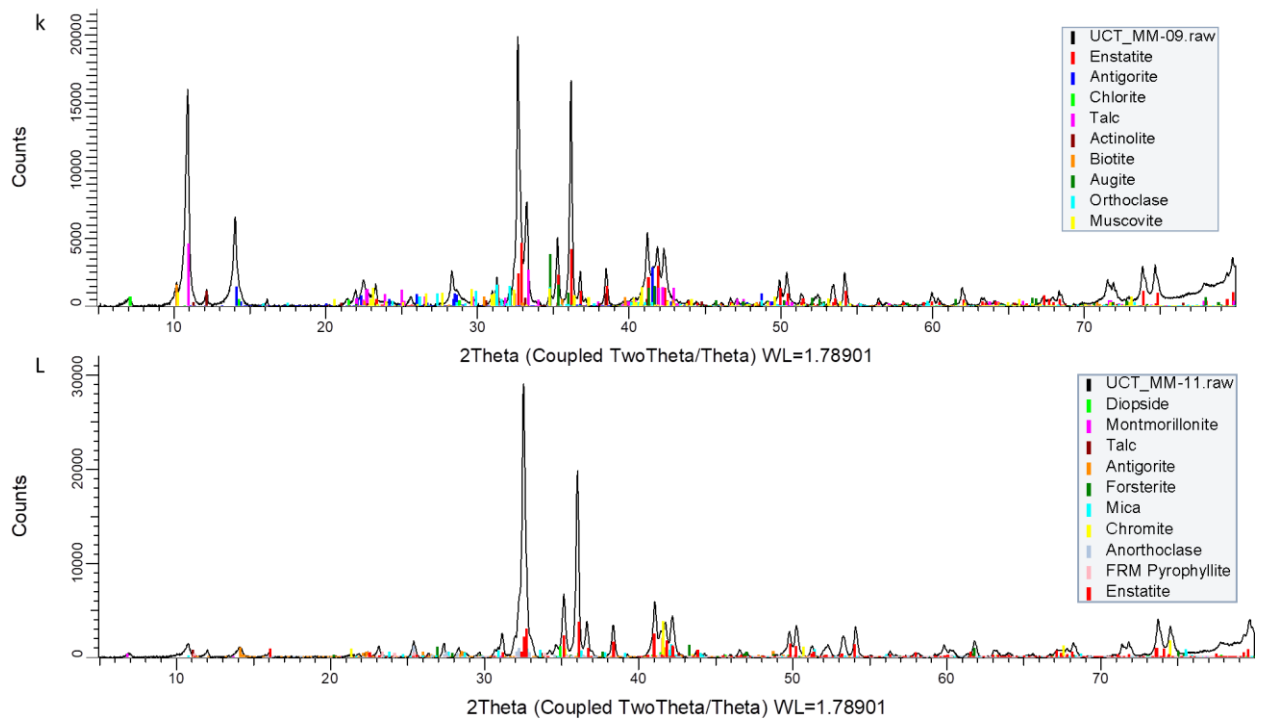


Figure C2: X-ray diffractogram for rock types in Drill core TU277. (g) Anorthosite, (h) Altered harzburgite, (i) Altered harzburgite, (j) Pegmatoidal olivine-pyroxenite, (k) Pegmatoidal pyroxenite and (L) Feldspathic pyroxenite.

Appendix D: Hyperspectral imaging

Table D1: Readily identified mineral assemblage detected by HS camera FENIX and OWL. with manually logged mineral assemblage on drill core TU277.

Borehole TU277			Mineral ID				
Depth (m)	Sample ID	Lithology	RGB	FENIX	OWL		
81.54		Mottled Anorthosite	Pl. Pxn. Ol	Srp. Sap. Cl. Ep	Uncl ± Alu. An		
	PPM 129686			Ill. Preh. Ms. Sap			
81.64							
	PPM 129687	Pegmatoidal pyroxenite	Qz. K-sp	Amp. Cl. talc.	Ap. Cl. Bt. Ep. Opx		
81.94				Srp			
	PPM 129689	Harzburgite	Ol. Cpx. Srp. Cl	Srp. Sap	Ap. Cl		
	PPM 129690			Cl			
				Cl. Ap			
	PPM 129692			Srp	Cl		
	PPM 129693	Pegmatite		Sap. Cl. Amp	Cl. Bt. Qz. Ep. Opx		
	PPM 129694						
	PPM 129695	Harzburgite					
	PPM 129700	Fine Srp					
		Harzburgite			Srp. minor Cl and Amp	Cl. Ep	
	PPM 129703	Fine Srp					
		Harzburgite					
	PPM 129705	Fine Srp					
	PPM 129706						
85.89							
	PPM 129707	Pegmatoidal ol-pyroxenite	Pxn. Ol. Cl	Srp. Cl. Ill. Sap. Ep			Cl. Ap
	PPM 129710			Srp. talc. Amp	Ap. Cl. Bt. Opx		
				Srp. Cl. Sap. Amp	Cl. Ap. Bt. Ms		
86.58							
86.77	PPM 129713	Feldspathic pyroxenite	Pxn	Talc	Ap. Ep. Opx		

Table D2: Readily identified mineral assemblage detected by HS camera FENIX and OWL. with manually logged mineral assemblage on drill core RD015.

Borehole RD015			Mineral ID			
Depth (m)	Sample ID	Lithology	RGB	FENIX	OWL	
23.82	SED 05514	Anorthosite	Fsp. Ol. opx	Sp. Ill. Preh. Ep. Ms	Uncl	
	SED 05515	Cal. Anorthosite	V.cal	V.sap. V.cal	Ap. Cl. Opx	
23.92						
	SED 05516	Calcitic Harzburgite	Ol. Opx. V.cal. Cl	Srp. Sap. V.cal. Ill. Sap	Uncl. Ap. Cl. Bt. Cal	
	SED 5310				Uncl. Ap. Cl. Ep	
24.38						
	SED 05313	Fine Srpentinite	Srp. Pl. Mgt	Srp. V.Amp. Cal	Cl. Amp	
	SED 05314	Harzburgite	Ol. Opx. Srp. Cl	Srp. V.cal	Uncl ± Cl	
	SED 5315-16			Uncl ± Ap. Cl		
	SED 05317			Chloritized harzburgite	Ms/Bt. Cl. Srp	Uncl ± Ap. Ep. Cl. opx
		Harzburgite	Ol. Opx. Cl. Srp		Uncl	
	SED 05318/19	Fine Srpentinite	Srp. Chl. Mgt			
				Srp ± Cl. Ill. Preh		
	SED 05319	Harzburgite	Cl. Ol. Opx		Cl	
	75/75			Ap/Cl		
	SED 5320			Uncl +- Ap. Cl		
	SED 05321	Fine Srpentinite	Srp. Chl. Mgt			
	SED 5321	Harzburgite				
	SED 05322		Ol. Opx		Ill	
	SED 05325		Opx	Srp. Ill. preh. Cl	Uncl. Ap.Cl	
28.14						
	SED 05327	Pegmatoidal ol-pyroxenite	Pxn. Ol	Srp. talc. Amp. Sap. Cl. ill	Ap. Cl. Bt. Ep ± Uncl	
	SED 05328			Srp		Cl. Ap. Bt
	SED 05329			Sap. talc. Amp. Srp		
28.90						
	SED 05330	Feldspathic Pyroxenite	Bt. Pxn. Fsp	Uncl ± Srp	Ap. Cl. Bt	
29.10	SED 05331				Ap. Cl. Bt. Ep	

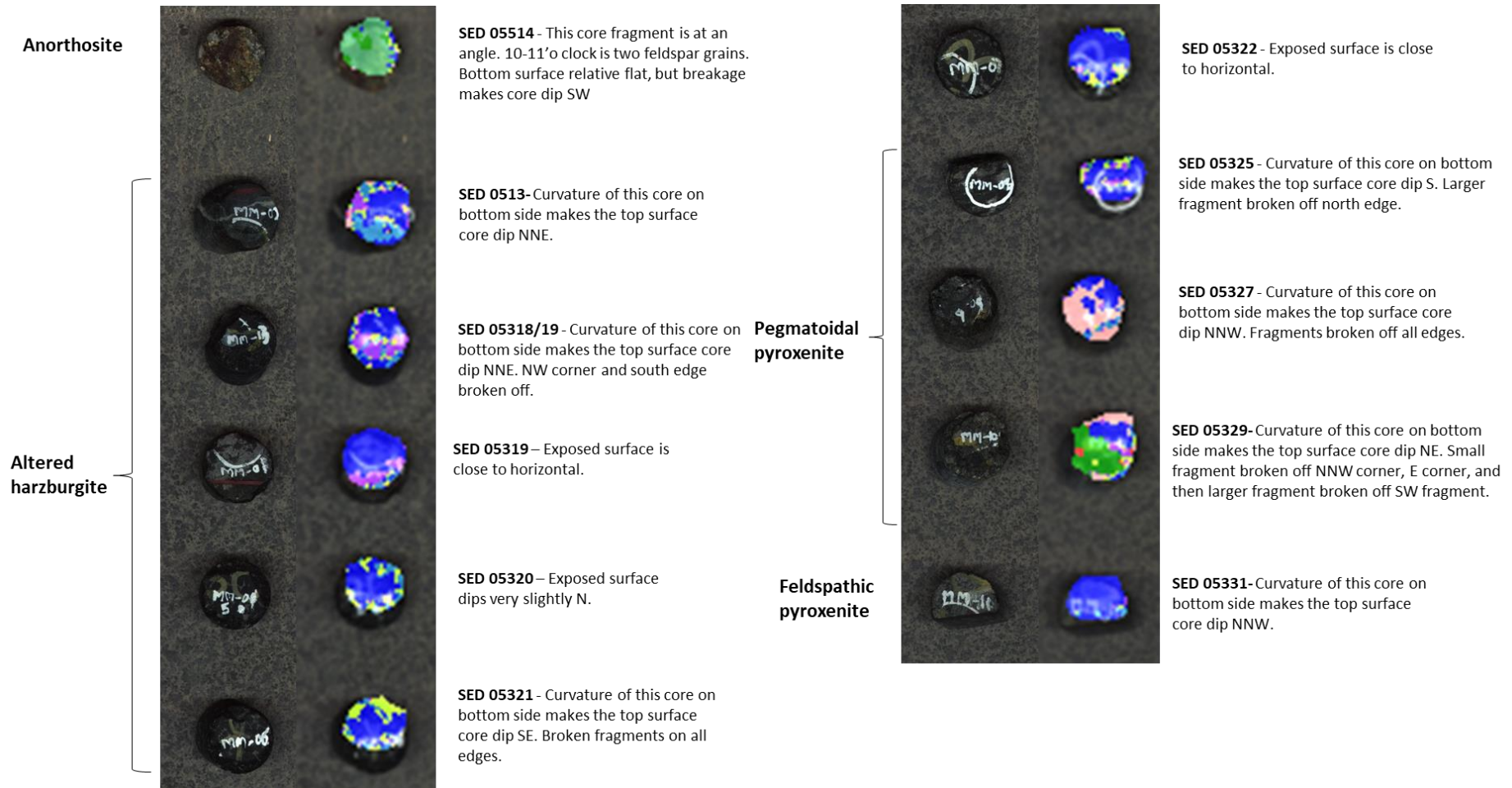


Figure D1: RGB images overlapped with HSI mineral maps for drill core RD015 to check areas scanned in the core. Some side areas are scanned due to cores dipping severely and having larger fragments.

Appendix

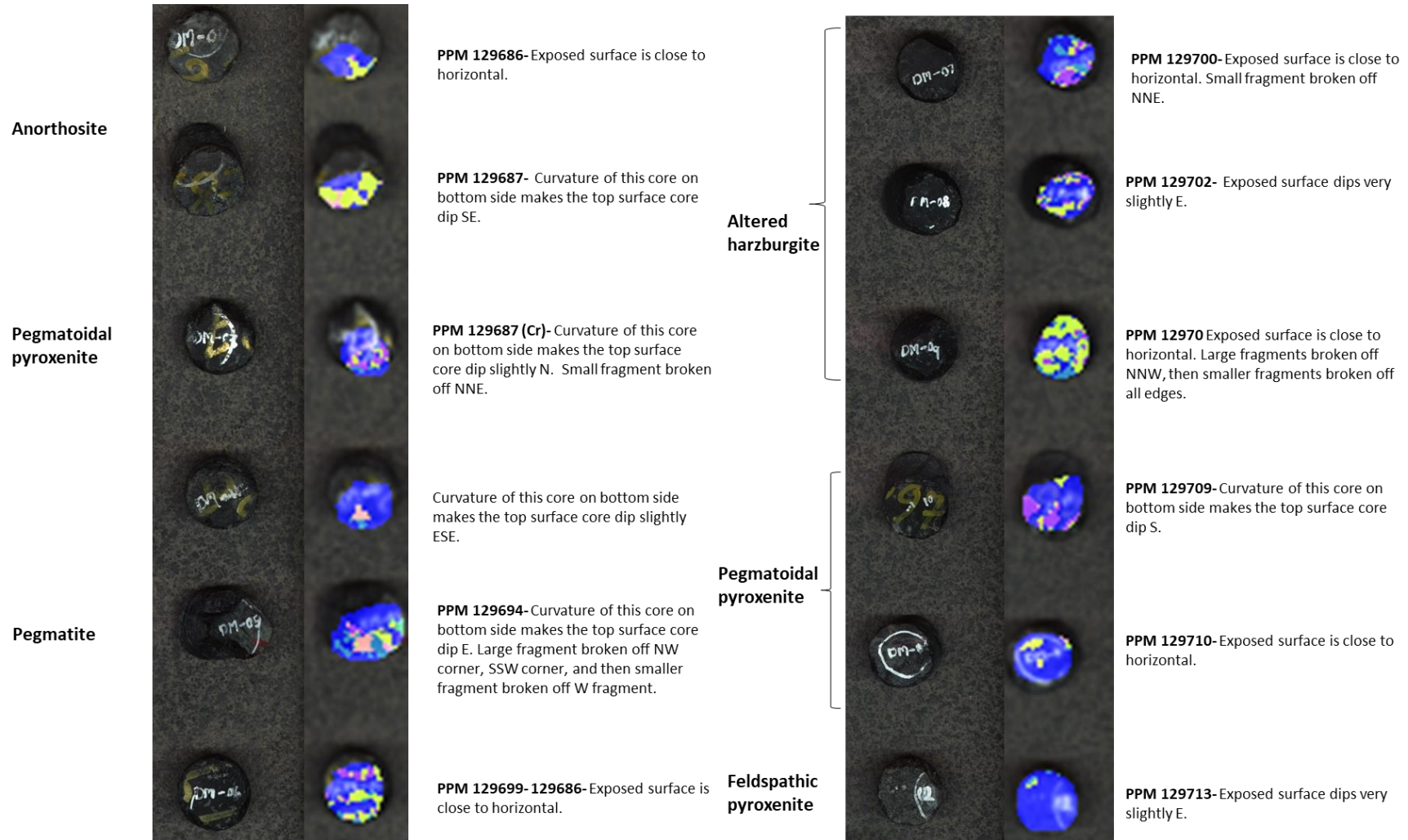


Figure D2: RGB images overlapped with HSI mineral maps for drill core TU277 to check areas scanned in the core. Fifty to seventy percent of the anorthosite is not scanned. Most unscanned areas are tilted due to the curvature of the cores.

Figure C5: Mini cores scanned on the curving side of the cylindrical cores.

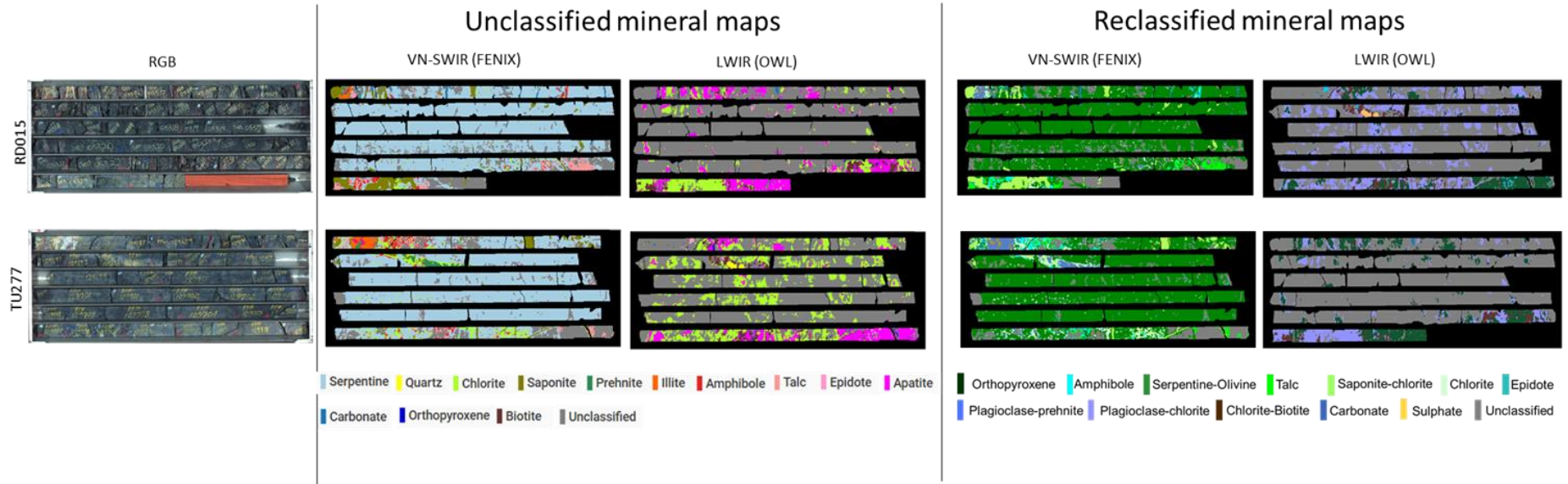


Figure D3: Mineral maps before and after spectral and mineral reclassification.

HSI spectral signatures.

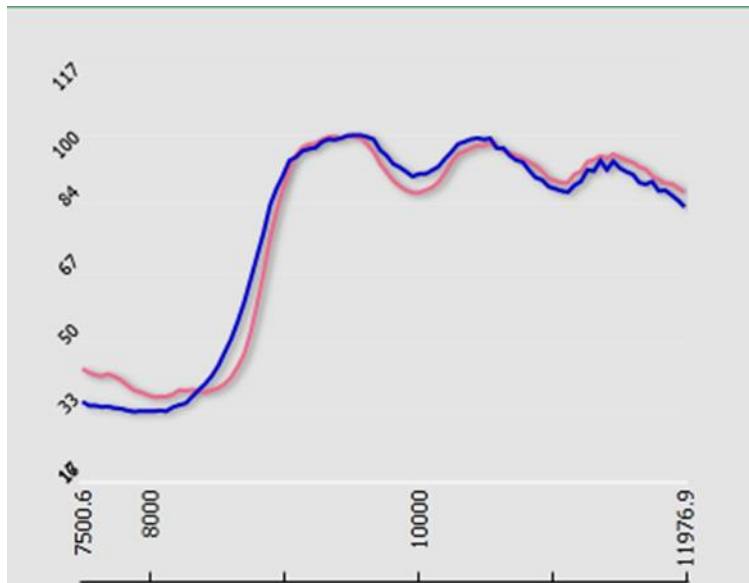


Figure D4: Apatite spectra detected by LWIR matched with OPX spectra from the TC matching library. Apatite-Pink and Orthopyroxene-blue

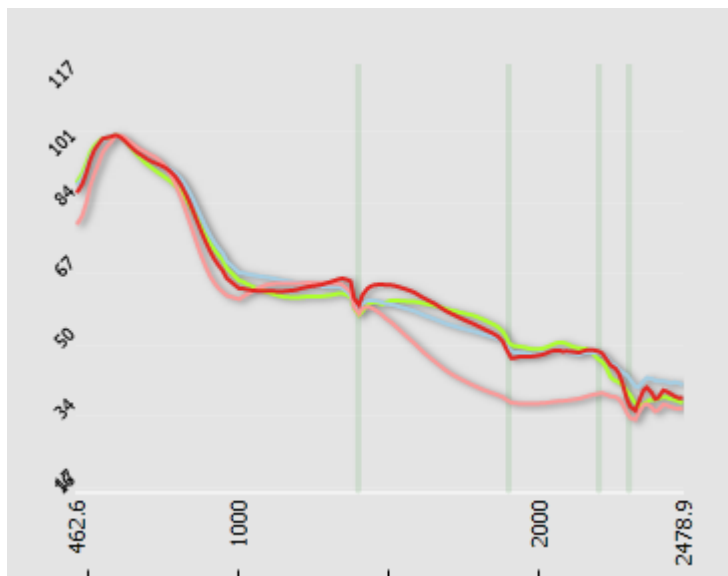


Figure D5: Amphibole-red, serpentine-blue, Chlorite-green, and talc-pink have similar spectral signatures and can only be distinguished by spectral absorption between the wavelength of 2400 and 2480.

Mineral texture

Table D3: Summary of the median grain sizes (d50) values calculated for specific minerals in the rock types for drill core RD015. The values presented in this table are in micrometre (μm). Minerals that do not respond under the specific sensor and interconnect minerals that gave only one value are annotated with a hyphen (-).

Rock type	Minerals	SWIR	LWIR
Anorthosite	Prehnite-plagioclase	-	-
	Chlorite-plagioclase	-	1353
Altered harzburgite	Serpentine-olivine	5598	-
	Orthopyroxene	-	7319
	Chlorite plagioclase	-	5080
Pegmatoidal pyroxenite	Serpentine-olivine	2001.63	-
	Prehnite-plagioclase	1434	-
	Chlorite plagioclase	-	5080
Feldspathic Pyroxenite	Serpentine-olivine	1330	-
	Orthopyroxene	-	9255
	Chlorite plagioclase	-	1050

Table D4: Summary of the median grain sizes (d50) values calculated for specific minerals in the rock types for drill core TU277. The values presented in this table are in micrometre (μm). Minerals that do not respond under the specific sensor and interconnect minerals that gave only one value are annotated with a hyphen (-).

Rock type	Minerals	SWIR	LWIR
Anorthosite	Prehnite-plagioclase	-	-
	Plagioclase	-	3424
Altered harzburgite	Serpentine-olivine	2754	-
	Chlorite plagioclase	-	-
Pegmatoidal pyroxenite	Serpentine-olivine	7872	-
	Orthopyroxene	-	1904
	Chlorite plagioclase	-	2930
Feldspathic Pyroxenite	Orthopyroxene	-	8754
	Chlorite plagioclase	-	2730

Appendix

Table D5: The relative error at 2σ for drill core TU277 mineral grades from QEMSCAN and HSI (SWIR and LWIR).

TU277 Minerals	Anorthosite			Pegmatoidal pyroxenite			Altered harzburgite			Pegmatoidal pyroxenite			Feldspathic pyroxenite		
	QEMSCAN	SWIR	LWIR	QEMSCAN	SWIR	LWIR	QEMSCAN	SWIR	LWIR	QEMSCAN	SWIR	LWIR	QEMSCAN	SWIR	LWIR
Carbonate					3.1			3.2			23.5			2.39	
Olivine	3.8			1.8			6.3			0.4			10.72		
OPX	0.3		1.7	0.3			0.3			0.2		2.9	0.1		0.6
CPX	0.2		4.1	1.1			4.4			1.8			0.9		
Amphibole	3			3			10.9			2			6.2		
Serpentine		94.5		0.3	2		0.1	2.1		0.3	1.4		0		
Talc		31.4		0			0	6.6		3.5	7.7		0		
Chlorite	0.5	13.7		0.6	3.1		0.5	1.4		0.7	2.7		1.4	1.33	
Epidote	0.4		3.1	0.8			0.6			0.5		2.6	3.7		
Plagioclase	0.3		13.3	0.5		12.7	0.6		15.7	0.5			0.4		6.6
Mica	0.5		4.3	2.8			2.6			1.7		1.5	3.4		0.8
Chromite	10.11			0.3			4.6			1.1			0		
Fe-oxides				0.9			1			1.64			0		
BMS	14.3			1.5						2.5			0		
Unclassified	5.8	16.3	0.9	11.2	0.6	13.6	8.9	0.7	14.6	3.7	0.5	0.5	6.8	96.28	4.4

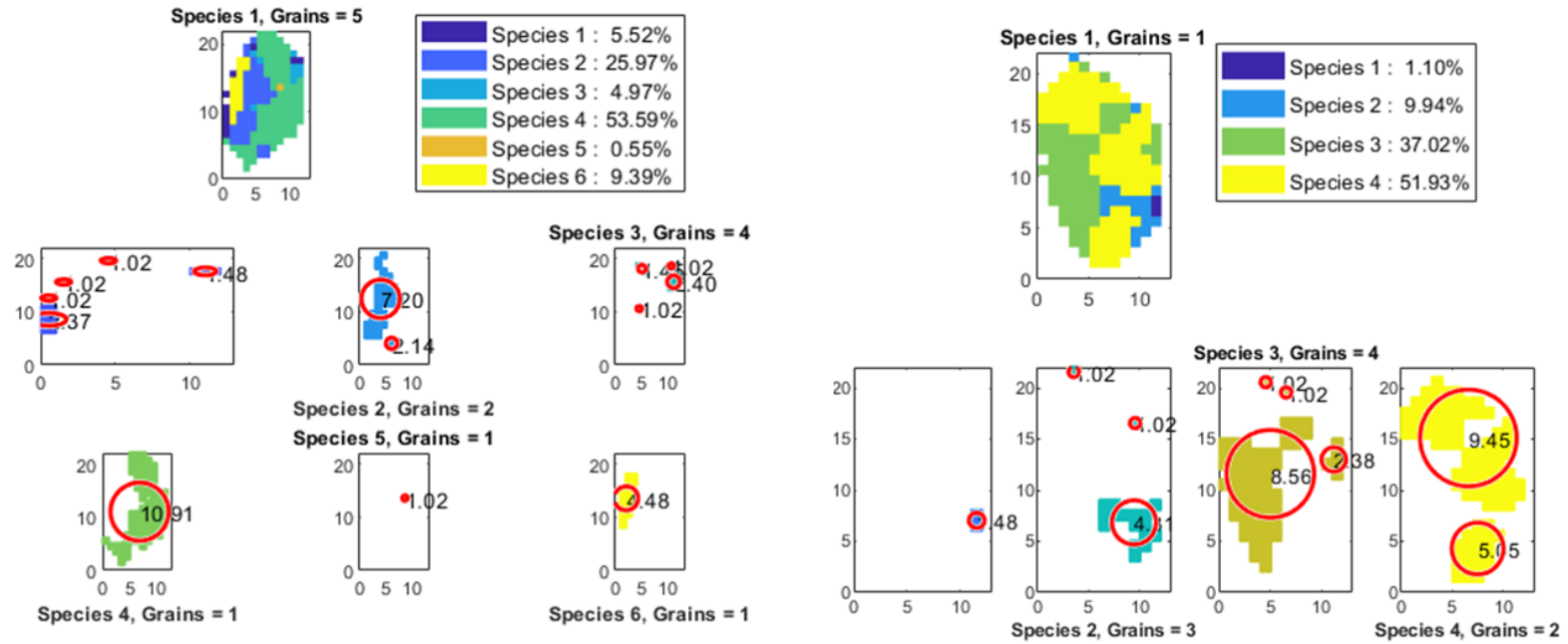
Appendix

Table D6: The relative error at 2σ for drill core RD015 mineral grades from QEMSCAN and HSI (SWIR and LWIR).

RD015 Minerals	Anorthosite			Altered harzburgite			Pegmatoidal ol-pyroxenite			Pegmatoidal pyroxenite			Feldspathic pyroxenite		
	QEMSCAN	SWIR	LWIR	QEMSCAN	SWIR	LWIR	QEMSCAN	SWIR	LWIR	QEMSCAN	SWIR	LWIR	QEMSCAN	SWIR	LWIR
Carbonate					3.5			7.7			4			3.3	
Olivine	3.82			6.3			0.8			1.2			1.81		
OPX	0.3			0.3		10.7	0.6			0.1		0.8	78.19		0.5
CPX	0.2			4.4			4.8			0.9			2.25		
Amphibole	3			10.9						8.3			0.05		
Serpentine				0.1	1.5		0.2	2.1			7.3			6.6	
Talc				0				9.4		16.6	0.9				
Chlorite	0.5	9.6		0.5	4.4		0.5	2.2		0.7	13.8		12.66	7.7	
Epidote	0.4	7.7		0.6		14.1	0.5						0.27		13.3
Plagioclase	0.3	0.4	47.1	0.6		16	0.3	4.6	18	1.4		1.6	4.65		7.7
Mica	0.5			2.6		22.5	1.2			2.8		1	0.06		1.3
Chromite	10.1			4.63			1.9			4.3			0.04		
Fe-oxides				1			0.9			11.7					
BMS	14.3			0						16.6					
unclassified	5.8	3		8.9	0.4	37	11.2	0.5	9	16.6	1.5	5.9	0.03	0.2	4

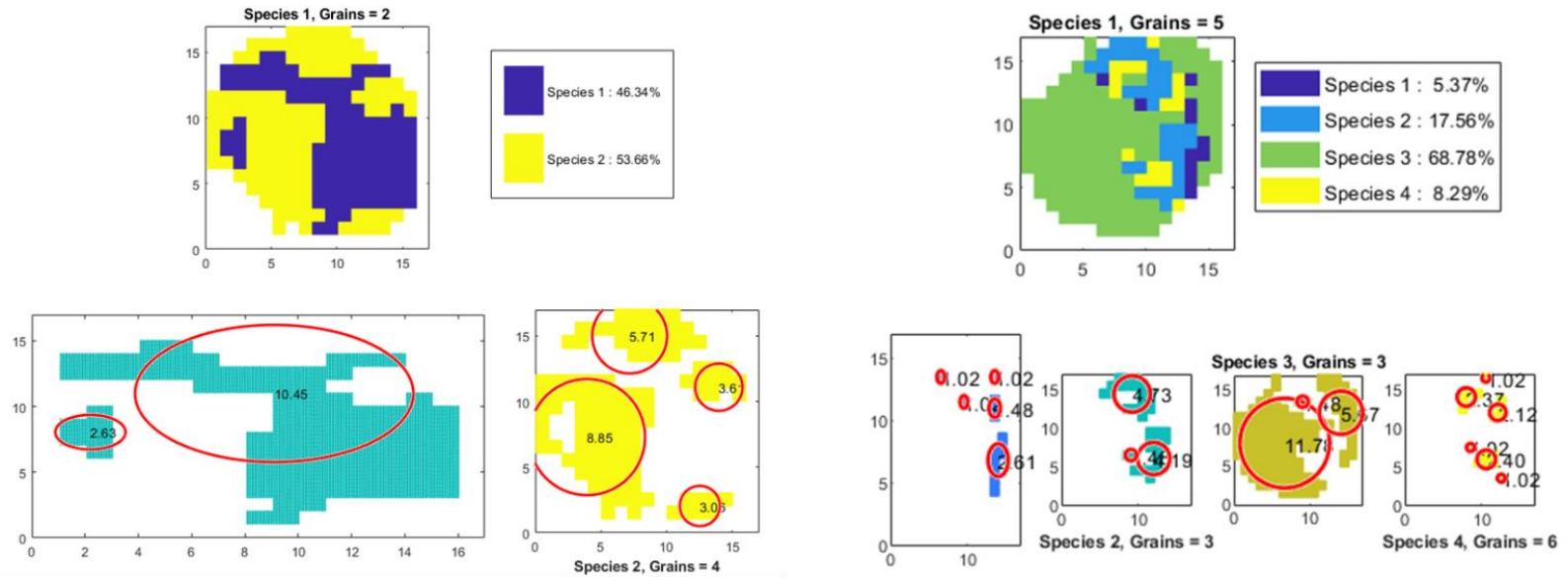
Grain size distributions on HSI mineral maps

a) TU277_Mottle anorthosite

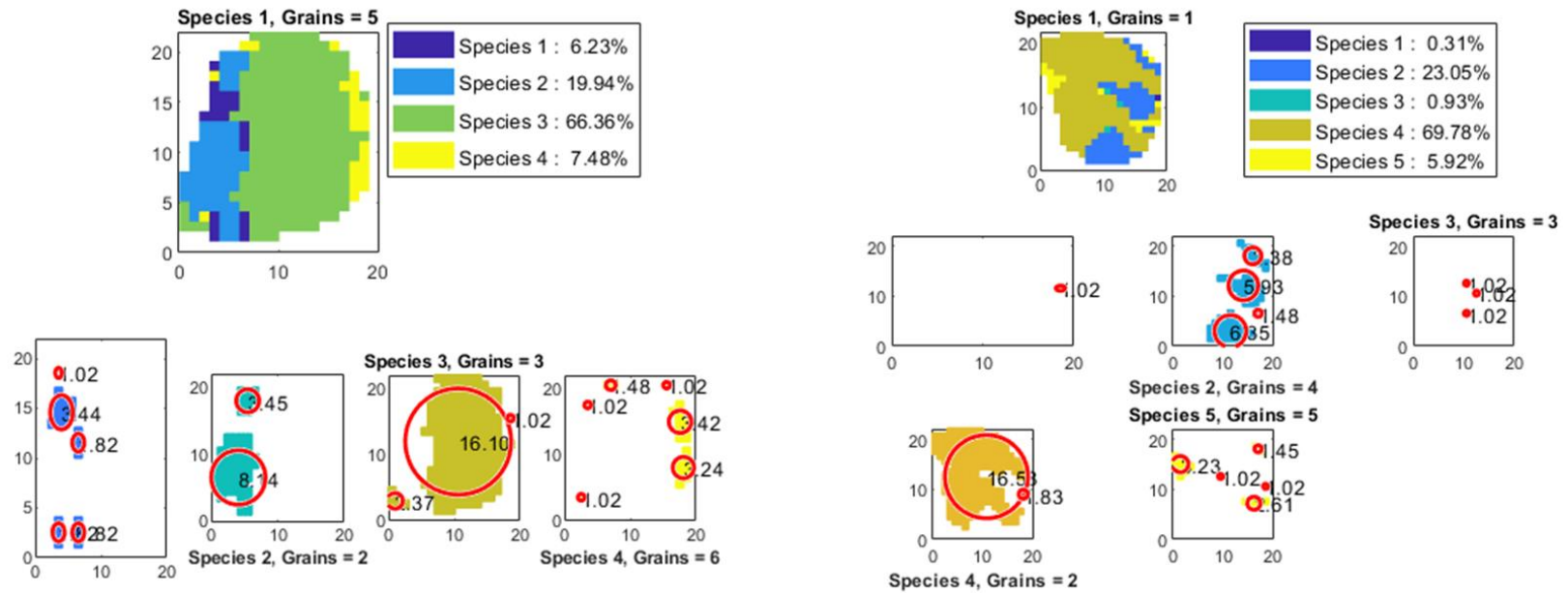


Appendix

b) TU277_Pegmatoidal olivine-pyroxenite



c) Drill core TU277_Pegmatoidal olivine-pyroxenite



d) TU277_Feldspathic pyroxenite

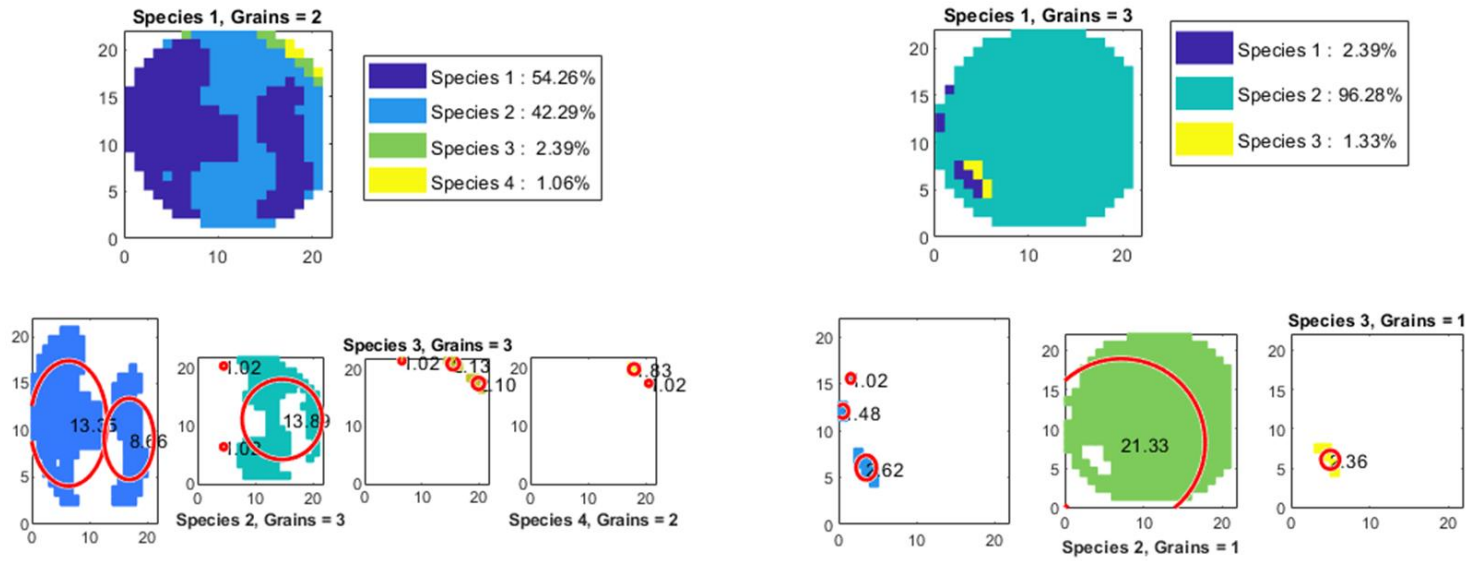
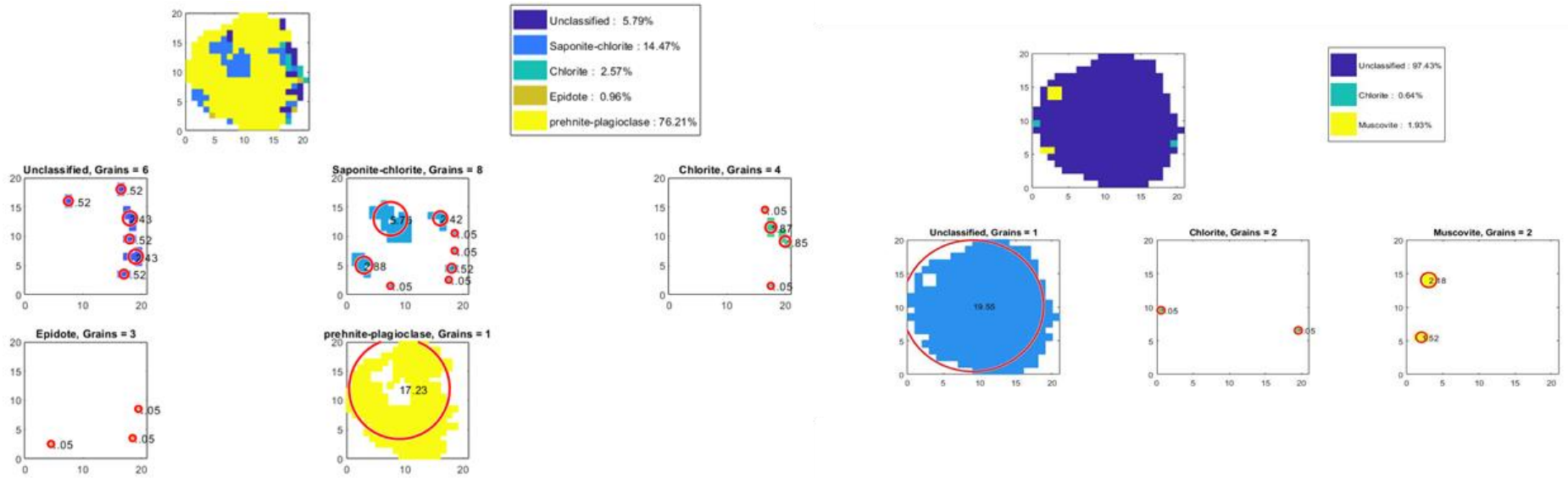


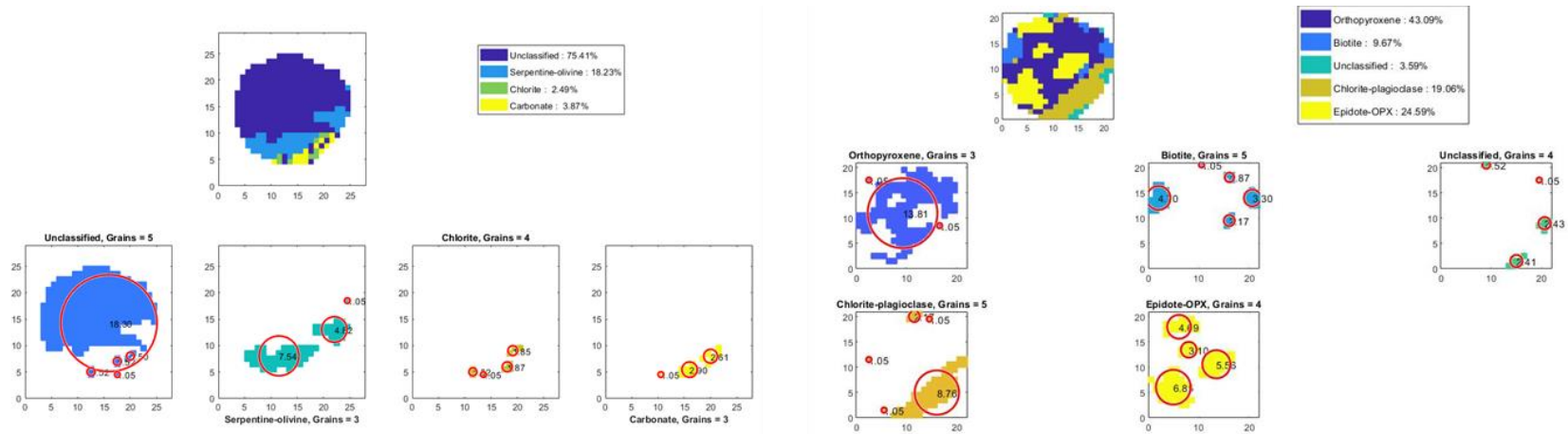
Figure D6: Hyperspectral grain size distribution for rock types in drill core TU277. Mineral maps for SWIR (left) and LWIR (right).

a) Drill core RD015_Anorthosite

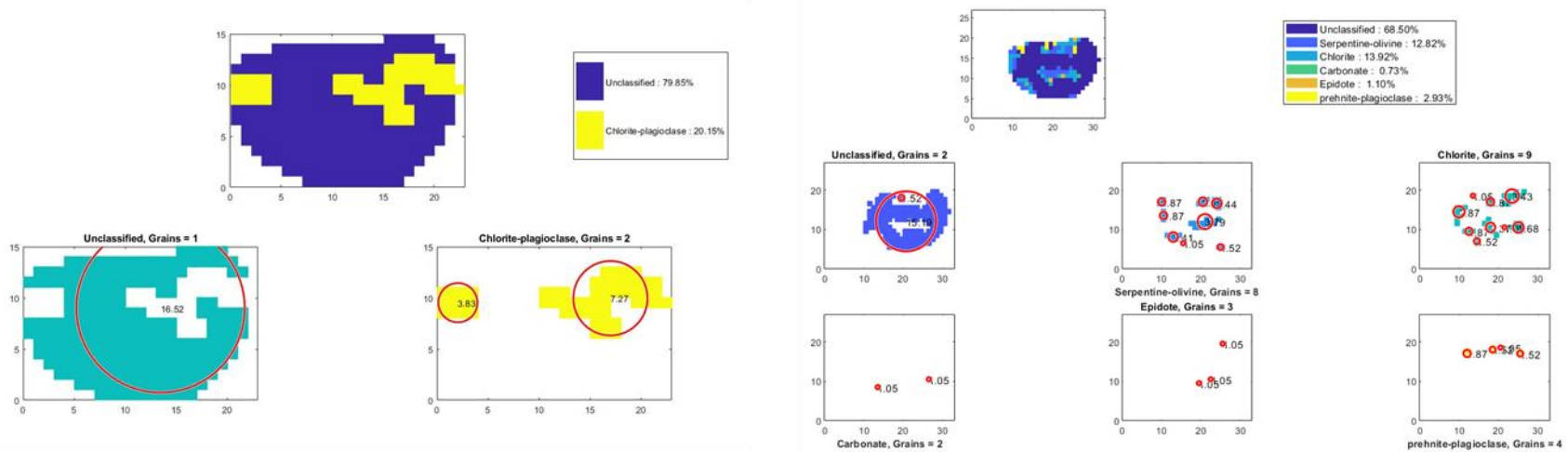


Appendix

b) Drill core RD015_Altered harzburgite



c) Drill core RD015_Pegmatoidal pyroxenite



Appendix E: X-ray computed tomography

Figure E1: Marked selected areas for 25 mm (diameter) mini cores drilled from the standard cores on every lithology observed from the stratigraphy; from the anorthosite of the Footwall Merensky to the feldspathic pegmatoidal pyroxenite of the UG2 Hanging wall.

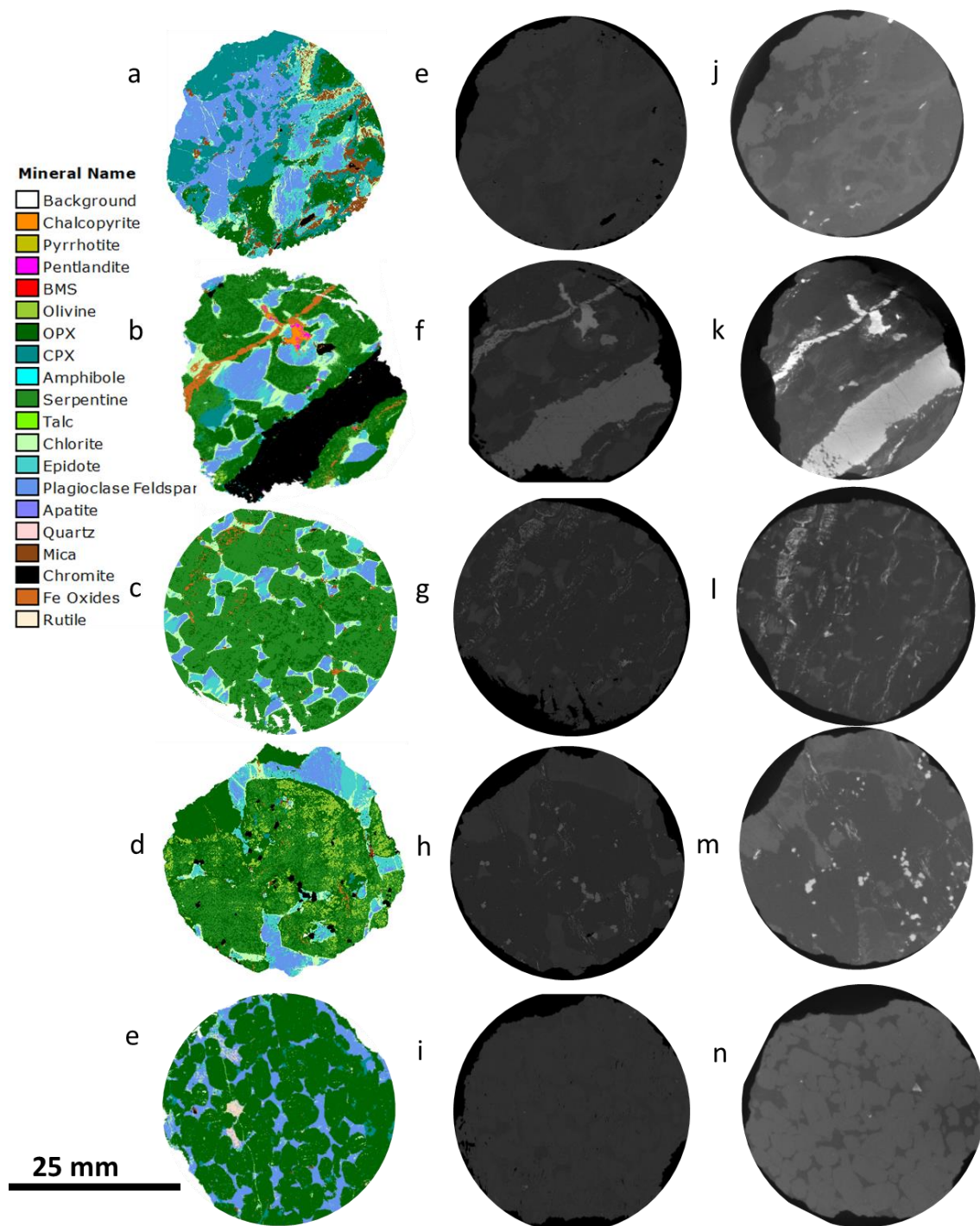


Figure E2: XCT image slices of mini cores selected from drill core RD015. Each slice represents an example of the different lithologies in the stratigraphy: (a-e) QEMSCAN false colour compositional field images. (f-i) QEMSCAN BSE images and (j-n) XCT grey value image slices.

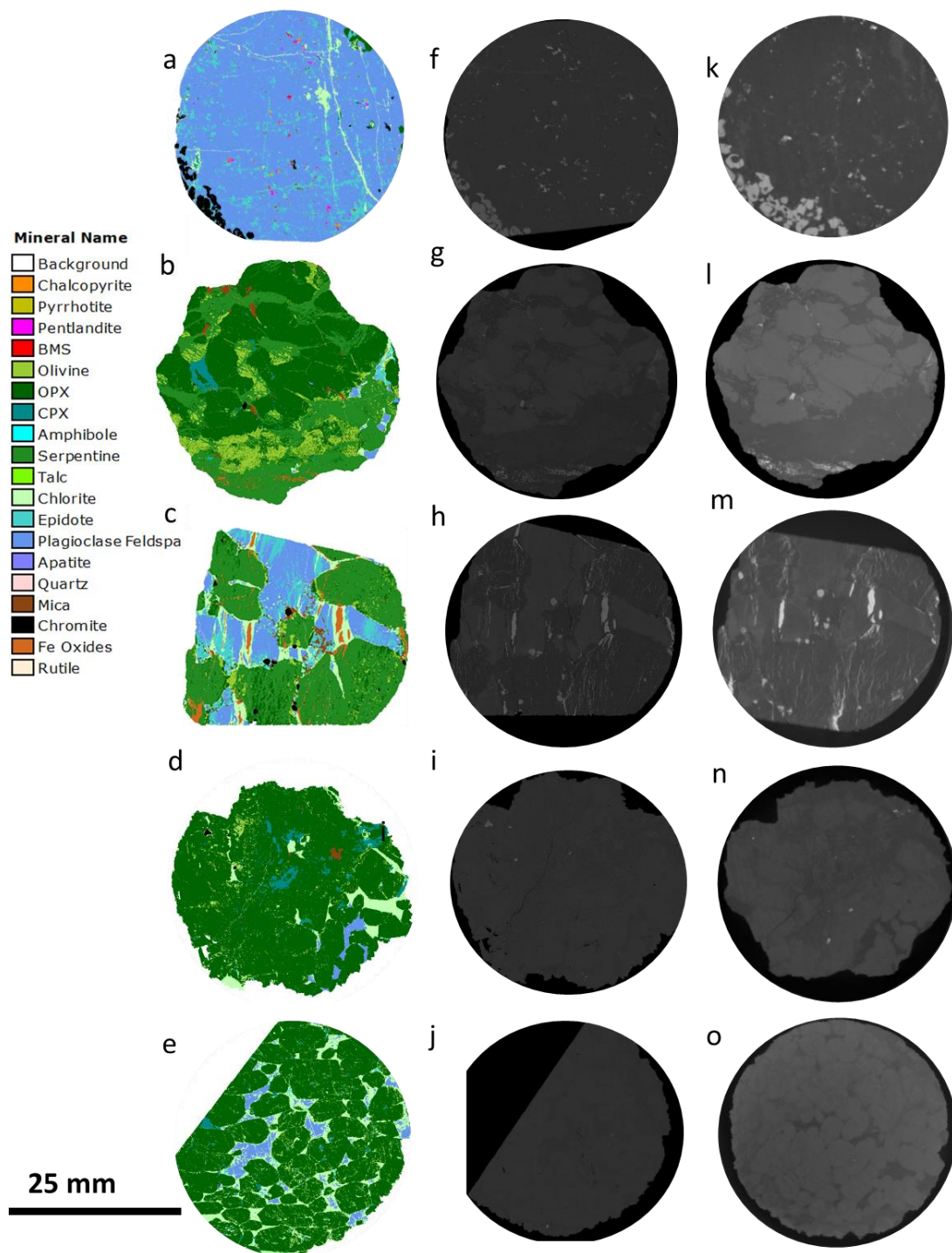
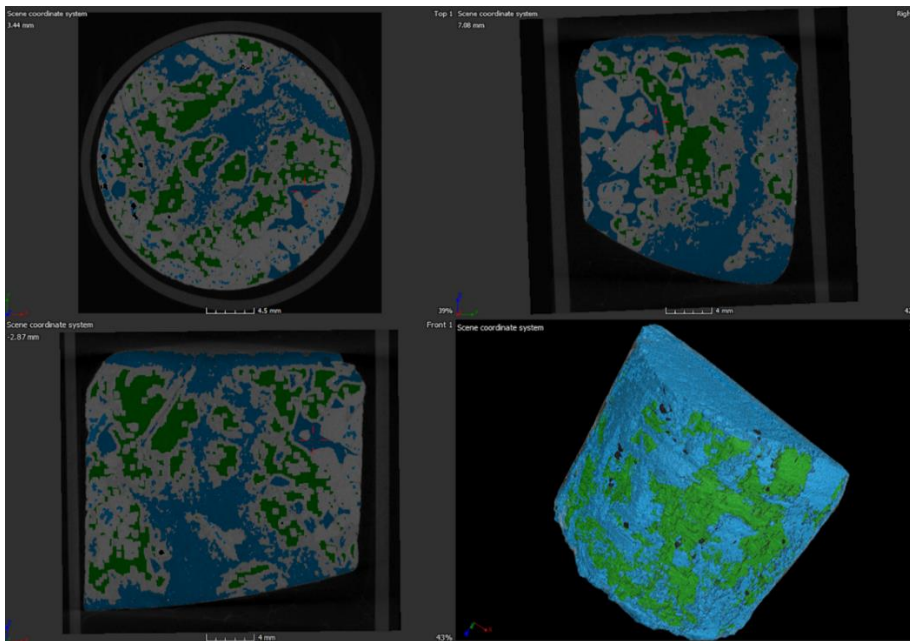


Figure E3: XCT image slices of mini cores selected from drill core RD015. Each slice represents an example of the different lithologies in the stratigraphy: (a-e) QEMSCAN false colour compositional field images. (f-i) QEMSCAN BSE images and (j-n) XCT grey value image slices.

Segmentation



E4: The illustration of the erode-dilate effect in four 3D view.

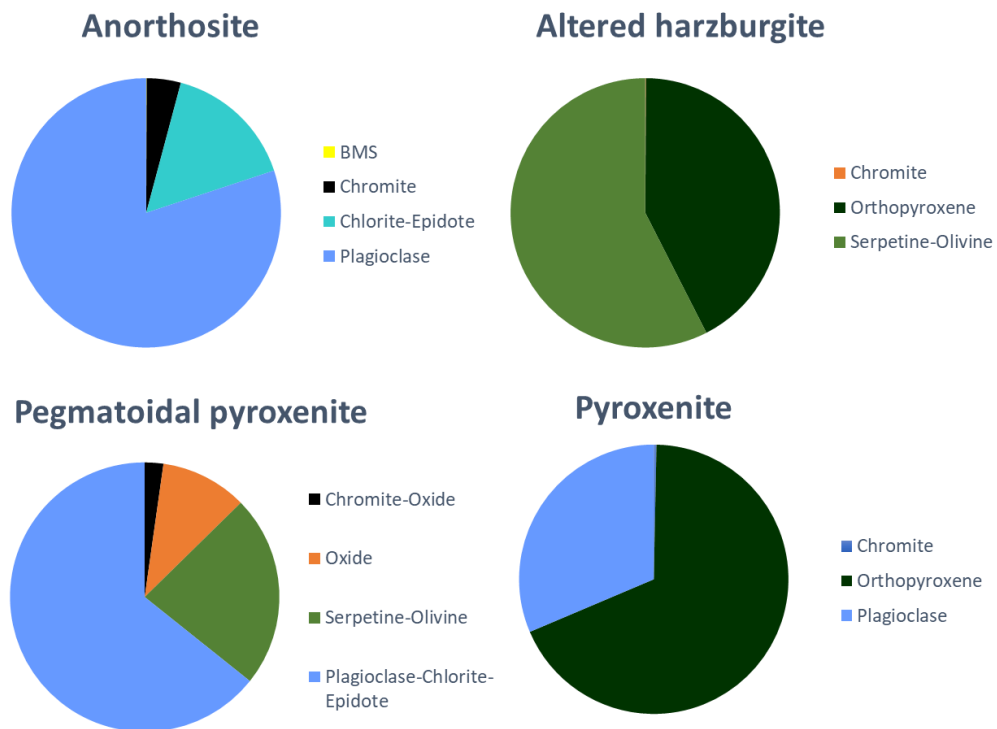


Figure E5: Mineral grades (in volume percent) for rock types in drill core RD015.

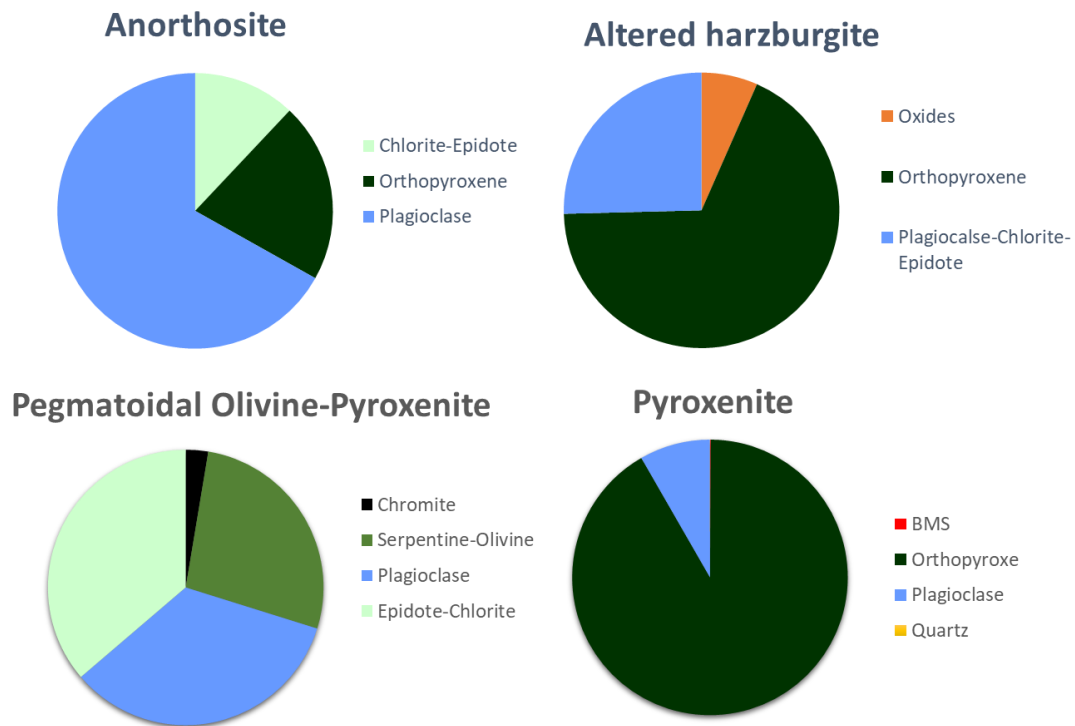
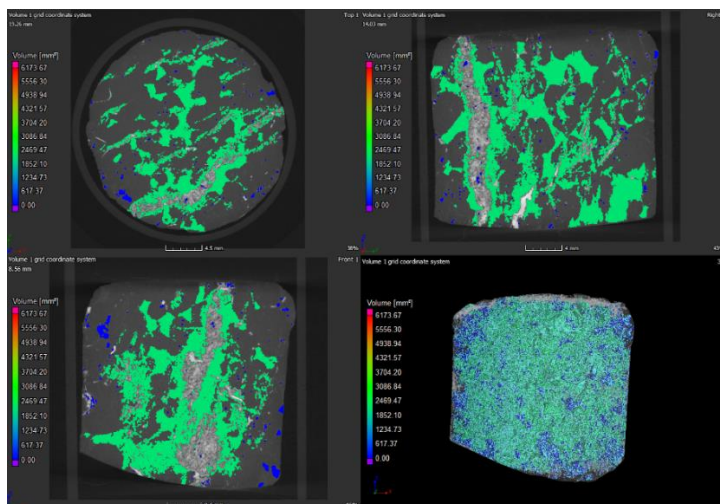


Figure E6: Mineral grades (in volume percent) for rock types in drill core RD015.

XCT Mineral texture



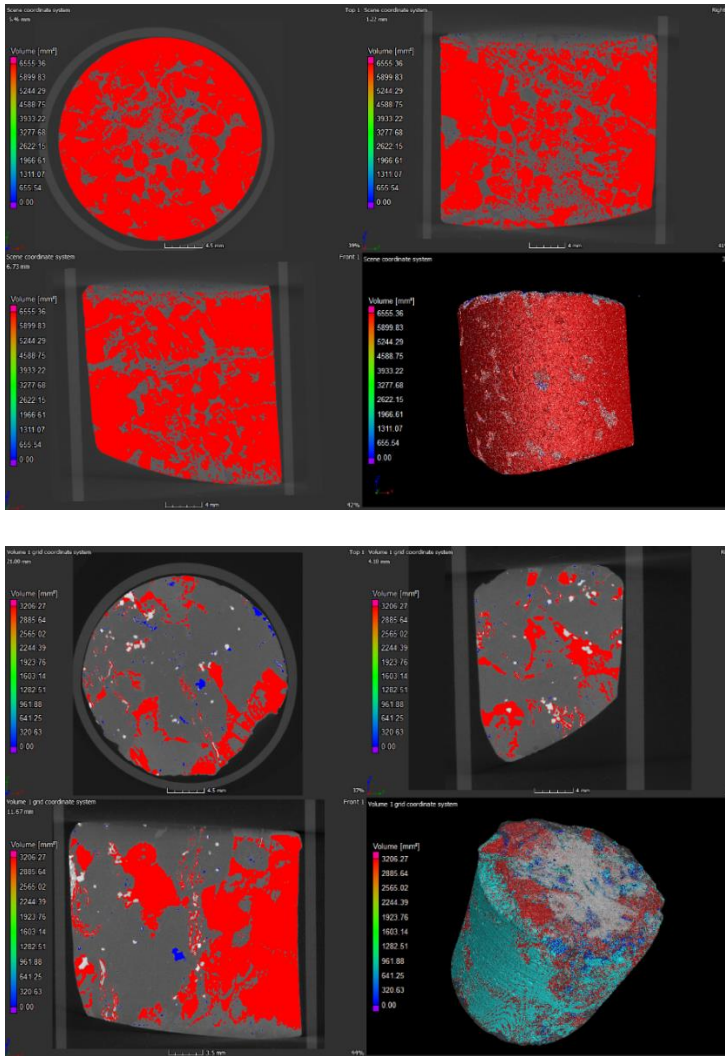


Figure E7: The grain size distribution of XCT grouped according to volume ranges shown in 4 views.

Table E1: Number of grains analysed for grain size for each mineral group used for grain sizes distribution curve.

		QEMSCAN		XCT	
Rock types	Minerals	TU277	RD015	TU277	RD015
Anorthosite	Plagioclase-chlorite	870	499	128403	5356
	OPX-CPX	1289	345	32458	
Altered harzburgite	OPX	226	3305	6061	12005
	Plagioclase-chlorite-epidote	277	-	21268	9231
	Serpentine-olivine	-	2311	-	-
Pegmatoidal pyroxenite	Serpentine-olivine	-	356	-	-
	Plagioclase-chlorite	913	2870	34388	6670
	Serpentine-olivine-OPX	388	3401	2106	4534
	OPX	1064	839	65096	110537

Feldspathic pyroxenite	Plagioclase-chlorite	3199	1715	4634	29556
------------------------	----------------------	------	------	------	-------

Table E2: Uncertainty calculations at 95% confidence interval for mineral grades (at drill core RD015) obtained in QEMSCAN, HSI and XCT, reported by area % (QEMSCAN and HSI) and volume % (XCT).

Rock names	Grouped Minerals	Error %			
		XCT	QEMSCAN	SWIR	LWIR
Anorthosite	Epidote	0.0	0.8	-	27.8
	Orthopyroxene	0.0	1.3	-	42.2
	Plagioclase	0.0	1.0	-	12.7
Altered harzburgite	Spinel-BMS	0.0	5.6	-	-
	Plagioclase-Chlorite-Epidote	0.0	4.2	-	13.6
	Serpentine-OPX	0.0	0.5	2.1	-
Pegmatoidal ol-pyroxenite	Spinel-BMS	0.0	5.3	-	-
	Serpentine-Olivine	0.0	0.7	1.4	-
	Plagioclase	0.0	1.2	-	-
	Epidote-Chlorite-OPX	0.0	0.5	-	7.0
pyroxenite	BMS	0.2	0	-	-
	Plagioclase	0.5	4.0	-	6.7
	Orthopyroxene	4.4	1.0	-	0.6

Appendix F: Online files

- QEMSCAN field images folder for drill core TU277 (**Field 1-6**) and RD015 (**Field 7-12**).
- Hyperspectral mineral maps folder for drill core TU277 for standard cores (**Field 1 and 2**) and mini cores (**1-1 to 2-2**); and drill core RD015 for standard core (**Field 3-4**) and mini cores (**Field 3-3 and 4-4**).
- XCT drill core volumes for drill core TU277 (**Stack 1-12**) and RD015 (**Stack 13-23**).

Files are available online at <https://figshare.com/s/bd7649d42035f9c697d5> or <https://doi.org/10.25375/uct.c.5757911> (once published)